Engineering signaling circuits using a cell-free synthetic biology approach

Engineering signaling circuits using a cell-free synthetic biology approach

PROEFSCHRIFT

ter verkrijging van de graad van doctor aan de Technische Universiteit Eindhoven, op gezag van de rector magnificus prof.dr.ir. F.P.T. Baaijens, voor een commissie aangewezen door het College voor Promoties, in het openbaar te verdedigen op maandag 11 juni 2018 om 16:00 uur

door

Lenny Helena Hendrika Meijer

geboren te Mill en Sint Hubert

Dit proefschrift is goedgekeurd door de promotoren en de samenstelling van de promotiecommissie is als volgt:

voorzitter:	prof. dr. ir. L. Brunsveld
1e promotor:	prof. dr. P.A.J. Hilbers
2e promotor:	prof. dr. M. Merkx
copromotor(en):	dr. ir. T.F.A. de Greef
leden:	prof. dr. ir. P. Jonkheijm (Universiteit Twente)
	prof. dr. C. Storm
	prof. dr. ir. I.K. Voets
adviseur(s):	dr. E. Spruijt (Radboud Universiteit Nijmegen)

Het onderzoek of ontwerp dat in dit proefschrift wordt beschreven is uitgevoerd in overeenstemming met de TU/e Gedragscode Wetenschapsbeoefening.

Cover illustration: Minke Nijenhuis
Printed by: Gildeprint

A catalogue record is available from the Eindhoven University of Technology Library.
ISBN: 978-90-386-4509-4

This work has been financially supported by the Netherlands Organization of Scientific Research (NWO-STIP 717.013.001)

Table of Contents

1

General introduction and outline

Abstract Unravelling the complex organization of molecular networks inside living cells is a key topic of both systems biology and synthetic biology. Simplified model systems have been engineered and constructed under controlled cell-free conditions with the goal of mimicking biological responses of intracellular circuits. These model systems reveal key principles of molecular programs that underlie the biological function of interest. Here, we first present an overview of key studies on cell-free biochemical modules that are able to emulate higher-order dynamics. Additionally, we discuss the effect of retroactivity, a phenomenon resulting from the interconnection of an upstream module to a downstream module. Importantly, while cell-free studies on molecular networks are often performed at high reactant concentrations in a well-stirred dilute environment, the cell's interior is an inhomogeneous crowded environment where reactions between biomolecules occur at low concentrations. We additionally discuss the stochastic nature of cellular reactions resulting from low concentrations of reactants and the effect of macromolecular crowding on biochemical reactions. Finally, we present recent work showing the versatility of programmable biochemical reaction networks in analytical and diagnostic applications.

The work in this chapter has partly been published in:
Hendrik W.H. van Roekel[ǂ], Bas J.H.M. Rosier[ǂ], Lenny H.H. Meijer[ǂ], Peter A.J. Hilbers, Albert J. Markvoort, Wilhelm T.S. Huck and Tom F.A. de Greef – Chemical Society Reviews, **2015**, 44, 7465

[ǂ] contributed equally to this work

1.1 Cell-free biochemical reaction networks

Understanding complex biological behaviour by cell-free reconstitution of purified biological components has been a well-established methodology. Many pioneering studies are concerned with the cell-free reconstitution of existing intracellular networks, such as oscillatory phosphorylation of KaiC by synergistic action of KaiA and KaiB.[1] Indeed, reconstruction of system-level properties of regulatory circuits using purified biochemical components can reveal key design principles and molecular programs that underlie the biological function of interest.[2] The advantage of a cell-free strategy relies on the controllable construction of molecular networks, which are completely defined and can be easily manipulated. Control over each component makes these networks amenable for quantitative and systematic analysis, allowing the extraction of cells network organization and correlated input-output patterns. For example, Lim and coworkers recently applied this strategy to obtain a deeper understanding of Ras GTPase signaling, which is a protein crucial in cell proliferation and morphology.[3] Ras GTPases bind GTP and hydrolyze it to GDP and P_i after which these products are released. However, these processes are very slow and, therefore, regulators that accelerate these reactions, including guanine exchange factors (GEFs) and GTPase activating proteins (GAFs) are essential in the catalytic cycle. While GEFs stimulate product release allowing reloading with GTP, GAFs promote hydrolysis of GTP. Activated Ras interacts with multiple competing downstream effectors in order to initiate signaling cascades. As such, the dynamics of the Ras GTPase cycle is not only determined by the Ras GTPase, but also involves the upstream regulators and downstream effectors. At the time, the biochemical knowledge of Ras and Ras-associated proteins was largely rooted in research towards the individual molecules, rather than a complete system of molecules in which the Ras GTPase can actively cycle. Lim et al. designed various system configurations of cell-free Ras networks (Figure 1.1B) and systemically mapped the effect of different network configurations on the dynamic shape of the system's response. They found that the concentration and type of upstream and downstream signaling proteins strongly affected the shape and timing of the effector response (Figure 1.1C). Furthermore, they showed that different configurations of the Ras system were able to give unique temporal outputs, even if the inputs were the same (Figure 1.1C). Therefore, cells can respond differently by modulating the configuration of Ras-related core proteins to their desired function. Furthermore, they showed that an off balance of the GAFs and GEFs, related to distorted outputs in oncogenic genes, could be restored by Ras-GEF positive feedback mechanisms. By

mapping the influence of each signaling component Lim and coworkers provided qualitative insights and behavioral principles of the information processing of the Ras system.

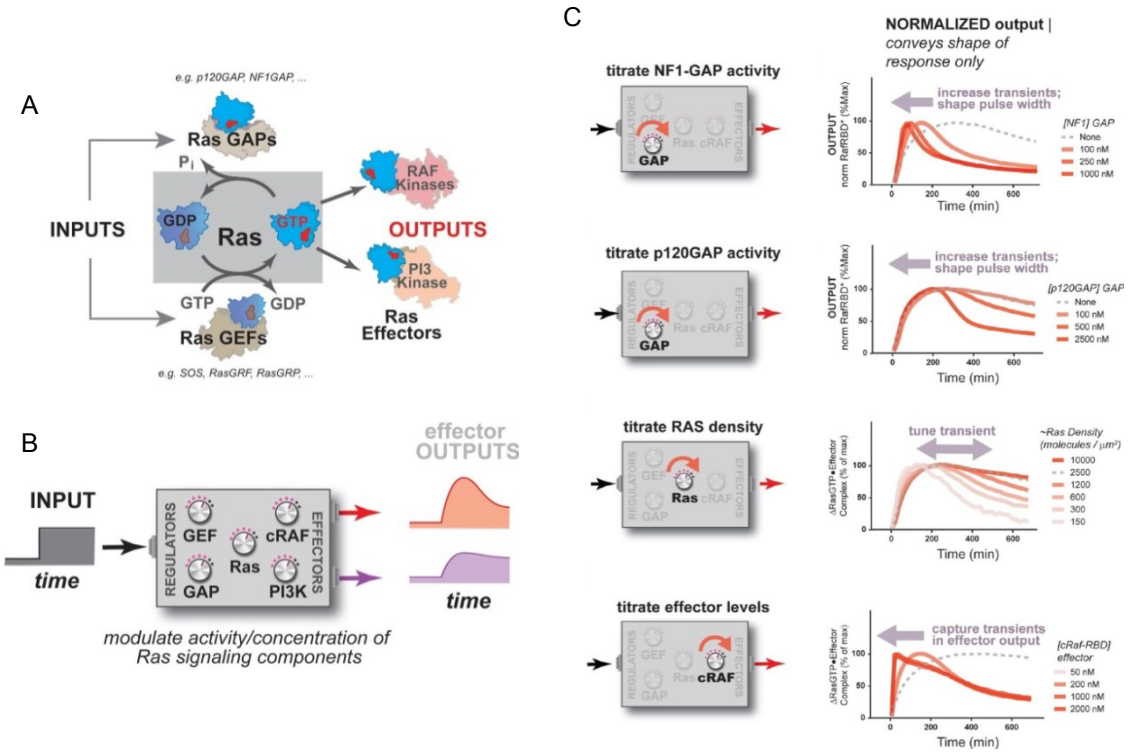

Figure 1.1: The Ras signaling system and its dynamics. A) Illustration of the Ras signaling system in which Ras is activated by guanine exchange factors (GEFs), and is deactivated by GTPase-activating proteins (GAPS). Activated Ras interacts with downstream effectors such as Raf or PI3, resulting in a measurable signal output. B) Simplification of the Ras signaling system, consisting of Ras and Ras regulators and effectors. The response output to an input varies according to the system configuration. C) Schematics and results of experiments in which a fixed step input is applied to different Ras signaling configurations. For each configuration the concentration of a single network component is varied. Figure adapted from reference 3.

Cell-free synthetic biology is concerned with the reconstitution of existing cellular networks and, in addition, the engineering of new model systems naturally not occurring in cells by applying a bottom-up approach. The reconstitution of existing system-level properties in a cell-free environment allows the isolation of the relevant characteristics and interactions that determine the specific system-level behaviour of interest which can now be described mathematically in a framework of simple theories. Bottom-up synthetic biology involves the engineering of new non-existing signaling circuits from scratch. These *de novo* circuits consist of naturally occurring biomolecules or derivatives with well-established functions, which are now used in an unnatural network configuration and, hence, these biomolecules govern the interplay naturally not occurring in cells. In the following section, we will focus on cell-free biochemical reaction networks (BRNs) engineered using the bottom-up approach

displaying various higher-order temporal functionalities including switching and oscillations. We limit the discussion to enzymatically driven systems, *i.e.* those that rely on enzymes to maintain their thermodynamic non-equilibrium state. While non-enzymatic biomolecular networks[4] are highly programmable and useful synthetic biological tools, intracellular networks use enzymatic reactions to achieve their function.

Living systems harness bi- and multistable molecular programs to store information concerning the state of a cell, and subsequently process this information to induce decision-making events. Kim, Winfree and co-workers[5] succeeded in the bottom-up design of a cell-free bistable enzymatically driven circuit based on synthetic deoxyribonucleic acid (DNA) templates known as genelets that are regulated by ribonucleic acid (RNA) transcripts. The researchers developed the so-called genelet toolbox in which RNA polymerase (RNAP) transcribes RNA regulators from genelets that in turn serve as excitatory or inhibitory regulators for the transcription of RNA regulators from other genelets. In this way, the elimination of genes and their associated production and degradation of proteins that are not involved in the circuit allows for systematic analysis by means of a fairly accurate quantitative description that is impossible to achieve in *in vivo* systems or crude cell extracts. In Figure 1.2A, the implementation of a genelet-based bistable switch is shown that consists of transcriptionally active and inactive double stranded DNA (dsDNA) species and interacting RNA regulators. RNA regulators serve as inhibitors I_1 and I_2 of transcription from genelets $\boldsymbol{SW_{21}}$ and $\boldsymbol{SW_{12}}$, respectively, by binding to the respective single stranded DNA (ssDNA) activators $\boldsymbol{A_1}$ and $\boldsymbol{A_2}$. Sequestration of activator DNA prevents formation of fully dsDNA resulting in a significant reduction of transcriptional activity. These reactions are designed to be very specific by appropriate choice of the base sequence. Activation is accomplished by degradation of RNA transcripts bound to the activator ($\boldsymbol{A_i I_i}$) resulting in the release of the sequestered DNA activator. Figure 1.2B shows the corresponding topology of the bistable BRN, while Figure 1.2C displays the experimentally constructed bifurcation diagram with the two activator ssDNA concentrations (A_2^{tot} for $\boldsymbol{SW_{12}}$ and A_1^{tot} for $\boldsymbol{SW_{21}}$) as bifurcation parameters. Figure 1.2D displays the switch activity time courses corresponding to high initial concentration of RNA inhibitor $\boldsymbol{I_1}$ (circles) or high initial concentration of RNA inhibitor $\boldsymbol{I_2}$ (lines). The system remains in the steady state that the investigators initiated, showing that two possible steady states exist. Further experiments to test the bistable circuit on hysteresis suggest that switching between steady states in a single experiment is possible at least once. The characterization of individual genelets proved sufficient for the authors to assemble a

bistable circuit, based on modularity and programmability of the components. The modularity of the genelet-toolbox have also allowed Kim, Murray and colleagues to assemble a synthetic transcriptional network that shows adaptation and fold change detection based on the incoherent feedforward loop (IFFL).[6]

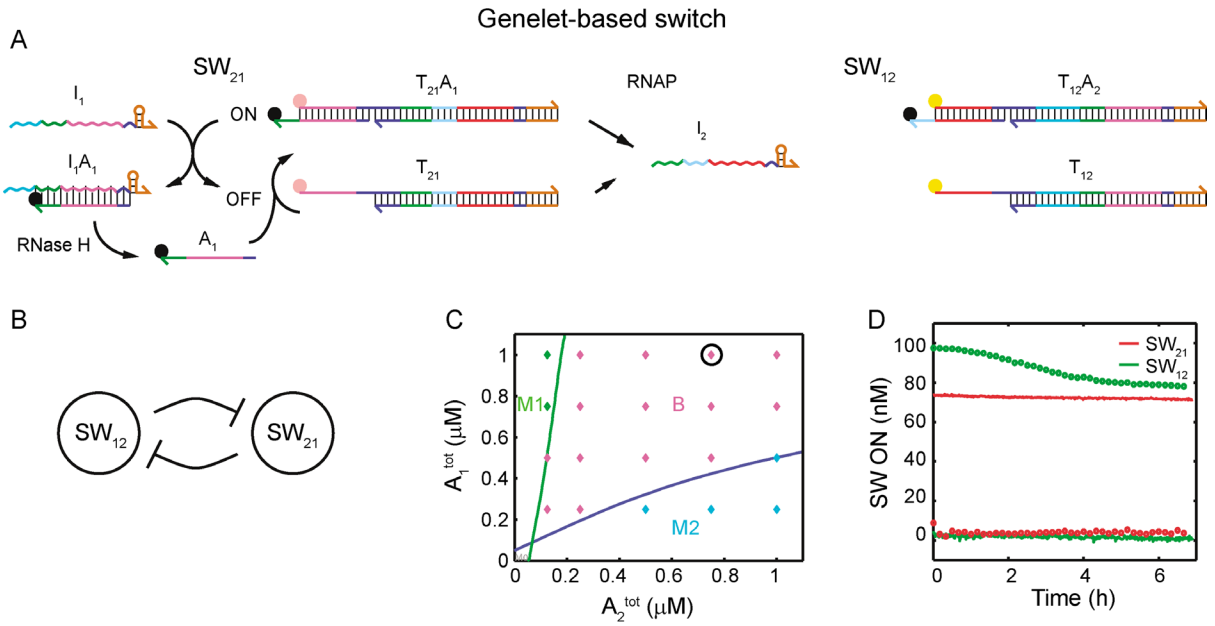

Figure 1.2: Cell-free synthetic genelet-based bistable switche. A) Implementation of the genelet-based switch based on synthetic template DNA from which RNA polymerase (RNAP) produces RNA regulators that in turn serve as excitatory or inhibitory regulators for the transcription of RNA regulators from other genelets, while RNase H degrades regulators from $A_i I_i$ complexes. B) Topology of the reaction scheme in A. C) Experimentally constructed bifurcation diagram, with pink data points corresponding to bistable behaviour. D) Switch activity time courses corresponding to the encircled data point in C, with high initial concentration of RNA inhibitor I_1 (circles) or high initial concentration of RNA inhibitor I_2 (lines). Figure adapted from reference 5.

Rondelez and co-workers[7] used a similar strategy to construct a bistable toggle switch, by introducing a modular toolbox by which biochemical networks of arbitrary complexity can be engineered *de novo* under well-controlled *in vitro* conditions (Figure 1.3A). The toolbox is based on DNA and the enzymes polymerase, exonuclease and nickase (PEN toolbox). Synthetic DNA templates are triggered by short ssDNA strands acting as regulating signals on the production of an output signal. Activation of templates by these ssDNA signals enables DNA polymerase to extend the oligomer-template pair resulting in fully hybridized dsDNA. Subsequently, these dsDNAs are nicked resulting in double-stranded complexes. Because these reactions are performed at a temperature close to the melting temperature of the partial duplexes, the input and output ssDNAs dissociate from their templates. Templates are inhibited by ssDNA strands that are complementary to part of the template's sequence, lack a

nickase recognition site and possess a two-base mismatch at their 3' ends which prevents extension of the partial duplex, rendering the template strand inactive. Signal and inhibition strands are degraded over time by exonuclease from which the template strands are protected by phosphorothioate modifications at their 5' ends. Figure 1.3B shows the six templates that comprise the toggle switch. Two templates, ***αtoα*** and ***βtoβ*** autocatalytically produce ssDNA species ***α*** and ***β*** while templates ***αtoiβ*** and ***βtoiα*** produce inhibitors upon activation by ***α*** and ***β*** respectively. These four templates comprise the bistable core (Figure 1.3C). Positive feedback is necessary in this system as reciprocal inhibition alone does not provide the ultrasensitive response necessary for bistability. To independently switch the system between the ***α***- and ***β***-state two additional templates, *i.e.* ***γtoα*** and ***δtoβ*** were employed (Figure 1.3B-C). The authors computationally predicted switching to the ***β***-state by addition of single-stranded ***δ*** and switching to the ***α***-state by addition of single-stranded ***γ*** (Figure 1.3D) and verified the bistable behaviour of the circuit experimentally (Figure 1.3E). The circuit could be switched two consecutive times in a single experiment after which resources were depleted and the concentrations of templates became too low, leading to loss of functionality of the switch. Finally, the authors presented the construction of a push-push memory circuit that responds to a single input that switches the state of the bistable core. Due to the size of the circuit (eight template strands), the reaction times of the push-push circuit are large and the circuit could only be switched once. Nonetheless, the size of the circuit is comparable to *in vivo* complexity of eight genes, which is amongst the largest realizations of synthetic genetic regulatory networks performed in cells. Moreover, the systematic engineering of the push-push circuit further demonstrates the modularity of the PEN toolbox.

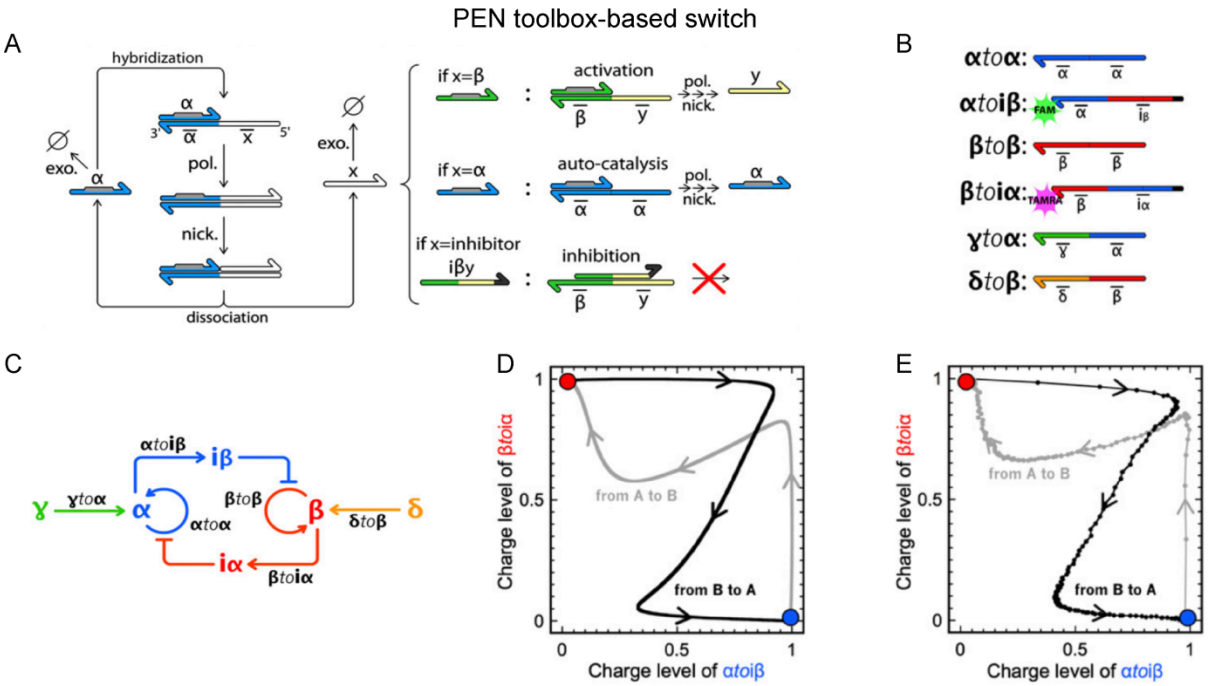

Figure 1.3: Cell-free PEN-based bistable switches. A) Reactions in the PEN toolbox: activator ssDNA α primes the synthetic template, after which it is extended by DNA polymerase resulting in dsDNA. Nickase cleaves this dsDNA in the backbone of the newly formed strand, resulting in dissociation of signal strand X. Depending on the sequence of X, three types of reactions can occur, *i.e.* activation, autocatalysis and inhibition. B) The six synthetic DNA templates of the bistable switch shown in G. C) Topological representation of the PEN toolbox-based switch. The single-stranded input signals γ and δ induce switching to the α- and β-state, respectively. D) Simulated predictions of switching to the β-state by δ (grey line) and of switching to the α-state by γ (black line). E) A single switching experiment starting in the α-state, which is first switched to the β-state by δ (grey line), and subsequently switched back to the α-state by γ (black line). Figure adapted from reference 7.

To even further predict *in silico* the dynamical behaviour of cell-free PEN-based reaction networks, De Greef and colleagues,[8] developed an automated approach in which PEN-based DNA circuits of arbitrary complexity were screened for prespecified temporal behaviour. Additionally, the authors reported software that optimizes the template sequences for which the biochemical network robustly shows the desired non-equilibrium behaviour, narrowing the gap between *in silico* prediction and *in vitro* realization of PEN-based circuits. The researchers verified their method by applying it to the previously described enzymatic DNA-based oscillator (*vide supra*) and used it to design a PEN-based adaptive BRN *in silico*.

Oscillations are a canonical example of out-of-equilibrium behaviour. Recently, several *in vitro* biochemical circuits exhibiting oscillations have been reported. Here, we highlight several pioneering studies in which oscillatory dynamics have been engineered in enzymatically driven networks, DNA circuits and cell-free transcription-translation-based systems, both under batch conditions and in open reactors. Examples of oscillating BRNs that

function under batch conditions include cell-free *in vitro* biochemical oscillators based on the genelet toolbox (Figure 1.4A) and the PEN toolbox (Figure 1.4B). Kim and Winfree constructed an oscillator using the genelet toolbox, which consists of two synthetic DNA templates that comprise a delayed negative feedback loop.[9] Two genelets, regulated by RNA activator $\boldsymbol{rA_1}$ and RNA inhibitor $\boldsymbol{rI_2}$ transcribed from genelet templates $\boldsymbol{SW_{12}}$ and $\boldsymbol{SW_{21}}$ respectively, govern the oscillatory behaviour. The circuit could show up to five complete cycles. The researchers then added a positive feedback loop with the use of a third genelet that modulated and extended the oscillatory regime and, importantly, demonstrated the modularity of this system. Rondelez and co-workers constructed a PEN toolbox-based oscillator (Figure 1.4B),[10] in an analogous manner as described for their bistable switch. The network topology consists of autocatalytic synthesis of primer $\boldsymbol{\alpha}$ which activates synthesis of primer $\boldsymbol{\beta}$ which in turn serves as a primer for the production of inhibitor $\boldsymbol{inh}$. Delayed inhibition of the autocatalytic synthesis of primer α results from the reversible sequestration of oligomer $\boldsymbol{inh}$ to $\boldsymbol{T_1}$. Highlighting the versatility of the methodology, the same group designed an *in vitro* enzymatic DNA-based network that emulated the complex dynamics of ecological systems,[11] including predator-prey oscillations, competition-induced chaos, and symbiotic synchronization.

Several groups have successfully engineered oscillating BRNs in open chemostats. Huck *et al.*[12] constructed a trypsin-based enzymatic oscillator under flow conditions and provided a modular approach to rationally design dissipative, tuneable and robust chemical networks. The methodology is based on translation of a basic network topology known to generate oscillations, *i.e.* a short positive feedback loop in combination with a delayed negative feedback mechanism. Positive feedback is implemented by autocatalytic production of trypsin ($\boldsymbol{E_1}^*$, Figure 1.4C) from trypsinogen ($\boldsymbol{E_1}$), while delayed inhibition is realized by a masked inhibitor that is converted in a fully active inhibitor by an enzymatic cascade based on trypsin and aminopeptidase. As the two enzymes that make up the negative feedback loop show a high selectivity towards their substrates, the rate of each step could be independently tuned. Using mathematical modelling, the correct balance between production and inactivation of trypsin necessary for sustained oscillatory behaviour was established resulting in sustained oscillations in the experimental concentration of trypsin for a wide range of flow rates. Furthermore, the authors show signal modulation by coupling of two biochemical networks each in a separate fluidic reactor, and by coupling of the out-of-equilibrium enzymatic network to complex coacervates.

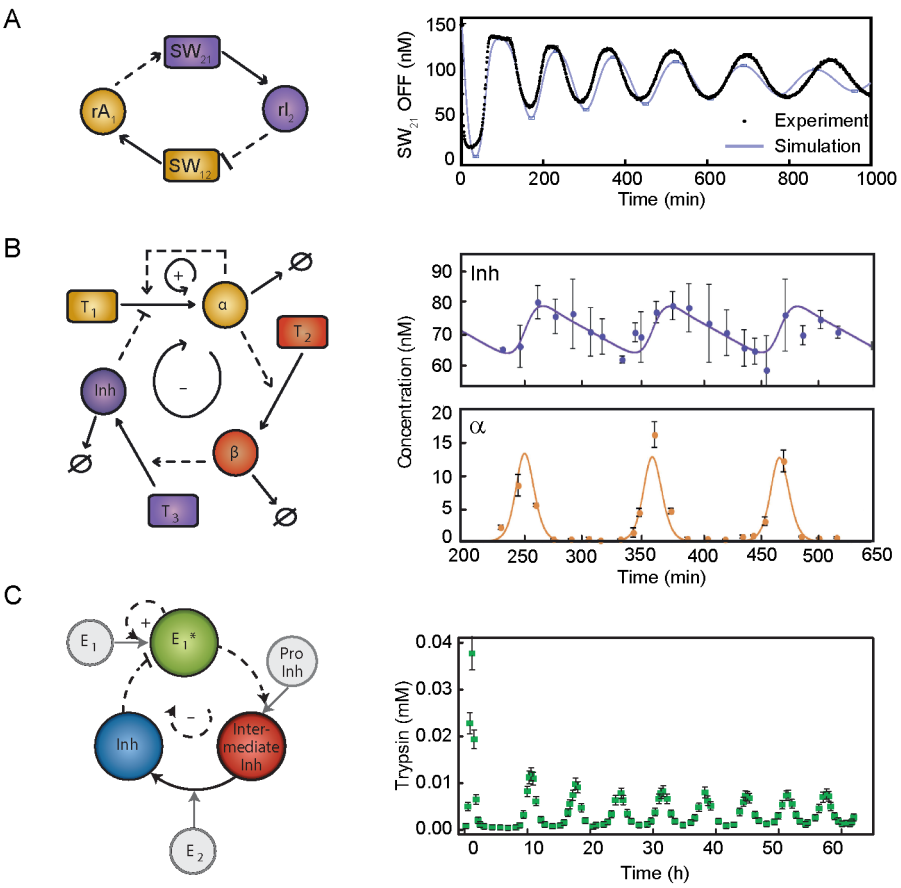

Figure 1.4: Oscillatory molecular networks designed *de novo*. A) Schematic representation of a genelet oscillator regulated by RNA activator ***rA1*** and RNA inhibitor ***rI2*** transcribed from genelet templates ***SW12*** and ***SW21*** (left). Experimental and simulated traces of the transcriptional oscillator. Figure adapted from reference 9. B) Schematic representation of the PEN-based oscillator, including autocatalysis, activation, inhibition and degradation of primers and single-stranded DNA strands (left). The oscillatory traces of single stranded species from experiments (dots) are shown on the right and can be fully described by a computational model (line). Figure adapted from reference 10. C) Schematic representation of the trypsin-based enzymatic oscillator (left). Experimental traces show sustained oscillations in the concentration of trypsin for approximately 65 hours. Figure adapted from reference 12.

Cell-free transcription and translation chemistry (TxTl) allows the engineering of biomolecular circuits based on transfer of information between genes. Because the transcription and translation rates of cell-free TxTl systems decrease in time under batch conditions, experiments need to be conducted in a continuous flow setup allowing constant steady-state transcription and translation rate by exchange of reagents. Maerkl *et al.* constructed and implemented a genetic oscillator using pneumatically controlled microfluidic reactors with volumes in the nanoliter regime.[13] Importantly, the genetic oscillator was subjected to continuous flow allowing exchange of reagents and forcing the system out-of-equilibrium resulting in sustained oscillations for extended periods of time (Figure 1.5A). The circuit design combines a short range positive feedback loop with delayed repression. The

positive feedback loop is based on an autogene consisting of a gene encoding for T3 RNA polymerase and its cognate T3 promoter. Inhibition of the autogene is achieved by production of TetR repressor which binds to TetR operator sites on the T3 promoter of the autogene. Because production of TetR repressor has to be delayed to achieve sustained oscillations, the authors introduced an Amber stop codon in the *tetR* gene resulting in premature termination of *tetR* mRNA translation. The translation rate can be increased by production of Amber suppressor tRNA which is in turn under control of the T3 autogene. Inspection of the phase diagram of the cell-free TxTl oscillator with respect to the *supD* DNA template concentrations and the dilution rate reveals that oscillations are observed for almost all concentrations of *supD* template. Furthermore, it reveals a decrease in the oscillation period with increasing dilution rate with oscillatory behaviour generally being established at high dilution rates. Showing the generality of cell-free TxTl systems as a tool to engineer programmable molecular circuits, Bar-Ziv, Noireaux and colleagues assembled artificial cells based on two-dimensional compartments containing DNA-brushes. Programmable protein synthesis is achieved by diffusion of *Escherichia coli* (*E. coli*) cell extract through thin capillaries that connect the compartments to a central feeding channel (Figure 1.5B).[14] Oscillatory dynamics of the genetic network is accomplished by a mixed DNA-brush encoding for an activator-repressor gene network in each compartment. The temporal period in the activator concentration scaled linearly with the length of the capillary channel, demonstrating the effect of diffusion and compartment geometry on oscillatory dynamics under non-stirred conditions. Moreover, by separating DNA-brushes encoding activator and repressor proteins into two connected compartments, the researchers demonstrated diffusion-based information transfer resulting in a spatiotemporal pulse with a period that scales linearly with the distance between the respective compartments.

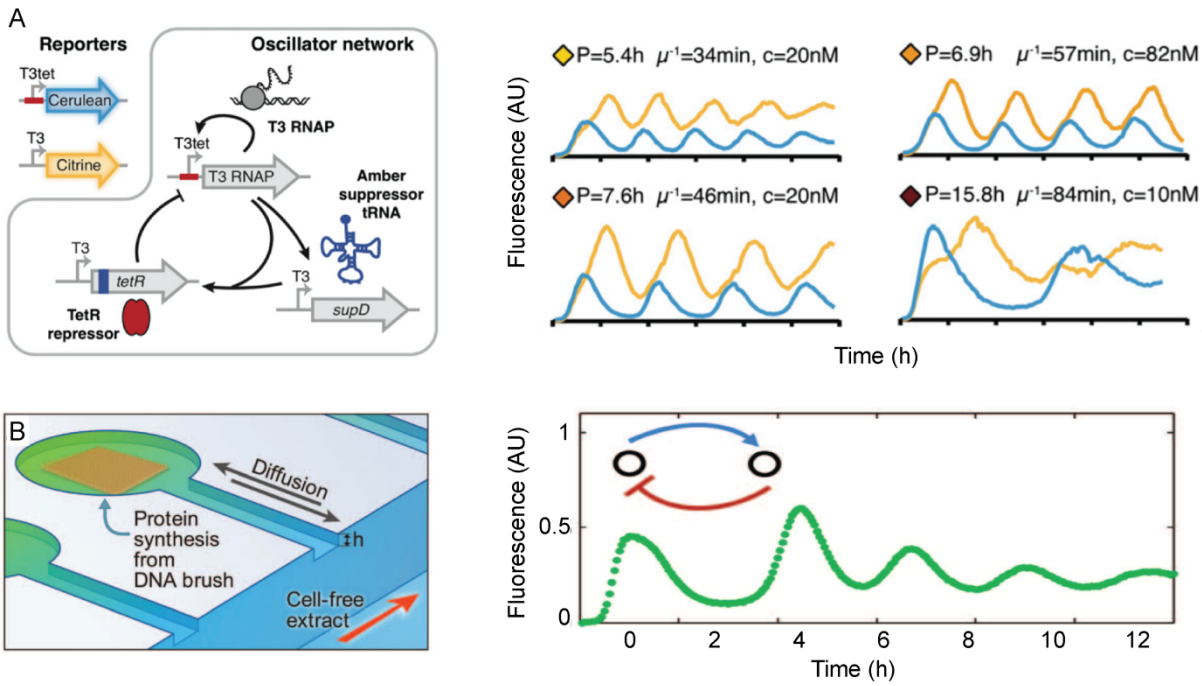

Figure 1.5: In vitro oscillators based on cell-free transcription and translation. A) Operation scheme of the genetic oscillator consisting of an autocatalytic loop and delayed inhibition (left). The dynamic state of the system is measured using Cerulean and Citrine which are produced in parallel to T3RNAP and TetR repressor respectively. Oscillatory traces of Cerulean and Citrine show varying profiles and periods (P) at different supD gene concentrations (c) and different residence times (μ^{-1}) (right). Figure adapted from reference 13. B) Left: Design of the microfluidic chip in which DNA brushes are assembled in circular compartments and are connected through a capillary to a feeding channel. Activator-repressor genetic networks are assembled with sigma factor for activation and the lambda phage cI for repression. Right: GFP profile of oscillatory gene dynamics in an activator-repressor network measured in the compartment. Figure adapted from reference 14.

The above studies illustrate enzymatic and enzymatically driven nucleic acid-based reaction networks that display complex high-order temporal functionalities using a minimal set of components. Clearly, cell-free synthetic biologists are capable of emulating temporal out-of-equilibrium dynamics using a relatively small number of biomolecular components. Furthermore, these minimal systems are amenable to systematic design and quantitative analysis and, thereby, provide a framework in which the effect of the individual components to the overall dynamics can be studied in detail.

1.2 Modularity and Retroactivity

The definition of 'modularity' refers to a system consisting of independent modules which can be separated and recombined while keeping their internal function. It is therefore no surprise that well-characterized modular units are desired in the field of bottom-up synthetic biology as this allows the construction of large networks in a predictable manner. However, the interconnection of modules inevitably changes the dynamics of the upstream module, a

phenomenon known as retroactivity (Figure 1.6). For example, consider a water tank with an inlet and an outlet pipe and take a constant input flow as input and the pressure at the outlet pipe as output. Connecting the outlet pipe to a second barrel will increase the pressure at the outlet pipe and, hence, retroactivity to the output arises. Moreover, when the output flow is comparable to the input flow the downstream connection results in an increasing water level in the tank and possibly also affects the input flow. In other words, retroactivity to the input is low when the output flow is large compared to the input flow.

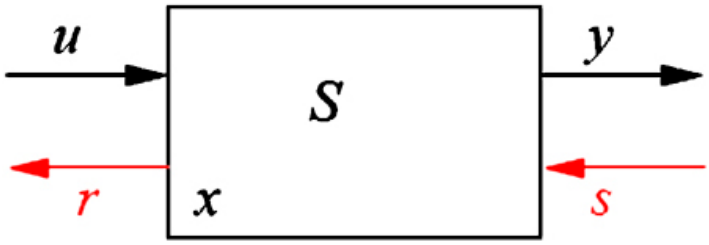

Figure 1.6: Symbolic representation of an input-output system connected to a downstream component. ***S*** denotes the system which has an internal state *x*, whereas ***u*** and ***y*** represent the input and of the system respectively. Interconnection of a downstream component results in retroactivity to the output (***s***) and retroactivity to the input (***r***). Figure from reference 15.

Del Vecchio and coworkers extensively studied *in silico* the effect of retroactivity on the output dynamics of an upstream transcriptional network resulting from interconnection to a downstream component (Figure 1.7).[15] The upstream network consists of a single gene which produces protein ***X*** (output) by activation of transcription factor *Z* (input). Protein ***X*** can reversibly bind to the downstream component and can be degraded. Figure 1.7A displays simulated results of the time evolution of ***X*** with a sinusoidal input function in presence and absence of the downstream component. Indeed, binding of ***X*** to the downstream component changes the dynamics of the upstream circuit. By singular perturbation analysis the authors show that retroactivity is small when the binding affinity of ***X*** to the downstream component is low or when the amount of ***X*** is large compared to the number of downstream component. Importantly, given a defined affinity of ***X*** with the downstream component and a defined number of downstream components, they revealed two methods to decrease retroactivity. Figure 1.7B displays an insulating device enabling insulation of the upstream and downstream transcriptional components by input amplification in combination with a negative feedback mechanism. The negative feedback mechanism is based on enhanced degradation of ***X*** by protease ***Y***, which is expressed from gene ***y***. The production rate of ***X*** and ***Y*** are controlled by the same gain parameter (*G*). The authors mathematically show that an increasing *G* results in

increased attenuation of retroactivity. Furthermore, this was also supported by simulations for which the results are displayed in Figure 1.7B. Besides, attenuation of retroactivity can also be achieved by separation of timescales between the dynamics of the upstream circuit and the dynamics at the interconnection of the upstream and downstream components. The authors theoretically analysed this situation with a model system (Figure 1.7C) in which ***Z*** phosphorylates protein ***X***, which is present in excess. Phosphorylated ***X***, $\boldsymbol{X_P}$ binds to the downstream component or is dephosphorylated by phosphatase ***Y***, which is also present in excess. Hence, the negative feedback relies on the action of the phosphatase that converts active protein to an inactive form. Del Vecchio and coworkers show mathematically and by simulations (Figure 1.7C) that retroactivity to the output is attenuated when the timescale of the phosphorylation-dephoshorylation reactions is much faster than the timescale of producing and degrading ***Z***. Besides *in silico* analysis, Del Vecchio and coworkers realized an *in vivo* model system in which retroactivity on the temporal dynamics of a gene transcription module was analysed.[16] The gene module produces repressor LacI which can reversibly bind to the downstream component. Interestingly, in the presence of the downstream component, the response of the module to induction showed a time delay, while a faster response was observed upon de-induction. This shows that the effect of retroactivity depends on the history of the system and was further supported with a theoretical model.

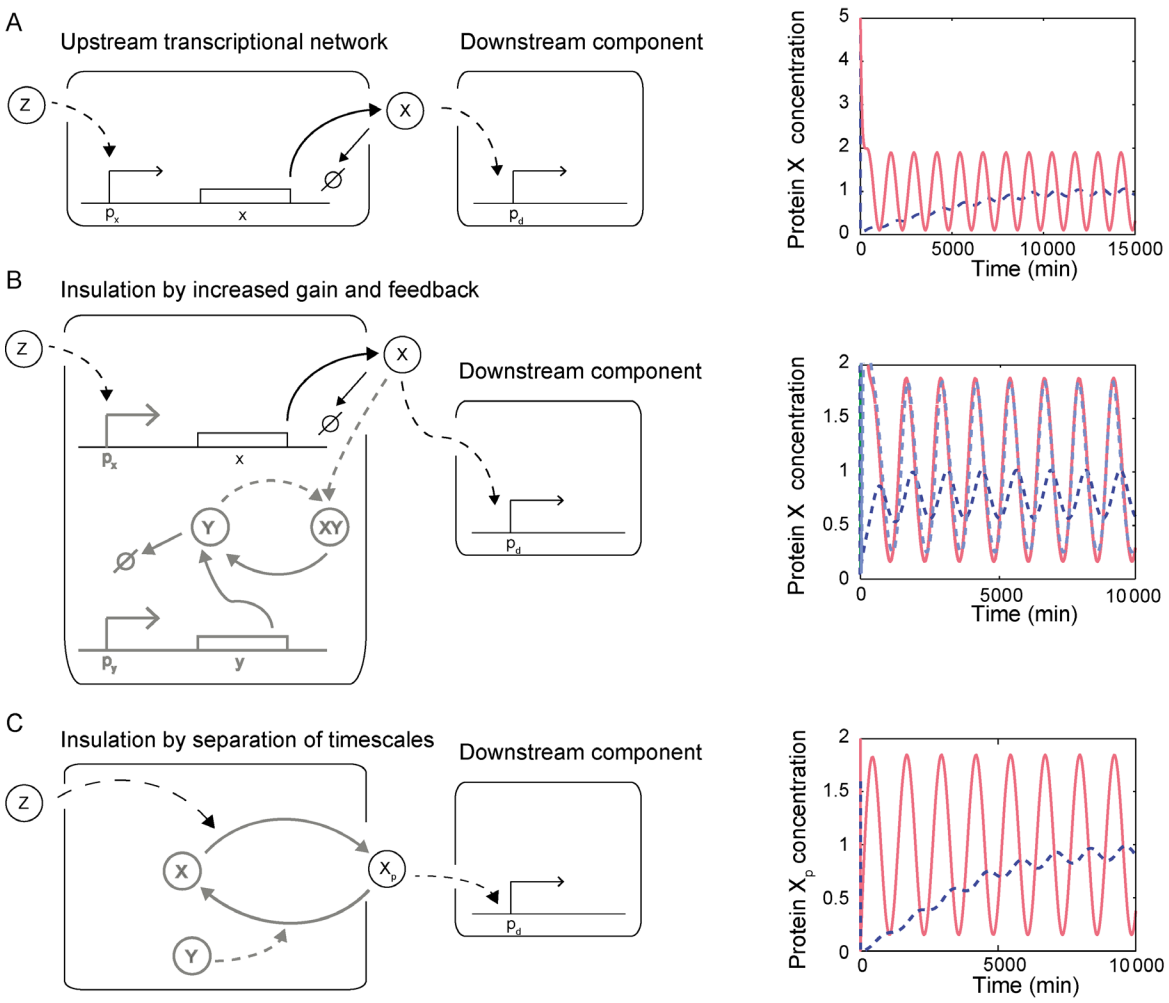

Figure 1.7: Retroactivity and insulation. A) Illustration of the in silico analysed transcriptional network and the downstream component. Transcription factor ***Z***, which is the input of the transcriptional component, reversibly binds to the promoter p_x and thereby activates gene expression resulting in protein ***X***. Protein ***X*** can be either degraded or can bind to the promotor p_d of a downstream load. The graph shows the time evolution of ***X*** of simulations given input ***Z*** a sinusoidal function, in absence (red) and presence (blue) of the downstream component. B) Schematic of the transcriptional component complemented with an insulation device (grey) and the downstream load. Insulation to the output ***X*** of the upstream circuit relies on input amplification in combination with a negative feedback loop. The negative feedback loop comprises the expression of protease ***Y*** from a constitutive promoter, which reversibly binds to ***X*** followed by the degradation of ***X***. The production rate of *X* and *Y* are controlled by the same gain parameter (*G*). The graph shows the time evolution of ***X*** given input ***Z*** a sinusoidal function, in absence (red) and in presence of the downstream component with G=10 (light purple) and G=1 (dark purple). Simulations were performed with the same parameter values as in (A). C) Schematics of the insulation device (grey) and the downstream load. Insulation is achieved by by phosphorylation and desphosphorylation of ***X***. To this end, ***Z*** reversibly binds to ***X*** after which **X** is phosphorylated (X_p). The negative feedback loop comprises the reversible binding of phosphate ***Y*** to X_p followed by dephosphorylation of X_p. to ***X***. Activated ***X***, X_p can reversibly bind to the downstream load. The graph shows the time evolution of ***X*** of simulations given input ***Z*** a sinusoidal function, in absence (red) and in presence of the downstream component with fast (light purple) and slow (dark purple) phosphorylation and dephoshorylation. Figure adapted from reference 15.

To further explore the modularity and resilience of the system, Murray, Simmel and co-workers[17] coupled the transcriptional genelet oscillator (*vide supra*) to several downstream loads including a DNA-based nanomechanical device and the production of a functional RNA molecule (Figure 1.8). Different mechanisms were employed to couple the oscillator to several downstream processes, and for each mechanism the impact of the load on the performance of the upstream 'core oscillator' was assessed on key characteristics such as the frequency and amplitude of the oscillatory response. Reduction of retroactivity and efficient activation of the downstream reaction circuit was achieved when the coupled process was driven by appropriately fast kinetics in combination with a high-amplitude oscillatory signal. The authors achieved near zero retroactivity with the introduction of a genelet module that functions as an insulator. The insulator is activated by DNA strand $\boldsymbol{A_2}$ and inhibited by RNA strand $\boldsymbol{rl_2}$, which are utilized and produced by the core oscillator respectively (Figure 1.8A-B). The insulator acts as an amplifier because small increases in the active genelet (only mildly affecting the core oscillator) drives transcription of large amounts of RNA transcript ***InsOut*** that controls the opening of a DNA tweezer. Degradation of ***InsOut*** occurs fast enough for the tweezer to follow the oscillations of the core BRN by periodically opening and closing (Figure 1.8C). Therefore, the insulator module not only demonstrates the modularity of the genelet toolbox but also greatly improves the utility of *in vitro* BRNs as insulation of the core circuit allows these networks to be utilized to drive functional downstream processes for example in DNA-based diagnostics.

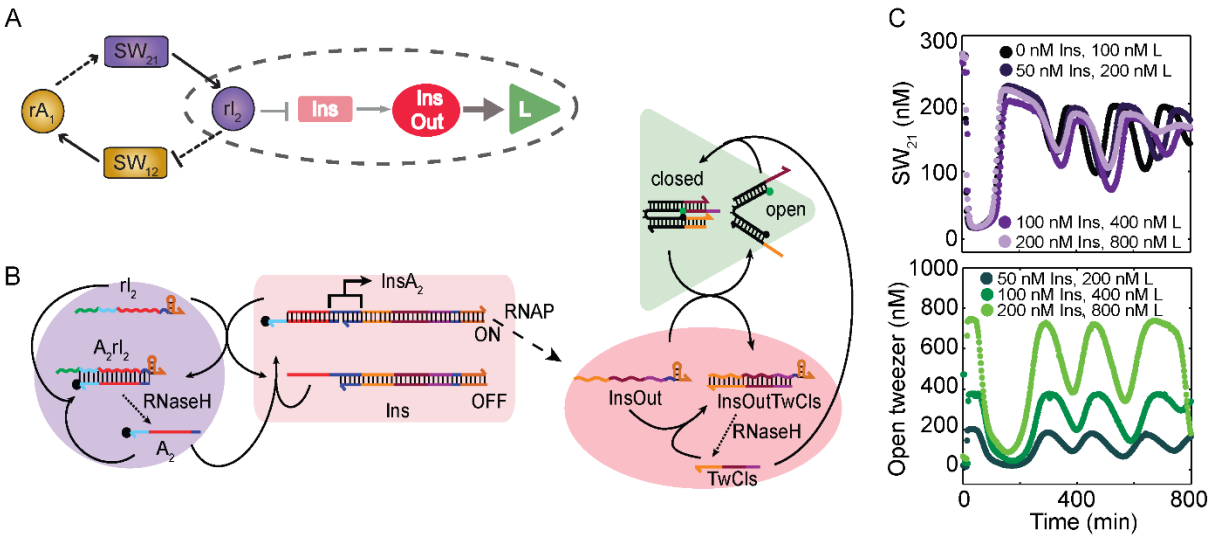

Figure 1.8: A) Schematic representation of a genelet oscillator coupled downstream to a load *via* an insulator module. B) Implementation of the genelet-based insulator based on synthetic template DNA from which RNAP produces RNA regulator ***InsOut*** that in turn opens the tweezer by displacing ***TwCls***. The insulator is inhibited by RNA regulator ***rI2*** which displaces activator ***A2*** from ***InsA2***. RNase H degrades regulators from ***A2rI2*** and ***InsOutTwCls*** complexes. C) Experimental traces of the transcriptional oscillator coupled to a downstream system shows the insensitivity of the system towards the load (the DNA tweezer) for various insulator and load concentrations. Figure adapted from reference 17.

From the point of view of constructing molecular systems *de novo*, it is desirable to have modular structures and, hence, low retroactivity at the interconnections between modules. However, it is not necessary that retroactivity has to be low for the functioning of a network, because parts of the system may have been finely tuned to work well with each other in a specific interconnected configuration. Moreover, retroactivity from sharing of resources can even provide additional robustness to molecular circuits.[8,18,19] Whether natural systems have been evolved with low retroactivity at the interconnections of functional units is a challenging question. Jacob, Alon and Hartwell suggest that modular structures convey an advantage over non-modular structures in evolutionary change.[20-22] Modular structures allow changes in a particular function of a cell by the reconfiguration of the connections between modules while the core functions embedded in the discrete modules remain unchanged. Moreover, optimizing a particular function of a cell in a non-modular configuration would be hard, because an improvement of one function probably goes along with a deterioration of another function. Supporting this idea, proteins that have many binding partners such as histones, actin and tubulin barely changed during evolution. Furthermore, theoretical studies have shown that mutations are less common when it affects multiple components.[23]

1.3 Stochastic effect and molecular crowding

While the construction of cell-free reaction networks has provided fundamental understanding of network structure and correlated function, these cell-free systems are not always representative of cellular environments as they are often studied under bulk test tube conditions in a well-stirred dilute mixture. Here, we focus on two factors which are mostly not included in cell-free studies of biochemical reaction networks but which significantly contribute to the dynamics and kinetics of reaction networks in cells including the low number of reactants and macromolecular crowding.

Stochastic biochemical reactions

Biochemical reaction networks inside cells involve many different biomolecules. Yet, the concentration of each biomolecule is rather low and, hence, a degree of randomness in these reaction networks is expected. It is generally accepted that the variation in gene expression results from the low number of reactants together with the stochastic nature of molecular collisions by diffusion.[24-26] Variation or noise in gene expression occurs in various molecular systems[27-29] and has been studied in different cells including prokaryotes and eukaryotes[30-32] as well as in stem cells,[33] cancer cells[34] and cells expressing viruses.[35] Importantly, protein expression involves multiple chemical steps each of which arguably contributes to the total fluctuation in protein level.[36] Several studies revealed important insights in how cells can exploit or suppress noise. Elowitz experimentally explored the cause of variation in gene expression and introduced the concepts of extrinsic and intrinsic noise (Figure 1.9),[37] which were mathematically analysed by Swain et al.[38] Extrinsic noise arises from fluctuations in the cellular state or composition and results in differences in gene expression between cells while fluctuations of gene expression of identical genes within one cell are correlated. By contrast, uncorrelated fluctuations of protein expression from two identical genes within a cell resulting from the stochasticity of biochemical processes or other factors, is considered as intrinsic noise. The two-gene reporter system developed by Elowitz et al. has been used as a reliable method to estimate[39] intrinsic and extrinsic noise of gene expression *in vivo*[32,40] and *in vitro*[41].

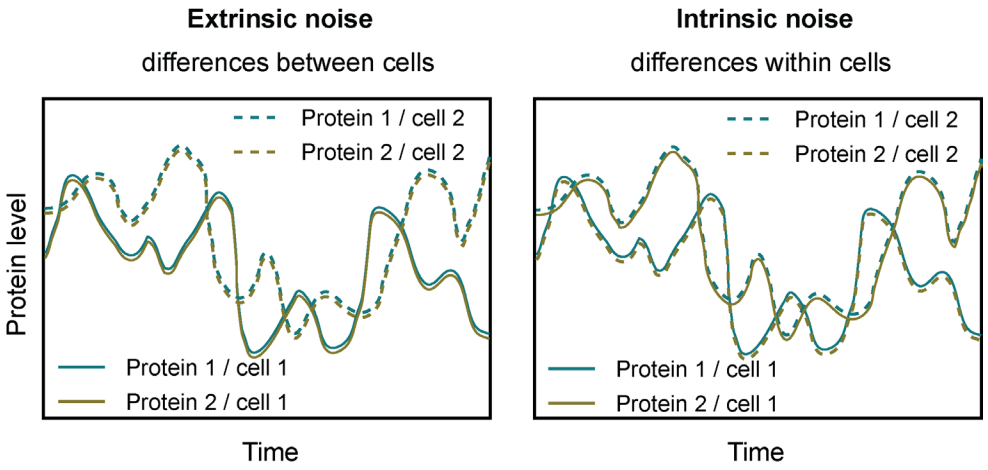

Figure 1.9: Uncorrelated and correlated noise in gene expression. Extrinsic noise is the variation in gene expression between cells while fluctuations of gene expression of identical genes (protein 1 and 2) within one cell are correlated. By contrast, uncorrelated fluctuations of protein expression from two identical genes (protein 1 and 2) within a cell are considered as intrinsic noise.

Ozbudak et al. shows that the variation in gene expression in cells of the prokaryote *Bacillus subtilis* depends on the rates of transcription and translation.[42] In line with another study in which the variation in gene expression was examined by theoretical analysis[43], noise was lower with frequent transcription and inefficient translation compared to infrequent transcription and efficient translation. Analogous, Elowitz et al. found that noise in protein expression in *E. coli* increases with decreasing transcription rate.[37] Most genetic circuits display feedback control involving repressors, transcription factors, mediators and chromatin remodeling each of which contributes to the variation in gene expression or possibly serve as coping mechanisms.[44] For example, the number and location of transcription factor binding sites can control noise in gene expression.[45] Additionally, several studies, including experimental and theoretical analysis, show that noise in gene expression is suppressed by negative autoregulation.[29,43,46] Noise has important biological consequences such as determining phenotypic variation in cellular populations,[47] all of which are affected by the magnitude and the frequency of the noise.[44,47-50] Small differences in protein expression may have either an environmental fitness advantage or disadvantage. Moreover, stochasticity may play an important role in cell differentiation or as a survival mechanism in fluctuating environments.[31,51,52]

It has become clear that we cannot ignore the stochasticity of biochemical reactions. Yet, the number of examples in which cell-free biochemical reaction networks are constructed using low concentrations of reactants is limited. One study, from Simmel and co-workers, involved

the *in vitro* compartmentalization of a transcriptional oscillator (*vide supra*) into microdroplets to study the effect of micro-scale encapsulation and stochasticity on cell-free biochemical reaction networks.[53] They analysed the robustness of the *in vitro* transcriptional oscillator at low concentrations by measuring large populations of microdroplets simultaneously. Synchronization among compartmentalized oscillators did not occur due to a lack of controlled communication between droplets, resulting in dynamical diversity of oscillatory behaviour among droplets in terms of amplitude, frequency and damping. Based on results of deterministic and stochastic models the researchers concluded that the dynamical diversity in oscillatory behaviour could be attributed to the statistical variation of reactant concentrations as a result of partitioning the system into droplets, rather than reflecting the intrinsic stochastic kinetics of the chemical reaction network itself. This extrinsic noise as a result of statistical variations during encapsulation of biochemical components is an important parameter when engineering artificial cells with preprogrammed temporal dynamics.

Macromolecular Crowding

While macromolecular crowding is ubiquitous in all types of cells and is known to affect the interactions between macromolecules it is mostly neglected by biochemists.[54,55] Macromolecular crowding in biological systems refers to the high concentration of total macromolecules inside cells and, thereby, a significant proportion of the volume inside cells is occupied and not accessible for other molecules. However, while the macromolecules occupy a significant volume of the cell, the concentration of each biomolecule is rather low and, therefore, the interior of the cell is crowded and not concentrated.[56] Crowding is a property which occurs inside and outside cells by various macromolecules including proteins, nucleic acids, RNA and polysaccharides. The total concentration of proteins inside *E. coli* ranges from 200-300 g L^{-1} while the total concentration of RNA typically ranges between 75-150 g L^{-1}. Together, these macromolecules occupy 20-30% of the cells cytoplasm[54,55] and it is no surprise reactions between molecules in cells are different than those in an *in vitro* set-up under dilute conditions. Whereas electrostatic or hydrophobic interactions between macromolecules affect the free energy profile of reactants and products, crowding specifically refers to the excluded volume effect which is a physical nonspecific phenomenon that only describes steric repulsion and does not take into account the interactions between macromolecules. The excluded volume effect depends on the relative sizes of the macromolecules of interest and the other background macromolecules (Figure 1.10).[57] For relatively small molecules the available volume is roughly equal to the fraction of the volume

that is not occupied by the background macromolecules. However, with a molecule with a size equal or larger than the background macromolecules, the available volume is considerably lower as the center of the molecule of interest cannot be closer to the background molecule where the surfaces of the two molecules contact each other.

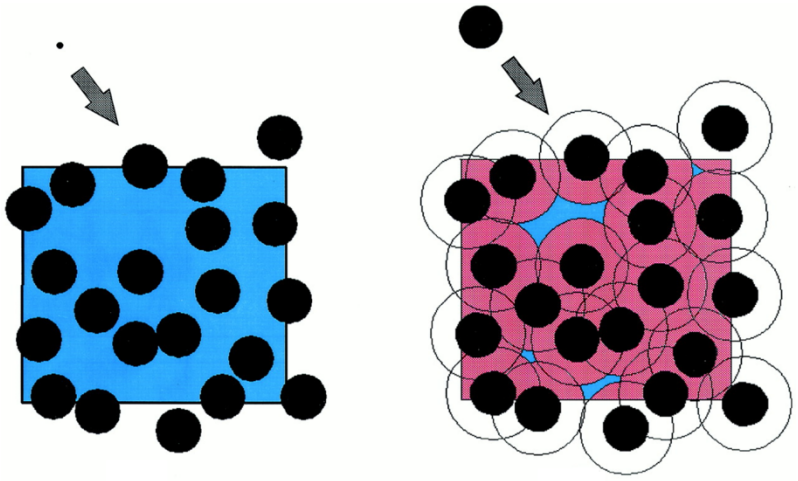

Figure 1.10: The excluded volume effect. The squares represent the volume which is for 30% occupied by spherical macromolecules. The available volume is shown in blue while the excluded volume is shown in pink. For relatively small molecules compared to the background macromolecules (left) the accessible volume is roughly 70%. For a molecule with a size equal or larger than the background molecules (right) the excluded volume is significantly larger than 70% as the centre of the molecule cannot approach the areas as indicated by the open circles. Figure from reference 57.

The effect of macromolecular crowding on biochemical reaction rates is rather complex and depends on the nature of each reaction. Macromolecular crowding increases the activity of macromolecules and limits diffusion, which have opposing effects on the reaction rate.[56] When the reaction rate is transition-state limited, the reaction rate increases with increasing crowder caused by a shift in thermodynamic equilibrium.[55,57] Depending on the size and shapes of the macromolecules, the thermodynamic association constant of two binding partners can increase two or three orders of magnitude in a crowded environment. This results from a decrease in the configurational entropy of a macromolecule in the presence of a crowder and, hence, the contribution to the total free energy of the solution is increased. However, the free energy of the unbound molecules increases more than the free energies of the transition state and the bound state. Therefore, the thermodynamic driving force shifts the equilibrium of the two binding partners to the associated state as this is energetically favorable. In conclusion, with increasing crowder the thermodynamic equilibria are shifted to the bound state and, hence, the system will be in a state where the least volume is excluded.

This thermodynamic effect has serious consequences on the activity of macromolecules.[54] However the effect on small molecules such as ions and metabolites is rather low (Figure 1.11A). Furthermore, the increase in activity coefficient is highly non-linear with respect to the crowder concentration, shown in Figure 1.11B. In the diffusion-controlled limit the reaction rate decreases with increasing crowder as the probability of reactants encountering decreases. Hence, even reactions which are transition-state limited will fall into diffusion-limited reactions at high crowder concentrations where the decreased encounter rate starts to dominate (Figure 1.11C).

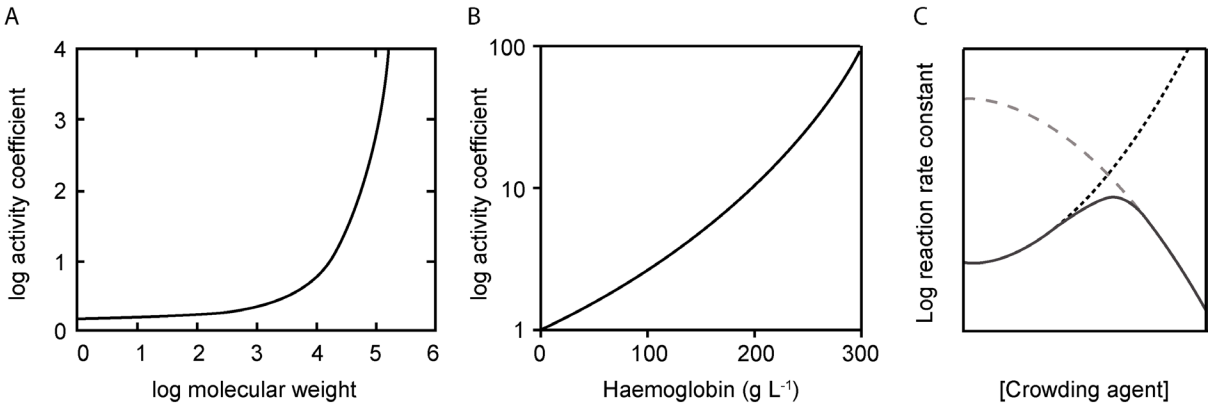

Figure 1.11: A) The activity coefficient (effective concentration / actual concentration) versus the molecular weight of a target molecule in a crowded solution. B) The activity coefficient (effective concentration / actual concentration) versus the concentration of Haemoglobin. C) The reaction rate constant versus the degree of crowding, where the reaction is diffusion-limited (grey dotted line) or transition state-limited (black dotted line). Reactions which are transition-state limited will fall into diffusion-limited reactions at high crowder concentrations (dark grey line). Figures adapted from reference 54.

Figure 1.12A shows that the effective diffusion coefficient of a macromolecule can decrease orders of magnitude in the presence of macromolecular crowding.[58] Yet, the kinetics of a diffusion-limited reaction in the presence of a crowder can increase as geometry and the related effect of subdiffusion start to play a significant role.[59] While in a dilute environment the reaction rate is independent on the starting point of the reactants, the initial positions of the reactants in presence of macromolecular crowding strongly influence the time it takes for a diffusing molecule to reach a target (Figure 1.12B), i.e. the first-passage time (FPT). When a molecule is located in close proximity to its target the reaction rate can increase several orders of magnitude.[59] Hence, co-localization of reactants inside cells is often advantageous[60] as this results in shorter activation times and increased reaction rates.[59,61] In describing normal or Brownian diffusion it is assumed that the solute diffuses in a continuous hydrodynamic fluid. However, this is not representative for biological systems as the

cytoplasm contains a heterogeneous distribution of many different molecules with various sizes. While macromolecular crowding in the cytoplasm of the cell decreases the effective diffusion coefficient over a long timescale or distance, the diffusion coefficient at short timescales is unchanged.[62,63] As the mean squared displacement (MSD) of molecules now becomes sub-linear this is often called subdiffusion (Figure 1.12C). Importantly, while the MSD determined from the average displacement of a population of molecules is linear, a single particle subjected to normal diffusion does not have a linear displacement in time and therefore, though in lower extent than in presence of crowder, also shows anomalous diffusion. An important consequence of this type of diffusion, is that molecules remain longer at their initial positions than anticipated[59,62] and, hence, may favor for example the search of a target gene by transcription factors in the nucleus[62,64] or reduces the time needed by an enzyme to reach its substrate.[65]

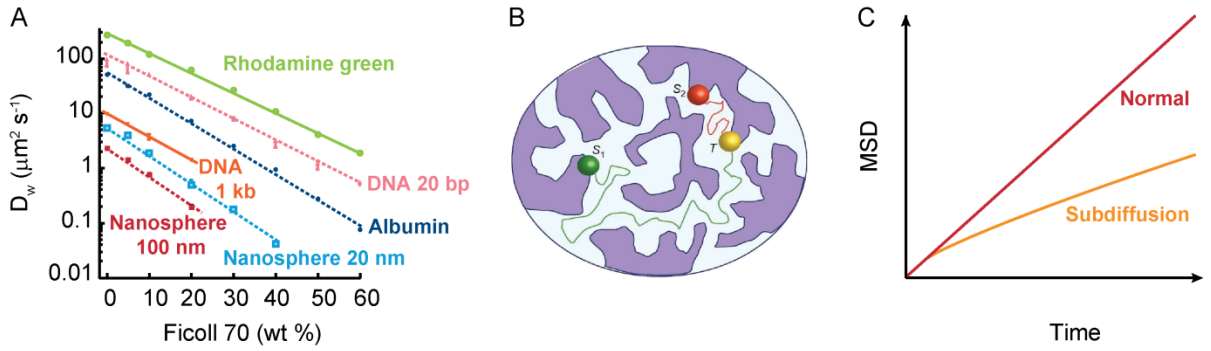

Figure 1.12: A) The diffusion coefficients of various macromolecules for a concentration range of a crowder, Ficoll 70. Figure from reference 58. B) The initial positions of reactants strongly affect the first passage time. The reaction between S_1 and T has a much longer first passage time compared to the reaction between S_2 and T. Figure from reference 59. C) Simulated MSD curves of a molecule subjected to normal (Brownian) diffusion and anomalous subdiffusion. Figure adapted from reference 59.

The effect of macromolecular crowding on biochemical reactions is complex and challenging to predict. Besides the opposing effects of crowding on reaction rates, cells have different micro-environments each containing different biomolecules. For example, *E. coli* have at least three micro-environments, including the immediate vicinity of the inner-plasma membrane, the interior and immediate vicinity of the nucleoid and the cytoplasm. While the plasma-membrane and nucleoid have high concentrations of phospholipids and proteins, and DNA respectively, the cytoplasm consists of other proteins at a lower concentration. Additionally, macromolecular confinement and adsorption are also important background reactions which contribute to molecular reactivity.[55,61] Different studies have been performed in order to

obtain a deeper understanding of the effect of macromolecular crowding in cells. For example, Zimmerman et al. showed in a cell-free set-up that macromolecular crowding increased the binding of DNA polymerase of *E. coli* to DNA and, thereby, enhanced DNA polymerase reaction rates.[66] As the experiments were performed under high ionic strength, which is otherwise an inhibitory condition, these results imply that crowding could increase the range of conditions for which the cell performs optimal. Similarly, in another cell-free study it was found that transcription rates in coarcervate droplets were enhanced in presence of macromolecular crowding.[67] Other cell-free studies show that addition of synthetic polymers increases transcription while translation is limited.[68] Additionally, Klumpp and coworkers[69] show that macromolecular crowding inhibits translation and finally limits cell growth in bacteria. Furthermore, macromolecular crowding has been reported to influence nucleus assembly in eukaryotic cells[70] and also significantly affects ribosomal assembly.[71] These examples demonstrate the importance of the effects of macromolecular crowding on the kinetics and the dynamics of the cell's machinery.

1.4 Aim and Outline of this thesis

The main goal of bottom-up synthetic biology is to obtain a deeper understanding of the *modus operandi* of molecular networks inside living cells by emulating a target property or feature of the cell. To this end, to make progress in this field extensive collaboration between physicists, chemists, biologists and mathematicians is required. Here, we have highlighted several studies in which cell-free biomolecular networks are engineered *de novo* using a bottom-up approach. Besides, we introduced two factors often neglected by biochemists, i.e. stochasticity and macromolecular crowding, which significantly contribute to the dynamics of reaction networks in cells. The goal of this thesis is to expand the scope of DNA-based molecular networks by developing tools enriching these networks and providing additional knowledge of biomolecular reactions in cells.

In **Chapter 2**, as an introduction to **Chapter 3**, we introduce the polymerase-exonuclease-nickase (PEN) toolbox, developed by Rondelez and co-workers. The PEN toolbox allows the construction of biochemical circuits emulation complex dynamic behaviour in time and space similar to those in natural cells. We implement an INVERTER circuit and a previously designed bistable switch and, additionally, we introduce a heuristic model which we use for the detailed characterization of PEN-based networks.

While regulatory circuits in cells control downstream processes through hierarchical layers of signal processing, coupling of enzymatically-driven DNA-based networks to downstream processes has rarely been reported. In **Chapter 3** we engineer hierarchical control of enzymatic actuators using the PEN-based bistable switch. We develop a translator module which converts signaling molecules from the upstream network to unique DNA strands driving downstream actuators with minimal retroactivity and support these findings with a detailed computational analysis.

To further expand the scope of DNA-based molecular programming, in **Chapter 4** we introduce a generic approach, based on antibody-templated strand exchange (ATSE), enabling the use of antibodies as input for DNA-based computing. Experiments showed the successful implementation of the ATSE reaction. In **Chapter 4** we develop a comprehensive model that describes the kinetics of the ATSE system. The model provides a fundamental understanding of the ATSE reaction and is used to find optimal concentration regimes and to study the effect of thermodynamics and kinetics of antibody–epitope binding.

While cell-free BRNs are often studied at high reactant concentrations in a well-stirred environment, the cell's interior is an inhomogeneous crowded environment where reactions between biomolecules occur at low concentrations. These low concentrations of biomolecules result in stochastic gene expression in cells. However, it is unknown how the physical environment contributes to the variation in gene expression level. Our experimental partners at the Radboud university developed a robust method to quantify the variation in cell-free gene expression in a controlled environment. In **Chapter 5** we study the variation in cell-free gene expression as a function of plasmid copy number and macromolecular crowding. To support the experimental findings and to obtain a detailed characterization of the experimental setup we develop two independent theoretical models. We find that decreasing diffusion coefficients and the formation of heterogeneous micro-environments caused by macromolecular crowding enhance uncorrelated noise in gene expression.

Chapter 6 reflects on the findings of the thesis and puts them in context of the field.

1.6 References

1. Nakajima, M. et al. Reconstitution of circadian oscillation of cyanobacterial KaiC phosphorylation in vitro. *Science* **308**, 414-415 (2005).
2. Noireaux, V., Bar-Ziv, R. & Libchaber, A. Principles of cell-free genetic circuit assembly. *Proc. Natl. Acad. Sci. U.S.A.* **100**, 12672-12677 (2003).
3. Coyle, S.M. & Lim, W.A. Mapping the functional versatility and fragility of Ras GTPase signaling circuits through in vitro network reconstitution. *eLife* **5**, e12435 (2016).
4. Seelig, G., Soloveichik, D., Zhang, D.Y. & Winfree, E. Enzyme-free nucleic acid logic circuits. *Science* **314**, 1585-1588 (2006).
5. Kim, J., White, K.S. & Winfree, E. Construction of an in vitro bistable circuit from synthetic transcriptional switches. *Mol. Syst. Biol.* **2**, 68-68 (2006).
6. Kim, J., Khetarpal, I., Sen, S. & Murray, R.M. Synthetic circuit for exact adaptation and fold-change detection. *Nucleic Acids Res.* **42**, 6078-6089 (2014).
7. Padirac, A., Fujii, T. & Rondelez, Y. Bottom-up construction of in vitro switchable memories. *Proc. Natl. Acad. Sci. U.S.A.* **109**, 3212-3220 (2012).
8. Van Roekel, H.W.H. et al. Automated design of programmable enzyme-driven DNA circuits. *ACS Synth. Biol.* **4**, 735-745 (2015).
9. Kim, J. & Winfree, E. Synthetic in vitro transcriptional oscillators. *Mol. Syst. Biol.* **7**(2011).
10. Montagne, K., Plasson, R., Sakai, Y., Fujii, T. & Rondelez, Y. Programming an in vitro DNA oscillator using a molecular networking strategy. *Mol. Syst. Biol.* **7**, 466 (2011).
11. Fujii, T. & Rondelez, Y. Predator - prey molecular ecosystems. *ACS Nano* **7**, 27-34 (2013).
12. Semenov, S.N. et al. Rational design of functional and tunable oscillating enzymatic networks. *Nat. Chem.* **7**, 160-165 (2015).
13. Niederholtmeyer, H., Stepanova, V. & Maerkl, S.J. Implementation of cell-free biological networks at steady state. *Proc. Natl. Acad. Sci. U.S.A.* **110**, 15985-15990 (2013).
14. Karzbrun, E., Tayar, A.M., Noireaux, V. & Bar-Ziv, R.H. Programmable on-chip DNA compartments as artificial cells. *Science* **345**, 829-832 (2014).
15. Del Vecchio, D., Ninfa, A.J. & Sontag, E.D. Modular cell biology: retroactivity and insulation. *Mol. Syst. Biol.* **4**, 161 (2008).
16. Jayanthi, S., Nilgiriwala, K.S. & Del Vecchio, D. Retroactivity controls the temporal dynamics of gene transcription. *ACS Synth. Biol.* **2**, 431-441 (2013).
17. Franco, E. et al. Timing molecular motion and production with a synthetic transcriptional clock. *Proc. Natl. Acad. Sci. U.S.A.* **108**, E784-E793 (2011).
18. Sriram, K., Soliman, S. & Fages, F. Dynamics of the interlocked positive feedback loops explaining the robust epigenetic switching in Candida albicans. *J. Theor. Biol.* **258**, 71-88 (2009).
19. Benítez, M. & Alvarez-Buylla, E.R. Dynamic-module redundancy confers robustness to the gene regulatory network involved in hair patterning of Arabidopsis epidermis. *Biosystems* **102**, 11-15 (2010).
20. Hartwell, L.H., Hopfield, J.J., Leibler, S. & Murray, A.W. From molecular to modular cell biology. *Nature* **402**, 47-52 (1999).
21. Alon, U. Biological networks: The tinkerer as an engineer. *Science* **301**, 1866-1867 (2003).
22. Jacob, F. Evolution and tinkering. *Science* **196**, 1161-1166 (1977).
23. Waxman, D. & Peck, J.R. Pleiotropy and the preservation of perfection. *Science* **279**, 1210-1213 (1998).
24. Shahrezaei, V. & Swain, P.S. The stochastic nature of biochemical networks. *Curr. Opin. Biotech.* **19**, 369-374 (2008).
25. Bratsun, D., Volfson, D., Tsimring, L.S. & Hasty, J. Delay-induced stochastic oscillations in gene regulation. *Proc. Natl. Acad. Sci. U.S.A.* **102**, 14593-14598 (2005).
26. Elowitz, M.B. & Leibler, S. A synthetic oscillatory network of transcriptional regulators. *Nature* **403**, 335-338 (2000).
27. Barkai, N. & Leibler, S. Biological rhythms: Circadian clocks limited by noise. *Nature* **403**, 267-268 (2000).

28. Levine, E. & Hwa, T. Stochastic fluctuations in metabolic pathways. *Proc. Natl. Acad. Sci. U.S.A.* **104**, 9224-9229 (2007).
29. Hensel, Z. et al. Stochastic expression dynamics of a transcription factor revealed by single-molecule noise analysis. *Nat. Struct. Mol. Biol.* **19**, 797-802 (2012).
30. Acar, M., Mettetal, J.T. & van Oudenaarden, A. Stochastic switching as a survival strategy in fluctuating environments. *Nat. Genet.* **40**, 471-475 (2008).
31. Maamar, H., Raj, A. & Dubnau, D. Noise in gene expression determines cell fate in Bacillus subtilis. *Science* **317**, 526-529 (2007).
32. Raser, J.M. & O'Shea, E.K. Control of stochasticity in eukaryotic gene expression. *Science* **304**, 1811-1814 (2004).
33. Chang, H.H., Hemberg, M., Barahona, M., Ingber, D.E. & Huang, S. Transcriptome-wide noise controls lineage choice in mammalian progenitor cells. *Nature* **453**, 544-547 (2008).
34. Gupta, Piyush B. et al. Stochastic state transitions give rise to phenotypic equilibrium in populations of cancer cells. *Cell* **146**, 633-644 (2011).
35. Weinberger, L.S., Burnett, J.C., Toettcher, J.E., Arkin, A.P. & Schaffer, D.V. Stochastic gene expression in a lentiviral positive-feedback loop: HIV-1 Tat fluctuations drive phenotypic diversity. *Cell* **122**, 169-182 (2005).
36. Munsky, B., Neuert, G. & van Oudenaarden, A. Using gene expression noise to understand gene regulation. *Science* **336**, 183-187 (2012).
37. Elowitz, M.B., Levine, A.J., Siggia, E.D. & Swain, P.S. Stochastic Gene Expression in a Single Cell. *Science* **297**, 1183-1186 (2002).
38. Swain, P.S., Elowitz, M.B. & Siggia, E.D. Intrinsic and extrinsic contributions to stochasticity in gene expression. *Proc. Natl. Acad. Sci. U.S.A.* **99**, 12795-12800 (2002).
39. Hilfinger, A. & Paulsson, J. Separating intrinsic from extrinsic fluctuations in dynamic biological systems. *Proc. Natl. Acad. Sci. U.S.A.* **108**, 12167-12172 (2011).
40. Cai, L., Friedman, N. & Xie, X.S. Stochastic protein expression in individual cells at the single molecule level. *Nature* **440**, 358-362 (2006).
41. Nishimura, K., Tsuru, S., Suzuki, H. & Yomo, T. Stochasticity in gene expression in a cell-sized compartment. *ACS Synth. Biol.* **4**, 566–576 (2014).
42. Ozbudak, E.M., Thattai, M., Kurtser, I., Grossman, A.D. & van Oudenaarden, A. Regulation of noise in the expression of a single gene. *Nat. Genet.* **31**, 69-73 (2002).
43. Thattai, M. & van Oudenaarden, A. Intrinsic noise in gene regulatory networks. *Proc. Natl. Acad. Sci. U.S.A.* **98**, 8614-8619 (2001).
44. Raj, A. & van Oudenaarden, A. Nature, Nurture, or Chance: Stochastic Gene Expression and Its Consequences. *Cell* **135**, 216-226 (2008).
45. Murphy, K.F., Balázsi, G. & Collins, J.J. Combinatorial promoter design for engineering noisy gene expression. *Proc. Natl. Acad. Sci. U.S.A.* **104**, 12726-12731 (2007).
46. Becskei, A. & Serrano, L. Engineering stability in gene networks by autoregulation. *Nature* **405**, 590-593 (2000).
47. Gene-Wei, L. & Xie, X.S. Central dogma at the single-molecule level in living cells. *Nature* **475**, 308-315 (2011).
48. Raser, J.M. & O'Shea, E.K. Noise in gene expression: Origins, consequences, and control. *Science* **309**, 2010-2013 (2005).
49. Eldar, A. & Elowitz, M.B. Functional roles for noise in genetic circuits. *Nature* **467**, 167-173 (2010).
50. Mary, E.L. & Michael, C.K. The role of physiological heterogeneity in microbial population behavior. *Nat. Chem. Biol.* **6**, 705-712 (2010).
51. Süel, G.M., Kulkarni, R.P., Dworkin, J., Garcia-Ojalvo, J. & Elowitz, M.B. Tunability and Noise Dependence in Differentiation Dynamics. *Science* **315**, 1716-1719 (2007).
52. Süel, G.M., Garcia-Ojalvo, J., Liberman, L.M. & Elowitz, M.B. An excitable gene regulatory circuit induces transient cellular differentiation. *Nature* **440**, 545-550 (2006).
53. Weitz, M. et al. Diversity in the dynamical behaviour of a compartmentalized programmable biochemical oscillator. *Nat. Chem.* **6**, 295-302 (2014).

54. Ellis, R.J. Macromolecular crowding: an important but neglected aspect of the intracellular environment. *Curr. Opin. Struct. Biol.* **11**, 114-119 (2001).
55. Minton, A.P. How can biochemical reactions within cells differ from those in test tubes? *J. Cell Sci.* **119**, 2863-2869 (2006).
56. Ellis, R.J. Macromolecular crowding: obvious but underappreciated. *Trends Biochem. Sci.* **26**, 597-604 (2001).
57. Minton, A.P. The Influence of macromolecular crowding and macromolecular confinement on biochemical reactions in physiological media. *J. Biol. Chem.* **276**, 10577-10580 (2001).
58. Dix, J.A. & Verkman, A.S. Crowding effects on diffusion in solutions and cells. *Ann. Rev. Biophys.* **37**, 247-263 (2008).
59. Bénichou, O., Chevalier, C., Klafter, J., Meyer, B. & Voituriez, R. Geometry-controlled kinetics. *Nat. Chem.* **2**, 472 (2010).
60. Kolesov, G., Wunderlich, Z., Laikova, O.N., Gelfand, M.S. & Mirny, L.A. How gene order is influenced by the biophysics of transcription regulation. *Proc. Natl. Acad. Sci. U.S.A.* **104**, 13948-13953 (2007).
61. Zhou, H.-X., Rivas, G. & Minton, A.P. Macromolecular crowding and confinement: Biochemical, biophysical, and potential physiological consequences. *Ann. Rev. Biophys.* **37**, 375-397 (2008).
62. Golding, I. & Cox, E.C. Physical nature of bacterial cytoplasm. *Phys. Rev. Lett.* **96**, 098102 (2006).
63. Banks, D.S. & Fradin, C. Anomalous diffusion of proteins due to molecular crowding. *Biophys. J.* **89**, 2960-2971 (2005).
64. Guigas, G. & Weiss, M. Sampling the cell with anomalous diffusion—The discovery of slowness. *Biophys. J.* **94**, 90-94 (2008).
65. Esmaeili Sereshiki, L., Lomholt, M.A. & Metzler, R. A solution to the subdiffusion-efficiency paradox: Inactive states enhance reaction efficiency at subdiffusion conditions in living cells. *Europhys. Lett.* **97**, 20008. (2012).
66. Zimmerman, S.B. & Harrison, B. Macromolecular crowding increases binding of DNA polymerase to DNA: an adaptive effect. *Proc. Natl. Acad. Sci. U.S.A.* **84**, 1871-1875 (1987).
67. Sokolova, E. et al. Enhanced transcription rates in membrane-free protocells formed by coacervation of cell lysate. *Proc. Natl. Acad. Sci. U.S.A.* **110**, 11692-11697 (2013).
68. Ge, X., Luo, D. & Xu, J. Cell-free protein expression under macromolecular crowding conditions. *PLoS ONE* **6**, e28707 (2011).
69. Klumpp, S., Scott, M., Pedersen, S. & Hwa, T. Molecular crowding limits translation and cell growth. *Proc. Natl. Acad. Sci. U.S.A.* **110**, 16754-16759 (2013).
70. Richter, K., Nessling, M. & Lichter, P. Experimental evidence for the influence of molecular crowding on nuclear architecture. *J. Cell. Sci.* **120**, 1673-1680 (2007).
71. Zimmerman, S.B. & Trach, S.O. Effects of macromolecular crowding on the association of E.coli ribosomal particles. *Nucleic Acids Res.* **16**, 6309-6326 (1988).

2

An introduction to PEN-based reaction networks

Abstract Cell-free synthetic biology entails the *de novo* engineering of complex biomolecular networks from simple molecules using a bottom-up approach. It aims to create biochemical reaction networks which act and respond in a versatile and adaptive manner by precisely programmed dynamics. Theoretical and experimental studies of such simplified biochemical networks allow the extraction of fundamental design principles of cellular network organization and correlated function in natural cells. Rondelez and co-workers developed a toolbox based on DNA replication, nicking, and degradation by polymerase, exonuclease and nickase (PEN toolbox) enabling the construction of biochemical networks emulation complex dynamic behaviour in time and space. Here, as an introduction to *Chapter 3*, we implement a PEN-based INVERTER circuit and a previously designed PEN-based bistable switch and introduce a novel heuristic model which we use for the detailed characterization of PEN-based networks.

Part of the work in this chapter has been published in:
Hendrik W.H. van Roekel, Lenny H.H. Meijer, Saeed Masroor, Zandra C. Félix Garza, André Estévez-Torres, Yannick Rondelez, Antonios Zagaris, Mark A. Peletier, Peter A.J. Hilbers and Tom F.A. de Greef – ACS Synthetic Biology, **2015**, 4, 735

2.1 Introduction

Synthetic biology is an emerging field in bioengineering in which scientists challenge the complexity of nature by building new biological systems using engineering principles. While reductionism, which is the idea that every complex phenomenon can be explained by analysing the simplest, basic physical mechanisms, has provided a wealth of knowledge about individual cellular components, it has not provided insights into complete cellular systems. For this reason, present-day synthetic biology also focusses on whole systems of interacting biochemical components. To this end, Rondelez and co-workers introduced a cell-free modular toolbox consisting of DNA and the enzymes polymerase, exonuclease and nickase (PEN toolbox).[1] The nucleic acid templates carry the connectivity information of the network in which regulators, produced from the templates by polymerase and nickase, activate or inhibit other templates. Furthermore, degradation of the regulator strands by exonuclease maintains the system in an out-of-equilibrium state. The PEN toolbox has already allowed the construction of various circuits executing temporal and spatiotemporal dynamics. The first network constructed using the PEN toolbox is the 'Oligator'. The network topology consists of autocatalytic synthesis of a primer which activates the production of its own inhibitor via a delayed mechanism giving rise to oscillations. Highlighting the versatility of the methodology, the same group designed an *in vitro* enzymatic DNA-based bistable switch[2] and a network that emulated the complex dynamics of ecological systems,[3] including predator-prey oscillations, competition-induced chaos, and symbiotic synchronization. While the PEN toolbox comprises only a few components, the non-linear nature of these molecular circuits makes their design and implementation often counter-intuitive. In an insightful study, Rondelez and coworkers mapped the bifurcation diagrams of the oscillator and the switch from which parameter regimes could be detected where the network functions optimally and where the dynamics are bifurcated.[4] In addition to finding optimal regimes, this also increases the understanding of the behaviour of these PEN-based circuits. Moreover, they introduced a method to tune and enhance nonlinearities by manipulating the degradation pathways via a drain template and show that these saturable deactivation pathways can enhance the functional performance of the networks.[5] Though mostly resulting from structural modifications, nonlinearities are very common in cells and even are essential for the function of networks.[6-9] While temporal out-of-equilibrium behaviour under homogeneous conditions has provided key insights

into the fundamental design principles behind topology and function, the coupling of reactions with diffusion in spatially extended systems is essential to understand the complex spatial ordering and dynamic behaviour of the intra- and intercellular environment. To this end, Estévez-Torres, Rondelez and colleagues employed the PEN toolbox to engineer a cell-free reaction network displaying predator-prey oscillations in a quasi-two-dimensional closed reactor.[10] When the DNA fragments and the three enzymes are homogeneously distributed in a spatially extended reactor, traveling waves of predator chasing prey were observed. One-dimensional reaction-diffusion models agreed well with experimental data and the relation between front velocity and reaction parameters, such as the diffusion coefficient of the predator species and the concentration of polymerase, was found to obey the Fisher-Kolmogorov relation. Additionally, Rondelez and coworkers created a PEN-based system consisting of two bistable switches in a spatial concentration gradient of one of the oligonucleotides (Figure 2.1A).[11] They showed that the system self-organized in a spatiotemporal manner with stable and sharp fronts whose positions were controlled by the concentration gradient of the oligonucleotides. Likewise, morphogen gradients *in vivo* are responsible for a wide range of important regulatory functions, such as neuron polarization, spatial organization during mitosis and morphogenesis.[12,13] Even further extending on the reaction-diffusion mechanisms, Rondelez et al. engineered a system in which the encoding templates are immobilized on microscopic particles, which are now able to receive and emit signals (Figure 2.1B).[14] Using this set-up they were able to create populations in which diffusive signals between particles enabled long-distance communication resulting in collective behaviour and spatial patterns. These examples demonstrate the versatility and modularity of the PEN toolbox for the *in vitro* construction of networks emulating spatiotemporal behaviour with fundamental characteristics as can be found in the spatiotemporal dynamics of proteins inside cells.

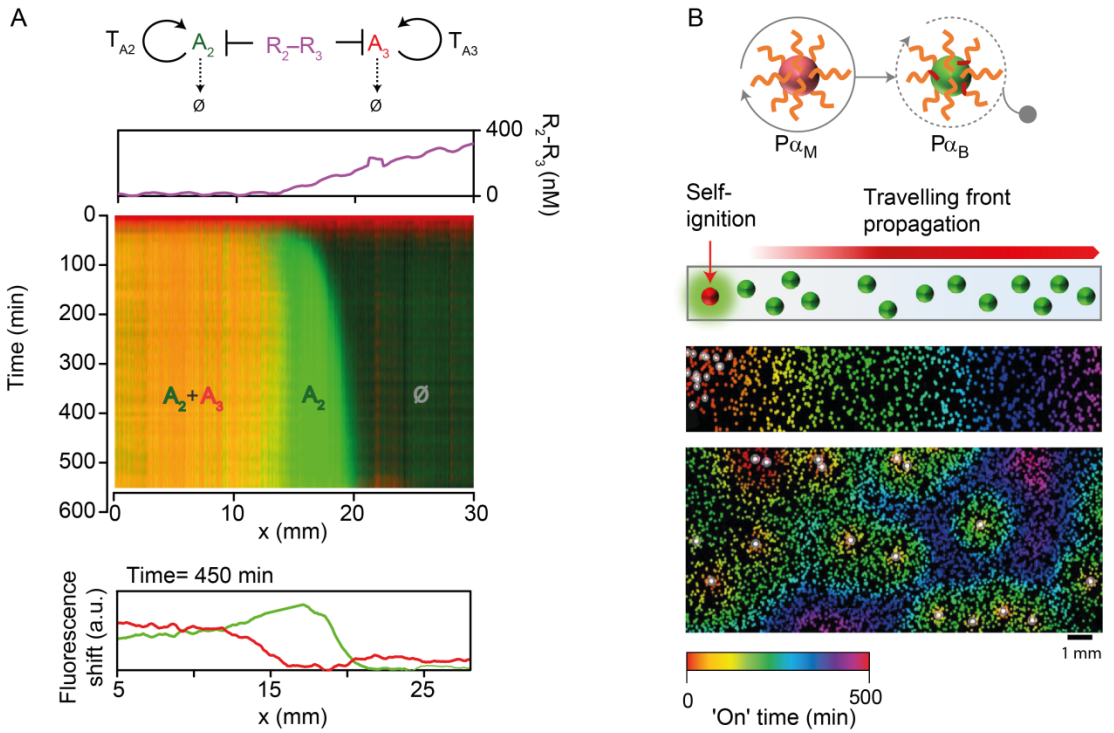

Figure 2.1: Spatiotemporal dynamics of PEN-based reaction networks. A) A PEN-based network comprising two autocatalytic templates T_{A2} and T_{A3} from which the primers A_2 and A_3 are produced. The templates are coupled by a bifunctional morphogen R_2-R_3 which inhibits autocatalysis of both primers by sequestering the templates. The kymograph shows the time evolution of the network in a spatial concentration gradient of R_2-R_3 (purple) resulting in three different regions. The lower graph shows the fluorescence shift over distance in steady-state of the network. Figure adapted from reference 11. B) A PEN-based network based on two types of microparticles, including $P\alpha_M$ which bears autocatalytic templates for the production of primer α and $P\alpha_M$ which bears the same autocatalytic template together with a deactivating strand sequestering α. The signal is triggered by the self-ignition dye-barcoded agents, $P\alpha_M$,. This results in an inhomogeneous concentration of α and activation of neighboring $P\alpha_B$ when the concentration of α exceeds the threshold to trigger $P\alpha_B$. Activated $P\alpha_B$ fluorescence and propagate the signal resulting in a travelling front that activate all particles. The experimental results show the travelling front propagation across a population of $P\alpha_B$ with different disposition of $P\alpha_M$ (white spots) in the microchamber. The colour of the particles represents the time of amplification of α for each particle. Figure adapted from reference 14.

Here, as an introduction to *Chapter 3*, we focus on the bottom-up design of PEN-based reaction networks, including an INVERTER network and the previously designed bistable switch. Furthermore, we introduce a heuristic model, which is also applied in *Chapter 3*, to obtain a deeper understanding of the mechanistic of PEN-based reaction networks.

2.2 Toolbox modules

Rondelez and co-workers introduced a methodology in which enzymatically-enriched DNA-based networks of arbitrary complexity can be engineered in an artificial, non-living and well-controlled setting.[1] The methodology, shown in Figure 2.2, includes activation, inhibition and destruction of short primers (~11 nucleotides) and single-stranded DNA (ssDNA) inhibitors

(~16 nucleotides) carried out by polymerase, exonuclease and nickase (PEN toolbox). Figure 2.2A shows the activation module in which synthetic DNA templates (~22 nucleotides) are activated by input primers (***I***) acting as regulatory signals for the production of an output single stranded DNA (ssDNA) (***O***). Activation of templates by these ssDNA signals enables DNA polymerase to extend the oligomer-template pair resulting in fully hybridized double stranded DNA (dsDNA). Subsequently, these dsDNAs are nicked resulting in double-stranded complexes. Because these reactions are performed at a temperature close to the melting temperature of the partial duplexes, the input and output ssDNAs dissociate from their templates. In order to analyse the dynamics of the activation module, an experiment was performed in which the production of the output ssDNA was followed in time by the DNA intercalating dye Evagreen which binds strongly to double stranded DNA (dsDNA) and weakly to ssDNA. The time traces show the results of an experiment for a concentration range of input and where output ***α*** is the primer for its own production by binding to the 3' end of the template ***αtoα***, resulting in autocatalytic amplification of ***α***. The traces first have a sigmoidal profile, caused by increasing (partial) duplex of ***αtoα*** and ***α*** followed by autocatalysis. However, when the template strands become saturated the traces continue linearly, resulting from the fluorescence of Evagreen binding to free ssDNA ***α*** which is now produced linearly. Notably, the increase in fluorescence does not correspond to the production rate of ***α*** as Evagreen binds more efficient to dsDNA compared to ssDNA, explaining the decrease in slope in the fluorescent traces as the template becomes saturated. Importantly, the curves increasingly shift to the right with decreasing concentration of initial input while the steepness or profile of the curves are independent of the initial input concentration, which is characteristic for autocatalysis.[15] Templates are inhibited by ssDNA strands that are complementary to part of the template's sequence, lack a nickase recognition site and possess a two-base mismatch at their 3' ends which prevents extension of the partial duplex, rendering the template strand inactive (Figure 2.2B). An experiment was performed in which autocatalysis of ***α*** was followed for a concentration range of inhibitor. The traces show an increasingly gradual curve with increasing concentration of inhibitor caused by damping of the autocatalytic effect by the inhibitor. However, as the reaction proceeds ***α*** increasingly outcompetes the inhibitor and the damping effect will disappear. Importantly, input, output and inhibitor strands are degraded over time by exonuclease, shown in Figure 2.2C. Indeed, experimental results, in which the degradation of a ssDNA was followed using the DNA intercalating dye Evagreen, show a decrease in the concentration of ssDNA over time in the

presence of exonuclease. Template strands should not be degraded and, therefore, are protected from degradation by phosphorothioate modifications at their 5' ends.[2]

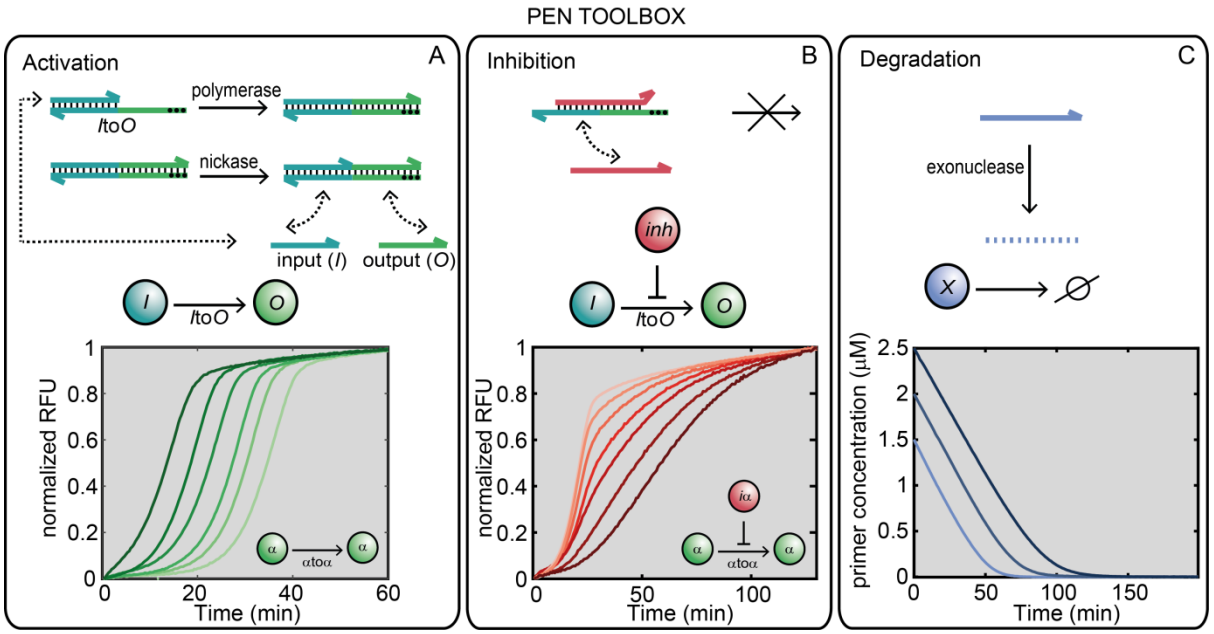

Figure 2.2: Experimental characterization of the PEN toolbox, which comprises three modules including activation, inhibition and degradation. The template strands are protected from degradation by 5' end phosphorothioate backbone modifications indicated by the black dots. All experiments were conducted at 42°C in a master mix as described in *Paragraph* 2.5. The sequences of the DNA strands used in the experiments are provided in Table 2.1. A) Activation is achieved by binding of input ssDNA signals (e.g. primer ***I***) to their target template (e.g. ***ItoO***) which results, after action of polymerase and nickase, in the return of the input ssDNA signal and a newly formed output ssDNA (e.g. oligomer ***O***), which dissociate from the template because these reactions are performed around the melting temperature of the partial duplexes. The graph shows results of an experiment in which autocatalytic amplification of ***α*** is performed for a concentration range of initial primer ***α*** including 10, 20, 50, 100, 200 and 500 pM (light to dark color) in the presence of polymerase (1 U/mL), nickase (6.25 U/mL) and 20 nM ***αtoα*** and initiated by addition of ***α***. B) Inhibition of the activation module is achieved by binding of an inhibitor strand to the target template, preventing the input primer from binding to respective template. The graph shows results of an experiment in which autocatalytic amplification of ***α*** is performed for a concentration range of inhibitor ***iα*** including 0, 20, 30, 40, 50, 60 and 70 nM (light to dark color) in the presence of polymerase (1 U/mL), nickase (6.25 U/mL) and 20 nM ***αtoα*** and initiated by addition of 500 pM ***α***. C) Signal and inhibition strands are degraded over time by exonuclease. The graph shows experimental results of degradation of 1500, 2000 and 2500 nM (light to dark color) ssDNA ***iβ*** by 10 nM exonuclease.

2.3 A heuristic model

In order to analyse the mechanistic of PEN-based reaction networks in more detail we constructed a heuristic model in collaboration with our theoretical partners dr. E. Steur and Prof. R.A. van Santen. As the heuristic model is a strong simplification of the experiments we only use the model to observe and analyse trends. Following [1], we assume that the production of a primer ***y*** on a template ***T*** and an activator ***x***

$$x + T \underset{k_{-1}}{\overset{k_1}{\rightleftharpoons}} xT \xrightarrow{k_2} x + y + T$$

can be described by the Michaelis-Menten approximation:

$$\frac{d[y]}{dt} = \frac{V[x]}{K + [x]}; \quad K = \frac{k_{-1} + k_2}{k_1} \tag{2.1}$$

Here the square bracket notation [ ] is used to denote the concentration of the corresponding species. The maximal production rate V is assumed to be proportional to the total concentration of ***T***. Furthermore, the second step with reaction rate k_2 comprises two enzymatic reactions including polymerization and nicking. We assume $k_2 << k_{-1}$ and K becomes the thermodynamic dissociation constant of ***x*** on ***T*** which can be experimentally determined (Table 2.2 and *Paragraph* 2.5). Figure 2.3A shows the simulated traces of autocatalytic amplification of ***α***, using a K of 6 nM. Initially, the production rate of ***α*** increases resulting from autocatalysis. However, when the concentration of ***α*** is much larger than K the production rate only depends on V, similar to the saturation of the template in the experiments. Moreover, an increasing concentration of initial primer ***α*** decreases the duration at which the maximal production rate is reached which is in agreement with the experimental data (Figure 2.2A).

Inhibition of the activation module by a competitive inhibitor is described by Equation 2.2:

$$\frac{d[y]}{dt} = \frac{V[x]}{K + [x] + \lambda_y [iy]} \tag{2.2}$$

where ***iy*** is the inhibitor and constant λ_y is proportional to the ratio of the thermodynamic dissociation constant of ***x*** and the thermodynamic dissociation constant of ***iy*** (Table 2.2). Figure 2.3B shows the simulated traces of autocatalytic amplification of ***α*** in presence of a concentration range of ***iα***. Again, results of the model agree with experimental data as the traces show an increasingly gradual curve with increasing concentration of inhibitor. Furthermore, as the reaction proceeds ***α*** increasingly outcompetes the inhibitor and the production rate can be approximated by V.

The degradation of a primer ***x*** by exonuclease (***E***),

$$x + E \rightleftharpoons xE \longrightarrow E$$

is described by the Michaelis-Menten equation including competition between substrates:

$$\frac{d[x]}{dt} = -\frac{V_{exo}[x]}{K_{exo}\left(1 + \frac{[x]}{K_{exo}} + \frac{[y]}{K_{exo}} + \ldots\right)} \tag{2.3}$$

with V_{exo} the maximal degradation rate and the Michaelis-Menten constant K_{exo}. Indeed, as shown in Figure 2.3C this formula satisfies the requirements to describe the degradation of ssDNA by exonuclease. Moreover, the simulated traces were obtained by non-linear least squares optimization of the experimental data of Figure 2.2C giving parameter values for V_{exo} and K_{exo} (*Paragraph* 2.5 and Table 2.2).

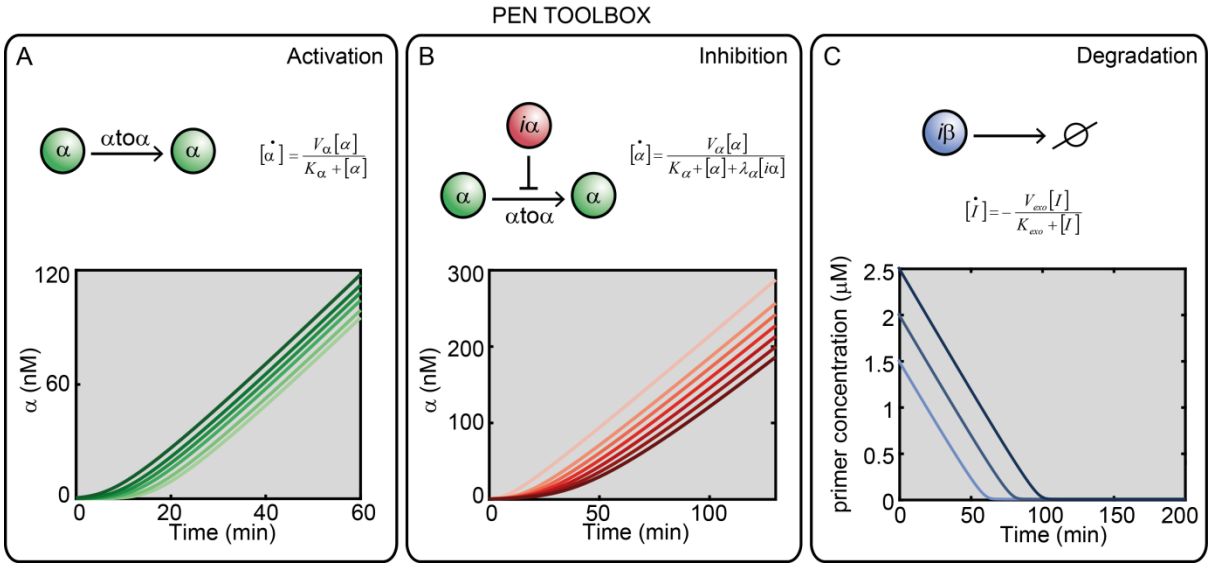

Figure 2.3: Simulations of the three modules of the PEN toolbox. A) Results of simulations of the activation module (Equation 2.1) where autocatalytic amplification of ***α*** is simulated for a concentration range of initial primer ***α*** including 10, 20, 50, 100, 200 and 500 pM (light to dark color) with V_α = 2.5 nM min^{-1} and K_α = 6 nM. B) Results of simulations of the inhibition mechanism (Equation 2.2) where autocatalytic amplification of ***α*** is simulated for a concentration range of inhibitor ***iα*** including 0, 20, 30, 40, 50, 60 and 70 nM (light to dark color) and initiated with 500 pM of primer ***α*** with V_α = 2.5 nM min^{-1}, K_α = 6 nM and λ_α = 0.25. C) Results of non-linear least squares optimization op the experimental results in Figure 2.2C (*Paragraph* 2.5), giving values of 27 nM min^{-1} and 45 nM for parameters V_{exo} and K_{exo} respectively.

2.3 PEN-based reaction networks

INVERTER

The INVERTER network is based on an autocatalytic module which can be inhibited by addition of an input resulting in an output that is inverted compared to the change in input (Figure 2.4). The INVERTER is activated by addition of ***α*** which is initially amplified until it reaches steady-state in which production and degradation due to exonuclease are balanced (Figure 2.4A). Applying a pulse of input ***β*** at this point initiates the production of ***iα*** which inhibits the autocatalytic production of output ***α***. As input strand ***β*** gets degraded the production of inhibitor ***iα*** decreases resulting in an increase of activity of the autocatalytic module. As a result, after some time the PEN-based INVERTER returns to its pre-stimulus steady-state. Hence, the INVERTER network shows a pulse response after injection of input ***β*** which can be characterized by its amplitude and response time which is the time needed to recover to the pre-stimulus steady-state. Experiments were performed with increasing concentrations of template ***αtoα***. The dynamics of the INVERTER network were followed by N-quenching,[16] which monitors oligomer hybridization to templates by a change in fluorescence. As can be observed from Figure 2.4B the experimental results show, as expected, a decreasing response time and amplitude with increasing ***αtoα***. In order to validate the heuristic model we simulated the trajectories of ***β***, ***iα***, ***α***, and ***iβ*** based on Equations 2.1-2.3 giving the following set of ordinary differential equations (ODEs):

$$\frac{d[\beta]}{dt} = -\frac{V_{exo}[\beta]}{K_{exo} + [\alpha] + [\beta] + [i\alpha] + [i\beta]}; \tag{2.4a}$$

$$\frac{d[i\alpha]}{dt} = \frac{V_{i\alpha}[\beta]}{K_{\beta} + [\beta]} - \frac{V_{exo}[i\alpha]}{K_{exo} + [\alpha] + [\beta] + [i\alpha] + [i\beta]}; \tag{2.4b}$$

$$\frac{d[\alpha]}{dt} = \frac{V_{\alpha}[\alpha]}{K_{\alpha} + [\alpha] + \lambda_{\alpha}[i\alpha]} - \frac{V_{exo}[\alpha]}{K_{exo} + [\alpha] + [\beta] + [i\alpha] + [i\beta]}; \tag{2.4c}$$

$$\frac{d[i\beta]}{dt} = \frac{V_{i\beta}[\alpha]}{K_{\alpha} + [\alpha]} - \frac{V_{exo}[i\beta]}{K_{exo} + [\alpha] + [\beta] + [i\alpha] + [i\beta]}; \tag{2.4d}$$

Figure 2.4C displays the dynamics of the INVERTER using the heuristic model for a concentration range of template ***αtoα***, which is simulated by varying V_{α}. The simulations show a decreasing response time and amplitude with increasing ***αtoα*** and, hence, we can conclude that the overall dynamics of the heuristic model qualitatively agree with

experimental data. In the next paragraph we show that the heuristic model can also be applied to other network topologies showing the generality and versatility of the model.

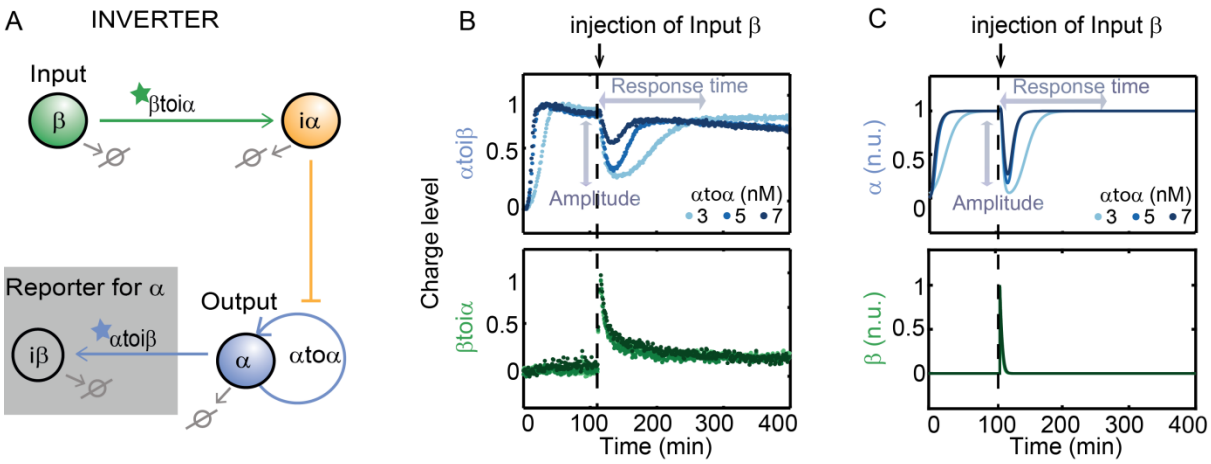

Figure 2.4: PEN-based INVERTER network. **A)** Schematic illustration of the PEN-based INVERTER network. comprising an autocatalytic module producing activator ***α*** which is inhibited by addition of input ***β*** via inhibitor species ***iα*** resulting in an output that is inverted compared to the change in input. Multiplex monitoring of the dynamics of the network is performed using endogenous template ***βtoiα*** and an exogenous template ***αtoiβ*** which are 3'-end fluorescently labeled with DY530 and FAM respectively. B) Results of experiments which were conducted as described in *Paragraph* 2.5 for different concentrations of ***αtoα*** in the presence of 20 nM of ***βtoiα*** and ***αtoiβ***, 10 U/mL Bst 2.0 warmstart DNA polymerase, 25 U/mL Nt. bstNBI and 50 nM ttRecJ. The INVERTER is activated by addition of 0.5 nM ***α*** which is initially amplified until it reaches steady-state in which production by polymerase and nickase and degradation due to exonuclease are balanced. Applying a pulse of 30 nM of input ***β*** at this point initiates the production of ***iα*** which inhibits autocatalytic production of output ***α***. As input strand ***β*** gets degraded the system returns to its pre-stimulus steady-state. Hence, the INVERTER network shows a pulse response after injection of input ***β*** which can be characterized by its amplitude and response time which is the time needed to recover to the pre-stimulus steady-state. C) Results of simulations using the heuristic model (Equation 2.4) for the same concentration range of template ***αtoα*** as used in the experiments in (B). The values for the parameters, which were either experimentally determined or empirically chosen according to the criteria as described in *Paragraph 2.2*, are shown in Table 2.2.

SWITCH

The two-state switchable network as described in reference 1, was constructed by joining two complementary INVERTER circuits (Fig. 2.5A) giving a symmetrical topology in which two autocatalytic modules dynamically repress each other. The core of the network consists of four templates including the mutually exclusive autocatalytic templates ***αtoα*** and ***βtoβ*** that produce key species ***α*** and ***β***, and the inhibitory templates ***αtoiβ*** and ***βtoiα*** from which inhibitors are produced cross-sequestering the autocatalytic templates. The network is defined to be in the α-state when the concentration of ***α*** is high and the concentration of ***β*** is low as a result of high activity of ***αtoα*** which represses the autocatalytic ***βtoβ*** node via template ***αtoiβ***. Likewise, the network is defined to be in the β-state when the concentration of ***β*** is high and

the concentration of ***α*** is low corresponding to high activity of ***βtoβ*** which represses the autocatalytic ***αtoα*** node via ***βtoiα***. Furthermore, two more templates ***γtoα*** and ***δtoβ*** are included which serve as receivers for external inputs ***γ*** and ***δ*** resulting in a long-lasting pulse of ***α*** or ***β***, unbalancing the circuit and stimulating the network to switch. Experiments were performed in which the switch was first triggered to the α-state (Figure 2.5B). Indeed, reversible switching to the β-state and α-state is achieved by injection of ***δ*** and ***γ*** respectively. Interestingly, switching between states is characterized by the biphasic evolution of the charge levels of ***αtoiβ*** and ***βtoiα***. Given the switch is in the α-state, applying a pulse of ***δ*** results in a relatively fast increase of ***β*** by the activated template ***δtoβ***. The increase in ***β*** activates template ***βtoiα*** resulting in the production of ***iα***, and hence, together with the action of exonuclease ***α*** starts to decrease. However, ***α***, and therefore, ***iβ*** are still present resulting in a decrease in ***β*** as ***βtoβ*** is still inhibited and the primers are degraded. Importantly, when ***δ*** is degraded completely, the switch has already reached the basin of attraction of ***β*** and the network switches. Notably, as the Gibbs free energy of DNA hybridization of the two complementary INVERTER circuits are not equal, careful tuning of the template strand concentrations is required to obtain a network which is bistable. To this end, we analysed bistability of the network for a concentration range of ***αtoα*** and ***βtoβ***. Figure 2.5B shows successful switching for three concentrations of ***αtoα***. In order to validate the heuristic model and to analyse the bistable switch in more detail the model that describes the INVERTER was adapted to the topology of the bistable switch resulting in the following set of ODEs:

$$\frac{d[\gamma]}{dt} = -\frac{V_{exo}[\gamma]}{K_{exo}+[\gamma]+[\delta]+[\alpha]+[\beta]+[i\alpha]+[i\beta]}; \tag{2.5a}$$

$$\frac{d[\alpha]}{dt} = \frac{V_{\gamma}[\gamma]}{K_{\gamma}+[\gamma]} + \frac{V_{\alpha}[\alpha]}{K_{\alpha}+[\alpha]+\lambda_{\alpha}[i\alpha]} - \frac{V_{exo}[\alpha]}{K_{exo}+[\gamma]+[\delta]+[\alpha]+[\beta]+[i\alpha]+[i\beta]}; \tag{2.5b}$$

$$\frac{d[i\beta]}{dt} = \frac{V_{i\beta}[\alpha]}{K_{\alpha}+[\alpha]} - \frac{V_{exo}[i\beta]}{K_{exo}+[\gamma]+[\delta]+[\alpha]+[\beta]+[i\alpha]+[i\beta]}; \tag{2.5c}$$

$$\frac{d[\delta]}{dt} = -\frac{V_{exo}[\delta]}{K_{exo}+[\gamma]+[\delta]+[\alpha]+[\beta]+[i\alpha]+[i\beta]}; \tag{2.5d}$$

$$\frac{d[\beta]}{dt} = \frac{V_{\delta}[\delta]}{K_{\delta}+[\delta]} + \frac{V_{\beta}[\beta]}{K_{\beta}+[\beta]+\lambda_{\beta}[i\beta]} - \frac{V_{exo}[\beta]}{K_{exo}+[\gamma]+[\delta]+[\alpha]+[\beta]+[i\alpha]+[i\beta]}; \tag{2.5e}$$

$$\frac{d[i\alpha]}{dt} = \frac{V_{i\alpha}[\beta]}{K_{\beta}+[\beta]} - \frac{V_{exo}[i\alpha]}{K_{exo}+[\gamma]+[\delta]+[\alpha]+[\beta]+[i\alpha]+[i\beta]}; \tag{2.5f}$$

Indeed, applying Equations 2.1-2.3 to the topology of the bistable switch results in a heuristic model which qualitatively describes the experimental traces of the bistable switch (Figure 2.5D). Results of both experiments and simulations show an increasing switching time from the α- to the β -state with increasing concentration of ***αtoα***, while the results show the reverse for switching from the β- to α-state. Using the theoretical model we can obtain the separatrix of the bistable switch (Figure 2.5C), which shifts in favor of the α-state with increasing concentration of ***αtoα***. Interestingly, the separatrices are not linear but shift increasingly in favor of the β-state with increasing concentrations of ***α*** and ***β***. This can be explained by the dissimilar thermodynamic dissociation constants of ***α*** and ***β*** (and ***iα*** and ***iβ***) and dissimilar concentrations of ***αtoα*** and ***βtoβ*** (and ***αtoiβ*** and ***βtoiα***). These factors cause a disproportional increase in activated templates ***αtoα*** and ***βtoβ*** (and ***αtoiβ*** and ***βtoiα***) with proportional increase in ***α*** and ***β***. Even though the PEN toolbox was designed using simple molecular rules, such nonlinearities make the dynamics often surprisingly complex and non-intuitive and, therefore, the model gives valuable insights in the mechanistic of the network and provides optimal parameter regimes.

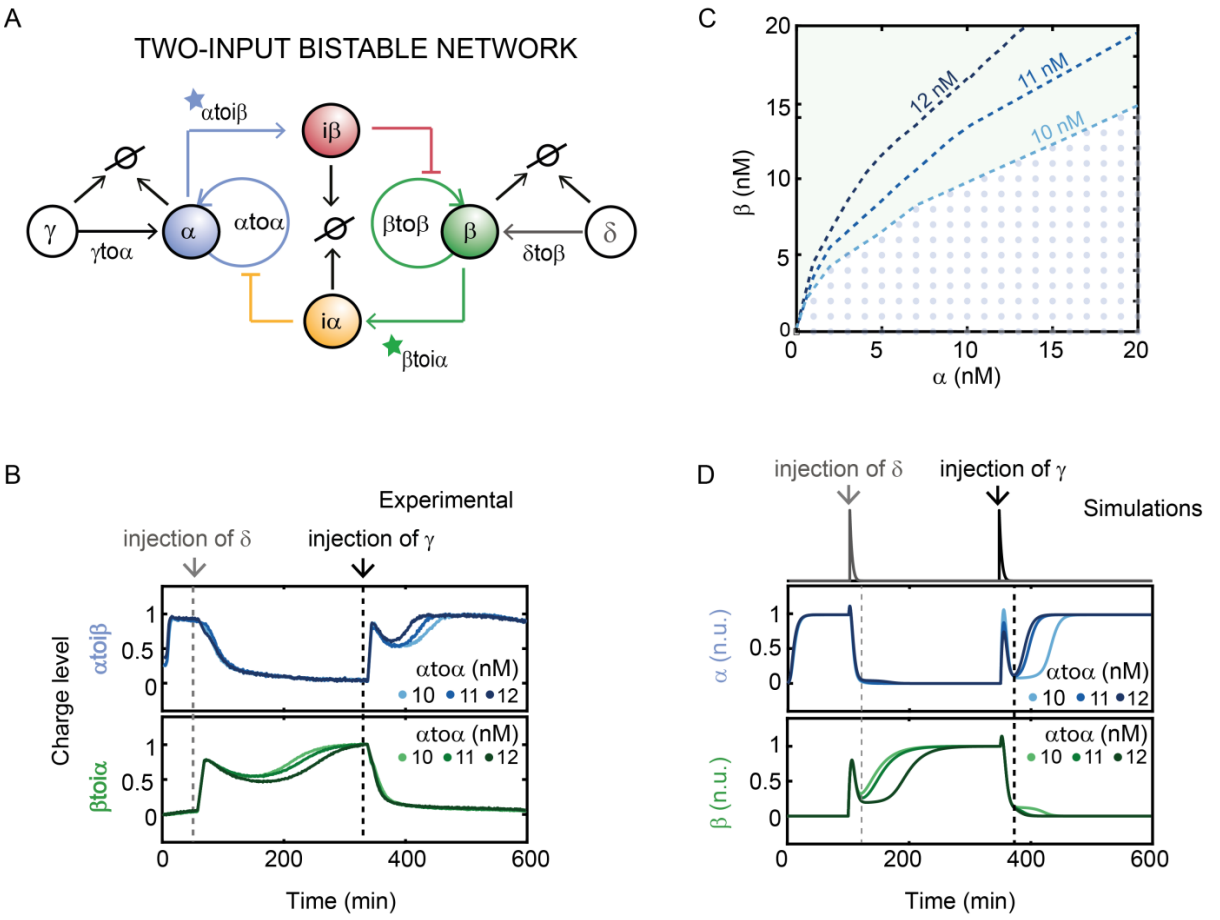

Figure 2.5: PEN-based two-input switchable network. A) Schematic illustration of the bistable switch which consists of four templates including the autocatalytic templates ***atoα*** and ***βtoβ*** and the inhibitory templates ***atoiβ*** and ***βtoiα***. The network switches between states upon injection of ***γ*** and ***δ*** which are received by templates ***γtoα*** and ***δtoβ***. The dynamics of the bistable switch are followed via N-quenching using templates ***βtoiα*** and ***atoiβ*** which are 3'-end labeled with a DY530 and FAM fluorophore respectively. B) Results of experiments which were performed as described in *Paragraph* 2.5 for a concentration range of ***atoα*** and initiated with 1 nM of ***α***. The dotted lines show the time points at which 30 nM of the Inputs ***δ*** and ***γ*** were added. Experiments were conducted using 20 nM ***βtoiα***, 15 nM ***atoiβ***, 24 nM ***βtoβ***, 10 nM ***γtoα*** and ***δtoβ***, 10 U/mL Bst 2.0 warmstart DNA polymerase, 10 U/mL Nt. bstNBI and 200 nM ttRecJ. The charge level is the normalized fluorescence of the signal of DY530 and FAM fluorophores which is 0 in the absence of template's input primer and 1 at the steady-state value of primer ***β*** and ***α*** respectively. C) Separatrices (dotted lines) in the (α,β)-plane for a concentration range of ***atoα*** including 10, 11 and 12 nM obtained using the heuristic model. The basin of attraction of the switch was analysed for different initial concentrations of ***α*** and ***β***. Besides no input, the switch evolves to the α-(area with blue circles) or β-state (green area) dependent on the initial concentrations of ***α*** and ***β***. The values for the parameters, which were either experimentally determined or empirically chosen according to the criteria as described in *Paragraph* 2.2, are shown in Table 2.2. D) Results of simulations performed using the heuristic model (Equation 2.5). The time traces of ***γ*** and ***δ*** are shown on top of the graphs which were injected with a concentration of 30 nM. The dotted lines indicate the time points at which ***γ*** and ***δ*** are degraded completely (<0.01 nM). Simulations were performed for the same concentration range of ***atoα*** as in the experiments. The traces of ***α*** and ***β*** were converted to normalized units (n.u.) by normalizing ***α*** and ***β*** to their steady-state concentrations.

2.4 Discussion

Herein we have shown the details of the methodology of the PEN toolbox and implemented two PEN-based networks *in vitro*. Furthermore, the dynamics of both the INVERTER and bistable switch could be theoretically predicted using a new model, validating the modularity and versatility of our heuristic approach. Moreover, the model gives valuable insights in the nonlinear mechanistic of PEN-based circuits. In the following *Chapter* we expand the PEN-toolbox by designing an additional module, enabling the coupling of PEN-based circuits to downstream actuators.

2.5 Experimental section

Materials. Oligonucleotides (Table 2.1) were obtained from Integrated DNA Technologies (IDTDNA) or Biomers and were purified using High Performance Liquid Chromatography (HPLC). Templates which are not 5' end labeled with a fluorophore or a quencher have three phosphorothioate backbone modifications at the 5' end preventing them from degradation. Furthermore, since 3'-OH can be extended by DNA polymerase, the templates were ordered with a phosphate modification at their 3' end to prevent circuit leakage. Templates at which primers are produced inevitably have an additional nickase recognition site at the template's output site. Based on previous work,[2] to decrease the affinity of the nicking enzyme for the output site the thymine base in the nickase recognition site at the template's output was replaced with a uracil base. Concentrations of DNA were verified using UV-spectrophotometry. The nicking enzyme and polymerase were obtained from NEB, while ttRecJ, a thermophilic equivalent of the RecJ enzyme from Thermus Thermophilus was obtained from Dr. A. Estévez-Torres.

PEN-based experiments. Throughout the study, reactions of total volume 20 µL were assembled in a master mix, containing 20 mM Tris-HCl, 10 mM KCl, 50 mM NaCl, 10 mM $(NH_4)_2SO_4$, 8 mM $MgSO_4$, 0.1% Triton x-100, 400 µM of each deoxyribonucleotide triphosphates (dNTP; New England Biolabs (NEB)), 0.1% Synperonic F108 (Sigma Aldrich), 2 µM Netropsin (Sigma Aldrich), 1 mg/mL Bovine Serum Albumine (BSA; NEB), 4 mM Dithiothreitol (DTT) and a pH of 8.8. A 4x stock solution of the master mix was prepared, excluding BSA and DTT, which were added during reaction assembly together with enzymes and oligonucleotides. The activity of each batch of ttRecJ was determined using the experiments as described in Supplementary Fig. 20 and batch to batch variations were compensated by changing the enzyme concentration. For experiments in which injections

were done during the experiment an oil layer (15 µL) was used to prevent a shift of the signal after injection. Experiments were performed at a temperature of 42 °C and fluorescence was recorded over time (CFX96 PCR machine).

Experimental data of FAM and DY530 were handled by subtracting the raw data by a baseline curve. This baseline curve was measured for both the FAM and DY530 channels in presence of the inhibition templates and in absence of amplification of $\boldsymbol{\alpha}$ and $\boldsymbol{\beta}$ respectively. Subsequently, the signal of DY530 and FAM fluorophores were normalized to the charge levels of $\boldsymbol{\beta to i\alpha}$ and $\boldsymbol{\alpha to i\beta}$ which is 0 in the absence of template's input primer and 1 at the steady-state value of primer $\boldsymbol{\beta}$ and $\boldsymbol{\alpha}$ respectively.

Determining thermodynamic dissociation constants of DNA hybridization. The thermodynamic dissociation constants of DNA hybridization were determined from melting curves, obtained using JASCO V-650 spectrophotometer and a 1 cm path length cuvette with a volume of 200 µL. UV absorbance of the partial duplexes was measured at a wavelength of 260 nm as a function of temperature. A temperature gradient of 1°C min^{-1} was used, since melting and cooling profiles were significantly similar at this gradient. The melting curves were converted to absorbance and were used for non-linear least squares analysis using the following equation to obtain the enthalpy and entropy:[17]

$$\theta(T) = 1 + \frac{1}{2C_0 \exp\left(-\frac{\Delta H^o - T\Delta S^o}{RT}\right)} \pm \sqrt{\frac{4C_0 \exp\left(-\frac{\Delta H^o - T\Delta S^o}{RT}\right) + 1}{4C_0^2 \exp\left(-\frac{2\left(\Delta H^o - T\Delta S^o\right)}{RT}\right)}} \tag{2.6}$$

Where θ is the fraction of partially duplex, T is the temperature in Kelvin, R is the gas constant (kcal mol^{-1} K^{-1}), and C_0 is the initial concentration of the duplex DNA (M) divided by the molarity of water (M). Nonlinear least square optimization was performed to obtain the enthalpy (kcal mol^{-1} K^{-1}) and entropy (kcal mol^{-1}) which were used to determine the standard Gibb's free energy (kcal mol^{-1}) of DNA hybridization (from which the thermodynamic dissociation constant can be calculated) at a temperature of 42 °C:

$$\Delta G^o = \Delta H^o - T\Delta S^o \tag{2.7}$$

The thermodynamic dissociation constants of DNA hybridization are shown in Supplementary Table 2.2.

Determination of the kinetics of exonuclease. To characterize the kinetics of the exonuclease experiments were performed in which 1.5, 2 and 2.5 μM of a ssDNA strand was added to eppendorfs (white real-time PCR tube strips, Eppendorf) in minimal volumes. Then, master mix with the DNA intercalating dye EvaGreen (2x) and 10 nM exonuclease ttRecJ was added leading to a final volume of 20 μL. After all components were assembled the mixtures are vortexed and spinned down and subsequently the eppendorfs were placed in the Polymerase Chain Reaction (PCR) system (CFX96 from Bio-Rad) which was prewarmed at 42°C with a lid temperature of 70°C to prevent condensation. The relative fluorescence units (RFU) were measured over cycles of 12 seconds. For every datacurve the same analysis procedure was followed. The very first part (5 min) of the RFU versus time curve often contains an under or overshoot (*vide infra*), caused by equilibration effects. When this was observed the initial data was removed, and an estimate of these datapoints was made by extrapolation, i.e. by performing linear fitting to the first part of the raw data curve an estimate could be made of the RFU of the first datapoints. The RFU at the timepoint at which its values became constant, corresponding to the timepoint at which all non-protected primer was degraded by exonuclease, was subtracted from the datacurve, so that at $t = t_{end}$ an RFU of zero was obtained. Then, the RFU was converted to the concentration of ssDNA by dividing the RFU by a factor obtained by dividing the initial RFU by the initial concentration of degradable ssDNA. Using the datacurve obtained from the experiment, the Michaelis-Menten parameters, V_{max} and K_{exo}, were determined by non-linear least squares fitting of Equation 2.3.

Software. ODE simulations were performed using Matlab's (R2016b) built-in *ode45* solver. Furthermore, non-linear least squares fitting was performed using the Levenberg-Marquardt algorithm. To prevent entrapment in local minima of the cost function, Latin Hypercube sampling was used to create twenty initial parameter vectors, with values in between an interval of 0.01 and 100 times of the expected parameter value. From these twenty initial parameter values the parameter values corresponding to the lowest residual sum of squares was selected. using the Matlab routine *lsqnonlin* which uses a subspace trust-region method based on the interior-reflective Newton method.

Table 2.1: DNA sequences of the INVERTER and bistable switch

		Sequence (5' -> 3')	Length (# bases)	3' mod
INVERTER/Bistable switch				
Templates	***αtoα***	C*C*A*AGAC***U***CAG-CCAAGACTCAG	22	phosphate
	βtoβ	A*A*C*AGAC***U***CGA-AACAGACTCGA	22	phosphate
	αtoiβ	T*T*A*CTCGAAACAGAC-CCAAGACTCAG	26	FAM
	βtoiα	T*T*A*CTCAGCCAAGAC-AACAGACTCGA	26	DY530
	γtoα	C*C*A*AGAC***U***CAG-GCATGACTCAT	22	phosphate
	δtoβ	A*A*C*AGAC***U***CGA-CACTGACTCCT	22	phosphate
Inputs	***α***	CTGAGTCTTGG	11	
	β	TCGAGTCTGTT	11	
	γ	ATGAGTCATGC	11	
	δ	AGGAGTCAGTG	11	
Inhibitors	***iα***	GTCTTGGCTGAGTAA	15	
	iβ	GTCTGTTTCGAGTAA	15	

[1] * Indicate phosphorothioate modifications

[2] Complementary sequences are represented by the colors, except for ***iα*** and ***iβ*** with the autocatalytic templates

[3] Underlined sequences represent the nickase recognition site

[4] Replacement of thymine by an uracil is indicated in italic bold

[5] Different domains in the sequences are separated by '-'

Table 2.2: Model parameters

Parameters determined in separate experiments			
Thermodynamic dissociation constants of DNA hybridization			
K_{α}	6 nM	$K_{i\beta}$	0.86 nM
K_{β}	24 nM	K_{γ}	26 nM
$K_{i\alpha}$	0.25 nM	K_{δ}	18 nM
Exonuclease (10 nM)			
V_{exo}	27 nM min^{-1}	K_{exo}	45 nM
Empirical model parameters			
V_{γ}	8.5 nM min^{-1}	$V_{i\beta}$	0.8 nM min^{-1}
V_{δ}	7.2 nM min^{-1}	λ_{α}	25
V_{α}	6.5 nM min^{-1}	λ_{β}	28
V_{β}	15 nM min^{-1}	V_{exo}*	23.4 nM min^{-1}
$V_{i\alpha}$	1.6 nM min^{-1}		

* The parameter V_{exo} was estimated to be lower than experimentally determined in isolation, since sequestration of exonuclease by the templates is present. We manually adapted this value.

2.6 References

1. Montagne, K., Plasson, R., Sakai, Y., Fujii, T. & Rondelez, Y. Programming an in vitro DNA oscillator using a molecular networking strategy. *Mol. Syst. Biol.* **7**, 466 (2011).
2. Padirac, A., Fujii, T. & Rondelez, Y. Bottom-up construction of in vitro switchable memories. *Proc. Natl. Acad. Sci. U.S.A.* **109**, 3212-3220 (2012).
3. Fujii, T. & Rondelez, Y. Predator - prey molecular ecosystems. *ACS Nano* **7**, 27-34 (2013).
4. Genot, A.J. et al. High-resolution mapping of bifurcations in nonlinear biochemical circuits. *Nat. Chem.* **8**, 760-767 (2016).
5. Montagne, K., Gines, G., Fujii, T. & Rondelez, Y. Boosting functionality of synthetic DNA circuits with tailored deactivation. *Nat. Comm.* **7**, 13474 (2016).
6. Trunnell, N.B., Poon, A.C., Kim, S.Y. & Ferrell, J.E. Ultrasensitivity in the regulation of Cdc25C by Cdk1. *Mol. cell* **41**, 263-274 (2011).
7. Süel, G.M., Garcia-Ojalvo, J., Liberman, L.M. & Elowitz, M.B. An excitable gene regulatory circuit induces transient cellular differentiation. *Nature* **440**, 545-550 (2006).
8. Buchler, N.E., Gerland, U. & Hwa, T. Nonlinear protein degradation and the function of genetic circuits. *Proc. Natl. Acad. Sci. U.S.A.* **102**, 9559-9564 (2005).
9. Nguyen, L. et al. Switches, excitable responses and oscillations in the Ring1B/Bmi1 ubiquitination system. *PLoS Comput. Biol.* **7**, e1002317 (2011).
10. Padirac, A., Fujii, T., Estévez-Torres, A. & Rondelez, Y. Spatial waves in synthetic biochemical networks. *J. Am. Chem. Soc.* **135**, 14586-14592 (2013).
11. Zadorin, A.S. et al. Synthesis and materialization of a reaction–diffusion French flag pattern. *Nat. Chem.* **advance online publication** (2017).
12. Brandman, O. & Meyer, T. Feedback loops shape cellular signals in space and time. *Science* **322**, 390-395 (2008).
13. Karsenti, E. Self-organization in cell biology: a brief history. *Nat. Rev. Mol. Cell Biol.* **9**, 255-262 (2008).
14. Gines, G. et al. Microscopic agents programmed by DNA circuits. *Nat. Nanotech.* **advance online publication** (2017).
15. Bissette, A.J. & Fletcher, S.P. Mechanisms of autocatalysis. *Angew. Chem. Int. Ed.* **52**, 12800-12826 (2013).
16. Padirac, A., Fujii, T. & Rondelez, Y. Quencher-free multiplexed monitoring of DNA reaction circuits. *Nucleic Acids Res.* **40**, e118 (2012).
17. Chen, Y.J. & Huang, X. DNA sequencing by denaturation: Principle and thermodynamic simulations. *Anal. Biochem.* **384**, 170-179 (2009).

3

Hierarchical control of enzymatic actuators using PEN-based switchable memories

Abstract Inspired by signaling networks in living cells, DNA-based programming aims for the engineering of biochemical networks capable of advanced regulatory and computational functions under controlled cell-free conditions. While regulatory circuits in cells control downstream processes through hierarchical layers of signal processing, coupling of enzymatically-driven DNA-based networks to downstream processes has rarely been reported. Here, we expand the scope of molecular programming by engineering hierarchical control of enzymatic actuators using feedback-controlled DNA-circuits capable of advanced regulatory dynamics. We developed a translator module which converts signaling molecules from the upstream network to unique DNA strands driving downstream actuators with minimal retroactivity and support these findings with a detailed computational analysis. We show our modular approach by coupling of a previously engineered switchable memories circuit to downstream actuators based on β-lactamase and luciferase. To the best of our knowledge, our work demonstrates one of the most advanced DNA-based circuits regarding complexity and versatility.

The work in this chapter has been published in:
Lenny H.H. Meijer, Alex Joesaar, Erik Steur, Wouter Engelen, Rutger A. van Santen, Maarten Merkx and Tom F.A. de Greef – Nature Communications, **2017**, 8, 1117

3.1 Introduction

DNA has proven to be a versatile building block for the construction of functional devices useful in diagnostics and therapeutics,[1] including nanostructures for the delivery of cargo,[2-4] molecular walkers,[5] or actuators which mechanically control protein activity.[6-11] Additionally, synthetic molecular platforms based on enzyme-free DNA strand exchange are highly amenable for the rational design of reaction networks due to the predictable thermodynamics of DNA binding enabling the engineering of networks with functionalities such as amplification,[12,13] thresholding[14,15] or Boolean and arithmetic operations.[16-18] Enzymatically-driven DNA-based networks exhibit greater nonlinear kinetics, higher turnover rates and, thereby, further increase the range of dynamic behaviours.[19] Recent work has shown that transcriptional circuits in which genelets, i.e. DNA templates that produce RNA regulators for other genelets, can yield switches,[20] oscillators,[21,22] and adaptive dynamics.[23] In addition, networks based on DNA replication, nicking, and degradation have shown to be highly modular and have been engineered to display stable oscillations,[24] multistability,[25] traveling waves,[26,27] and chaotic dynamics.[28] These cell-free circuits provide a simple and well-controlled platform to implement various types of regulatory functions, which increases our understanding of the design principles underlying specific cellular tasks.[29] Interestingly, regulatory circuits with specific topology-function correlation inside living cells are not isolated but interconnected to downstream processes resulting in hierarchical layers of signal generation and processing.[29] However, coupling of enzymatically-driven DNA-based networks displaying higher-order dynamics to downstream processes has rarely been reported. Franco and co-workers realized the control of a DNA tweezer using a genelet-based oscillator and demonstrated an insulating device to reduce retroactivity.[22,30] However, to the best of our knowledge the control of enzymatic actuators by dissipative, enzymatically-driven DNA circuits has not been reported. Here, we engineer and implement hierarchical control of biochemical actuators, such as a NanoLuc-based actuator[31] and a self-inhibitory TEM1 β-lactamase construct,[9] using an upstream polymerase-exonuclease-nickase (PEN)-based switchable memories circuit.[25] We developed a translator module enabling the translation of the dynamic state of the upstream network to the directed control of the downstream enzymatic actuators (Figure 3.1A) with minimal retroactivity.[32,33] Our design strategy for the translator module harnesses several design criteria resulting in minimal retroactivity as validated by experiments and corroborated by a theoretical analysis. The translator module improves the utility of feedback-controlled DNA circuits as it interfaces complex information

processing molecular programs to functional downstream enzymatic processes in a modular and orthogonal fashion. By precise and careful tuning of many different enzymatic reactions and a fundamental understanding on the origin of retroactivity, we are able to demonstrate hierarchical control of enzymatic actuators by dissipative DNA-circuits.

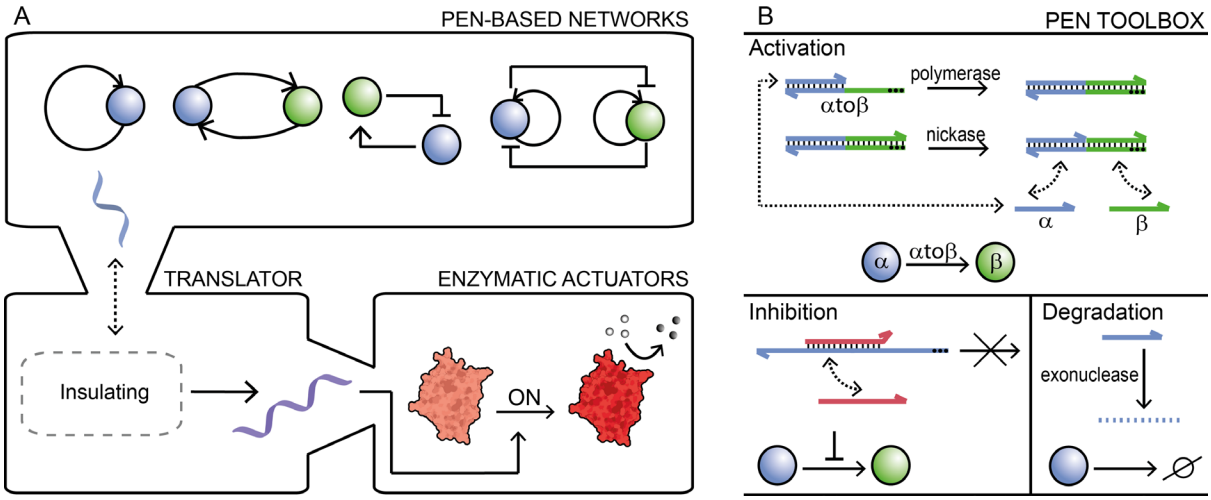

Figure 3.1: Controlling enzymatic actuators using dissipative DNA-based circuits. A) The dynamics of PEN-based circuits is used to time and control downstream processes. In this work a translator module was designed that translates output strands from the upstream network to unique regulatory DNA strands, which in turn drive enzymatic actuators, while insulating the upstream network from the additional load. B) Enzyme driven DNA-based circuits based on the PEN toolbox comprise three modules including activation, inhibition and degradation. Activation is achieved by binding of input ssDNA signals (e.g. primer ***α***) to their target template (e.g. ***αtoβ***) which enables DNA polymerase to extend the oligomer-template pair, followed by nicking of the elongated strand. This results in the return of the input ssDNA signal and a newly formed output ssDNA (e.g. oligomer ***β***), which dissociate from the template because these reactions are performed around the melting temperature of the partial duplexes. The activation of templates can be inhibited by ssDNA strands that are complementary to part of the template's sequence, and possess a two-base mismatch at their 3' ends which prevents extension of the partial duplex, rendering the template strand inactive. Finally, signal and inhibition strands are degraded over time by exonuclease. The template strands are protected from degradation by 5' end phosphorothioate backbone modifications indicated by the black dots.

3.2 Coupling PEN-based networks to a translator module

As shown in *Chapter* 2, PEN-based networks are highly modular as templates can be connected so that they control each other's activity resulting in a wide range of out-of-equilibrium dynamics.[24-28] However, the toolbox makes use of relatively short single-stranded primers that have a melting temperature around the experimental temperature of 42 °C, limiting the PEN toolbox from activation of DNA-based enzymatic actuators which typically require much longer activator strands.[6-11,31,34] We developed a PEN-based translator module which translates the short primers from the PEN toolbox to relatively long output DNA strands (> 30 bases). Ideally, the translator module should completely isolate the upstream network from the enzymatic actuators as this would allow modular connection of PEN-based

circuits to downstream processes. Inevitably, the translator module provides a load to the upstream circuit. The interconnection should therefore be designed to have a minimal effect on the dynamics of the core network, i.e. retroactivity should be minimized. Previous studies have shown that the retroactivity from a downstream system can be attenuated either by connecting the load via a large gain and/or by separation of timescales,[22,30,32,33,35] i.e. the dynamics of the interface connecting the load to the upstream network should be fast compared to the intrinsic dynamics of the core network itself.

Based on these considerations the PEN-based translator module was designed to provide a high gain while only transiently sequestering the output of the upstream DNA system (Figure 3.2A). Primer ***α*** from the upstream network reversibly binds to the 3' end of template ***αtoX***, with forward and backward rates (minutes, Table 3.2) that are substantially faster than the timescale of the dynamics of the PEN toolbox (hours). Template ***αtoX*** is protected from degradation by phosphorothioate modifications at its 5' end and, hence, the load to the upstream circuit is time invariant. Similar to the activation module of the PEN toolbox, the polymerase extends ***α*** followed by the action of nickase resulting in a nicked duplex regenerating ***α*** and producing output strand ***X***. While ***α*** reversibly dissociates from the template, ***X*** is tightly bound and can only be released via DNA polymerase mediated strand-displacement during extension of ***α***, which now can activate a downstream enzymatic actuator. Subsequently, the nickase hydrolyses the upper strand of the duplex after which a new cycle starts resulting in linear amplification of ***X***. Besides minimizing the retroactivity to the dynamics of the upstream reaction network, these features result in a translator module that responds fast, thereby transducing the state of the upstream network almost instantaneously (*vide infra*).

To provide proof-of-principle for the translator module, we characterized the performance of the translator module isolated from the upstream network (Figure 3.2B-D). To this end, an experiment was performed for a concentration range of ***αtoX*** in presence of polymerase and nickase and the output ***X*** was quantified using a molecular beacon. As expected, addition of ***α*** results in linear amplification of ***X*** (Figure 3.2B and Figure S3.1) eventually opening all available molecular beacons. To quantify the kinetics and gain of the translator module in more detail, the production rate of ***X*** was determined for a concentration range of ***αtoX*** (Figure 3.1B). For low concentrations of ***αtoX***, the data shows a linear increase of the production rate while for higher concentrations the production rate levels off. While the concentration of ***α-αtoX*** increases linear with ***αtoX*** for the concentration range used in these

experiments (Table 3.2), saturation of the enzymes limits the rate at which strand ***X*** can be produced.

Next we quantified the gain of the translator module using Equation 3.1:

$$Gain = \frac{d[X]/dt}{[\alpha - \alpha toX]}; \quad (3.1)$$

with d[***X***]/dt the production rate of ***X*** in nM hours^{-1} and [***α- αtoX***] the concentration (in nM) of the partial duplex consisting of input ***α*** bound to template ***αtoX*** calculated using the thermodynamic dissociation constant (Table 3.2). The results reveal a decreasing gain from 9 hour^{-1} to 6 hour^{-1} with increasing concentration of translator template, i.e. per hour one input produces 9 to 6 outputs depending on the concentration of translator template. The decrease in gain with increasing concentration of translator template is the result of the hyperbolic dependence of the production rate on the concentration of translator template. Importantly, the PEN toolbox includes an exonuclease which degrades produced DNA strands in the reaction network. In order to test the compatibility of exonuclease with the translator module, experiments were performed in the presence of polymerase, nickase and exonuclease (Figure 3.2C). The results show that the translator module is able to amplify ***X*** even in the presence of exonuclease. Further experiments reveal that that the translator module is able to produce sequences of different lengths with very similar kinetics (Figure 3.2D), showing the modular performance of the translator. Based on these results we conclude that the translator module should be generally applicable to allow control of downstream DNA-templated biochemical reactions by PEN-based networks.

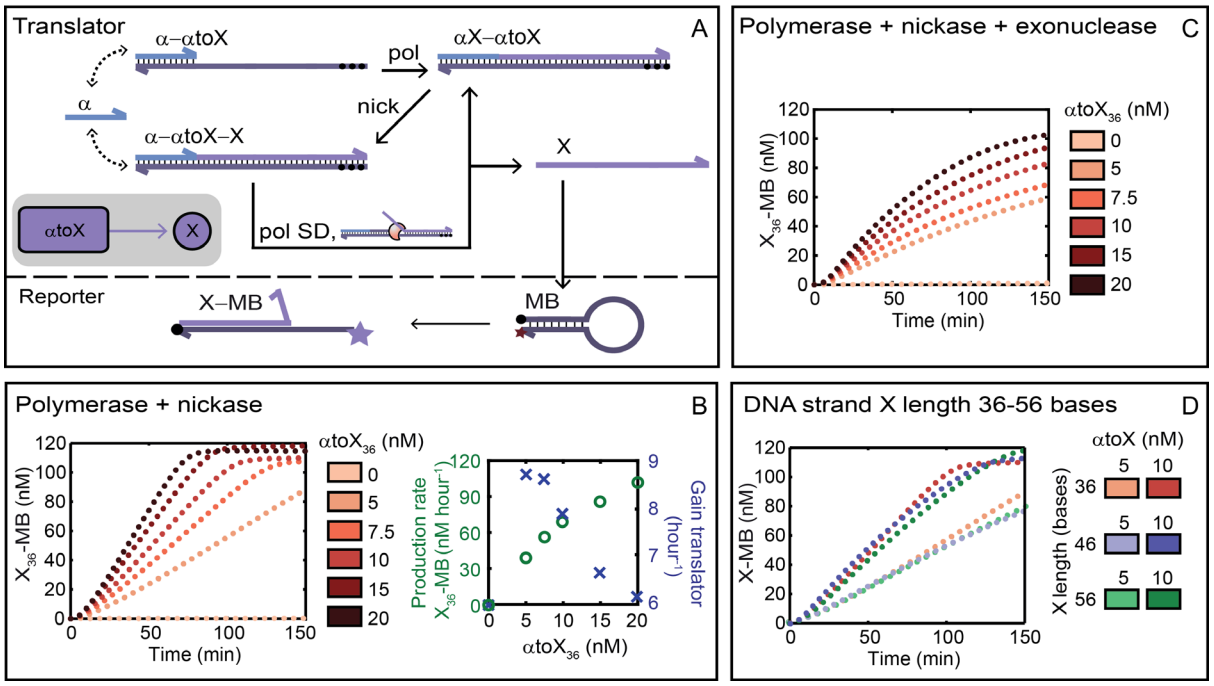

Figure 3.2: Characterization of the translator module. A) The design of the translator module in which an output ssDNA of the upstream network (e.g. primer ***α***) hybridizes to the template strand (***αtoX***) of the translator module. After the action of polymerase (pol) and nickase (nick) the input primer reversibly dissociates, while the relatively long output strand (ssDNA ***X***) is released via polymerase-mediated strand displacement (pol SD). The reaction cycle continues resulting in linear amplification. The black dots at the 5' end of DNA strands represent phosphorothioate backbone modifications. A simplified illustration of the translator module is shown on the left. The production of output ***X*** was quantified using a molecular beacon (***MB$_x$***). B) Experimental traces of the linear amplification of ***X$_{36}$*** (36 bases) performed for a concentration range of the translator template ***αtoX*** in presence of polymerase (15 U/mL) and nickase (10 U/mL) and initiated by addition of ***α***. The production rate of ***X$_{36}$-MB*** and gain of the translator for the concentration range of translator template were determined from the slope of the experimental traces in the linear regime. The gain (Equation 3.1) is defined by the number of output ***X*** produced per unit time (1 hour) per complex of primer ***α*** bound to template ***αtoX*** calculated using the thermodynamic dissociation constant (Table 3.2). C) Experimental traces of the linear amplification of ***X$_{36}$*** (36 bases) performed for a concentration range of the translator template ***αtoX*** in presence of polymerase (15 U/mL), nickase (10 U/mL) and exonuclease (200 nM) and initiated by addition of ***α*** protected with phosphorothioate modifications at its 5'-end (Figure S3.2). D) The performance of the translator module for varying sequences and lengths of ***X***. The experiment was performed starting with 10 nM of ***αtoX*** in the presence of 15 U/mL polymerase and 10 U/mL nickase and initiated by addition of ***α***. Experiments were carried out as described in *Paragraph* 3.8. Fluorescence was converted to concentration using a standard curve (Figure S3.16).

3.3 Retroactivity of the translator module connected to a simple PEN-based circuit

In order to assess the retroactivity that arises from connecting the translator module to an upstream network, we first coupled the translator module to a PEN-based INVERTER circuit (Figure 3.3A), described in detail in *Chapter* 2. Briefly, the INVERTER network is based on an autocatalytic module producing activator ***α*** which is inhibited by addition of input ***β*** resulting in an output that is inverted compared to the change in input. The INVERTER network shows a pulse response after injection of input ***β***, characterized by its amplitude and

response time (Figure 3.3). The dynamics of the INVERTER network were followed by N-quenching,[36] which monitors oligomer hybridization to templates by a change in fluorescence. Experiments were performed with increasing concentrations of translator template ***αtoσ*** while the concentration of output ***σ*** was assessed using a molecular beacon (***MB***). As can be observed from Figure 3.3B the experimental results show increasing production of ***σ*** for higher concentrations of ***αtoσ***. More importantly, the production of ***σ*** ceases upon injection of ***β*** and continues when the INVERTER returns to pre-stimulus steady-state showing that the production rate of ***σ*** follows the dynamics of the INVERTER circuit instantaneously. In addition, the results show a very gradual change in dynamics of the INVERTER for increasing concentrations of translator template, indicating low retroactivity.

To further quantify the retroactivity that arises from coupling of the translator module to the PEN-based circuit, we, in collaboration with our theoretical partners dr. E. Steur and Prof. R.A. van Santen, expanded the model of the INVERTER described in *Chapter* 2 to include the effect the additional load, The minimal model allows us to rationalize the effect of increasing loads on the dynamics of the INVERTER network. The model consists of a set of ordinary differential equations (ODEs) expressing the trajectories of ***β***, ***iα***, ***α***, ***σ***, ***MB***, ***σ-MB*** and ***iβ***:

$$\frac{d[\beta]}{dt} = -\frac{V_{exo}[\beta]}{K_{exo}+[\alpha]+[\beta]+[i\alpha]+[i\beta]+[\sigma]}; \tag{3.2a}$$

$$\frac{d[i\alpha]}{dt} = \frac{V_{i\alpha}[\beta]}{K_{i\alpha}+[\beta]} - \frac{V_{exo}[i\alpha]}{K_{exo}+[\alpha]+[\beta]+[i\alpha]+[i\beta]+[\sigma]}; \tag{3.2b}$$

$$\frac{d[\alpha]}{dt} = \frac{V_{\alpha}[\alpha]}{K_{\alpha}+[\alpha]+\lambda_{\alpha}[i\alpha]} - \frac{V_{exo}[\alpha]}{K_{exo}+[\alpha]+[\beta]+[i\alpha]+[i\beta]+[\sigma]} - \frac{V_{L\alpha}[\alpha]}{K_{L\alpha}+[\alpha]} + k_{\alpha}[\theta]; \tag{3.2c}$$

$$\frac{d[\sigma]}{dt} = \frac{V_{L\alpha}[\alpha]}{K_{L\alpha}+[\alpha]} - \frac{V_{exo}[\sigma]}{K_{exo}+[\alpha]+[\beta]+[i\alpha]+[i\beta]+[\sigma]} - k_{rep}[\sigma][MB]; \tag{3.2d}$$

$$\frac{d[MB]}{dt} = -k_{rep}[\sigma][MB]; \qquad \frac{d[\sigma-MB]}{dt} = k_{rep}[\sigma][MB]; \tag{3.2e/f}$$

$$\frac{d[i\beta]}{dt} = \frac{V_{i\beta}[\alpha]}{K_{i\beta}+[\alpha]} - \frac{V_{exo}[i\beta]}{K_{exo}+[\alpha]+[\beta]+[i\alpha]+[i\beta]+[\sigma]}; \tag{3.2g}$$

$$\frac{d[\theta]}{dt} = \rho\frac{V_{L\alpha}[\alpha]}{K_{L\alpha}+[\alpha]} - k_{\alpha}[\theta]; \tag{3.2h}$$

As described in detail in *Chapter* 2, the production of oligomers $\boldsymbol{\alpha}$, $\boldsymbol{i\alpha}$, $\boldsymbol{\sigma}$ and $\boldsymbol{i\beta}$ by polymerase and nickase is described by a single Michaelis-Menten approximation with the maximum rates (V_i) and the Michaelis-Menten parameter (K_i), while inhibition of production is denoted by λ (Equation 3.2c). Furthermore, degradation is modeled by a Michaelis-Menten approximation which includes terms that describe competition between the substrates. Binding of $\boldsymbol{\sigma}$ to the reporter (***MB***) is described as a single step with second-order rate constant (k_{rep}, Equation 3.2d-f). The two final terms in Equation 3.2c take into account the change in the concentration of $\boldsymbol{\alpha}$ caused by the reversible sequestration of $\boldsymbol{\alpha}$ by the translator module. While the second last term represents the amount of $\boldsymbol{\alpha}$ that is sequestered by the translator for production of $\boldsymbol{\sigma}$, the last term accounts for the reproduction of $\boldsymbol{\alpha}$ due to the dissociation of $\boldsymbol{\alpha}$ from the nicked state of the translator module. The rate of reproduction of $\boldsymbol{\alpha}$ is given by $\boldsymbol{\theta}$, representing the concentration of nicked translator module, linearly scaled with the dissociation rate constant of $\boldsymbol{\alpha}$ (k_α). Specifically, the dissociation rate constant of $\boldsymbol{\alpha}$ is determined by the equilibrium dissociation constant ($K_{L\alpha}$) as the association rate constant is invariable for primers with lengths exceeding five bases.[37] We introduced a constant ρ which models the fraction of translator module being in the nicked state ($\boldsymbol{\alpha}$—$\boldsymbol{\alpha to\sigma}$—$\boldsymbol{\sigma}$), depending on the timescale of nicking the duplex ($\boldsymbol{\alpha\sigma}$—$\boldsymbol{\alpha to\sigma}$) relative to the timescale of the polymerase strand-displacement reaction. In the extreme case of ρ=1, the equilibrium of the two states of the translator module is shifted to the nicked state (minimal inherent retroactivity) and, hence, the amount of $\boldsymbol{\alpha}$ reproduced depends on $K_{L\alpha}$. In the other extreme case, i.e. ρ=0, the equilibrium of the two states of the translator module is fully shifted to the duplex conformation ($\boldsymbol{\alpha\sigma}$—$\boldsymbol{\alpha to\sigma}$) and, therefore, no $\boldsymbol{\alpha}$ is reproduced independent on $K_{L\alpha}$ (maximal inherent retroactivity). In summary, retroactivity is determined by the translator concentration, $K_{L\alpha}$ and ρ which is an inherent property of the translator module. While in principle retroactivity could also arise due to global coupling arising from competition of primers for exonuclease, the influence of this effect was found to be negligible (Figure S3.3).

While the kinetic parameters and the equilibrium dissociation constants were measured in separate experiments (*Paragraph* 3.8, Figure S3.18 and S3.19 and Table 3.2) the parameter ρ is defined by the system-dependent enzyme competition between polymerase and nickase (Figure S3.17). Figure 3.3C displays the dynamics of the INVERTER and translator using the heuristic model for two values of ρ. The simulations show that coupling of the translator template results in a delay in the response of the INVERTER independent of the value of ρ while a decreased amplitude with increasing translator template is only observed for a value

of ρ close to 1. Hence, the overall dynamics of the heuristic model qualitatively agree with experimental data for a value of ρ close to 1 indicating low inherent retroactivity arising from the load of the translator module. Thus, by constructing a minimal model we could identify properties significantly contributing to the dynamics of our system and specifically, determine and understand the origin of retroactivity.

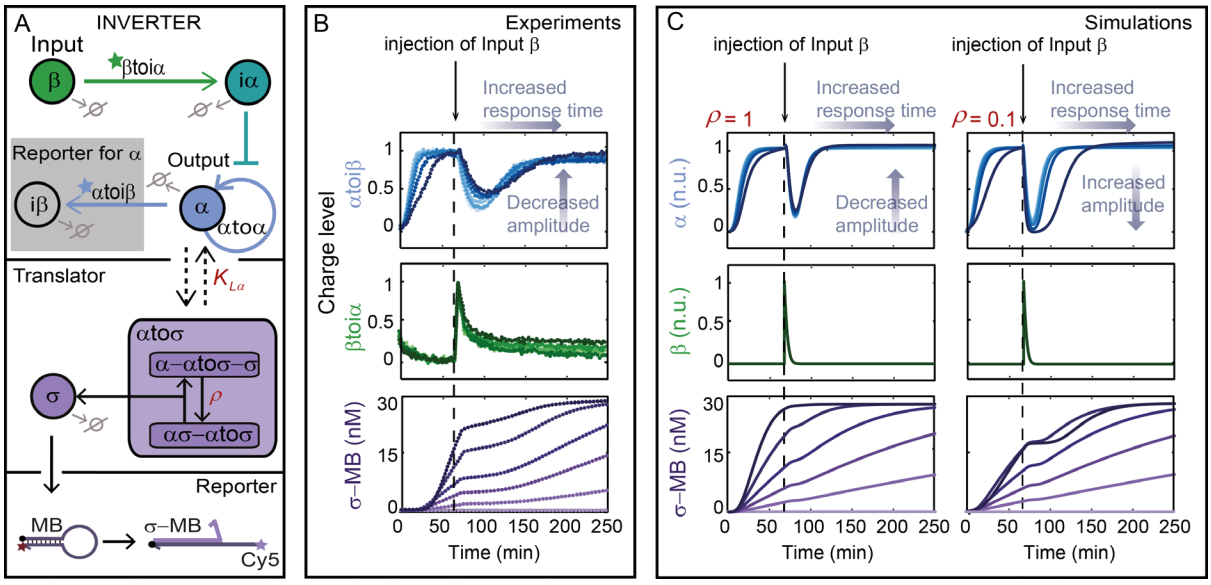

Figure 3.3: Coupling of the translator module to an upstream INVERTER network. A) Schematic illustration of the translator module coupled to a PEN-based INVERTER network. Multiplex monitoring of the dynamics of the network is performed using endogenous template ***βtoiα*** and an exogenous template ***αtoiβ*** which are 3'-end fluorescently labeled with DY530 and FAM respectively while the output strand ***σ*** of the translator module is measured via a molecular beacon (MB) bearing a fluorophore-quencher pair. B) Results of the experiments which were conducted for 0, 2, 5, 10, 20 and 40 nM (light to dark) of translator template ***αtoσ*** in the presence of 7 nM ***αtoα***, 20 nM of ***βtoiα*** and ***αtoiβ***, 30 nM molecular beacon, 10 U/mL Bst 2.0 warmstart DNA polymerase, 25 U/mL Nt. bstNBI and 50 nM ttRecJ. The INVERTER is activated by addition of 0.5 nM ***α*** which is initially amplified until it reaches steady-state in which production by polymerase and nickase and degradation due to exonuclease are balanced. Applying a pulse of 30 nM of input ***β*** at this point initiates the production of ***iα*** which inhibits autocatalytic production of output ***α***. As input strand ***β*** gets degraded the system returns its pre-stimulus steady-state. Hence, the INVERTER network shows a pulse response after injection of input ***β*** which can be characterized by its amplitude and response time which is the time needed to recover to the pre-stimulus steady-state. The charge level is the normalized fluorescence of the signal of DY530 and FAM fluorophores which is 0 in the absence of template's input primer and 1 at the maximal or steady-state value of primer ***β*** and ***α*** respectively. The fluorescence of Cy5 fluorophore was converted to concentration of DNA strand ***σ*** using a standard curve (Figure S3.16). C) Results of simulations using the heuristic model with parameter values as shown in Table 3.2 and with the same concentrations of translator template as used during the experiments in (b) and for different values of ρ. The traces were converted to normalized units (n.u.) by normalizing ***α*** to the steady-state concentration and normalizing ***β*** to its maximum value.

3.4 Connecting the translator module to a two-input bistable switch

Biochemical circuits with specific topology-function relationship inside cells are interconnected to downstream processes and, thereby, regulate the time-dependent control of protein production. Analogous to the hierarchical layers of signal generation and processing in natural cells, we next explored the possibility to engineer and implement orthogonal control of two enzymatic actuators regulated by a synthetic bistable switch.[25] The two-state switchable network as described in *Chapter* 2 was constructed by joining two complementary INVERTER circuits (Figure 3.4A) giving a symmetrical topology in which two autocatalytic modules dynamically repress each other. Orthogonal control of enzymatic actuators by the bistable switch can be achieved by coupling two distinct translator modules to primers $\boldsymbol{\alpha}$ and $\boldsymbol{\beta}$. To validate the activation of the translator modules by these species, a system was constructed in which first a single translator module, $\boldsymbol{\alpha to \sigma}$ or $\boldsymbol{\beta to \sigma}$, was coupled to $\boldsymbol{\alpha}$ or $\boldsymbol{\beta}$ respectively. Results of control experiments of the translator coupled to $\boldsymbol{\alpha}$ or $\boldsymbol{\beta}$ revealed that the production rate of translator output follows the dynamics of the switch (Figure S3.4). To assess the effect of retroactivity arising from the additional load of the translator module to the switch, we systematically increased the concentration of translator template coupled to either $\boldsymbol{\alpha}$ or $\boldsymbol{\beta}$ and switched the network from the α- to the β-state and conversely (Figure 3.4B). The experimental trajectories show that we are able to switch the network both ways when the translator template is coupled to $\boldsymbol{\beta}$. Furthermore, we were able to switch the network from the α- to the β-state when the translator is coupled to $\boldsymbol{\alpha}$. However, the trajectories of switching the network from the β- to the α-state in this case show an initial increase in $\boldsymbol{\alpha}$ after applying a pulse of $\boldsymbol{\gamma}$, followed by a return to the β-state, indicating failure of switching to the α-state. To obtain a fundamental understanding of these observations, the heuristic model that describes the bistable switch (*Chapter* 2) was expanded to include the translator module. The trajectories obtained by the theoretical model correlated well with the experimental results (Figure 3.4B). Interestingly, while ρ was close to 1 for the INVERTER circuit, a value of 0.4 was obtained for the bistable switch indicating an increased inherent retroactivity from the translator module compared to the INVERTER circuit likely due to a change in the system-dependent enzyme competition between polymerase and nickase (Figure S3.17). To analyse the effect of retroactivity, we computationally determined the bistable regime using the concentration of $\boldsymbol{\gamma}$ and $\boldsymbol{\delta}$ as bifurcation parameters in the absence of translator module and when the translator module is coupled to $\boldsymbol{\alpha}$ or $\boldsymbol{\beta}$ (Figure 3.4C). The bifurcation diagram of the switch isolated from the translator module shows an asymmetry to the inputs as more $\boldsymbol{\gamma}$ than $\boldsymbol{\delta}$

is required to obtain bistability, indicating a stronger preference of the β-state as also observed from the seperatrix and computed switching planes (Figure S3.22A and S3.23) As previously noted, this imbalance can be explained by asymmetrical kinetics arising from differences in DNA hybridization Gibbs free energy (Table 3.2).[25] Coupling of the translator template to $\boldsymbol{\beta}$ results in a shift in the separatrix and switching plane in favor of the α-state (Figure S3.22A and S3.23). As a result, a decrease in asymmetry to the inputs $\boldsymbol{\gamma}$ and $\boldsymbol{\delta}$ and consequently, an increase in bistable domain is observed indicating that, counterintuitively, coupling of a load to a bistable network can enhance the robustness of the upstream circuit by the retroactivity from the load. By contrast, the computed bifurcation diagram obtained by coupling of the translator module to $\boldsymbol{\alpha}$ shows a decrease in the range of inputs that generate bistability caused by a shift in the seperatrix in favor of the β-state (Figure S3.22A and S3.23) further increasing the asymmetry of the two states. Hence, retroactivity resulting from the additional load of the translator template to $\boldsymbol{\alpha}$ narrows the parameter region, mostly by a shift in concentration of $\boldsymbol{\gamma}$, for which bistable behaviour is observed. Our theoretical model predicts that bistability can be recovered at high concentrations of input $\boldsymbol{\gamma}$ (> 50 nM). Indeed, experimental results show switching from the β- to the α-state with 10 nM of the translator module coupled to $\boldsymbol{\alpha}$ upon injection of 50 nM $\boldsymbol{\gamma}$ (Figure S3.5) in accordance with our theoretical predictions. In summary, retroactivity from coupling of the translator module to $\boldsymbol{\alpha}$ or $\boldsymbol{\beta}$ can either increase or decrease the input range for which bistable behaviour can be observed which depends on the asymmetry of the switch in isolation. Notably, the retroactivity that arises from coupling of the translator module to $\boldsymbol{\alpha}$ is relatively large compared to coupling to $\boldsymbol{\beta}$, as visualized by the larger shift in the bistable domain. While the intrinsic retroactivity constant ρ and the concentration of translator module was equal for both states of the switch, the dissociation rate constant of $\boldsymbol{\alpha}$ is smaller than that of $\boldsymbol{\beta}$ arising from a lower equilibrium dissociation constant (Table 3.2) accounting for the larger retroactivity. We validated this by computing the seperatrices for different values of $K_{L\alpha}$ or $K_{L\beta}$ showing an increased shift with decreasing dissociation constant (Figure S3.22).

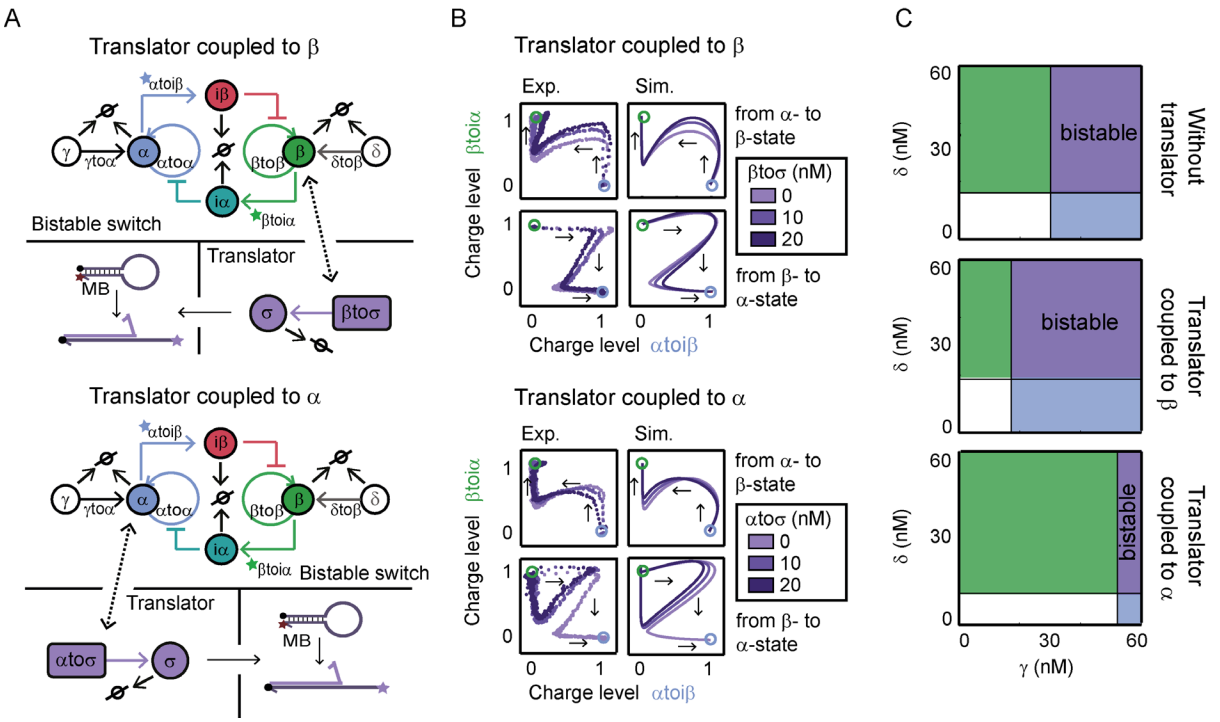

Figure 3.4: Characterizing retroactivity from coupling of the translator module to the memories circuit. A) Schematic illustration of the system, in which the translator module is coupled to ***α*** or ***β*** of the PEN-based bistable switch. The core of the bistable switch consists of four templates including the autocatalytic templates ***atoα*** and ***βtoβ*** and the inhibitory templates ***αtoiβ*** and ***βtoiα***. The network switches between states upon injection of ***γ*** and ***δ*** which are received by templates ***γtoα*** and ***δtoβ***. The dynamics of the bistable switch are followed via N-quenching using templates ***βtoiα*** and ***αtoiβ*** which are 3'-end labeled with a DY530 and FAM fluorophore respectively. B) Experimental (Exp.) and simulated (Sim.) phase diagrams for a concentration range of translator template coupled to ***α*** or ***β***. Experiments were carried out as described in *Paragraph* 3.8 using 20 nM ***βtoiα***, 15 nM ***αtoiβ***, 24 nM ***βtoβ***, 10 nM ***atoα***, ***γtoα*** and ***δtoβ***, 15 U/mL Bst 2.0 warmstart DNA polymerase, 10 U/mL Nt. bstNBI and 200 nM ttRecJ. The switch was either equilibrated to its α-state and 30 nM ***δ*** was injected for switching to the β-state or the switch was equilibrated to its β-state and 30 nM ***γ*** was injected for switching to the α-state. The charge level is the normalized fluorescence of the signal of DY530 and FAM fluorophores which is 0 in the absence of template's input primer and 1 at the steady-state value of primer ***β*** and ***α*** respectively. The blue and green circles represent the α- and β-state respectively. Simulations were performed using the heuristic model with parameter values as shown in Table 3.2. The traces were converted to normalized units (n.u.) by normalizing ***α*** and ***β*** to their steady-state concentrations. C) Bifurcation diagrams of the switch in isolation and with 10 nM of translator module coupled to ***β*** or ***α*** as a function of inputs ***γ*** and ***δ*** obtained using the heuristic model with parameter values as shown in Table 3.2. The monostable domains of ***α*** and ***β*** are shown in blue and green respectively while the bistable domain is shown in purple.

3.5 Control of enzymatic actuators by the translator module

Having established the translator module as a versatile method to translate short ssDNA from the upstream circuit to long DNA strands with minimal retroactivity, we next investigate the possibility to control enzymatic actuators by the translator module. To this end a bioluminescent actuator and a self-inhibitory TEM1 β-lactamase construct were used (Figure 3.5). The bioluminescent actuator is based on a previously reported design[31] and consists of a NanoLuc enzyme conjugated to an oligonucleotide, which hybridizes to a template 3'-end

labeled with a FAM fluorophore (Figure 3.5a). In the closed state this template forms a stem-loop structure which brings the FAM fluorophore and NanoLuc in close proximity resulting in Bioluminescence Resonance Energy Transfer (BRET) between the NanoLuc donor and FAM acceptor dye. Transient opening of the stem-loop structure of the NanoLuc-based actuator was accomplished by the translator template ***αtoσ*** producing activator strand ***σ***, which hybridizes to the loop of the NanoLuc-based actuator and, thereby, via strand displacement disrupts the stem structure. In accordance, the experimental data shows a gradual decrease in BRET ratio after initiation of the translator module, which can be followed in time. Positive (+) and negative (-) controls were run in parallel to account for the decrease in BRET efficiency over time (*Paragraph* 3.8). The rate of opening of the stem-loop structure of the enzymatic actuator can be fine-tuned by the concentration of translator module which scales with the production rate of its output strand (*vide supra*). Likewise, the activity of the TEM1 β-lactamase enzyme was controlled by an orthogonal translator module (Figure 3.5B). β-lactamases are enzymes produced by bacteria to provide antibiotic resistance and are often used as reporter enzymes or to install antibiotic resistance.[38] Using a previously reported design,[9] the activity of TEM1 β-lactamase is controlled by modulation of the interaction of this enzyme with the β-lactamase inhibitor protein BLIP.[9] Specifically, the proteins are conjugated to different oligonucleotides which hybridize to a template connecting the enzyme and inhibitor. Activation of TEM1 β-lactamase is achieved by translator template ***βtoξ*** producing activator strand ***ξ*** which hybridizes to the loop of the self-inhibitory TEM1 β-lactamase actuator and, thereby, separating enzyme and inhibitor. The activity of TEM1 β-lactamase was determined by measuring the hydrolysis rate of a fluorescent substrate. Positive (+) and negative controls (-) were run in parallel to account for the loss in activity of TEM1 β-lactamase in the PEN-toolbox buffer (*Paragraph* 3.8). As observed from the experimental results, the activity of the TEM1 β-lactamase was equal to the background activity prior to initiation of the translator module, while almost complete activation was achieved after 30 minutes of incubation with initiator ***β***. Because of the high binding affinity of the activator strands ***σ*** and ***ξ***, the opening of the stem-loop structure of the NanoLuc-based actuator and the activation of the self-inhibitory TEM1 β-lactamase construct are irreversible. These results show that the translator module is compatible with the NanoLuc-based actuator and the self-inhibitory TEM1 β-lactamase construct and, importantly, reveals it to be a flexible method for the controlled and efficient activation of these actuators.

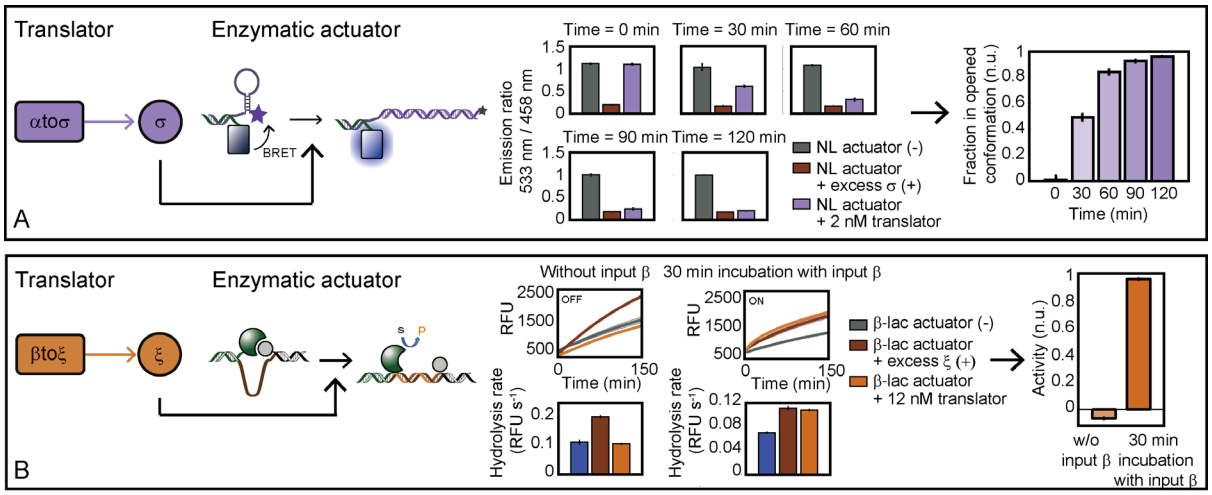

Figure 3.5: The control of enzymatic actuators by the translator module. A) Schematic illustration (left) and experimental results (right) of controlling a NanoLuc (NL)-based actuator by the translator module. Experiments were performed using 2 nM of ***atoσ***, 5 nM of the NanoLuc-based actuator, 15 U/mL Bst 2.0 warmstart DNA polymerase, 10 U/mL Nt. bstNBI and initiated with 30 nM ***α***. The opening of the stem-loop structure of the NanoLuc-based actuator was quantified at intervals of 30 minutes by measuring the BRET ratio between between the NanoLuc donor (em. = 458 nm) and FAM acceptor dye (em. = 533 nm). The translator module was omitted for negative (-) and positive (+) controls and excess of DNA strand ***σ*** was added for the positive controls. Experiments were performed in triplicate and the fraction in opened conformation in normalized units (n.u.) was calculated by subtracting the mean BRET ratio of the positive controls and normalizing to the mean BRET ratio of the negative controls. Error bars and shaded areas represent the standard error of the mean of the experiments. B) Schematic illustration (left) and experimental results (right) of the activation of the self-inhibitory TEM1 β-lactamase (β-lac) actuator by the translator module. Experiments were performed using 12 nM ***βtoξ***, 2.5 nM TEM1 β-lactamase/BLIP actuator, 15 U/mL Bst 2.0 warmstart DNA polymerase, 10 U/mL Nt. bstNBI and initiated with 30 nM ***β***. The activity of TEM1 β-lactamase was measured at time = 0 min prior to initiation with ***β*** and 30 minutes after activation of the translator module and was quantified by measuring the hydrolysis rate of fluorogenic substrate CCF2-FA obtained from the linear regime of the fluorescent time traces. The translator module was omitted for negative (-) and positive (+) controls and excess of DNA strand ***ξ*** was added for the positive controls. Experiments were performed in triplicate and the activity in normalized units (n.u.) was calculated by subtracting the mean hydrolysis rate of the negative controls and normalizing to the mean hydrolysis rate of the positive controls. Error bars and shaded area's represent the standard error of the mean of the experiments.

3.6 Orthogonal control of enzymatic actuators by switchable memories circuit

Having characterized the translator module as a generic method to control enzymatic actuators and to translate short oligomers to long output strands with minimal retroactivity, we implemented the control of the enzymatic actuators by the PEN-based bistable switch. First, we showed the control of either the self-inhibitory TEM1 β-lactamase construct (Figure S3.8) or the NanoLuc-based actuator (Figure S3.9 and S3.10) by one of the two states of the switch. Subsequently, we investigated whether it is possible to implement orthogonal control of the enzymatic actuators by the two states of the switch. To this end, we constructed a system in which the NanoLuc-based actuator was controlled by coupling of ***α*** to translator template ***atoσ***, while the self-inhibitory TEM1 β-lactamase construct was controlled by

coupling of $\boldsymbol{\beta}$ via translator template $\boldsymbol{\beta to \xi}$ (Figure 3.6A). Because of technical reasons the control of the actuators could not be directly followed in the samples (*Paragraph* 3.8). Therefore, the activity of TEM1 β-lactamase and the conformation of the NanoLuc-based actuator were determined at four different states of the switch by taking aliquots and measuring the hydrolysis rate or BRET ratio immediately after addition of the NanoLuc and β-lactamase substrates. We measured the production rate of $\boldsymbol{\sigma}$ and $\boldsymbol{\xi}$ using parallel experiments in which the enzymatic actuators were replaced with two orthogonal molecular beacons. Control experiments were performed showing no interference of the molecular beacons and actuators with the bistable switch (Figure S3.14 and S3.15). Furthermore, experiments were performed in the absence of the orthogonal translator modules to quantify the retroactivity to the dynamics of the bistable switch that arises due to the additional load. Indeed, the results displayed in Figure 3.6B (and Figure S3.11) reveal that the retroactivity that arises from coupling of the orthogonal set of translator modules to the dynamics of the upstream bistable circuit is low. Importantly, the results in Figure 3.6B show that production of $\boldsymbol{\sigma}$ is initiated after activation of the α-state of the switch while the production rate of $\boldsymbol{\xi}$ is zero indicating that the switch has adopted the α-state. In agreement, we observe a decrease in BRET ratio 50 minutes after initiation of the switch as shown in the bar graphs in Figure 3.6C. In contrast the TEM1 β-lactamase based actuator is not activated in the α-state as shown by the overlapping fluorescent traces of the hydrolysis of CCF2-FA of the samples and negative controls (Figure 3.6C). For a clear visualization the BRET ratio and hydrolysis rate of the samples were normalized to positive and negative controls (*Paragraph* 3.8). Figure 3.6D shows an increased opening of the stem-loop structure of the NanoLuc-based actuator towards ~1/4 of its fully opened conformation 50 minutes after initiation of the switch. Next, we injected input $\boldsymbol{\delta}$ to switch the network to the β-state, as observed from the biphasic evolution of the charge levels of $\boldsymbol{\alpha to i \beta}$ and $\boldsymbol{\beta to i \alpha}$. This results in the downstream activation of $\boldsymbol{\beta to \xi}$ and the production of $\boldsymbol{\xi}$, while the production of $\boldsymbol{\sigma}$ ceases. The hydrolysis rate of the TEM1 β-lactamase construct and BRET ratio of the NanoLuc-based actuator including (-) and (+) controls were measured again 250 minutes after injection of $\boldsymbol{\delta}$**.** The results show that the TEM1 β-lactamase enzyme is completely activated while the stem-loop structure of the NanoLuc-based actuator has only slightly opened. Switching the network back to the α-state by injection of input $\boldsymbol{\gamma}$ results in continued production of $\boldsymbol{\sigma}$ while production of $\boldsymbol{\xi}$ ceases. Likewise, an increase in opened conformation of the NanoLuc-based actuator is observed 200 minutes after injection of $\boldsymbol{\gamma}$, while the TEM1 β-lactamase enzyme stays at its completely

activated state. These results demonstrate that we are able to successfully time and control the activity of enzymatic actuators by the dynamics of the bistable switch by judicious design of orthogonal translator modules with low retroactivity.

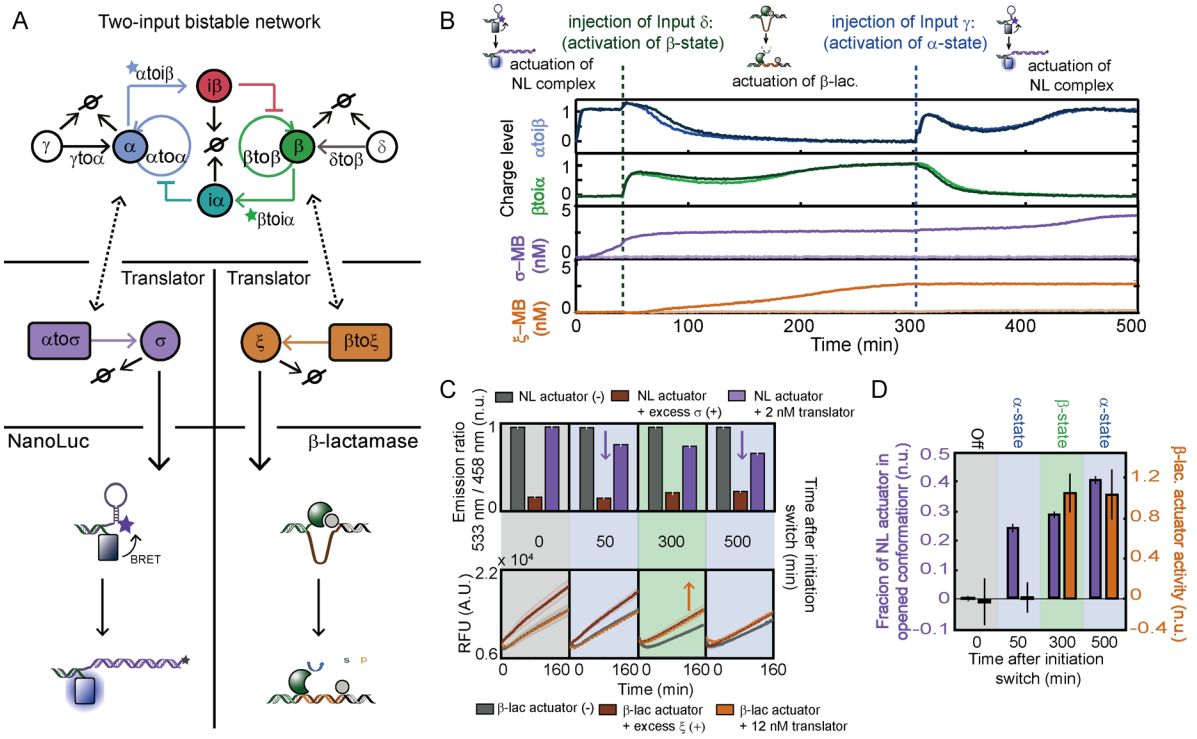

Figure 3.6: Control of two orthogonal enzymatic actuators by a switchable memories circuit. A) Schematics of the experiment in which the switch controls a NanoLuc-based actuator and a self-inhibitory TEM1 β-lactamase construct. B-D**,** Results of the experiments, carried out as described in *Paragraph* 3.8, using 20 nM ***βtoiα***, 15 nM ***αtoiβ***, 24 nM ***βtoβ***, 10 nM ***αtoα***, ***γtoα*** and ***δtoβ***, 15 U/mL Bst 2.0 warmstart DNA polymerase, 10 U/mL Nt. bstNBI and 200 nM ttRecJ. Reactions were performed in presence of the actuators or molecular beacons. The switch was initiated with 1 nM ***α***. B) The graphs show the dynamics of the switch and the production of ***σ*** and ***ξ*** measured using molecular beacons (5 nM $\boldsymbol{MB_{\sigma}}$ and 2.5 nM $\boldsymbol{MB_{\xi}}$) (Figure S3.16) in absence (light color) and in presence (dark color) of the translator modules (2 nM ***αtoσ*** and 12 nM ***βtoξ)***. The charge level is the normalized fluorescence of the signal of DY530 and FAM fluorophores which is 0 in the absence of template's input primer and 1 at the steady-state value of ***β*** and ***α*** respectively. The dotted lines show the time points at which 30 nM of the Inputs ***δ*** and ***γ*** were added. In parallel, experiments were run where the molecular beacons were replaced with the enzymatic actuators (5 nM of the NanoLuc-based actuator and 2.5 nM TEM1 β-lactamase actuator). C) and D) The state of the actuators was measured at four time points including negative (-) and positive (+) controls (Figure S3.12 and S3.13 and *Paragraph* 3.8). Error bars and shaded area's represent the standard error of the mean of the experiments. Experiments were performed in plurality (>3) and at three different days. C) The bar graphs displaying the BRET ratio were normalized to the mean of the negative controls for a clear visualization. D) The activity or fraction in opened conformation of the actuators were calculated by normalizing to positive and negative controls (*Paragraph* 3.8).

3.7 Discussion

Our work shows the possibility of connecting enzymatically-enriched DNA circuits that are capable of displaying higher-order regulatory behaviour to a variety of biochemical actuators *in vitro*, such as a TEM1 β-lactamase and a luciferase based system. Previously, non-enzymatic, nucleotide-based logic circuits have been used to engineer autonomous cell-free systems capable of programmable manipulation of protein activity *in vitro*.[15,39,40] While non-enzymatic circuits are capable of basic information processing functions such as logic operations, amplification and input thresholding, enzymatically-driven systems can display a much broader range of system-level behaviours such as bistability, oscillations and perfect adaptation.[41,42] Each of these dynamic regulatory behaviours comes with a unique set of information processing functions. For example, bistable circuits in the living cell can generate sharp input thresholds and can either reversibly or irreversibly switch to an activated state.[43] In addition, bistable gene regulatory networks can also act as dynamic noise filters by ignoring transient changes in the input signal.[44] Perfect adaptation, another type of non-equilibrium dynamic behaviour, is an important feature of cellular regulation and is typically used to generate homeostatic behaviour.[45] Finally, oscillatory circuits in living cells are not only used for time-keeping functions but can also transmit information via coding and decoding of temporal signaling patterns.[46] These examples indicate that protein activity controlled via enzymatically-enriched nucleic acid-based computing systems can yield autonomous cell-free systems with more advanced information processing functions than is currently possible.

While modularity has often been cited as a key advantage of nucleic-acid based chemical systems, our work reveals that in order to reliably connect an upstream DNA-based network to a downstream enzymatic load, retroactivity has to be taken into account. Our theoretical analysis shows that biochemical loads can bias the dynamical properties of bistable switches based on reciprocal inhibition in a manner that depends critically on the strength of the two states in the absence of load. In the living cell, bistability is found in many important gene regulatory networks and signal transduction pathways that regulate cell proliferation,[47] cell-fate determination[48] and Ras activation.[49] However, in many cases the mathematical models that describe these regulatory circuits do not incorporate the effects of downstream components while these are certainly present. In an insightful study, Prasad and co-workers[50] theoretically analysed the effect of downstream loads on bistable genetic and signaling switches and found that the addition of load changes the underlying potential energy

landscape skewing it in favour of the unloaded side. In addition, the authors found that in some cases the additional downstream load can abrogate bistable dynamics. Our experimental results on the effect of downstream loads on the DNA-based bistable switch indeed confirm these predictions as we observe failure of switching dynamics when the load is coupled to the weaker α-state of the network. Furthermore, because the PEN-based bistable switch is inherently asymmetric due to a difference in binding affinity of the $\boldsymbol{\alpha}$ and $\boldsymbol{\beta}$ primers to their corresponding complementary sequences, the effect of a downstream load to each of the two states is also different. In the absence of load, the β-state is stronger than the α-state meaning the concentration of input $\boldsymbol{\delta}$ needed to switch the network to the β-state is lower compared to the concentration of input $\boldsymbol{\gamma}$ that is needed to switch the system to the α-state. The theoretical analysis shows that coupling of a downstream load to the weaker α-state results in further weakening of the α-state and a concomitant narrowing of the concentration range of $\boldsymbol{\delta}$ and $\boldsymbol{\gamma}$ for which bistability can be observed. However, when the load is applied to the stronger β-state of the switch, the potential energy landscape becomes more symmetric resulting in a larger input parameter range for which bistable behaviour can be observed. While in general low retroactivity is desired, our work shows that retroactivity not necessarily has a negative effect.

In summary, we have shown how a cell-free bistable switch can be used to time and control protein-based activity by engineering a new module enabling connection of the upstream circuit and downstream actuators, taking into account proper design constraints. By allowing the orthogonal integration of distinct molecular platforms our work represents a key step for the development of cell-free biochemical systems of increasing chemical complexity, providing the potential for new insights in cellular networks and ultimately the construction of synthetic cells.

3.8 Experimental section

Materials. Oligonucleotides (Table 3.1) were obtained from Integrated DNA Technologies (IDTDNA) or Biomers and were purified using High Performance Liquid Chromatography (HPLC). Templates which are not 5' end labeled with a fluorophore or a quencher have three phosphorothioate backbone modifications at the 5' end preventing them from degradation. Furthermore, since 3'-OH can be extended by DNA polymerase, the templates were ordered with a phosphate modification at their 3' end to prevent circuit leakage. Templates at which primers are produced inevitably have an additional nickase recognition site at the template's

output site. Based on previous work,[25] to decrease the affinity of the nicking enzyme for the output site the thymine base in the nickase recognition site at the template's output was replaced with a uracil base. Concentrations of DNA were verified using UV-spectrophotometry. The nicking enzyme and polymerase were obtained from NEB, while ttRecJ, a thermophilic equivalent of the RecJ enzyme from Thermus Thermophilus was obtained from Dr. A. Estévez-Torres.

PEN-based experiments. Throughout the study, reactions of total volume 20 μL were assembled in a master mix, containing 20 mM Tris-HCl, 10 mM KCl, 50 mM NaCl, 10 mM $(NH_4)_2SO_4$, 8 mM $MgSO_4$, 0.1% Triton x-100, 400 μM of each deoxyribonucleotide triphosphates (dNTP; New England Biolabs (NEB)), 0.1% Synperonic F108 (Sigma Aldrich), 2 μM Netropsin (Sigma Aldrich), 1 mg/mL Bovine Serum Albumine (BSA; NEB), 4 mM Dithiothreitol (DTT) and a pH of 8.8. A 4x stock solution of the master mix was prepared, excluding BSA and DTT, which were added during reaction assembly together with enzymes, oligonucleotides and enzymatic actuators (which were pre-assembled as described *vide infra*). The activity of each batch of ttRecJ was determined using the experiments as described in *Chapter* 2 and batch to batch variations were compensated by changing the enzyme concentration. For experiments in which injections were done during the experiment an oil layer (15 μL) was used to prevent a shift of the signal after injection. Experiments were performed at a temperature of 42°C and fluorescence was recorded over time (CFX96 PCR machine).

Experimental data of FAM and DY530 were handled by subtracting the raw data by a baseline curve. This baseline curve was measured for both the FAM and DY530 channels in presence of the inhibition templates and in absence of amplification of $\boldsymbol{\alpha}$ and $\boldsymbol{\beta}$ respectively. Subsequently, the signal of DY530 and FAM fluorophores were normalized to the charge levels of $\boldsymbol{\beta to i\alpha}$ and $\boldsymbol{\alpha to i\beta}$ which is 0 in the absence of template's input primer and 1 at the steady-state value of primer $\boldsymbol{\beta}$ and $\boldsymbol{\alpha}$ respectively. The fluorescence of Cy5 and ROX fluorophore attached to the molecular beacons were converted to concentration of DNA strand σ and DNA strand ξ respectively using a standard curve.

Assembling of the NanoLuc-based actuator. The NanoLuc-based actuator was constructed by our experimental partners W. Engelen and prof. M. Merkx. Protein-expression, conjugation and purification of NanoLuc was carried out as reported.[31] In short, a cysteine was genetically

inserted in the C-terminus of NanoLuc via site-directed mutagenesis and the plasmid was transformed into *E. coli* BL21(DE3). Subsequently, the cells were cultured in LB-medium and protein expression was induced at OD_{600} = 0.6 by the addition of 100 μM IPTG. After overnight expression at 18 °C the cells were lysed by centrifuging the cells at 10,000xg for 10 minutes and subsequently dissolving the pelleted cells in BugBuster protein extraction reagent (Novagen) and Benzonase endonuclease (Novagen). The lysed cells were subsequently centrifuged (40,000xg for 40 minutes) to obtain the soluble fraction, from which NanoLuc was purified using Ni^{2+}-affinity chromatography.

Amine-modified oligonucleotide (***ODN$_{NL}$***) was dissolved in PBS (100 mM NaPi, 150 mM NaCl, pH 7.2) to a final concentration of 1 mM and mixed with 20 equivalents of Sulfo-SMCC (freshly dissolved in DMSO to 20 mM) and incubated for 2 hours at room temperature while shaking at 850 rpm. Subsequently, the excess Sulfo-SMCC was removed by extracting the maleimide-activated oligonucleotide by 3 rounds of ethanol precipitations and the oligonucleotide was dried under vacuum. Prior to oligonucleotide conjugation, NanoLuc was buffer exchanged to 100 mM sodium phosphate, pH 7.0 by gel-filtration (PD-10 desalting column) and directly added to a 3-fold molar excess of maleimide-activated oligonucleotide and allowed to react for 2 hours at room temperature while shaking at 850 rpm. Subsequently, the oligonucleotide-NanoLuc conjugate (***NL-ODN$_{NL}$***) was purified by consecutive Ni^{2+}-affinity chromatography to remove excess oligonucleotide and anion-exchange chromatography to remove unconjugated protein. The NanoLuc actuator was hybridized prior to use by mixing together 100 nM ***NL-ODN$_{NL}$*** and 120 nM ***NLlink-σ*** and left at room temperature for at least one hour.

Assembling of the β-lactamase actuator. The β-lactamase actuator was constructed by our experimental partners W. Engelen and prof. M. Merkx. Protein-expression, conjugation and purification of β-LactamaseE104D and BLIP were carried out by W. Engelen and prof. M. Merkx as previously reported.[9] Furthermore, the complex was hybridized prior to use by mixing together 100 nM βlac-ODN, 200 nM BLIP-ODN and 120 nM βlacLink-ε and left at room temperature for at least one hour.

Measuring the conformational state of the NanoLuc-based actuator. Because of technical reasons the hydrolysis rate of the TEM1 β-lactamase actuator and BRET ratio of the NanoLuc-based actuator could not be measured over time in the samples directly. NanoGlo

(substrate for NanoLuc) is not compatible with the PEN toolbox and somehow has an effect on the dynamics of the PEN based network. Moreover, BRET detection could not be performed by the CFX96 PCR machine in which the switching behavior was followed. Even so, the excitation and emission filters of the CFX96 PCR were not compatible with the excitation and emission wavelength of converted CCF2-FA substrate of TEM1 β-lactamase. Hence, the conformation of the NanoLuc-based actuator, controlled by the translator module in absence (Figure 3.5) or presence (Figure 3.6) of the switch, was determined by taking 16 uL of the sample (out of 20 µl) and transferred to a 396 wells plate prefilled with 20 µL of master mix and 25 µL oil to prevent condensation. Negative and positive controls were carried out in parallel. Negative controls were run to quantify the decrease in BRET efficiency of the NanoLuc-based actuator at different time intervals and, therefore, the translator module(s) were omitted in the reactions of the negative controls (all other components were exactly the same as in the samples). Positive controls were run to quantify the BRET signal for maximal opening of the NanoLuc-based actuator at different time intervals. For positive controls the translator module(s) were also omitted in the reactions and excess of DNA strand σ (200 nM) was added to the wells plate (all other components were exactly the same as in the samples). Then, the plate was put in the centrifuge at 1000 rpm for 30 seconds. After 10 minutes incubation at 42 °C in the plate reader (Tecan, Spark 10M) 4 µL of 50x diluted Nano-Glo (Promega) was added after which the mixtures were mixed and an emission spectrum (from 400 nm to 650 nm) was measured. The BRET ratio between 533 nm and 458 nm was calculated and the fraction of opened stem-loop structure of the NanoLuc-based actuator was calculated by subtracting the mean BRET ratio of the positive controls and normalizing to the mean BRET ratio of the negative controls.

Measuring the activity of the β-lactamase actuator. Because of technical reasons the hydrolysis rate of the TEM1 β-lactamase actuator and BRET ratio of the NanoLuc-based actuator could not be measured over time in the samples directly. NanoGlo (substrate for NanoLuc) is not compatible with the PEN toolbox and somehow has an effect on the dynamics of the PEN based network. Moreover, BRET detection could not be performed by the CFX96 PCR machine in which the switching behavior was followed. Even so, the excitation and emission filters of the CFX96 PCR were not compatible with the excitation and emission wavelength of converted CCF2-FA substrate of TEM1 β-lactamase. Hence, the activity of TEM1 β-lactamase, activated by the translator module in absence (Figure 3.5) or

presence (Figure 3.6) of the switch, was determined by taking 16 uL of the sample (out of 20 µl) and transferred to a 396 wells plate prefilled with 20 µL of master mix and 25 µL oil to prevent condensation. Negative and positive controls were carried out in parallel. Negative controls were run to account for the change in activity of TEM1 β-lactamase/BLIP/ξ complex in the PEN-toolbox buffer. For negative controls the translator module(s) were omitted in the reactions (all other components were exactly the same as in the samples). Positive controls were run to quantify the hydrolysis rate of maximal activated TEM1 β-lactamase/BLIP/ξ complex (Figure S3.6 and S3.7). For positive controls the translator module(s) were also omitted in the reactions and excess of DNA strand ξ (100 nM) was added to the wells plate (all other components were exactly the same as in the samples). Then, the plate was put in the centrifuge at 1000 rpm for 30 seconds. After 10 minutes incubation at 42 °C in the plate reader (Tecan, Safire) 4 µL of 20 µM CCF2-FA (Invitrogen) was added after which the mixtures were mixed and fluorescence (ex: 410 nm; em: 447 nm) was measured for at least 150 minutes. The hydrolysis rate of β-lactamase was determined by fitting the slope between 50 and 150 minutes. The activity was normalized by subtracting the mean hydrolysis rate of the negative controls and normalizing to the mean hydrolysis rate of the positive controls.

Determination of the forward rate constant of DNA hybridization. To characterize the forward rate constant of DNA hybridization (k_a) experiments were performed using the stopped-flow device (BioLogic, MOS-500 spectrophotometer equipped with a SFM-2000 mixing system) with a dead time of 0.25 ms in absorbance mode (Figure S3.18 and Table 3.2). Multiple experiments (>6) were performed in which absorbance was recorded over time at 42 °C after mixing 1 µM of primer ***β*** to 1 µM of template ***δtoβ*** both in 1 x TE buffer complemented with 0.06 M Na^+, 0.008 M Mg^{2+} and preheated at 42 °C. This yielded final concentrations of 500 nM primer β and 500 nM of template δtoβ. The raw data was subtracted by the absorbance at time = 0. Subsequently, the absorbance was converted to concentration of duplex (dsDNA) by assuming the reaction was equilibrated in 5 seconds and the experimentally determined thermodynamic dissociation constant. Finally, the mean of the multiple experiments was determined for further analysis. To obtain the second-order rate constant (k_a) non-linear least squares multiple-curve fitting was performed using the Matlab routine lsqnonlin with a subspace trust-region method based on the interior-reflective Newton method. The hybridization dissociation equilibrium constant was determined experimentally and was fixed during the non-linear least-square analysis. The value of the k_a is shown in Table 3.2.

Determination of the kinetics of the molecular beacon. To characterize the kinetics of the molecular beacon, experiments in triplicate were performed in which the molecular beacon in master mix without enzymes was added to a cuvette which was preheated at 42 °C in a fluorescence spectrophotometer (Carry Eclipse equipped with a Varian Peltier Multicell Holder and a Cary Temperature Controller). Subsequently, the fluorescence of the molecular beacon was measured to obtain the baseline fluorescence. Then, DNA strand $\boldsymbol{\sigma}$ was added giving a volume of 120 µL after which the mixture was suspended and measurement started at 42 °C. Data handling was done for each single curve in the same way. First, the baseline fluorescence was determined by taking the mean of a one minute measurement of the fluorescence from the molecular beacon. After this, the fluorescence from the measurement was subtracted by this baseline value. Subsequently, the missing points due to suspending (10-15 seconds) were estimated by extrapolation. Then, the fluorescence was converted to concentration of opened beacon by assuming the reaction was equilibrated in 18 minutes. An ODE model based on the bimolecular reaction model of DNA strand displacement was developed to describe the kinetics of this step.[5] To obtain the second-order rate constant (k_{rep}) of the toehold mediated strand displacement reaction non-linear least-square optimization of the experimental kinetic traces (Figure S3.19) to the mathematical model was performed. The Matlab routine lsqnonlin with a subspace trust-region method based on the interior-reflective Newton method was applied, yielding a k_{rep} of 5.3×10^7 M^{-1} min^{-1}.

Determination of the thermodynamic dissociation constant of DNA hybridization. This is described in detail in *Chapter* 2 and the values of the parameters are shown in Table 3.2.

Determination of the kinetics of exonuclease. This is described in detail in *Chapter* 2 and the values of the parameters are shown in Table 3.2.

Table 3.1: DNA sequences

		Sequence (5' -> 3')	Length (# bases)	3' mod	5' mod
INVERTER/Bistable switch					
Templates	***ατoα***	C*C*A*AGAC***U***CAG-CCAAGACTCAG	22	phosphate	
	βtoβ	A*A*C*AGAC***U***CGA-AACAGACTCGA	22	phosphate	
	ατoiβ	T*T*A*CTCGAAACAGAC-CCAAGACTCAG	26	FAM	
	βtoiα	T*T*A*CTCAGCCAAGAC-AACAGACTCGA	26	DY530	
	γtoα	C*C*A*AGAC***U***CAG-GCATGACTCAT	22	phosphate	
	δtoβ	A*A*C*AGAC***U***CGA-CACTGACTCCT	22	phosphate	
Inputs	***α***	CTGAGTCTTGG	11		
	β	TCGAGTCTGTT	11		
	γ	ATGAGTCATGC	11		
	δ	AGGAGTCAGTG	11		
Inhibitors	***iα***	GTCTTGGCTGAGTAA	15		
	iβ	GTCTGTTTCGAGTAA	15		
Translator in isolation from upstream and downstream network (Figure 3.2)					
Template	***ατoX$_{36}$***	G*T*A*GTAGTTCATTAGTGTCGTTCGTTCACAGTAATA-CCAAGACTCAG	46	phosphate	
Output	***X$_{36}$***	TATTACTGTGAACGAACGACACTAATGAACTACTAC	36		
Template	***ατoX$_{46}$***	C*G*T*TCGTATGGTAGTAGTTCATTAGTGTCGTTCGTTCACAGTAATA-CCAAGACTCAG	46	phosphate	
Output	***X$_{46}$***	TATTACTGTGAACGAACGACACTAATGAACTACTACCATACGAACG	36		

Table 3.1 (continued): DNA sequences

		Sequence (5' -> 3')	Length (# bases)	3' mod	5' mod
Translator in isolation from upstream and downstream network (Figure 3.2)					
Template	$\alpha to X_{56}$	G*C*G*TATTCAGCGTTCGTATGG TAGTAGTTCATTAGTGTCGTTCG TTCACAGTAATA-CCAAGACTCAG	46	phosphate	
Output	X_{56}	TATTACTGTGAACGAACGACACT AATGAACTACTACCATACGAACG CTGAATACGC	36		
Reporter	MB_X	*TATTACTGTGA*-GTAGTTCATTAGTGTCGTTCGT-*TCACAGTAATA*	44	Iowa Black RQ-Sp	Cy5
Translator INVERTER (Figure 3.3)					
Template	$\alpha to \sigma$	T*A*T*TACTGTGAGTAGTTCATT AGTGTC GTTCGTTC-CCAAGACTCAG	46	phosphate	
Output	σ	GAACGAACGACACTAATGAACT ACTCACAGTAATA	35		
Reporters	MB_σ	*TATTACTGTGAG*-TAGTTCATTAGTGTCGTTCGT-*CTCACAGTAATA*	45	Iowa Black RQ-Sp	Cy5
Orthogonal system (Figure 3.4-3.6)					
Templates	$\alpha to \sigma$	T*A*T*TACTGTGAGTAGTTCATT AGTGTC GTTCGTTC-CCAAGACTCAG	46	phosphate	
	$\beta to \sigma$ *(Fig. 4)*	T*A*T*TACTGTGAGTAGTTCATT AGTGTCGTTCGTTC-AACAGACTCGA	46	phosphate	
	$\beta to \varepsilon$ *(Fig. 5, 6)*	C*A*A*CACAACCCACAACACAC CACCACCGCAACCACCCACCACC AACACCA-AACAGACTCGA	61	phosphate	
Outputs	σ	GAACGAACGACACTAATGAACT ACTCACAGTAATA	35		
	ξ	TGGTGTTGGTGGTGGGTGGTTGC GGTGGTGGTGTGTTGTGGGTTGT GTTG	50		

Table 3.1 (continued): DNA sequences

		Sequence (5' -> 3')	Length (# bases)	3' mod	5' mod
Orthogonal system (Figure 3.4-3.6)					
Molecular beacons	***MB*$_{\sigma}$**	*TATTACTGTGAG-*TAGTTCATTAGTGTCGTTCGT-*CTCACAGTAATA*	45	Iowa Black RQ-Sp	Cy5
	***MB*$_{\xi}$**	*CAACACAACCCA-*CAACACACCACCACCGCAACC-*TGGGTTGTGTTG*	45	Iowa BlackRQ-Sp	ROX
β*lac*-actuator	***βlac-ODN***	TGTCACCGATGAAACTGTCTA	21	C_6-Amine	
	BLIP-ODN	GTGATGTAGGTGGTAGAGGAA	21		Amine-C_6
	βlacLink-ξ	TTCCTCTACCACCTACATCAC-CAACACAACCCACAACACACCACCACCGCAACCACCCACCACCAACACCA-TAGACAGTTTCATCGGTGACA	92		
NanoLuc-actuator	***NL-ODN*$_{NL}$**	GTGATGTAGGTGGTAGAGGAA	21		Amine
	NLlink-σ	T*T*C*CTCTACCACCTACATCAC-*TATTACTGTGAG-*TAGTTCATTAGTGTCGTTCGT-*CTCACAGTAATA*	66	FAM	

[1] * Indicate phosphorothioate modifications

[2] Complementary sequences are represented by the colors, except for ***iα*** and ***iβ*** with the autocatalytic templates

[3] Underlined sequences represent the nickase recognition site

[4] Replacement of thymine by an uracil is indicated in italic bold

[5] The complementary sequences of the stem of the molecular beacons is denoted in italic

[6] Different domains in the sequences are separated by '-'

Table 3.2: Model parameters

Parameters determined in separate experiments			
Thermodynamic dissociation constants of DNA hybridization			
$K_\alpha/K_{L\alpha}$	6 nM	$K_{i\beta}$	0.86 nM
$K_\beta/K_{L\beta}$	24 nM	K_γ	26 nM
$K_{i\alpha}$	0.25 nM	K_δ	18 nM
DNA association rate constant (k_a)			
0.13 nM^{-1} min^{-1}			
Exonuclease (10 nM)			
V_{exo}	27 nM min^{-1}	K_{exo}	45 nM
Rate constant of toehold-mediated strand displacement of the reporter (k_{rep})			
5.3 x 10^7 M^{-1} min^{-1}			
Empirical model parameters			
V_γ	8.5 nM min^{-1}	$V_{i\beta}$	0.8 nM min^{-1}
V_δ	7.2 nM min^{-1}	λ_α	25
V_α	6.5 nM min^{-1}	λ_β	28
V_β	15 nM min^{-1}	V_{exo}^*	23.4 nM min^{-1}
$V_{i\alpha}$	1.6 nM min^{-1}		

* The parameter V_{exo} was estimated to be lower as experimentally determined in isolation, since sequestration of exonuclease by the templates is present. We manually adapted this value.

Supplementary Information I: Supplementary figures

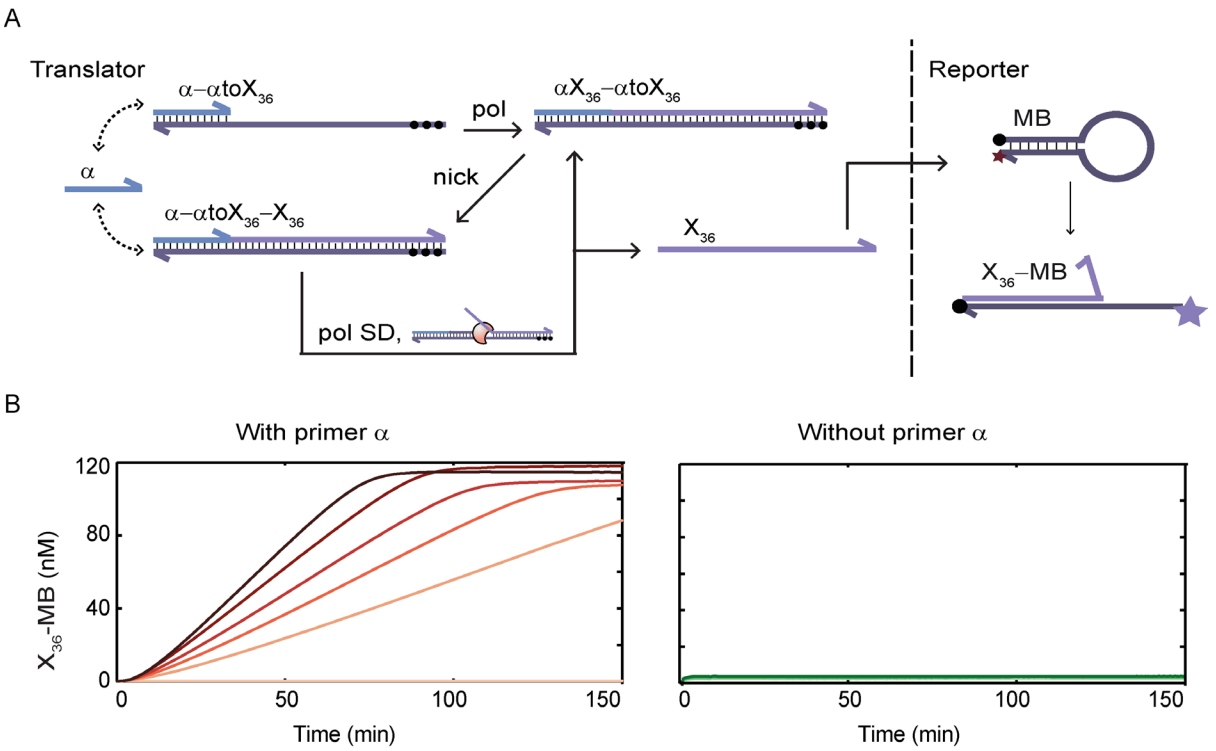

Figure S3.1: Production of DNA strand X_{36} requires the presence of translator module and primer α. A) Schematic illustration of the reactions, which were carried out as described in *Paragraph* 3.8 (PEN-based experiments). The black dots at the 5'-end of the DNA strands represent phosphorothioate modifications which protect the DNA strand from degradation. B) An experiment was performed in the presence and absence of 50 nM of primer ***α*** and using 0, 5, 7.5, 10, 15 and 20 nM (from light to dark color) of translator template ***αtoX*$_{36}$** in the presence of molecular beacon ***MB*$_x$**, 10 U/mL Nt. bstNBI and 15 U/mL Bst. 2.0 warmstart DNA polymerase. Fluorescence was converted to concentration using a standard curve (Figure S3.16). The results in Figure S3.1 show an increase in fluorescence when both primer ***α*** and translator are present evidencing that the increase in fluorescence is only caused by the production of DNA strand ***X*$_{36}$** and, importantly, not by any unwanted background reaction.

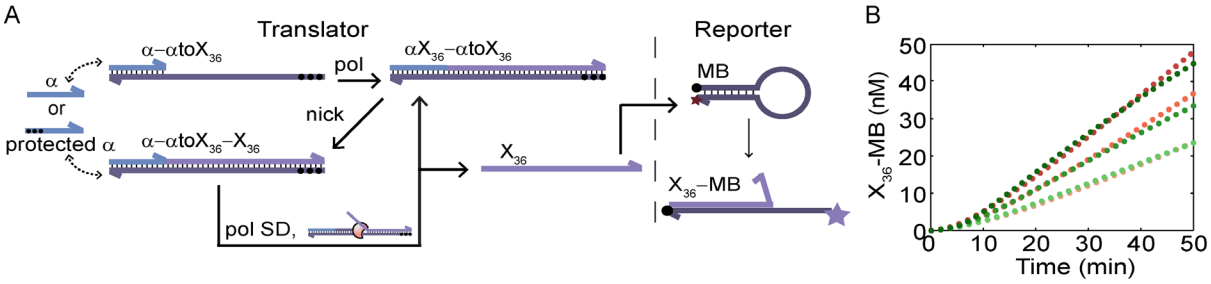

Figure S3.2: Comparing the production rate of DNA strand X_{36} using primer α or protected primer α. A) Schematic illustration of the experiment in which the translator module produces DNA strand $\boldsymbol{X_{36}}$ using primer $\boldsymbol{\alpha}$ or protected primer $\boldsymbol{\alpha}$ and measured with a molecular beacon. Experiments were performed as described in *Paragraph* 3.8 (PEN-based experiments). The black dots represent phosphorothioate modifications. The experiment was performed using 5, 7.5 and 10 nM (from light to dark color) of translator template $\boldsymbol{\alpha toX_{36}}$ in the presence of 10 U/mL Nt.BstNBI, 15 U/mL Bst 2.0 warmstart and molecular beacon $\boldsymbol{MB_x}$ and initiated with 50 nM of unprotected primer $\boldsymbol{\alpha}$ or 50 nM of protected primer $\boldsymbol{\alpha}$. B) Results of the experiments which show a similar production rate of $\boldsymbol{X_{36}}$ using either unprotected (red dotted lines) or protected (green dotted lines) primer $\boldsymbol{\alpha}$.

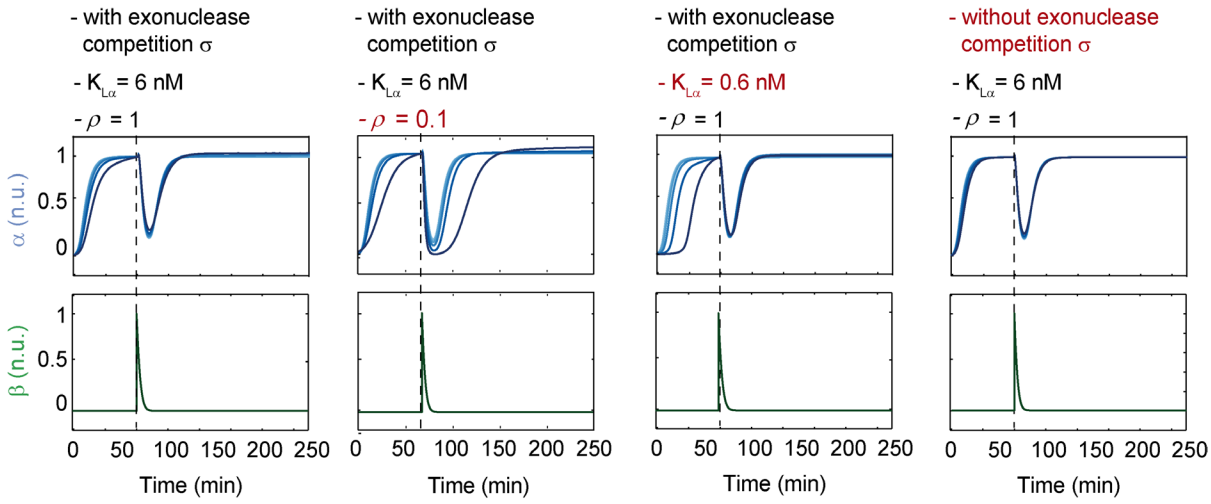

Figure S3.3: Analysis of parameters potentially contributing to retroactivity. Simulations were performed using the heuristic model (Supplementary Information II) with the same concentrations of translator template as used for the experiments in Figure 3.3b. Besides the translator concentration the parameters ρ, $K_{L\alpha}$ and the competition term of $\boldsymbol{\sigma}$ in the Michaelis-Menten derivation of exonuclease can contribute to retroactivity in theory. The results of the simulations show the dynamics of the INVERTER circuit for a concentration range of translator module with one of these parameters modified as indicated in red. The traces were converted to normalized units (n.u.) by normalizing $\boldsymbol{\alpha}$ to the steady-state concentration and normalizing $\boldsymbol{\beta}$ to its maximum value. These results show that parameters ρ and $K_{L\alpha}$ have a significant contribution to retroactivity while the competition term of $\boldsymbol{\sigma}$ of the Michaelis-Menten derivation of exonuclease has a relatively small contribution to retroactivity.

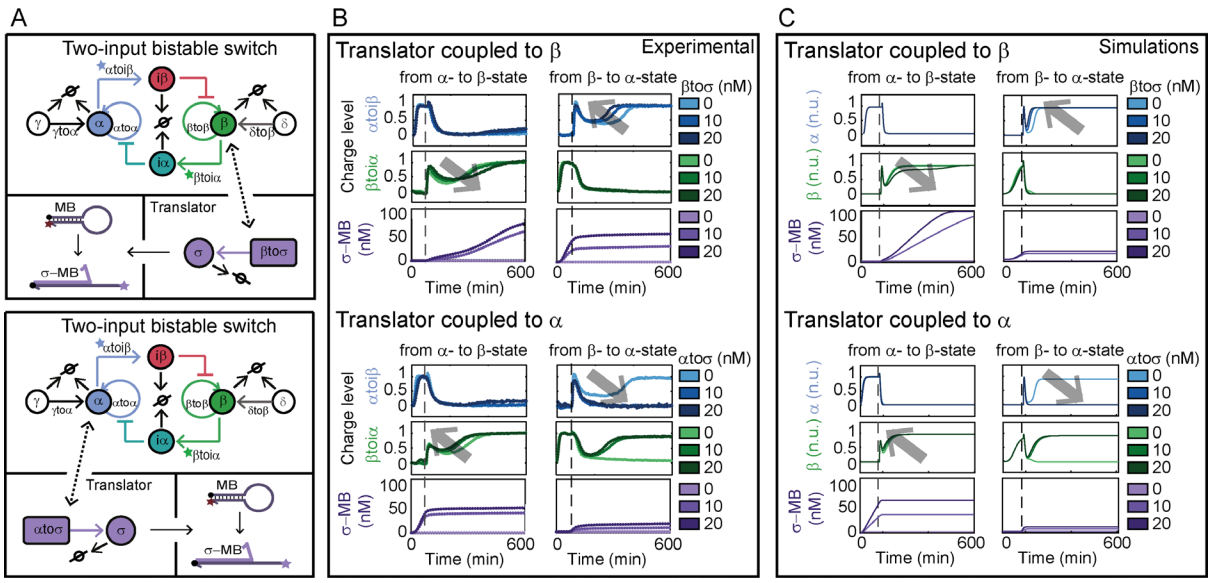

Figure S3.4: Coupling of the translator module to a two-input bistable switch. A) Schematic illustration of the system, in which the translator module is coupled to ***β*** or ***α*** of the PEN-based bistable switch. The core of the bistable switch consists of four templates including the autocatalytic templates ***αtoα*** and ***βtoβ*** and the inhibitory templates ***αtoiβ*** and ***βtoiα***. The network switches between states upon injection of ***γ*** and ***δ*** which are received by templates ***γtoα*** and ***δtoβ***. The dynamics of the bistable switch are followed via N-quenching using templates ***βtoiα*** and ***αtoiβ*** which are 3'-end labeled with a DY530 and FAM fluorophore respectively. B) Results of the experiments in which a concentration range of translator template was coupled to ***β*** or ***α***. The sequence of the translator template was adapted for coupling to ***β*** enabling the translator module to receive ***β*** as input primer while producing ***σ*** as output strand. Experiments were carried out as described in *Paragraph* 3.8 (PEN-based experiments) using 20 nM ***βtoiα***, 15 nM ***αtoiβ***, 24 nM ***βtoβ***, 10 nM ***αtoα***, ***γtoα*** and ***δtoβ***, 10 U/mL Bst 2.0 warmstart DNA polymerase, 10 U/mL Nt. bstNBI and 200 nM ttRecJ. The switch was initiated with 1 nM of ***α*** when the network was switched from the α- to the β-state, while the network was initiated with 1 nM of ***β*** when switched from the β- to the α-state. The dotted lines indicate the time point at which 30 nM ***δ*** (from α- to β-state) and ***γ*** (from β- to α-state) was injected. The charge level is the normalized fluorescence of the signal of DY530 and FAM fluorophores which is 0 in the absence of template's input primer and 1 at the steady-state value of primer ***β*** and ***α*** respectively. The results of the translator coupled to ***α*** or ***β*** show the production rate of ***σ*** follows the dynamics of the switch instantaneously. Furthermore, the effect of retroactivity from the translator coupled to ***α*** or ***β*** was analysed by plotting the data in the phase plane of ***αtoiβ*** and ***βtoiα*** (Figure 3.4). C) Results of simulations performed using the heuristic model (Supplementary Information II). The traces of ***α*** and ***β*** were converted to normalized units (n.u.) by normalizing ***α*** and ***β*** to their steady-state concentration. The results show the same trend in the dynamics of the switch with increasing translator module as for the experiments.

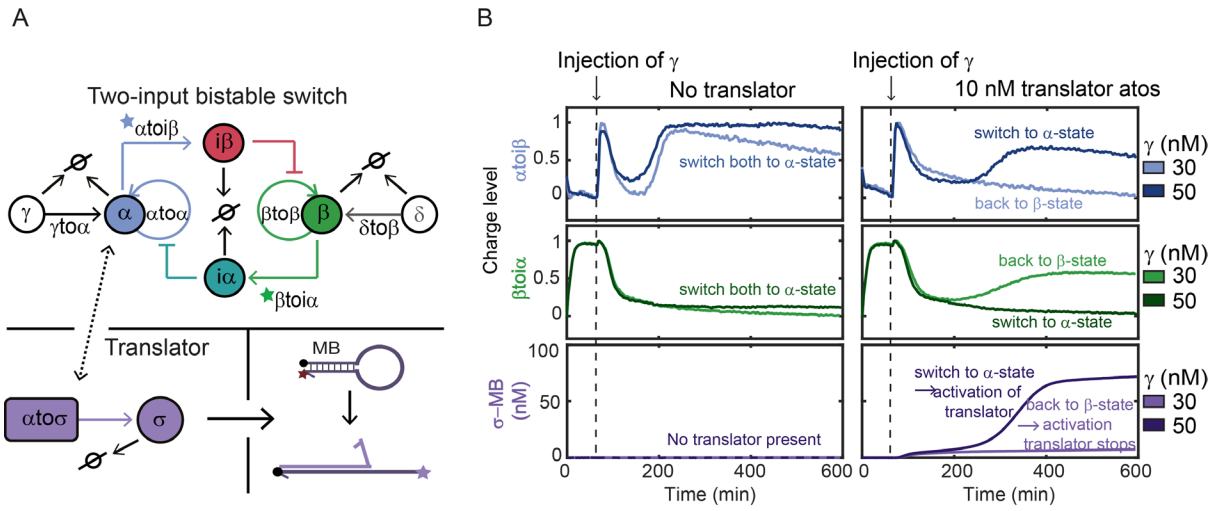

Figure S3.5: Switching from the β- to the α-state with no translator and with the translator module coupled to *α*. A) Schematic illustration of the system, in which the translator module is coupled to ***α*** of the PEN-based bistable switch. The core of the bistable switch consists of four templates including the autocatalytic templates ***αtoα*** and ***βtoβ*** and the inhibitory templates ***αtoiβ*** and ***βtoiα***. The network starts in the β-state and switches from the β- to the α-stat upon injection of ***γ*** which is received by template ***γtoα***. The dynamics of the bistable switch are followed via N-quenching using templates ***βtoiα*** and ***αtoiβ*** which are 3'-end labeled with a DY530 and FAM fluorophore respectively. B) Results of the experiments in which switching from the β- to the α-state was initiated with 30 nM or 50 nM ***γ*** in absence of translator module and with 10 nM of the translator module (***αtoσ***) coupled to ***α***. Experiments were carried out as described in *Paragraph* 3.8 (PEN-based experiments) using 20 nM ***βtoiα***, 15 nM ***αtoiβ***, 24 nM ***βtoβ***, 10 nM ***αtoα***, ***γtoα*** and ***δtoβ***, 10 U/mL Bst 2.0 warmstart DNA polymerase, 10 U/mL Nt. bstNBI and 200 nM ttRecJ. The switch was initiated with 1 nM of ***β***. The dotted lines indicate the time point at which 30 nM or 50 nM ***γ*** was injected. The charge level is the normalized fluorescence of the signal of DY530 and FAM fluorophores which is 0 in the absence of template's input primer and 1 at the steady-state value of primer ***β*** and ***α*** respectively. The results show switching from the β- to the α-state without translator module after injection of both 30 nM and 50 nM of ***γ***, while switching from the β- to the α-state with 10 nM of the translator module coupled to ***α*** only succeeded after injection of 50 nM of ***γ***. Hence, these results verify the predictions of the theoretical model as illustrated in the bifurcation diagrams in Figure 3.4.

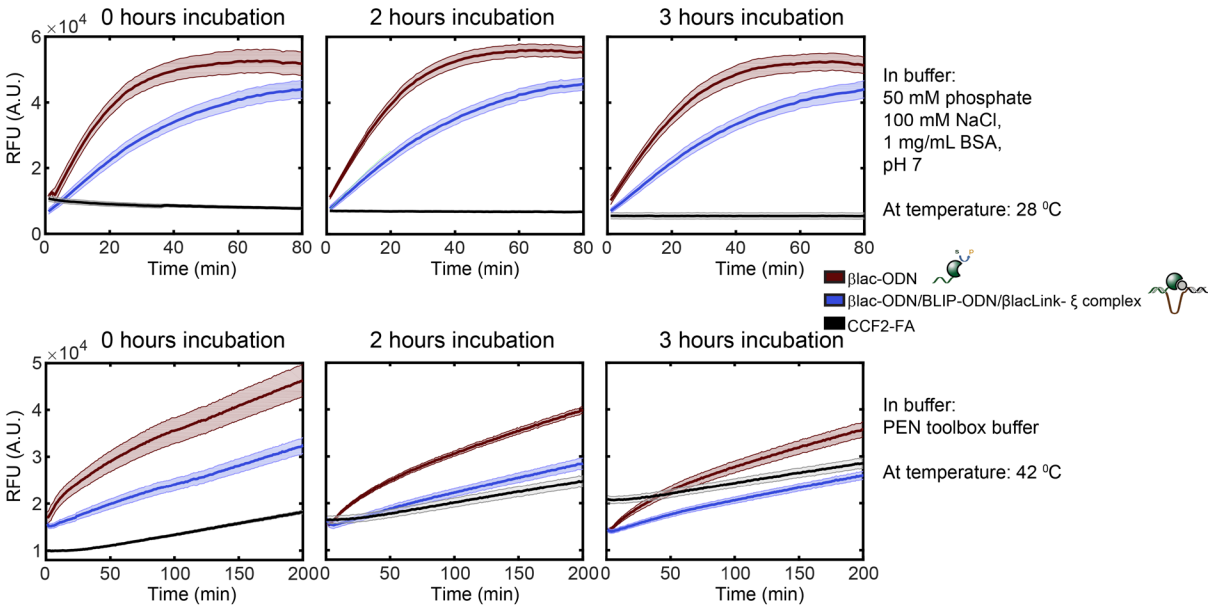

Figure S3.6: Comparing the β-lactamase actuator in the original buffer at 28 °C and in the PEN toolbox buffer at 42 °C. 1 nM of β-lactamase-ODN (dark red) or 1 nM β-lactamase-ODN in complex with BLIP-ODN and DNA linker (βlacLink-ξ) in ratio 1:2:1.2 were incubated in a 396 wells-plate with a volume of 36 µL and 25 µL oil to prevent evaporation for different time periods as shown above the graphs. The experiment was performed in either the original buffer[9] (upper graphs) or PEN toolbox buffer (lower graphs, *Paragraph* 3.8 (PEN-based experiments)). Enzymatic activity of TEM1 β-lactamase was measured by adding 4 µL fluorescent substrate CCF2-FA (final concentration of 2 µM) prior to the measurement (Tecan, Safire). Furthermore, experiments were performed where CCF2-FA substrate was incubated on its own as shown by the grey traces. Shaded area's represent the standard deviation of the mean of the experiments. The results show that the β-lactamase-ODN (dark red) and the β-lac/BLIP/template complex (blue) are relatively stable in the original buffer at 28 °C for at least 3 hours. However, β-lactamase-ODN (dark red) and the self-inhibitory β-lactamase construct (blue) show a decrease in activity in PEN toolbox buffer at 42 °C over time. Furthermore, while CCF2-FA is stable in the original buffer at 28 °C it is slowly hydrolyzed in PEN toolbox buffer at 42 °C.

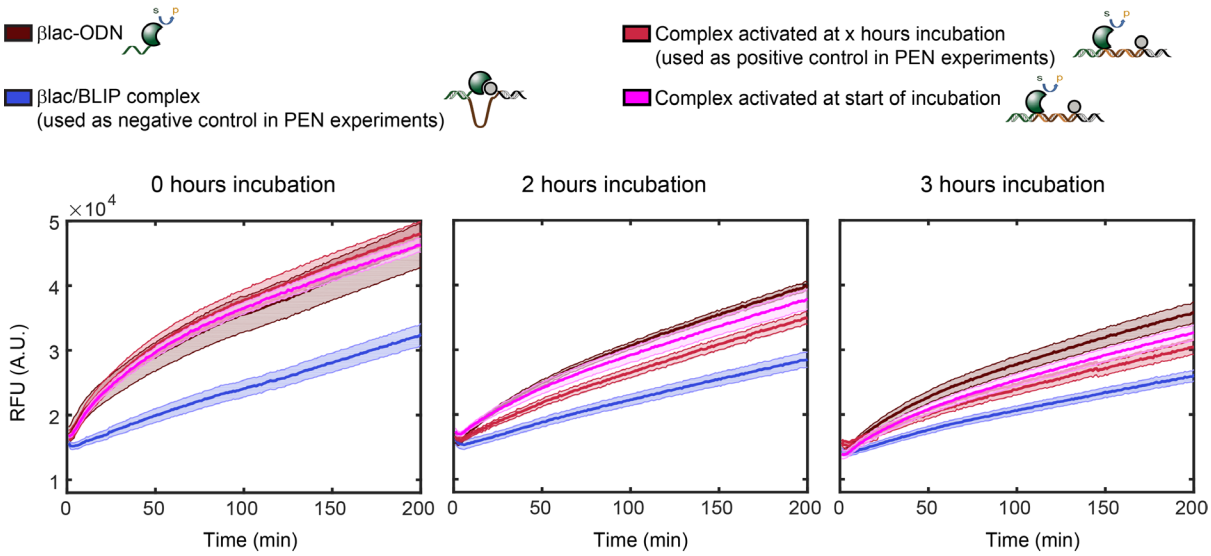

Figure S3.7: The activation of the β-lactamase actuator in the PEN toolbox buffer at 42 °C for different incubation periods. 1 nM of β-lactamase-ODN or 1 nM β-lactamase-ODN in complex with BLIP-ODN and DNA linker ***βlacLink-ξ*** (ratio 1:2:1.2) were incubated in a volume of 36 µL with 25 µL oil to prevent evaporation for different time periods as shown above the graphs. The experiment was performed in the PEN toolbox buffer (*Paragraph* 3.8). Samples included the β-lactamase-ODN (dark red), the inactivated complex (blue), the complex activated (with 50 nM ***ξ***) at the start of the incubation (pink) and the complex activated (with 50 nM ***ξ***) at 'X' hours (red) as indicated above the graphs. Enzymatic activity of TEM1 β-lactamase was measured by adding 4 µL fluorescent substrate CCF2-FA (final concentration of 2 µM) prior to the measurement (Tecan, Safire). Shaded area's represent the standard deviation of the mean of the experiments. The results show that TEM1 β-lactamase decreases in activity over incubation time. However, the activated complexes (pink and red traces) after 2 and 3 hours incubation do not reach the activity of the free β-lactamase-ODN. Moreover, the increase in activity by activation of the complex becomes lower with increasing incubation time of the inactivated complex (red traces). Possibly the TEM1 β-lactamase is less stable in complex with BLIP compared to the free TEM1 β-lactamase-ODN. Furthermore, the complex possibly dissociates over time explaining why the negative control (blue) decreases less in activity compared to the free TEM1 β-lactamase-ODN (dark red). For these reasons, as a positive control we use the complex activated (by ***ξ***) after 'x' hours in the PEN toolbox environment.

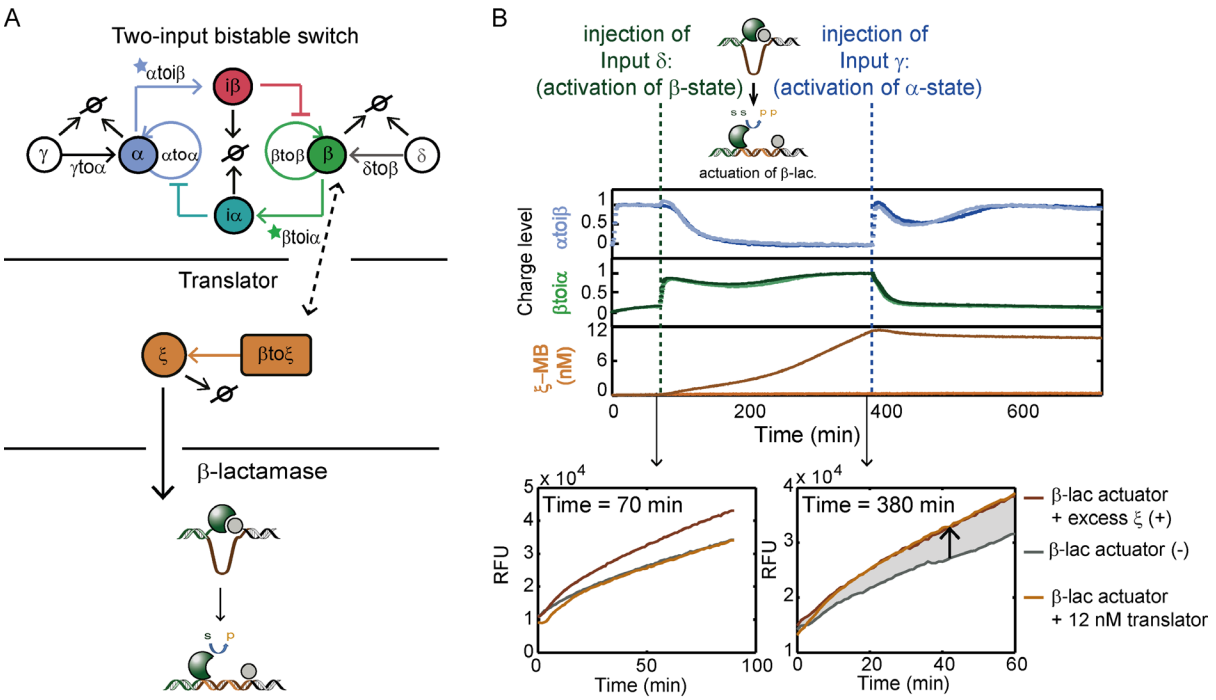

Figure S3.8: Controlling the activity of a TEM1 β-lactamase enzyme by a two-input bistable switch. A) Schematics of the experiment in which the two-input bistable network is used to control the activity of a self-inhibitory TEM1 β-lactamase construct. B) Results of the experiments which were carried out as described in *Paragraph* 3.8 (PEN-based experiments) using 20 nM ***βtoiα***, ***αtoiβ***, and ***βtoβ***, 10 nM ***αtoα***, ***γtoα*** and ***δtoβ***, 15 U/mL Bst 2.0 warmstart DNA polymerase, 10 U/mL Nt. bstNBI, 75 nM ttRecJ, 5 nM self-inhibitory TEM1 β-lactamase construct or 20 nM molecular beacon $\boldsymbol{MB_{\xi}}$ in absence and presence of 10 nM ***βtoξ*** and initiated with 1 nM of ***α***. The upper three graphs show the dynamics of the bistable switch and the production of DNA strand ***ξ*** measured using a molecular beacon labeled with ROX fluorophore and a quencher. The dotted lines show the time at which the Inputs ***δ*** and ***γ*** were added. The charge level is the normalized fluorescence of the signal of DY530 and FAM fluorophores which is 0 in the absence of template's input primer and 1 at the steady-state value of primer ***β*** and ***α*** respectively. The fluorescence of the ROX fluorophore was converted to concentration of DNA strand ***ξ*** using a standard curve (Figure S3.16). The experiments were performed in presence (dark blue, green and dark yellow) and absence (light blue, light green and light yellow) of translator module and the results show that the dynamics of the bistable switch are not disturbed by addition of the translator module. In parallel, experiments were run were the molecular beacon was replaced with the self-inhibitory TEM1 β-lactamase construct. The activity of the TEM1 β-lactamase was determined at two different states of the switch including 70 and 380 minutes after initiation of the switch, indicated by the black arrows, by measuring the conversion rate of fluorogenic substrate CCF2-FA. Negative and positive controls were carried out in parallel. For negative controls (grey) the translator module was omitted in the reactions. For positive controls (red) the translator module was also omitted and excess of DNA strand ***ξ*** (100 nM) was added to the wells plate. The results show we are able to control the activity of the self-inhibitory TEM1 β-lactamase construct by the dynamics of the bistable switch.

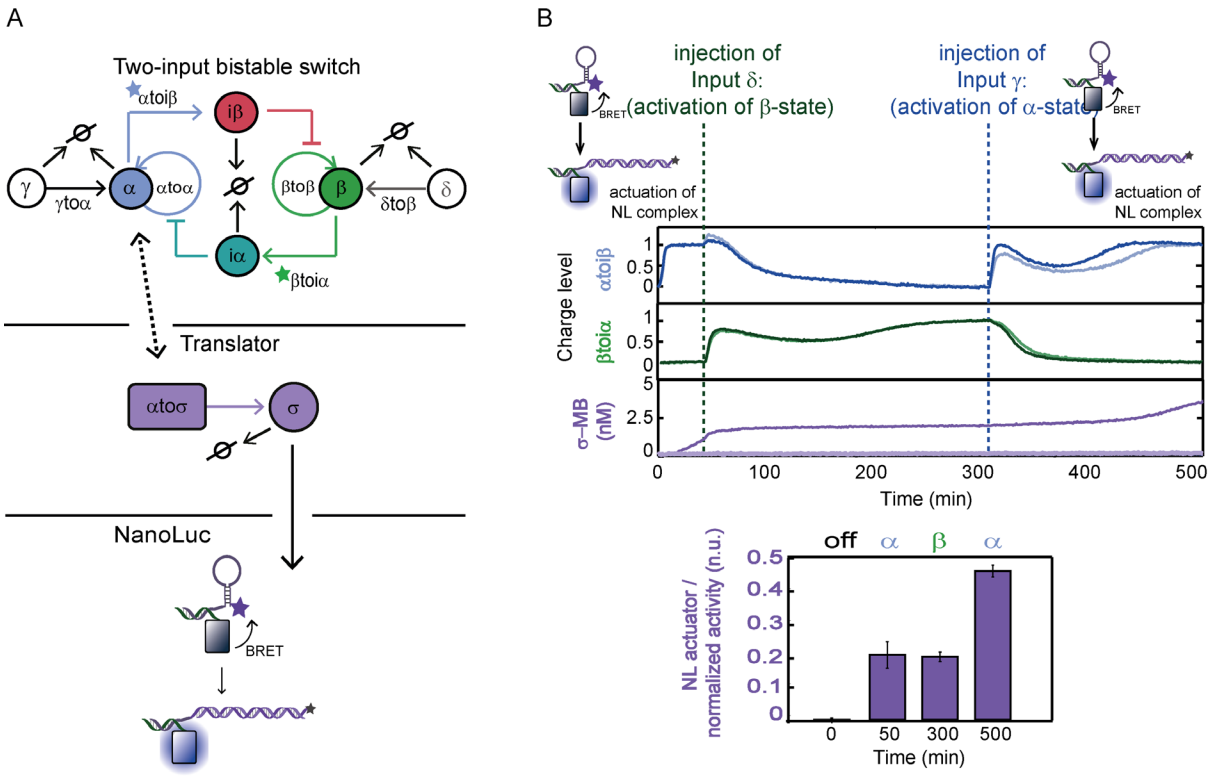

Figure S3.9: Control of a NanoLuc-based enzymatic actuator by a two-input bistable switch. A) Schematics of the experiment in which the two-input bistable network is used to control a NanoLuc-based enzymatic actuator. B) Results of the experiments which were carried out as described in *Paragraph* 3.8 using 20 nM ***βtoiα***, 15 nM ***αtoiβ***, 24 nM ***βtoβ***, 10 nM ***αtoα***, ***γtoα*** and ***δtoβ***, 15 U/mL Bst 2.0 warmstart DNA polymerase, 10 U/mL Nt. bstNBI, 200 nM ttRecJ, 5 nM NanoLuc actuator or molecular beacon $\boldsymbol{MB_\sigma}$ in absence and presence of 2 nM ***αtoσ*** and initiated with 1 nM of ***α***. The upper three graphs show the dynamics of the bistable switch and the production of DNA strand ***σ*** measured using a molecular beacon labeled with Cy5 fluorophore and a quencher. The dotted lines show the time at which the Inputs ***δ*** and ***γ*** were added. The charge level is the normalized fluorescence of the signal of DY530 and FAM fluorophores which is 0 in the absence of template's input primer and 1 at the steady-state value of primer ***β*** and ***α*** respectively. The fluorescence of the Cy5 fluorophore was converted to concentration of DNA strand ***σ*** using a standard curve (Figure S3.16). The experiments were performed in presence (dark blue, green and yellow) and absence (light blue, light green and light yellow) of translator module and the results show that the dynamics of the bistable switch are not disturbed by addition of the translator module. In parallel, experiments were run were the molecular beacon was replaced with the NanoLuc-based enzymatic actuator. The conformational state of the actuator was determined at different states of the switch including 0, 50, 300 and 500 minutes after initiation of the switch by primer ***α***, shown in the bar graph. The fraction of opened conformation in normalized units (n.u.) was calculated by subtracting the mean BRET ratio of the positive controls and normalizing to the mean BRET ratio of the negative controls (Figure S3.10). For negative and positive controls the translator module was omitted and excess of DNA strand ***σ*** was added for the positive control. Error bars represent the standard deviation of the mean of the experiments performed in triplicate. The results show we are able to control the NanoLuc-based actuator by the dynamics of the bistable switch.

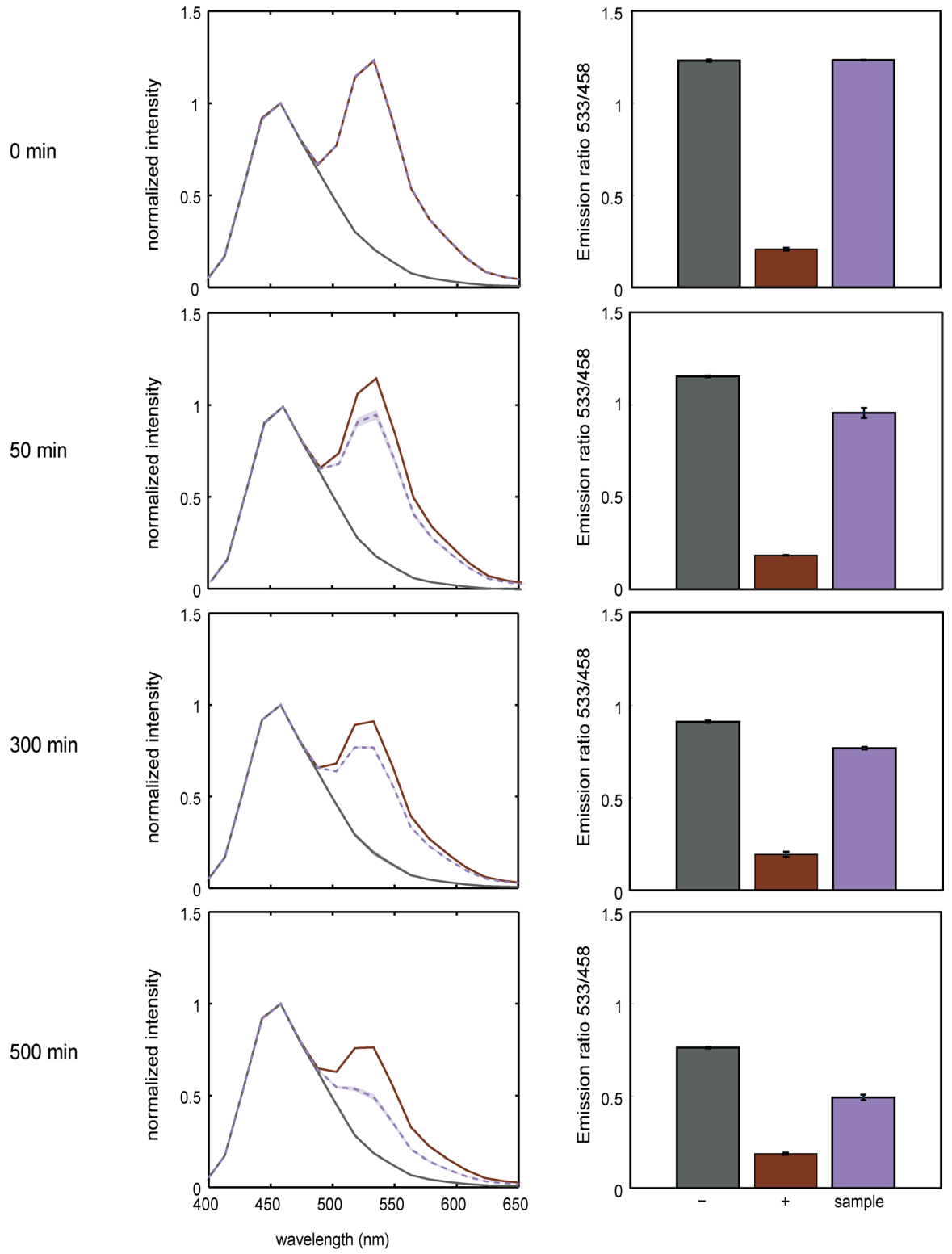

Figure S3.10: Normalized raw data of the control of the NanoLuc-complex at different states of the switch (Figure S3.9). A detailed description of the protocol can be found in *Paragraph* 3.8. For negative (–, grey) and positive (+, red) controls the translator module was omitted and excess of DNA strand σ was added to the wells plate for the positive controls. The BRET ratio at 533 nm and 458 nm was calculated for samples and controls. Experiments were performed in triplicate. Error bars and shaded area's represent the standard deviation of the mean of the experiments.

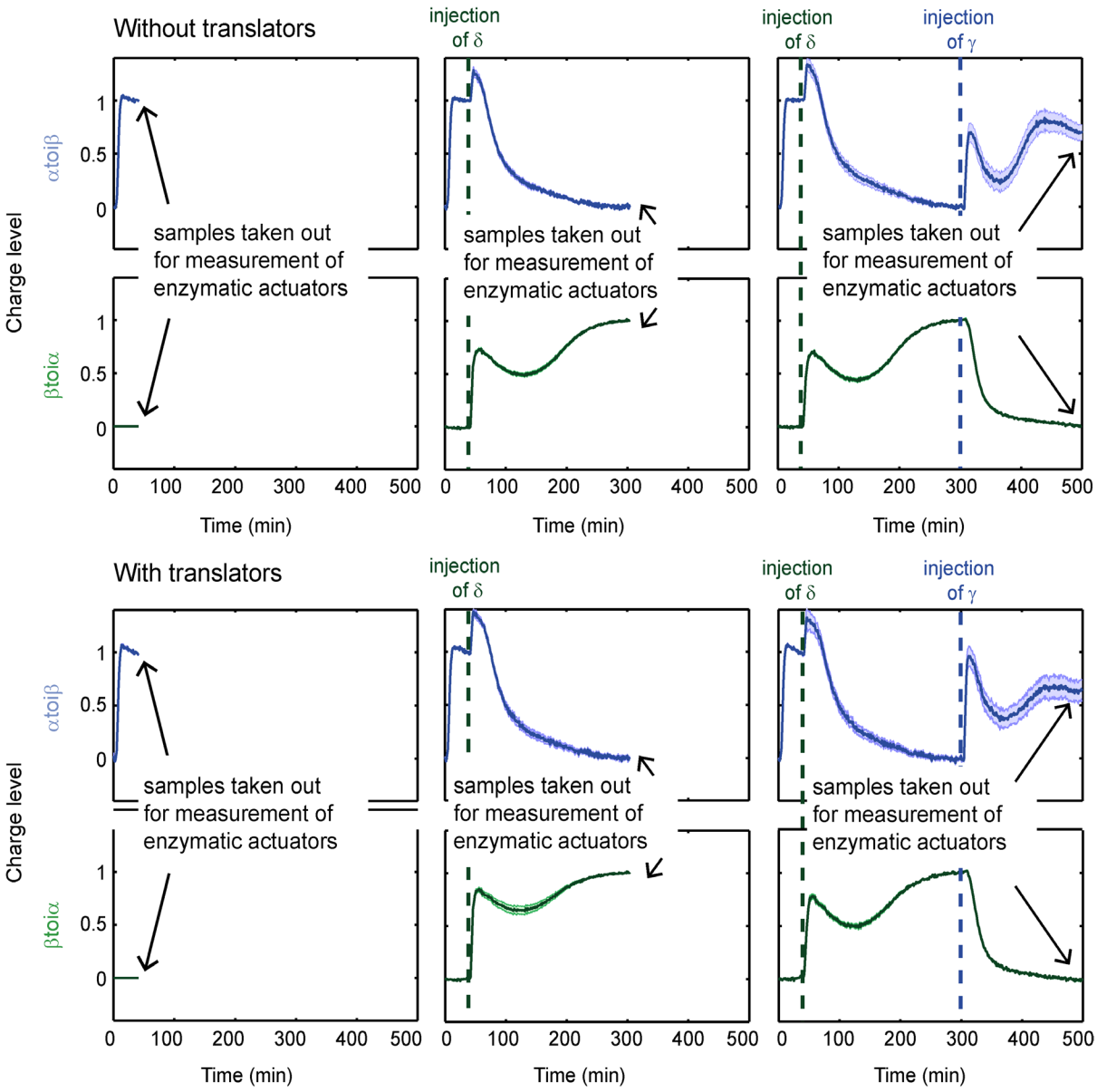

Figure S3.11: Raw data displaying the dynamics of the switch while probing the activity of the enzymatic actuators (Figure 3.6). Experiments were carried out as described in *Paragraph* 3.8 in absence of translator templates (for the measurement of the positive and negative controls in determining the activity of the enzymatic actuators) and in presence of the orthogonal set of translator templates including ***αtoσ*** and ***βtoξ***. The charge level is the normalized fluorescence of the signal of DY530 and FAM fluorophores which is 0 in the absence of template's input primer and 1 at the steady-state value of primer ***β*** and ***α*** respectively. The dotted lines show the time points at which 30 nM of Input ***δ*** or ***γ*** was added. Shaded area's represent the standard deviation of the mean of the experiments. Experiments were performed in duplicate at three different days.

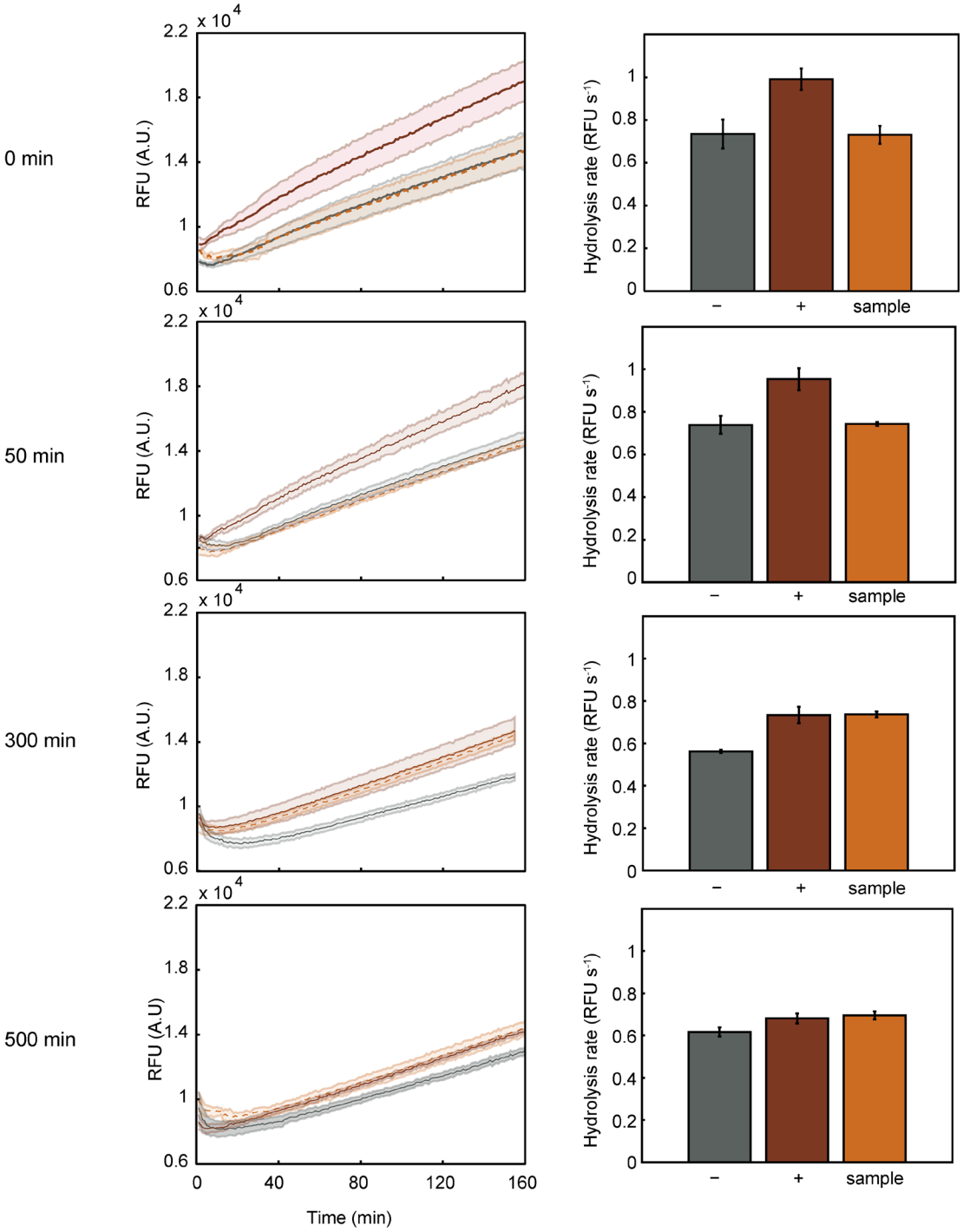

Figure S3.12: Raw data of the activity of β-lactamase at different states of the switch (Figure 3.6). The activity of β-lactamase was measured by adding CCF2-FA to the samples after which fluorescence at 447 nm was measured. A detailed description of the protocol can be found in *Paragraph* 3.8. Conversion of CCF2-FA is shown on the left for the different states of the switch. For negative (–, grey) and positive (+, red) controls the translator templates ***atoσ*** and ***βtoξ*** were omitted and excess of DNA strand ***ξ*** was added to the wells plate for the positive controls. The activity of β-lactamase was determined by deriving the slope between 50 and 150 minutes, shown on the right. Experiments were performed in duplicate at three different days. Error bars and shaded area's represent the standard deviation of the mean of the experiments.

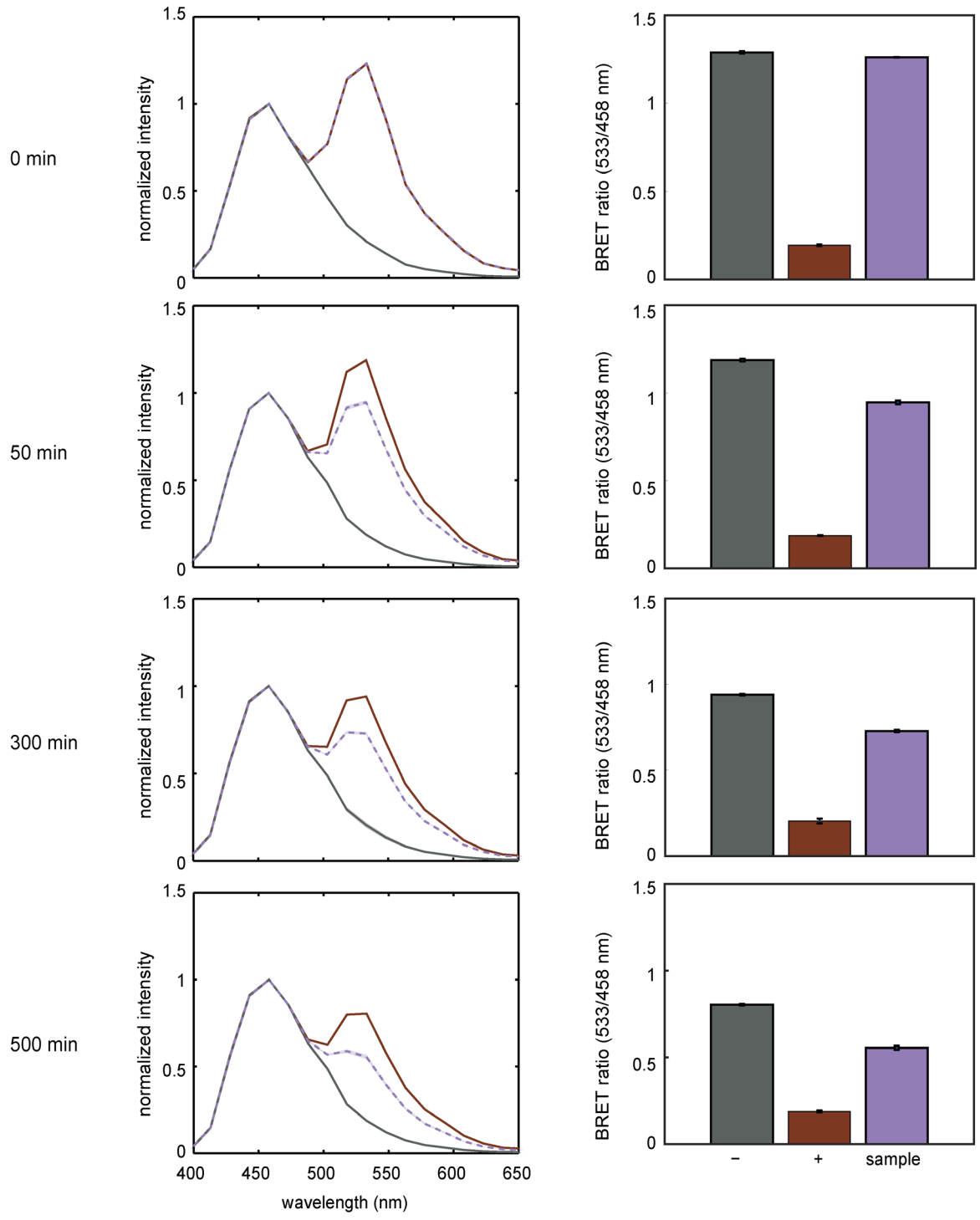

Figure S3.13: Normalized raw data of the control of the NanoLuc-complex at different states of the switch (Figure 3.6). A detailed description of the protocol can be found in *Paragraph* 3.8. For negative (–, grey) and positive (+, red) controls the translator templates ***atoσ*** and ***βtoξ*** were omitted and excess of DNA strand ***σ*** was added to the wells plate for the positive controls. The BRET ratio at 533 nm and 458 nm was calculated for samples and controls. Experiments were performed in duplicate at three different days. Error bars and shaded area's represent the standard deviation of the mean of the experiments.

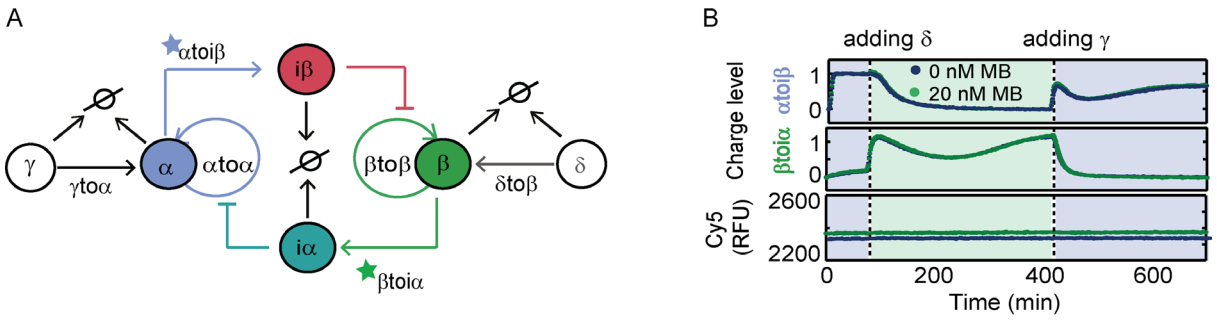

Figure S3.14: Characterizing the crosstalk between the molecular beacon and the switch. A) Schematic illustration of the switch. B) Results of the experiments which were performed as described in *Paragraph* 3.8 (PEN-based experiments) in absence of molecular beacon (blue) and in presence of 20 nM molecular beacon $\boldsymbol{MB_\sigma}$ (green). The black dotted lines are the timepoints at which primers $\boldsymbol{\delta}$ and $\boldsymbol{\gamma}$ were added respectively. Experiments were performed using 20 nM of $\boldsymbol{\beta toi\alpha}$, $\boldsymbol{\alpha toi\beta}$ and 20 nM $\boldsymbol{\beta to\beta}$, 12 nM $\boldsymbol{\alpha to\alpha}$, 10 U/mL Bst 2.0 warmstart DNA polymerase, 10 U/mL Nt. bstNBI and 50 nM ttRecJ. The experiment is initiated with 1 nM of primer $\boldsymbol{\alpha}$ and, hence, the $\boldsymbol{\alpha}$-side of the switch is initiated first. The charge level is the normalized fluorescence of the signal of DY530 and FAM fluorophores which is 0 in the absence of template's input primer and 1 at the steady-state value of primer $\boldsymbol{\beta}$ and $\boldsymbol{\alpha}$ respectively. The experiments show the molecular beacon does not interact with the switch and does not change the dynamics significantly. Furthermore, the results on the bottom show the molecular beacon is not opened in these reaction mixtures.

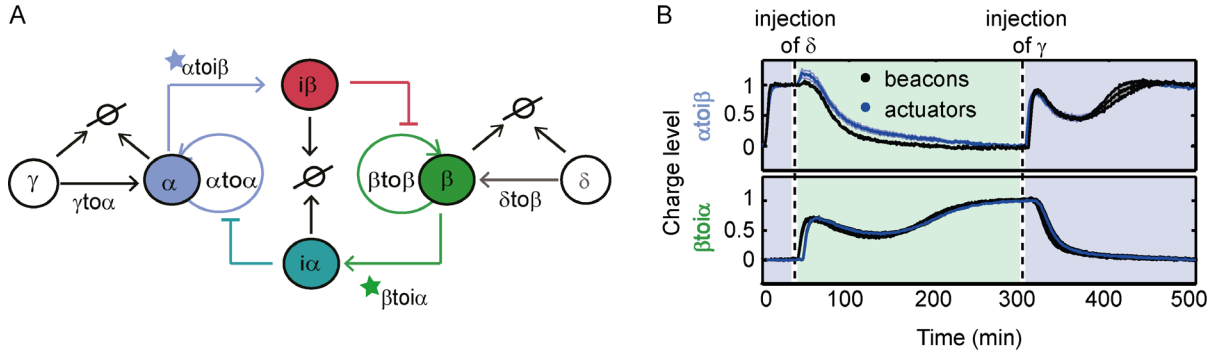

Figure S3.15: Characterizing crosstalk between the enzymatic actuators and the switch. A) Schematic illustration of the switch. B) Results of the experiments which were performed as described in *Paragraph* 3.8 (PEN-based experiments) in presence of molecular beacons (black) or in presence of the enzymatic actuators (blue). The black dotted lines are the timepoints at which primers $\boldsymbol{\delta}$ and $\boldsymbol{\gamma}$ were added respectively. Experiments were performed using 20 nM $\boldsymbol{\beta toi\alpha}$, 15 nM $\boldsymbol{\alpha toi\beta}$, 24 nM $\boldsymbol{\beta to\beta}$, 10 nM $\boldsymbol{\alpha to\alpha}$, $\boldsymbol{\gamma to\alpha}$ and $\boldsymbol{\delta to\beta}$, 15 U/mL Bst 2.0 warmstart DNA polymerase, 10 U/mL Nt. bstNBI, 200 nM ttRecJ in presence of 5 nM NanoLuc actuator and 2.5 nM β-lactamase actuator or 5 nM $\boldsymbol{MB_\sigma}$ and 2.5 nM $\boldsymbol{MB_\xi}$. The experiment is initiated with 1 nM of primer $\boldsymbol{\alpha}$ and, hence, the α-side of the switch is initiated first. The charge level is the normalized fluorescence of the signal of DY530 and FAM fluorophores which is 0 in the absence of template's input primer and 1 at the steady-state value of primer $\boldsymbol{\beta}$ and $\boldsymbol{\alpha}$ respectively. Experiments were performed in duplicate. Shaded area's represent the standard deviation of the mean of the experiments. The experiments show that both enzymatic actuators have low cross-talk with the switch as evidenced by similar switching dynamics in the presence of beacons and actuators.

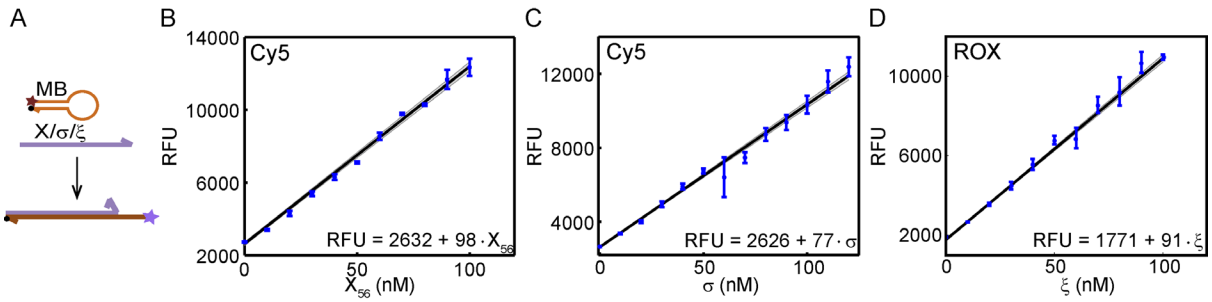

Figure S3.16: Standard curve of molecular beacons with different amounts of targets. A) Experiments were performed in mastermix without enzymes (*Paragraph* 3.8) and fluorescence was measured at 42 °C. B) Standard curve of molecular beacon $\boldsymbol{MB_x}$ and target $\boldsymbol{X_{56}}$. C) Standard curve of molecular beacon $\boldsymbol{MB_\sigma}$ and target $\boldsymbol{\sigma}$. D) Standard curve of molecular beacon $\boldsymbol{MB_\xi}$ and target $\boldsymbol{\xi}$. **b-d,** To obtain the slope the experimental data was fitted to a linear equation.

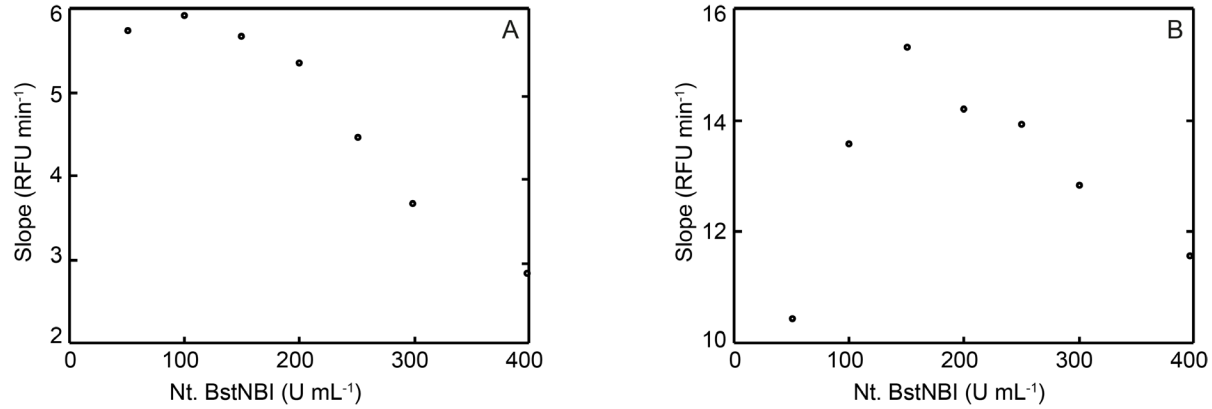

Figure S3.17: Amplification rate of α for a range of nickase. Experiments were performed for a range of nickase concentration and 20 U/mL Bst. polymerase 2.0 warmstart using 20 nM (A) or 60 nM (B) of autocatalytic template. The amplification rate first increases to an optimum with increasing concentration of nickase after which the amplification rate decreases with increasing concentration of nickase. Furthermore, the optimum ratio of nickase to polymerase is dependent on the concentration of the substrate.

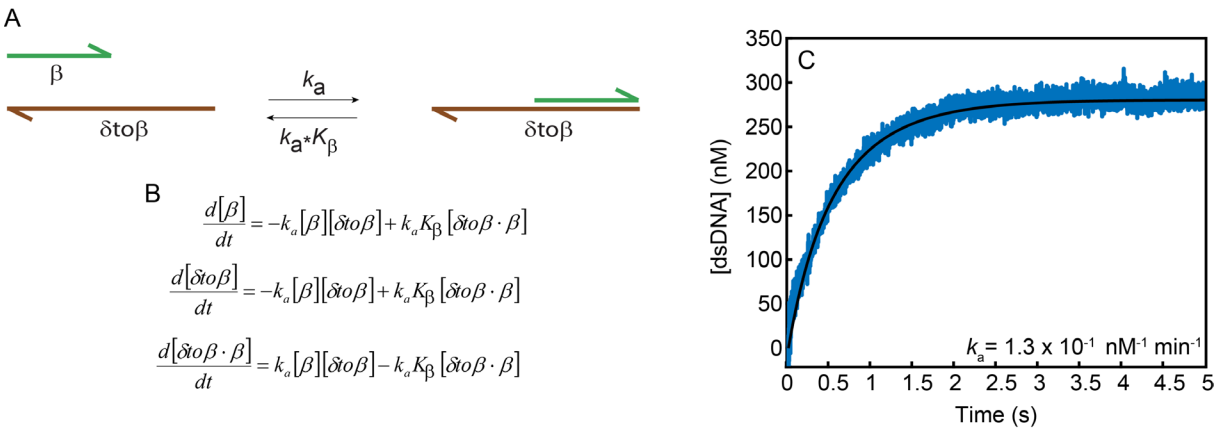

Figure S3.18: Characterization of the kinetics of DNA hybridization. A) Schematic illustration of DNA hybridization. B) Ordinary differential equations describing the kinetics of DNA hybridization. C) Results of non-linear least squares analysis (Table 3.2) of the data to the ODE model based on the equations in (B). Experiments were performed using 500 nM primer *β* and template *δtoβ* in 1x TE buffer with 0.06 nM Na^+ and 0.008 M Mg^{2+}. A detailed description of the experiment and analysis is provided in *Paragraph* 3.8.

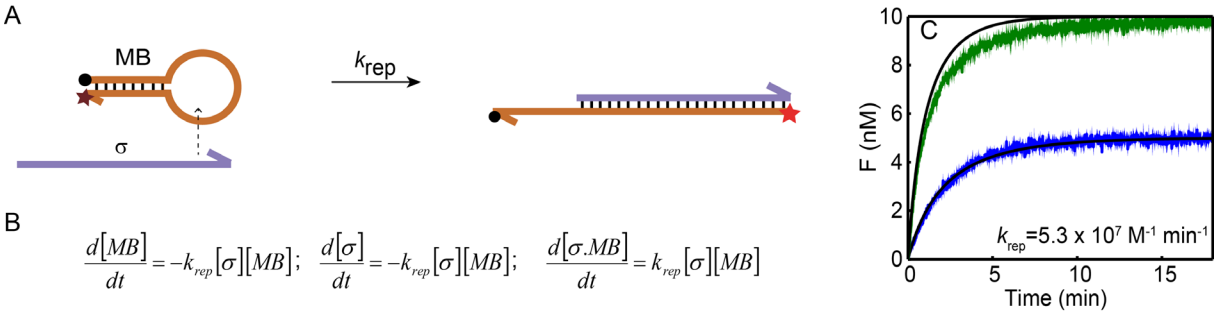

Figure S3.19: Characterization of the kinetics of the molecular beacon. A) Schematic illustration of the experiment in which DNA strand ***σ*** binds to the loop of the beacon followed by strand displacement disrupting the stem of the beacon resulting in an increase in fluorescence. B) Ordinary differential equations describing the kinetics of the molecular beacon using the bimolecular reaction approximation.[37] C) Experiments were performed using 10 nM of molecular beacon and 5 (blue) and 20 nM (green) of DNA strand ***σ*** respectively in mastermix without enzymes and fluorescence was recorded over time. Non-linear least squares optimization was performed using the ODE model in order to obtain an estimate for the second-order rate k_{rep} (Table 3.2). A detailed description of the experiment and analysis is provided in Supplementary Information II.

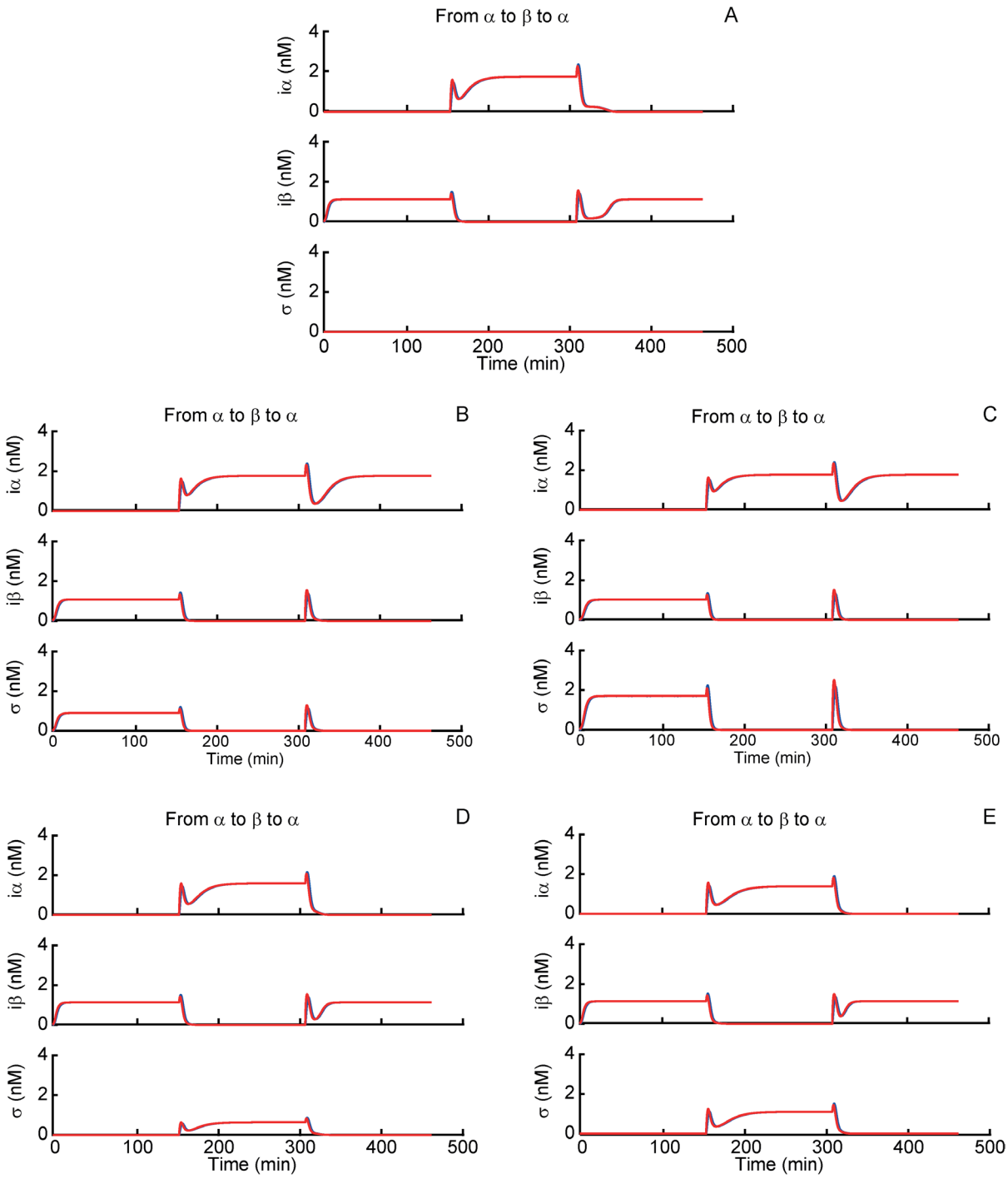

Figure S3.20: Comparison of dynamics of full heuristic model and the reduced model. ***iα***, ***iβ*** and ***σ*** obtained with the full heuristic model (blue) and its steady-state approximations $\mathbf{f}_{i\alpha}$, $f_{i\beta}$, and f_{σ} (red) for switches from ***α*** to ***β*** to ***α***. A) 0 nM translator. B) 10 nM translator at ***α*** ($V_{L\alpha}$ = 0.65 nM min^{-1}). C) 20 nM translator at ***α*** ($V_{L\alpha}$ = 1.3 nM min^{-1}). D) 10 nM translator at ***β*** ($V_{L\beta}$ = 0.65 nM min^{-1}). E) 20 nM translator at ***β*** ($V_{L\beta}$ = 1.3 nM min^{-1}). Switches are initiated at t = 160 min and t = 310 min. Switching from ***α*** to ***β*** is initiated by a ***δ***-pulse and switching from ***β*** to ***α*** is initiated by a ***γ***-pulse. The dynamical behavior of the heuristic model and its reduction are qualitative similar. Using the reduced model separatrices and switching planes are obtained (Figure S3.22 and S3.23). A detailed description of the heuristic model and its steady-state approximations is provided in Supplementary Information II.

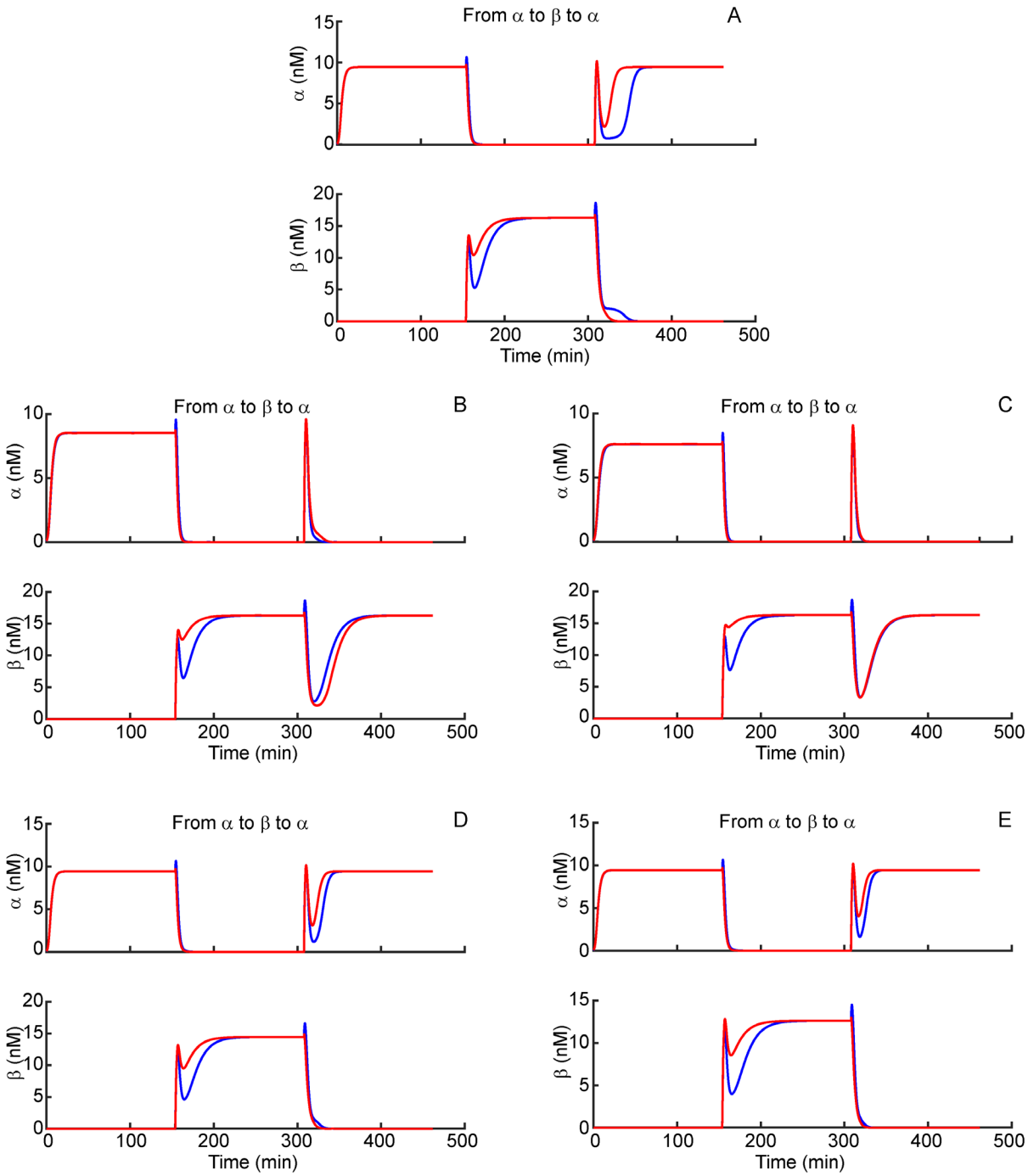

Figure S3.21: Comparison of dynamics of full heuristic model and the reduced model. Comparison of trajectories of the heuristic model (blue) and the reduced model (red) for switches from $\boldsymbol{\alpha}$ to $\boldsymbol{\beta}$ to $\boldsymbol{\alpha}$. A) 0 nM translator. B) 10 nM translator at $\boldsymbol{\alpha}$ ($V_{L\alpha} = 0.65$ nM min^{-1}). C) 20 nM translator at $\boldsymbol{\alpha}$ ($V_{L\alpha} = 1.3$ nM min^{-1}). D) 10 nM translator at $\boldsymbol{\beta}$ ($V_{L\beta} = 0.65$ nM min^{-1}). E) 20 nM translator at $\boldsymbol{\beta}$ ($V_{L\beta} = 1.3$ nM min^{-1}). Switches are initiated at t = 160 min and t = 310 min. Switching from $\boldsymbol{\alpha}$ to $\boldsymbol{\beta}$ is initiated by a $\boldsymbol{\delta}$-pulse and switching from $\boldsymbol{\beta}$ to $\boldsymbol{\alpha}$ is initiated by a $\boldsymbol{\gamma}$-pulse. The dynamical behavior of the heuristic model and its reduction are qualitative similar. Using the reduced model separatrices and switching planes are obtained (Figure S3.22 and S.3.23).

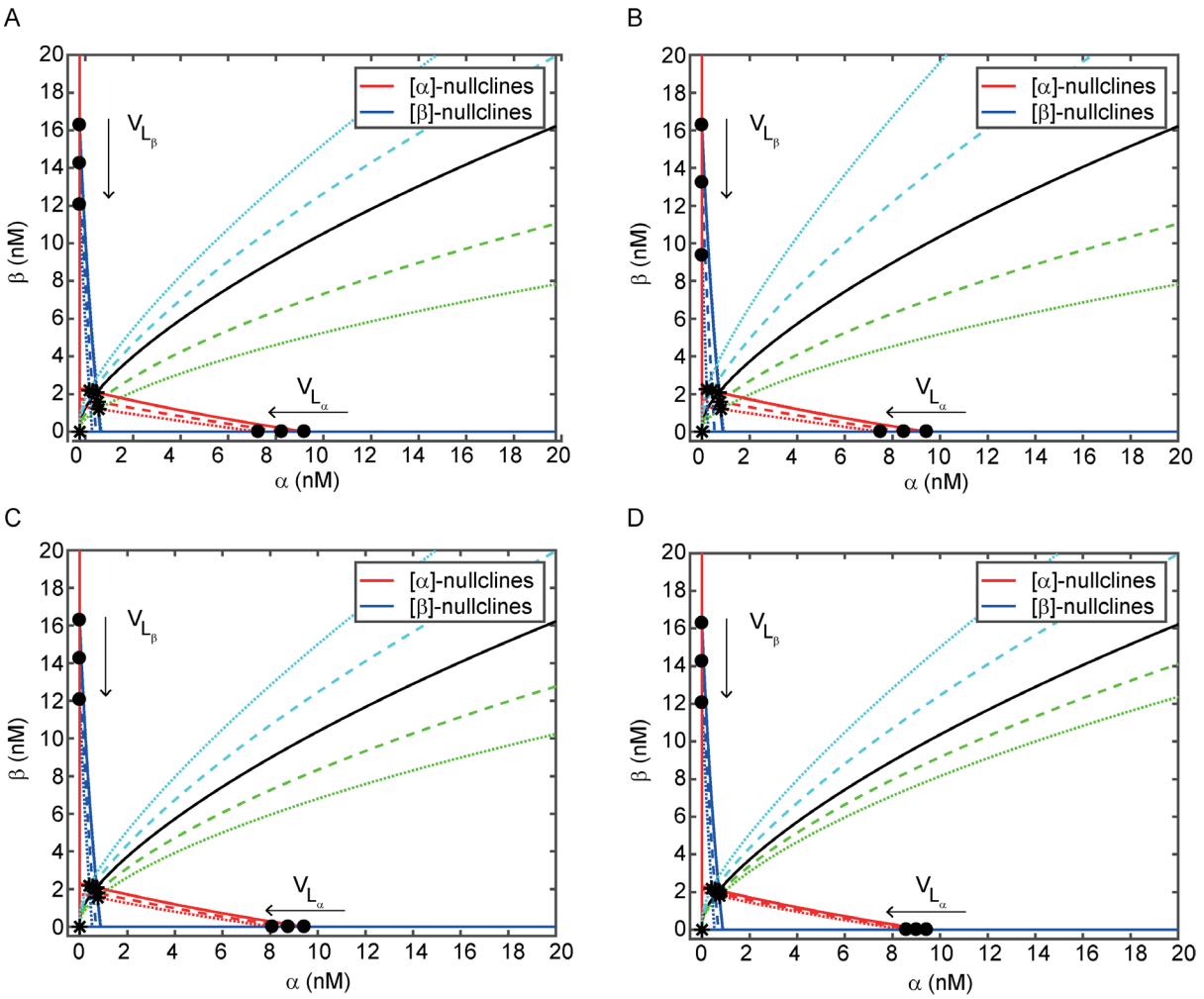

Figure S3.22: Nullclines and seperatrices of the switch without and with translator. Nullclines and separatrices in the (***α***,***β***)-plane for various combinations of $K_{L\alpha}$ and $K_{L\beta}$ were obtained using the reduced model (Supplementary Information II). A) $K_{L\alpha}$ = 6 nM, $K_{L\beta}$ = 24 nM B) $K_{L\alpha}$ = 6 nM, $K_{L\beta}$ = 12 nM C) $K_{L\alpha}$ = 12 nM, $K_{L\beta}$ = 24 nM D) $K_{L\alpha}$ = 24 nM, $K_{L\beta}$ = 24 nM. All other parameter are set to their nominal value. Solid lines correspond to absence of translator, dashed line represent presence of translator with load of 10 nM, dotted line represent presence of translator with load of 20 nM. Black line is the seperatrix in absence of translator, green (dashed, dotted) lines are seperatrices for the translator coupled to the ***α***-side of the switch, cyan (dashed, dotted) lines are seperatrices for the translator coupled to the ***β***-side of the switch. Black circles are the (locally) stable steady-states, stars indicate the unstable steady-states. These results show a shift in the nullclines and separatrices when the translator is coupled to the ***α***- or ***β***-side of the switch. Furthermore, the nullclines and separatrices with the translator module coupled show an increased shift with decreasing dissociation constant.

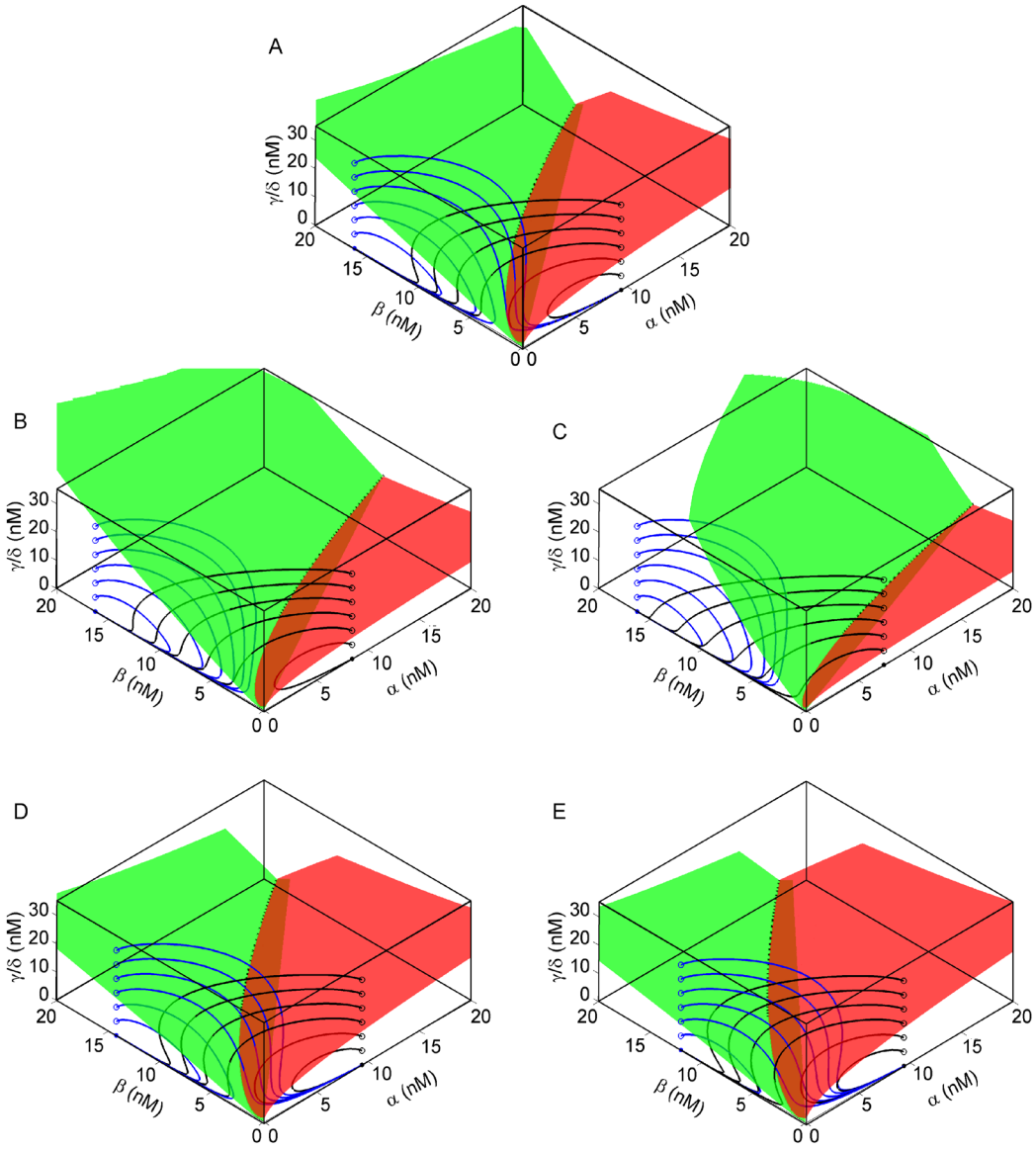

Figure S3.23: Computed switch-planes without and with translator module. Computed ***γ***-switch-planes (green) and ***δ***-switch-planes (red) for the switch without translator module and the translator module coupled to ***α*** or ***β***. A) Switch planes of switch without translator module. B) Switch-planes of switch with 10 nM translator module coupled to ***α*** ($V_{L\alpha}$ = 0.65 nM). C) Switch-planes of switch with 20 nM translator module coupled to ***α*** ($V_{L\alpha}$ = 1.3 nM). D) Switch-planes of switch with 10 nM translator module coupled to ***β*** ($V_{L\beta}$ = 0.65 nM). E) Switch-planes of switch with 20 nM translator module coupled to ***β*** ($V_{L\beta}$ = 1.3 nM). The switch-planes were obtained from the reduced model (Supplementary Information II). Black trajectories corresponding to a (successful/unsuccessful) switch from ***α*** to ***β***, blue trajectories corresponding to a (successful/unsuccessful) switch from ***β*** to ***α***. Black trajectories can not cross the red plane, blue trajectories can not cross the green plane. Open circles indicate the initial conditions and solid circles indicate the final steady-state. The switch-planes were computed with ***γ***/***δ*** pulses from 5 to 30 nM. Coupling of the translator template to ***β*** results in a shift in the switching plane in favor of the α-state. By contrast, coupling of the translator template to ***α*** results in a shift in the switching plane in favor of the β-state.

Supplementary Information II: A reduced model

In this section we present a reduced model of our heuristic model which was derived by dr. E. Steur. To reduce the model we:

- ignore the dynamics of the reporter (by setting either k_{rep} = 0 nM min^{-1} or MB_0 = 0 nM);
- assume that $i\alpha$, $i\beta$, σ and θ are instantly at steady-state.

The first condition is reasonable as the reporter has minor influence on the occurrence of a switch. (In particular, note that ***MB*** is only 'consumed' such that after some switches [***MB***] = 0 nM). The second assumptions are made without chemical nor mathematical justification. One of the main reasons for reduction is visualization of switch planes in three dimensions. However, from numerical simulations we observe that the steady-state assumption produces reasonably accurate results (Figure S3.20). Furthermore, as shown in Figure S3.21, the dynamical behavior of the heuristic model and its reduction are qualitative similar.

Denoting by:

$$[i\alpha] = f_{i\alpha}([\alpha],[\beta])$$

$$[i\beta] = f_{i\beta}([\alpha],[\beta])$$

$$[\sigma] = f_{\sigma}([\alpha],[\beta])$$

$$[\theta] = f_{\theta}([\alpha],[\beta])$$

the steady-states solutions of $i\alpha$, $i\beta$, σ and θ as function of and α and β, we obtain the reduced model:

$$\frac{d}{dt}[\gamma] = -\frac{V_{exo}[\gamma]}{K_{exo} + [\gamma] + [\delta] + [\alpha] + f_{i\alpha}([\alpha],[\beta]) + f_{i\beta}([\alpha],[\beta]) + f_{\sigma}([\alpha],[\beta])}$$

$$\frac{d}{dt}[\delta] = -\frac{V_{exo}[\delta]}{K_{exo} + [\gamma] + [\delta] + [\alpha] + f_{i\alpha}([\alpha],[\beta]) + f_{i\beta}([\alpha],[\beta]) + f_{\sigma}([\alpha],[\beta])}$$

$$\begin{aligned}\frac{d}{dt}[\alpha] = {} & \frac{V_{\gamma}[\gamma]}{K_{\gamma} + [\gamma]} + \frac{V_{\alpha}[\alpha]}{K_{\alpha} + [\alpha] + \lambda_{\alpha} f_{i\alpha}([\alpha],[\beta])} - (1-\rho)\frac{V_{L\alpha}[\alpha]}{K_{L\alpha} + [\alpha]} \\ & - \frac{V_{exo}[\alpha]}{K_{exo} + [\gamma] + [\delta] + [\alpha] + [\beta] + f_{i\alpha}([\alpha],[\beta]) + f_{i\beta}([\alpha],[\beta]) + f_{\sigma}([\alpha],[\beta])}\end{aligned} \tag{3.3}$$

$$\begin{aligned}\frac{d}{dt}[\beta] = {} & \frac{V_{\delta}[\delta]}{K_{\delta} + [\delta]} + \frac{V_{\beta}[\beta]}{K_{\beta} + [\beta] + \lambda_{\beta} f_{i\beta}([\alpha],[\beta])} - (1-\rho)\frac{V_{L\beta}[\beta]}{K_{L\beta} + [\beta]} \\ & - \frac{V_{exo}[\beta]}{K_{exo} + [\gamma] + [\delta] + [\alpha] + [\beta] + f_{i\alpha}([\alpha],[\beta]) + f_{i\beta}([\alpha],[\beta]) + f_{\sigma}([\alpha],[\beta])}\end{aligned}$$

where $V_{L\alpha}$ $V_{L\beta}$ = 0 (which implies that the translator is coupled to at most one side of the switch). The dynamics of the reduced model will be studied in detail, which provides valuable insights in the role of specific parameters in both the reduced model and the full model.

Nullclines

The nullclines of the bistable switch were computed by dr. E. Steur using the following procedure. Let us consider the dynamics of the reduced model with [$\boldsymbol{\gamma}$] = 0 nM and [$\boldsymbol{\delta}$] = 0 nM. We first determine the [$\boldsymbol{\alpha}$]-nullclines and [$\boldsymbol{\beta}$]-nullclines, i.e. the set set of points at which $\frac{d}{dt}[\alpha] = 0$ and $\frac{d}{dt}[\beta] = 0$ respectively.

Obviously, the points of intersection of the [$\boldsymbol{\alpha}$]-nullclines and [$\boldsymbol{\beta}$]-nullclines define the steady-state solutions of the reduced model. Note that:

$$[\alpha] = 0 \Rightarrow \frac{d}{dt}[\alpha] = 0 \text{ and } [\beta] = 0 \Rightarrow \frac{d}{dt}[\beta] = 0$$

such that ([$\boldsymbol{\alpha}$], [$\boldsymbol{\beta}$]) = (0, 0) is a steady-state solution. Furthermore, note that steady-state solutions of the reduced model coincide with (the [$\boldsymbol{\alpha}$] and [$\boldsymbol{\beta}$] part of) the steady-state solutions of the full model. Figure S3.22 shows the nullclines depending on coupling of the translator. In all these plots:

- $\frac{d}{dt}[\alpha]<0$ for point above the red nullclines.
- $\frac{d}{dt}[\alpha]>0$ for point below the red nullclines.

and

- $\frac{d}{dt}[\beta]<0$ for point right of the blue nullclines.
- $\frac{d}{dt}[\beta]>0$ for point left of the blue nullclines.

Computation of seperatrices and switch-planes

The separatrices shown in Figure S3.22 divide the ([***α***], [***β***])-plane in two regions; Solutions of the reduced model (with [***γ***] = [***δ***] = 0 nM) starting in the region below a seperatrix converge to the steady-state with positive [***α***] and zero [***β***], whereas solutions of the reduced model (with [***γ***] = [***δ***] = 0 nM) with initial conditions in the region above a seperatrix converge to the steady-state with zero [***α***] and positive [***β***]. The seperatrices were computed by dr. E. Steur using the following procedure:

1. Determine the positive steady-state solution (which is a saddle-point) and denote this positive steady-state by x_{ss}.
2. Determine the Jacobian matrix at x_{ss} and compute the eigenvalues and eigenvectors.
3. Let *u* be the eigenvector corresponding to the negative eigenvalue of the Jacobian and normalize *u* such that ||*u*|| = 1, then integrate the differential equations in negative *t* direction with initial conditions $x_{ss} + 10^{-8}u$ and $x_{ss} - 10^{-8}u$.[1]

Whether or not a switch from [***α***] to [***β***] or vice versa occurs can not be directly predicted from the location of the seperatrix; a switch is initiated by (the initial amplitude of) [***γ***] or [***δ***] rather than by controlling the initial conditions in the ([***α***],[***β***])-plane. To gain further insights in whether a switch will be successful or not we compute the so-called switch-planes. These switch-planes are global invariant manifolds in the ([***γ***],[***α***],[***β***])-space or ([***δ***],[***α***],[***β***])-space for switching from ***β*** to ***α*** or from ***α*** to ***β*** respectively. As the switch-planes are global invariant

[1] 1Let $\phi(t;x)$ be a solution of the systems through x. The stable manifold of x_{ss} is the set $W_s(x_{ss}) :=$ $\{x : \phi(t;x) \to x_{ss}$ as t $\to\infty\}$, the unstable manifold of x_{ss} is the set $W_u(x_{ss}) :=$ $\{x : \phi(t;x) \to x_{ss}$ as t $\to\infty\}$. As the positive steady-state is a saddle-point, invoking the stable and unstable manifold theorem,[51] $W_s(x_{ss})$ and $W_u(x_{ss})$ are tangent to the stable, respectively, unstable eigenspaces of the linearization at xss.

manifolds, they divide the corresponding space in two parts; The part below the switch-planes defines the points at which switches can not occur whereas for points above the switch-planes there will be a switch (Figure S3.23). Note that the intersection of the switch-planes with the ([$\boldsymbol{\alpha}$],[$\boldsymbol{\beta}$])-plane should be the seperatrix (that we have computed before). We shall briefly discuss the computation of the [$\boldsymbol{\gamma}$]-switch-plane. (Computation of the [$\boldsymbol{\delta}$]-switch-plane is done analogously.) In other words, we consider only switches from $\boldsymbol{\beta}$ to $\boldsymbol{\alpha}$ such that we can set [$\boldsymbol{\delta}$] = 0 (and, consequently, $\frac{d}{dt}[\delta]=0$). Thus the dynamics are described by the three-dimensional system of ODEs:

$$\frac{d}{dt}[\gamma] = -\frac{V_{exo}[\gamma]}{K_{exo}+[\gamma]+[\delta]+[\alpha]+f_{i\alpha}([\alpha],[\beta])+f_{i\beta}([\alpha],[\beta])+f_{\sigma}([\alpha],[\beta])}$$

$$\begin{aligned}\frac{d}{dt}[\alpha] = {} & \frac{V_{\gamma}[\gamma]}{K_{\gamma}+[\gamma]}+\frac{V_{\alpha}[\alpha]}{K_{\alpha}+[\alpha]+\lambda_{\alpha}f_{i\alpha}([\alpha],[\beta])}-(1-\rho)\frac{V_{L\alpha}[\alpha]}{K_{L\alpha}+[\alpha]} \\ & -\frac{V_{exo}[\alpha]}{K_{exo}+[\gamma]+[\delta]+[\alpha]+[\beta]+f_{i\alpha}([\alpha],[\beta])+f_{i\beta}([\alpha],[\beta])+f_{\sigma}([\alpha],[\beta])}\end{aligned} \tag{3.4}$$

$$\begin{aligned}\frac{d}{dt}[\beta] = {} & \frac{V_{\beta}[\beta]}{K_{\beta}+[\beta]+\lambda_{\beta}f_{i\beta}([\alpha],[\beta])}-(1-\rho)\frac{V_{L\beta}[\beta]}{K_{L\beta}+[\beta]} \\ & -\frac{V_{exo}[\beta]}{K_{exo}+[\gamma]+[\delta]+[\alpha]+[\beta]+f_{i\alpha}([\alpha],[\beta])+f_{i\beta}([\alpha],[\beta])+f_{\sigma}([\alpha],[\beta])}\end{aligned}$$

Because the switch-plane is the union of trajectories that converge to points on the seperatrix we can approximate the switch-planes by:

1. taking initial conditions for [$\boldsymbol{\alpha}$] and [$\boldsymbol{\beta}$] on the seperatrix and set the initial condition for [$\boldsymbol{\gamma}$] to be 10^{-8}.
2. integrate the three-dimensional system of ODEs in negative t direction.

It is interesting to note that the effect of asymmetry in the model (as the parameters of the α-side of the switch are not identical to those of the β-side) can be compensated for by coupling the translator to the β-side (Figure S3.23d-e). Furthermore, in case of the translator being coupled to the α-side a (unrealistically) high amplitude is needed for successful switching from $\boldsymbol{\beta}$ to $\boldsymbol{\alpha}$ (Figure S3.23b) and, in particular, Figure S3.23c).

3.9 References

1. Meng, H.-M. et al. Aptamer-integrated DNA nanostructures for biosensing, bioimaging and cancer therapy. *Chem. Soc. Rev.* **45**, 2583-2602 (2016).
2. Zhu, G. et al. Self-assembled, aptamer-tethered DNA nanotrains for targeted transport of molecular drugs in cancer theranostics. *Proc. Natl. Acad. Sci. U.S.A.* **110**, 7998-8003 (2013).
3. Li, J. et al. Self-assembled multivalent DNA nanostructures for noninvasive intracellular delivery of immunostimulatory CpG oligonucleotides. *ACS Nano* **5**, 8783-8789 (2011).
4. Ranallo, S., Prévost-Tremblay, C., Idili, A., Vallée-Bélisle, A. & Ricci, F. Antibody-powered nucleic acid release using a DNA-based nanomachine. *Nat. Commun.* **8**, 15150 (2017).
5. Gu, H., Chao, J., Xiao, S.-J. & Seeman, N.C. A proximity-based programmable DNA nanoscale assembly line. *Nature* **465**, 202-205 (2010).
6. Liu, M. et al. A DNA tweezer-actuated enzyme nanoreactor. *Nat. Commun.* **4**, 2127 (2013).
7. Zhou, C., Yang, Z. & Liu, D. Reversible regulation of protein binding affinity by a DNA machine. *J. Am. Chem. Soc.* **134**, 1416-1418 (2012).
8. Xin, L., Zhou, C., Yang, Z. & Liu, D. Regulation of an enzyme cascade reaction by a DNA machine. *Small* **9**, 3088-3091 (2013).
9. Janssen, B.M.G., Engelen, W. & Merkx, M. DNA-directed control of enzyme–inhibitor complex formation: a modular approach to reversibly switch enzyme activity. *ACS Synth. Biol.* **4**, 547-553 (2015).
10. Saghatelian, A., Guckian, K.M., Thayer, D.A. & Ghadiri, M.R. DNA detection and signal amplification via an engineered allosteric enzyme. *J. Am. Chem. Soc.* **125**, 344-345 (2003).
11. Ke, Y., Meyer, T., Shih, W.M. & Bellot, G. Regulation at a distance of biomolecular interactions using a DNA origami nanoactuator. *Nat. Commun.* **7**, 10935 (2016).
12. Zhang, D.Y., Turberfield, A.J., Yurke, B. & Winfree, E. Engineering entropy-driven reactions and networks catalyzed by DNA. *Science* **318**, 1121-1125 (2007).
13. Chen, X., Briggs, N., McLain, J.R. & Ellington, A.D. Stacking nonenzymatic circuits for high signal gain. *Proc. Natl. Acad. Sci. U.S.A.* **110**, 5386-5391 (2013).
14. Qian, L., Winfree, E. & Bruck, J. Neural network computation with DNA strand displacement cascades. *Nature* **475**, 368-372 (2011).
15. Han, D. et al. A logical molecular circuit for programmable and autonomous regulation of protein activity using DNA aptamer-protein interactions. *J. Am. Chem. Soc.* **134**, 20797-20804 (2012).
16. Seelig, G., Soloveichik, D., Zhang, D.Y. & Winfree, E. Enzyme-free nucleic acid logic circuits. *Science* **314**, 1585-1588 (2006).
17. Stojanovic, M.N., Mitchell, T.E. & Stefanovic, D. Deoxyribozyme-based logic gates. *J. Am. Chem. Soc.* **124**, 3555-3561 (2002).
18. Qian, L. & Winfree, E. Scaling up digital circuit computation with DNA strand displacement cascades. *Science* **332**, 1196-1201 (2011).
19. Han, D. et al. A cascade reaction network mimicking the basic functional steps of adaptive immune response. *Nat. Chem.* **7**, 835-841 (2015).
20. Kim, J., White, K.S. & Winfree, E. Construction of an in vitro bistable circuit from synthetic transcriptional switches. *Mol. Syst. Biol.* **2**(2006).
21. Kim, J. & Winfree, E. Synthetic in vitro transcriptional oscillators. *Mol. Syst. Biol.* **7**(2011).
22. Franco, E. et al. Timing molecular motion and production with a synthetic transcriptional clock. *Proc. Natl. Acad. Sci. U.S.A.* **108**, E784-E793 (2011).
23. Kim, J., Khetarpal, I., Sen, S. & Murray, R.M. Synthetic circuit for exact adaptation and fold-change detection. *Nucleic Acids Res.* **42**, 6078-6089 (2014).
24. Montagne, K., Plasson, R., Sakai, Y., Fujii, T. & Rondelez, Y. Programming an in vitro DNA oscillator using a molecular networking strategy. *Mol. Syst. Biol.* **7**, 466 (2011).
25. Padirac, A., Fujii, T. & Rondelez, Y. Bottom-up construction of in vitro switchable memories. *Proc. Natl. Acad. Sci. U.S.A.* **109**, 3212-3220 (2012).

26. Padirac, A., Fujii, T., Estévez-Torres, A. & Rondelez, Y. Spatial waves in synthetic biochemical networks. *J. Am. Chem. Soc.* **135**, 14586-14592 (2013).
27. Hasatani, K. et al. High-throughput and long-term observation of compartmentalized biochemical oscillators. *Chem. Commun.* **49**, 8090-8092 (2013).
28. Fujii, T. & Rondelez, Y. Predator - prey molecular ecosystems. *ACS Nano* **7**, 27-34 (2013).
29. Lim, W.A., Lee, C.M. & Tang, C. Design principles of regulatory networks: searching for the molecular algorithms of the cell. *Mol. Cell* **49**, 202-212 (2013).
30. Franco, E., Vecchio, D.D. & Murray, R.M. Design of insulating devices for in vitro synthetic circuits. in *Proc. IEEE Conf. Decis. Control* 4584-4589 (2009).
31. Engelen, W., van de Wiel, K.M., Meijer, L.H.H., Saha, B. & Merkx, M. Nucleic acid detection using BRET-beacons based on bioluminescent protein-DNA hybrids. *Chem. Commun.* **53**, 2862-2865 (2017).
32. Del Vecchio, D., Ninfa, A.J. & Sontag, E.D. Modular cell biology: retroactivity and insulation. *Mol. Syst. Biol.* **4**, 161 (2008).
33. Del Vecchio, D. A control theoretic framework for modular analysis and design of biomolecular networks. *Annu. Rev. Control* **37**, 333-345 (2013).
34. Gianneschi, N.C. & Ghadiri, M.R. Design of molecular logic devices based on a programmable DNA-regulated semi-synthetic enzyme. *Angew. Chem. Int. Ed. Engl.* **46**, 3955-3958 (2007).
35. Jayanthi, S., Nilgiriwala, K.S. & Del Vecchio, D. Retroactivity controls the temporal dynamics of gene transcription. *ACS Synth. Biol.* **2**, 431-441 (2013).
36. Padirac, A., Fujii, T. & Rondelez, Y. Quencher-free multiplexed monitoring of DNA reaction circuits. *Nucleic Acids Res.* **40**, e118 (2012).
37. Zhang, D.Y. & Winfree, E. Control of DNA strand displacement kinetics using toehold exchange. *J. Am. Chem. Soc.* **131**, 17303-17314 (2009).
38. Sohka, T. et al. An externally tunable bacterial band-pass filter. *Proc. Natl. Acad. Sci. U.S.A.* **106**, 10135-10140 (2009).
39. Prokup, A. & Deiters, A. Interfacing synthetic DNA logic operations with protein outputs. *Angew. Chem. Int. Ed. Engl.* **53**, 13192-13195 (2014).
40. Engelen, W., Meijer, L.H.H., Somers, B., de Greef, T.F.A. & Merkx, M. Antibody-controlled actuation of DNA-based molecular circuits. *Nat. Commun.* **8**, 14473 (2017).
41. Tyson, J.J., Chen, K.C. & Novak, B. Sniffers, buzzers, toggles and blinkers: dynamics of regulatory and signaling pathways in the cell. *Curr. Opin. Cell Biol.* **15**, 221-231 (2003).
42. Van Roekel, H.W.H. et al. Programmable chemical reaction networks: emulating regulatory functions in living cells using a bottom-up approach. *Chem. Soc. Rev.* **44**, 7465-7483 (2015).
43. Ferrell, J.E. & Xiong, W. Bistability in cell signaling: how to make continuous processes discontinuous, and reversible processes irreversible. *Chaos* **11**, 227-236 (2001).
44. Sokolik, C. et al. Transcription factor competition allows embryonic stem cells to distinguish authentic signals from noise. *Cell syst.* **1**, 117-129 (2015).
45. Yi, T.-M., Huang, Y., Simon, M.I. & Doyle, J. Robust perfect adaptation in bacterial chemotaxis through integral feedback control. *Proc. Natl. Acad. Sci. U.S.A.* **97**, 4649-4653 (2000).
46. Purvis, Jeremy E. & Lahav, G. Encoding and decoding cellular information through signaling dynamics. *Cell* **152**, 945-956 (2013).
47. Yao, G., Lee, T.J., Mori, S., Nevins, J.R. & You, L. A bistable Rb-E2F switch underlies the restriction point. *Nat. Cell Biol.* **10**, 476-482 (2008).
48. Chickarmane, V., Troein, C., Nuber, U.A., Sauro, H.M. & Peterson, C. Transcriptional dynamics of the embryonic stem cell switch. *PLoS Comput. Biol.* **2**, e123 (2006).
49. Das, J. et al. Digital signaling and hysteresis characterize Ras activation in lymphoid cells. *Cell* **136**, 337-351 (2009).
50. Lyons, S.M., Xu, W., Medford, J. & Prasad, A. Loads bias genetic and signaling switches in synthetic and natural systems. *PLoS Comput. Biol.* **10**, e1003533 (2014).

4

Antibody-controlled actuation of DNA-based molecular circuits

Abstract DNA nanotechnology has emerged as a versatile method for the construction of molecular nanodevices and complex reaction networks with sophisticated signal integration, processing and actuation properties. However, the actuation of these nanostructures and circuits mostly relies on DNA-based inputs, limiting their application in synthetic biology and molecular diagnostics. Here we expand the scope of DNA-based molecular programming by introducing a generic approach enabling the use of antibodies as input for DNA-based computing. The strategy, antibody-templated strand exchange (ATSE), involves the bivalent structure of antibodies as a template to stimulate DNA strand exchange thermodynamically and kinetically, resulting in a unique output strand as an input for DNA computing. Experiments, performed by W. Engelen, showed the successful implementation of the antibody-templated strand exchange (ATSE) reaction. In order to obtain a fundamental understanding of the ATSE reaction we here develop a comprehensive model that describes the kinetics of the ATSE system as a function of toehold length, thermodynamics and kinetics of antibody–epitope binding and concentration of reactants.

Part of the work in this chapter has been published in:
Wouter Engelen, Lenny H.H. Meijer, Bram Somers, Tom F.A. de Greef and Maarten Merkx – Nature Communications, **2017**, 8, 14473

4.1 Introduction

The synthetic accessibility and predictable Watson-Crick base pairing makes DNA a versatile building block for a broad range of applications in bionanotechnology. Examples range from the bottom-up construction of 3-dimensional nanostructures for the delivery of cargo[1] to molecular walkers,[2,3] motors[4,5] and complex DNA-based molecular circuits.[6-13] The advantage of DNA-based molecular nanostructures and circuits relies on their ability to sense and act at a molecular level with biological systems.[14-18] Moreover, autonomous DNA-based molecular circuits are potentially useful in theranostic devices as they translate a specific input signal to a biological activity according to a predefined algorithm.[19] Some examples of the downstream actuation of proteins by a DNA-based upstream circuit have been reported such as the activation of a split-luciferase[20] or the release of an antibody[21] by DNA-based Boolean logic operations, or the control of β-lactamase and a luciferase-based actuator by an upstream bistable switch.[22] However, with the exception of a few protein-binding aptamers,[19,23] the upstream actuation of DNA-based circuits relies on DNA-based input triggers. Here, we expand the scope of DNA-based molecular programming by developing a generic approach to use antibodies as inputs for DNA-based computing. Antibodies constitute regions which are highly specific and, therefore, are excellent biomarkers for infectious and autoimmune diseases. Additionally, they have proven to be useful as therapeutic agents.[24,25] The design strategy of our molecular system relies on DNA strand exchange[26] of peptide-functionalized oligonucleotides promoted by the bivalent architecture of antibodies as a template, resulting in a specific DNA output sequence. While experiments, performed by W. Engelen, demonstrate the efficiency and genericity of the antibody-templated strand exchange (ATSE) reaction, a kinetic model is required to obtain insights in kinetics and thermodynamics of the involved reaction steps. Here, we present a detailed theoretical characterization of this antibody-templated strand exchange reaction which describes the kinetics and thermodynamics of the ATSE system and is used to find relevant concentrations of reactants. The model provides a fundamental understanding of the ATSE reaction and is used to find optimal concentration regimes and to study the effect of thermodynamics and kinetics of antibody–epitope binding.

4.2 Antibody-templated strand exchange reactions

The mechanism of the antibody-templated toehold-mediated strand exchange reaction is shown in Figure 4.1A. The ATSE module comprises a partial duplex (**BO**) containing a short single-stranded overhang region, i.e. toehold (*T*),[26] and an invading strand (**I**). Conjugation of antibody-specific peptide epitopes to the 3′-ends of **B** and **I**, allows binding of **BO** and **I** to their target antibody. Binding of **I** to the toehold region of **BO** is followed by the displacement of the output strand (**O**). In absence of antibody this reaction is thermodynamically unfavourable as the number of base pairs in **BI** is lower than in **BO** and, hence, no output is produced. However, in presence of antibody the toehold exchange reaction is thermodynamically favourable as the product **BI** forms a bivalent interaction with the antibody, which has been shown to form a 1:1 complex with their target antibody with a 500-fold increase in affinity compared to the monovalent peptide-antibody interaction.[21,27] Moreover, the colocalization of **BI** and **O** at the antibody increases their effective concentrations and, thereby, enhances the rate of the exchange reaction.

The ATSE reaction was implemented by our experimental partners using a monoclonal antibody targeting the HA-tag, which is a peptide derived from the human influenza virus hemagglutinin protein. To follow the reaction over time the output strand **O** was measured by a reporter duplex (**Rep**) which releases, via toehold-mediated strand displacement (TMSD), a fluorescently labelled oligonucleotide. Importantly, to find the regime where background is minimal and the initiation of the ATSE reaction is fast the length of the toehold was systematically increased from 0 to 6 nucleotides (nt). Furthermore, the DNA strands were designed such that the product **BI** contains 24 basepairs. From Figure 4.1B it can be observed that in the absence of antibody the signal is minimal up to a toehold length of 3 nt. However, increasing the toehold beyond 3 nt drastically enhances the background reaction. In the presence of anti-HA antibody there is a significant increase in fluorescence even for a 1 nt toehold. Moreover, the strand exchange reaction rate is enhanced with increasing toehold length. In order to find the optimal toehold length, the apparent first-order rate constants for the ATSE reaction as a function of toehold length were determined in the presence and absence of anti-HA antibody (Figure 4.1C). While the increase of the apparent rate constant of the background is relatively low up to a toehold of 3 nt the increase of the apparent first order rate of the ATSE reaction ceases beyond 3 nt. Dividing the antibody-templated apparent

rate constant by the apparent rate constant of the background reaction (Figure 4.1D) gives a maximal signal-to-background ratio (S/B ratio) of ~100 using a toehold length of 3 nt.

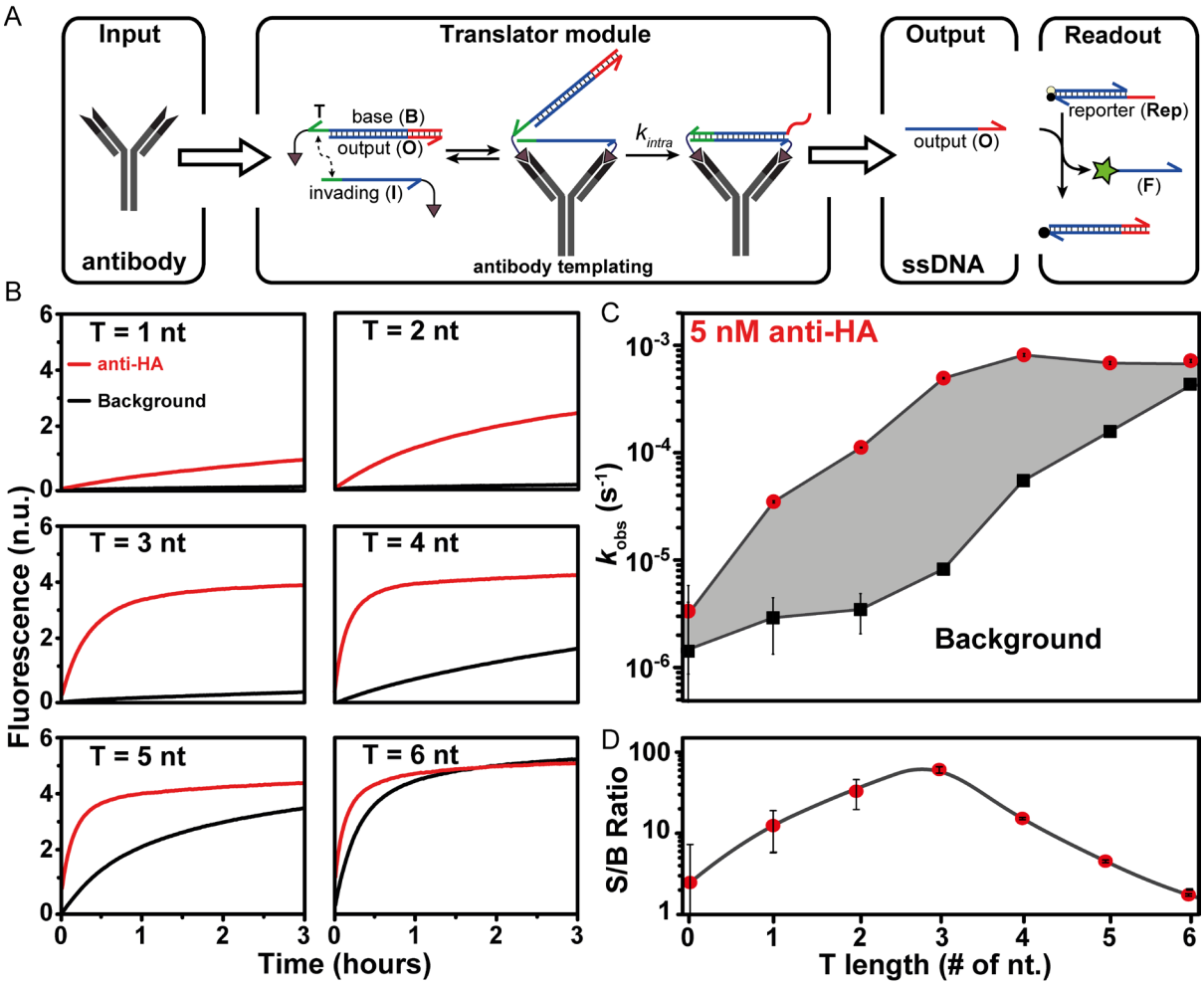

Figure 4.1 : Antibody-templated strand exchange enables the translation of an antibody to an output DNA strand. A) The design principle of the ATSE reaction in which toehold-mediated DNA strand exchange is promoted in presence of antibody by colocalization of the reactants BO and I resulting in a stable intramolecular bivalent complex and the release of the output strand (O). O is measured by a reporter duplex (Rep), which releases a fluorescently labeled oligonucleotide upon binding of O. In absence of the antibody strand exchange is unfavourable and the output strand (O) remains hybridized to the peptide-functionalized base strand (B). B) Results of experiments which were performed in the absence (black) and presence of anti-HA antibody (red) for varying toehold length (*T*). One normalized unit (n.u.) represents the fluorescence generated by Rep from 1 nM O. C) Apparent first-order rate constants (k_{obs}) as a function of *T* obtained from fitting a single exponential to the experimental traces in (B). D) Signal to background ratios as a function of *T* calculated by dividing the first-order rate constants in presence of antibody by the background rate constants. The experiments were conducted by mixing BO (5.5 nM), antibody (5 nM) and Reporter duplex (Rep, 10 nM) in TE/Mg^{2+}supplemented with 1 mg ml^{-1} BSA and allowed to equilibrate for 1 h at 28 °C. Finally, the ATSE reaction was induced by the addition of I (5 nM) and fluorescence intensities were recorded with a platereader for 3 hours at 28 °C. Error bars represent the standard error of k_{obs} obtained from the Fisher information matrix.

4.3 ODE model of the ATSE module

To provide a thorough understanding of the critical parameters that determine the performance of the ATSE reaction, we constructed a mechanistic kinetic model consisting of a set of ordinary differential equations (ODEs). The model describes the time-dependent concentrations of all start, intermediate and end products of the antibody-templated strand exchange reaction. Figure 4.2 shows the reactions on which the ODE model is based starting from the two different peptide-DNA conjugates **BO** and **I** carrying the same peptide-epitope and a bivalent antibody **Ab**. Binding of the peptide-DNA conjugates to the antibody results in intramolecular strand displacement and the release of DNA strand **O**, which binds to a partial reporter duplex **F·Q** (**Rep**) releasing fluorescent oligonucleotide **F** as a result of strand displacement by output strand **O**.

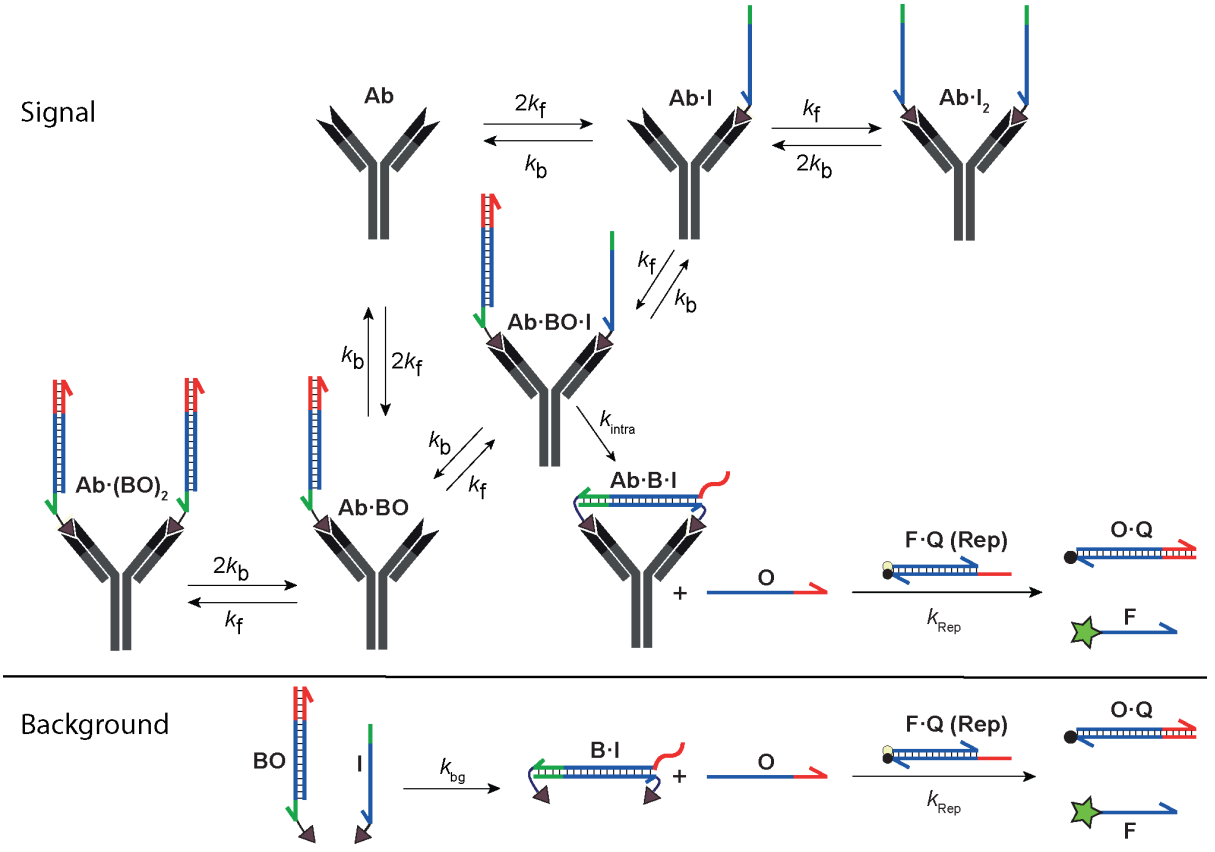

Figure 4.2: Overview of reactions in the theoretical model in the presence of antibody (signal) and absence of antibody (background).

To obtain an accurate model, most of the kinetic parameters were determined in separate experiments (Table 4.1),[28] including the association rate constant (k_f) for the binding of peptide-DNA conjugates to the anti-HA antibody and the forward rate constant (k_{rep}) of the toehold-mediated strand displacement of the reporter complex **F·Q** with ssDNA **O**. The

dissociation rate constant k_b was calculated from the association rate constant (k_a) and the dissociation equilibrium constant of peptide-DNA conjugates with the anti-HA antibody (K_d), which was also obtained independently. Moreover, the forward rate of the background reaction (k_{bg}) and the rate constant for the antibody-templated intramolecular toehold-mediated strand exchange reaction (k_{intra}) were determined as a function of toehold length as described vide infra.

Determination of the forward rate constant of the background reaction (k_{bg})

To determine the forward rate constant (k_{bg}) of the background reaction the experiment as shown in Figure 4.3A was performed. For each toehold length the fluorescence intensity was measurement in time in duplo and the mean was used for further analysis (Figure 4.3B).

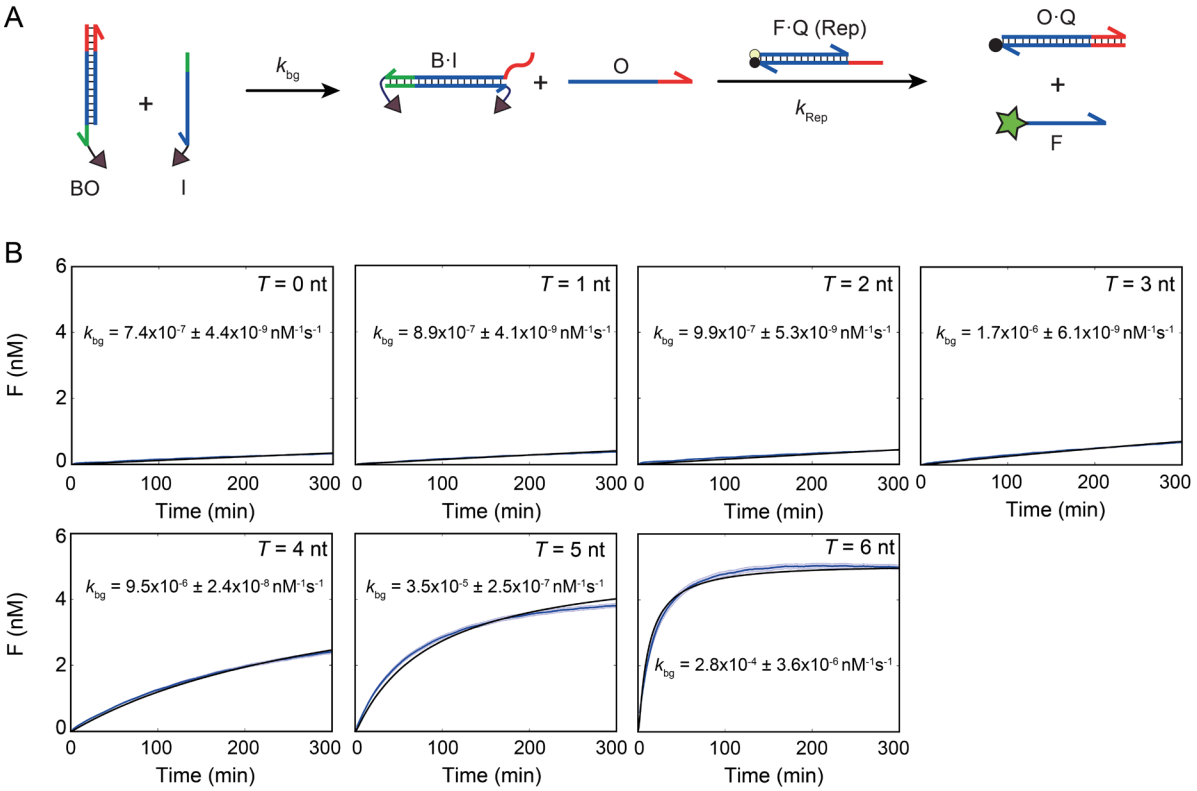

Figure 4.3: A) Schematic representation of the experiment performed to determine the forward rate constant of the background reaction. Peptide-DNA conjugate **I** can bind to a toehold on duplex **BO** and displace strand **O**. This reaction is assumed to be irreversible. DNA strand **O** can bind to reporter duplex **F·Q** and displace strand **F**, resulting in an increase in fluorescence. B) Background strand exchange reaction (blue) for the ATSE reaction components in the absence of antibody for a range of toehold lengths. The shaded area represents the standard error of the mean of duplicate experiments. Non-linear least-squares optimization of the data using the ODE model depicted in Equation 4.1 was performed (black) to obtain the forward rate constant of the background reaction (k_{bg}). Experiments were performed with 5.5 nM **BO**, 5 nM **I** and 10 nM **F·Q**.

First, the raw data was subtracted by a negative control where the **BO** duplexes were omitted. Subsequently, the fluorescence was converted to concentration of free oligonucleotide **F** using a control experiment in which 5.5 nM of **O** was mixed with 10 nM of **F·Q**. The fluorescence after completion of this reaction was used to calculate the conversion factor for fluorescence intensity to concentration of free **F**. A kinetic model was developed to characterize the kinetics of the background reaction:

$$\frac{d[BO]}{dt} = -k_{bg}[BO][I] \tag{4.1a}$$

$$\frac{d[I]}{dt} = -k_{bg}[BO][I] \tag{4.1b}$$

$$\frac{d[O]}{dt} = k_{bg}[BO][I] - k_{rep}[F \cdot Q][O] \tag{4.1c}$$

$$\frac{d[B \cdot I]}{dt} = k_{bg}[BO][I] \tag{4.1d}$$

$$\frac{d[F \cdot Q]}{dt} = -k_{rep}[F \cdot Q][O] \tag{4.1e}$$

$$\frac{d[O \cdot Q]}{dt} = k_{rep}[F \cdot Q][O] \tag{4.1f}$$

$$\frac{d[F]}{dt} = k_{rep}[F \cdot Q][O] \tag{4.1g}$$

To obtain the forward rate constant of the background reaction (k_{bg}) as function of toehold length non-linear least squares optimization of the ODE model in Equation 4.1 to the experimental data depicted in Figure 4.3B was performed with k_{rep} fixed to its experimentally determined value, using the Matlab routine *lsqnonlin* with a subspace trust-region method based on the interior-reflective Newton method. The lower bounds of the 95% confidence intervals and asymptotic standard errors were determined using the observed Fisher information matrix. Individual rate constants were obtained for the different toehold lengths (Table 4.1).

Determination of the intramolecular rate constant of cyclization of bivalent antibody with Peptide-DNA conjugates (k_{intra})

The set of ODE's describing the dynamics of the complete system was obtained by deriving an equation for each of the species in the network using mass-action kinetics. These equations were implemented in Matlab and solved numerically in time using parameters as in Table 4.1, resulting in a temporal evolution of all species in the system. The differential equations of the theoretical model were deduced from the reaction mechanisms shown in Figure 4.2 using the following assumptions:

1. In order to experimentally determine the association rate constant of binding of the peptide to the anti-HA antibody (k_f) and the thermodynamic dissociation constant of peptide-antibody binding (K_d) a fluorescently labeled peptide was used allowing kinetic studies by fluorescence and polarization assays.[28] In the mathematical model the k_f and k_b (calculated from k_f and K_d) of peptide-DNA conjugates to anti-HA antibody are assumed to be the same as the kinetics of binding and unbinding of fluorescently labeled peptide-epitopes to the antibody. Furthermore, a statistical factor is used when a peptide-oligonucleotide conjugate has two possibilities to bind or dissociate from the antibody.
2. The formation of the cyclic bivalent **Ab·B·I** is assumed to be irreversible on the time scale of the experiment. Previous work has shown that the dissociation rate for this very stable bivalent interaction is very low, requiring overnight equilibration for competition experiments.[27]
3. The cyclization of the antibody with the two heterogeneous peptide-DNA conjugates is described using an intramolecular rate constant (k_{intra}).
4. The toehold-mediated strand displacement of **F** from the reporter complex **F·Q** by DNA strand **O** is an irreversible reaction since the **O·Q** complex does not contain a toehold. The reaction is described using the bimolecular approximation developed by Zhang and Winfree.[26]
5. The background reaction as shown in Figure 4.3 is described using the bimolecular approximation and is assumed to be effectively irreversible as DNA strand **O** is sequestered by an excess of reporter complex **F·Q**.
6. Importantly, the background reaction can also take place in the presence of the antibody. Figure 4.4A shows all possible background reactions on the antibody. If this reaction happens it is assumed cyclization takes place, irrespective whether the other antigen binding site is occupied or not. In the mathematical model these multistep reactions are

coarse-grained into one step using a single rate constant k_{bg} and assuming that cyclization is relatively fast and irreversible (Figure 4.4B), irrespective whether the other antigen binding site is occupied or not. Notably, this cyclization results from intramolecular binding of a second peptide epitope and is therefore relatively fast, while cyclization in Figure 4.2 results from strand displacement. This background reaction with the peptide-DNA conjugates bound to the antibody effectively results in a decrease in free peptide-DNA conjugates **BO** and **I** and antibody as well as an increase in DNA strand **O** and cyclized complex (**Ab·B·I**). Therefore, these reactions are included in the mathematical model in the ODE's for free peptide-DNA conjugates **BO** and **I** and free **Ab** (Equation 4.10a-c).

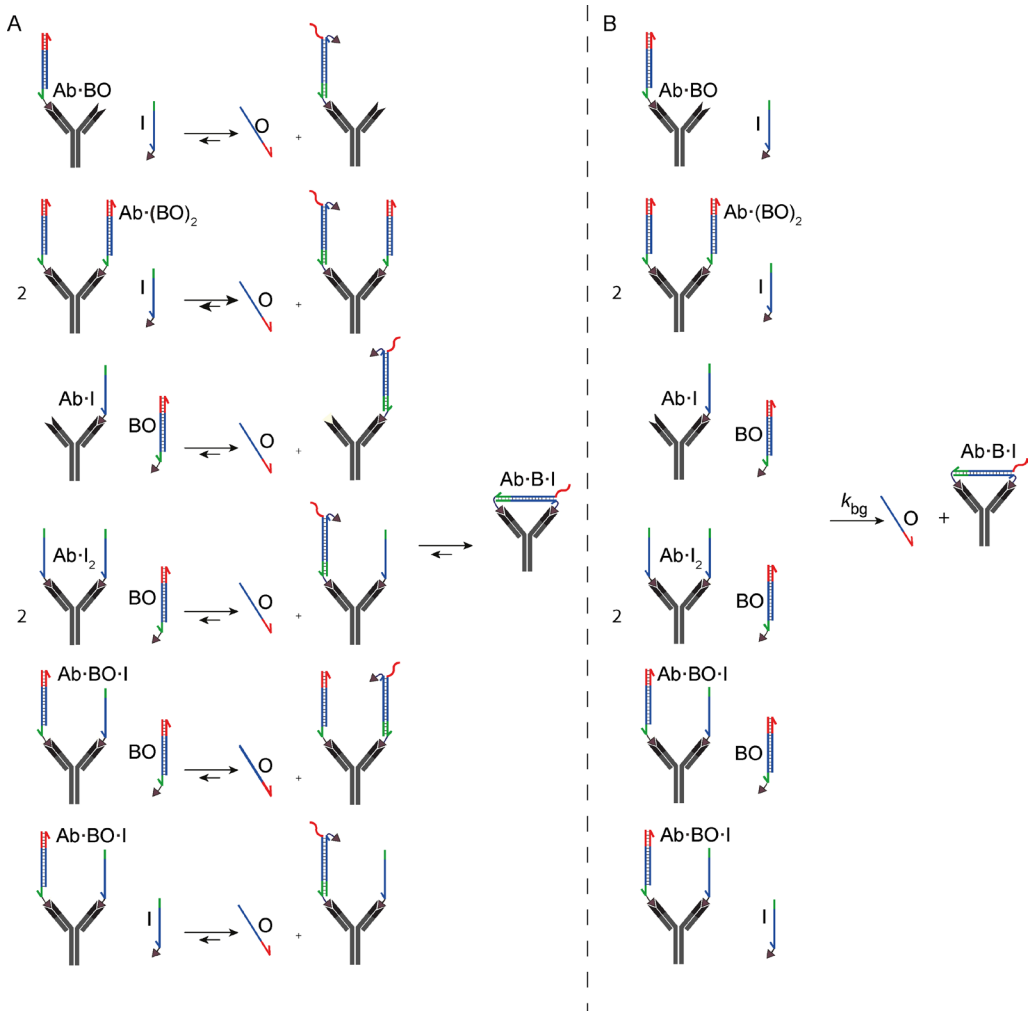

Figure 4.4: Additional background reactions of various antibody-complexes that were also included in the mathematical model. A) Schematic illustration of all possible background reactions at the antibody. A factor of two indicates this reaction has two possibilities to happen. B) All these background reactions are included in the mathematical model as a single step with the forward rate constant of the background (k_{bg}) being the rate limiting step.

7. Furthermore, the product of the background reaction (**B·I**), having two epitopes, is likely to bind to the antibody if there is a free antigen binding site available. Therefore, this reaction is also included in the model. Figure 4.5A shows the full reaction scheme, while in the kinetic model we use the simplified scheme in Figure 4.5B which is based on several assumptions. If an epitope of **B·I** binds to an antigen binding site of the antibody it is assumed cyclisation, caused by binding of the second epitope, is faster than dissociation of the peptide-DNA conjugate **B·I**. Furthermore, it is assumed this cyclisation is relatively fast and irreversible, irrespective whether the other antigen binding site is occupied or not. Therefore, the reactions in Figure 4.5A are coarse-grained into one step (Figure 4.5B) with the association rate constant of a single peptide-DNA conjugate to the antibody as the rate limiting step. The statistical factor of four is used because two epitopes can bind at two positions of the antibody, while a statistical factor of two is used when one of these positions is occupied.

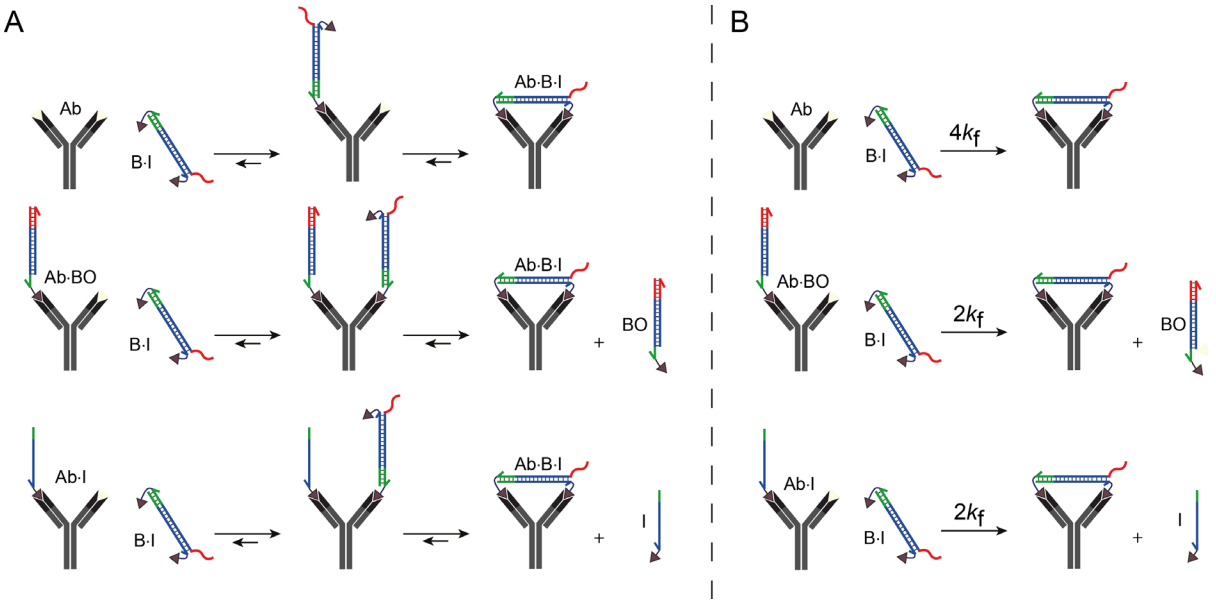

Figure 4.5: Background reaction product captures antibody. A) Illustration of the binding of peptide-DNA conjugate [**B·I**] to the antibody having at least one free antigen binding site, followed by cyclization. B) Illustration of the simplified reaction scheme which is used in the kinetic model.

Taking into account all these assumptions the dynamics of the system were obtained by deriving an ODE equation for each of the 14 species (Equation 4.10) in the network using the rate constants in Table 4.1.

$$\frac{d[Ab]}{dt} = k_b[Ab\cdot BO] - 2k_f[Ab][BO] + k_b[Ab\cdot I] - 2k_f[Ab][I] - k_{bg}([Ab\cdot BO][I] + 2[Ab\cdot(BO)_2][I] + [Ab\cdot I][BO] + 2[Ab\cdot I_2][BO]... + [Ab\cdot BO\cdot I][BO] + [Ab\cdot BO\cdot I][I]) - 4k_f[Ab][B\cdot I]; \quad (4.2a)$$

$$\frac{d[BO]}{dt} = k_b[Ab\cdot BO] - 2k_f[Ab][BO] + 2k_b[Ab\cdot(BO)_2] - k_f[Ab\cdot BO][BO] + k_b[Ab\cdot BO\cdot I] - k_f[Ab\cdot I][BO] - k_{bg}([BO][I] + [Ab\cdot BO][I] + 2[Ab\cdot(BO)_2][I] + [Ab\cdot I][BO]... + 2[Ab\cdot I_2][BO] + [Ab\cdot BO\cdot I][BO] + [Ab\cdot BO\cdot I][I]) + 2k_f[Ab\cdot BO][B\cdot I]; \quad (4.2b)$$

$$\frac{d[I]}{dt} = k_b[Ab\cdot I] - 2k_f[Ab][I] + 2k_b[Ab\cdot I_2] - k_f[Ab\cdot I][I] + k_b[Ab\cdot BO\cdot I] - k_f[Ab\cdot BO][I] - k_{bg}([BO][I] + [Ab\cdot BO][I] + 2[Ab\cdot(BO)_2][I] + [Ab\cdot I][BO]... + 2[Ab\cdot I_2][BO] + [Ab\cdot BO\cdot I][BO] + [Ab\cdot BO\cdot I][I]) + 2k_f[Ab\cdot I][B\cdot I]; \quad (4.2c)$$

$$\frac{d[Ab\cdot BO]}{dt} = -k_b[Ab\cdot BO] + 2k_f[Ab][BO] + 2k_b[Ab\cdot(BO)_2] - k_f[Ab\cdot BO][BO] + k_b[Ab\cdot BO\cdot I] - k_f[Ab\cdot BO][I]; \quad (4.2d)$$

$$\frac{d[Ab\cdot I]}{dt} = -k_b[Ab\cdot I] + 2k_f[Ab][I] + 2k_b[Ab\cdot I_2] - k_f[Ab\cdot I][I] + k_b[Ab\cdot BO\cdot I] - k_f[Ab\cdot I][BO]; \quad (4.2e)$$

$$\frac{d[Ab\cdot BO_2]}{dt} = -2k_b[Ab\cdot(BO)_2] + k_f[Ab\cdot BO][BO]; \quad (4.2f)$$

$$\frac{d[Ab\cdot I_2]}{dt} = -2k_b[Ab\cdot I_2] + k_f[Ab\cdot I][I]; \quad (4.2g)$$

$$\frac{d[Ab\cdot BO\cdot I]}{dt} = -2k_b[Ab\cdot BO\cdot I] + k_f[Ab\cdot BO][I] + k_f[Ab\cdot I][BO] - k_{intra}[Ab\cdot BO\cdot I]; \quad (4.2h)$$

$$\frac{d[Ab\cdot B\cdot I]}{dt} = k_{intra}[Ab\cdot BO\cdot I] + 4k_f[Ab][B\cdot I] + 2k_f[Ab\cdot BO][B\cdot I] + k_{bg}([Ab\cdot BO][I] + 2[Ab\cdot(BO)_2][I] + [Ab\cdot I][BO] + 2[Ab\cdot I_2][BO]... + [Ab\cdot BO\cdot I][BO] + [Ab\cdot BO\cdot I][I]) + 2k_f[Ab\cdot I][B\cdot I]; \quad (4.2i)$$

$$\frac{d[O]}{dt} = k_{intra}[Ab\cdot BO\cdot I] - k_{rep}[F\cdot Q][O] + k_{bg}([BO][I] + [Ab\cdot BO][I] + 2[Ab\cdot(BO)_2][I] + [Ab\cdot I][BO]... + 2[Ab\cdot I_2][BO] + [Ab\cdot BO\cdot I][BO] + [Ab\cdot BO\cdot I][I]); \quad (4.2j)$$

$$\frac{d[B\cdot I]}{dt} = k_{bg}[BO][I] - 4k_f[Ab][B\cdot I] - 2k_f[Ab\cdot BO][B\cdot I] - 2k_f[Ab\cdot I][B\cdot I]; \quad (4.2k)$$

$$\frac{d[F\cdot Q]}{dt} = -k_{rep}[F\cdot Q][O]; \quad \frac{d[O\cdot Q]}{dt} = k_{rep}[F\cdot Q][O]; \quad \frac{d[F]}{dt} = k_{rep}[F\cdot Q][O]; \quad (4.2l/m/n)$$

The only unknown kinetic parameter in the mathematical model is the rate constant of cyclization of bivalent anti-HA antibody with peptide-DNA conjugates (k_{intra}). An estimate of k_{intra} for each toehold length was obtained by performing non-linear least square analysis of the kinetic model using the experimental data of the complete system in presence of anti-HA antibody (Figure 4.6). The raw data of the experiments (performed in duplo) was subtracted by the fluorescence intensity of a control lacking **BO**. Subsequently, the fluorescence was converted to concentration of ssDNA **F** using a control experiment in which 5.5 nM of ssDNA **O** was mixed with 10 nM of reporter duplex (**F·Q**). The fluorescence after completion of the control experiment (subtracted by the fluorescence from the unreacted reporter complex) was used to calculate the conversion factor for fluorescence intensity to concentration of ssDNA **F**. To obtain the intramolecular rate constant of cyclization (k_{intra}) non-linear least squares optimization was performed (Figure 4.6) for each toehold length using Equations 4.10a-4.10n and the Matlab routine *lsqnonlin* with a subspace trust-region method based on the interior-reflective Newton method. The lower bounds of the 95% confidence intervals and asymptotic standard errors were determined using the observed Fisher information matrix. The concentration of antibody used in the non-linear least squares optimization was obtained experimentally from the ATSE reaction with a toehold of 3 nt, where it was assumed that the concentration of antibody was equal to the concentration of fluorescent product **F** after 300 min reaction. This reaction was chosen since the ATSE goes to complete conversion, whereas the contribution of the background reaction remains negligible. For a toehold length of 5 and 6 nucleotides, k_{intra} could not be determined reliably since the ATSE reaction at these toehold lengths is dominated by the background reaction.

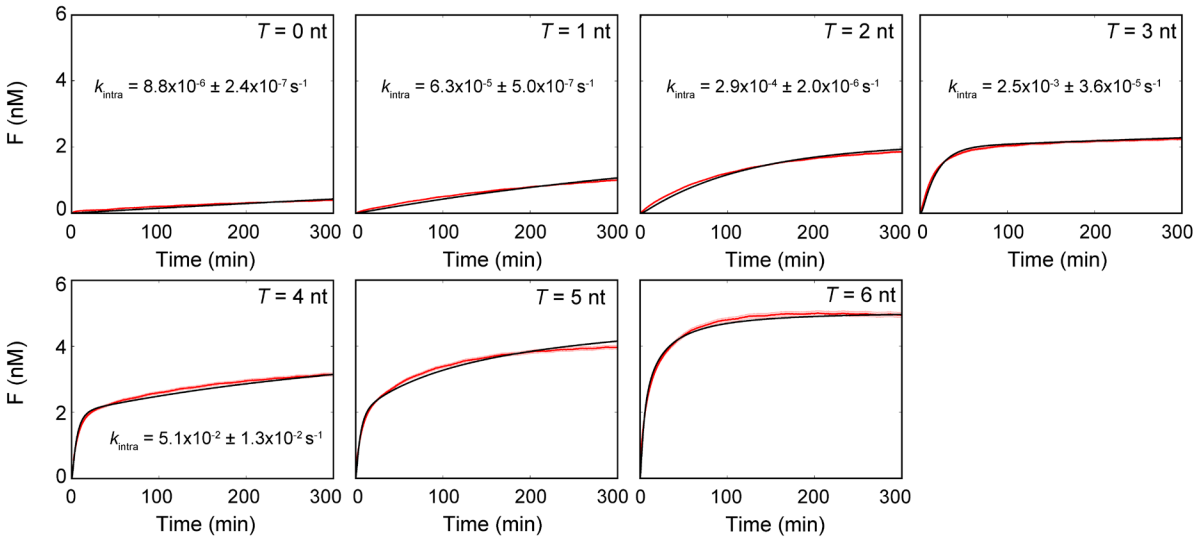

Figure 4.6: Experimental results of the system in presence of anti-HA antibody for a range of toehold lengths. The shaded area is the standard error of the mean of experiments performed in duplo. Non-linear least-squares optimization was performed (black) to obtain the rate constant of cyclisation via strand displacement (k_{intra}) using the differential equations of Table 4.1. Experiments were performed with 5.5 nM **BO**, 5 nM **I**, 2 nM **Ab** and 10 nM **FQ**.

Table 4.1: Overview of parameters used in mathematical model for which the values were obtained from non-linear least square analysis of experimental data.

Parameter	**Value**						
K_d **(nM)**	0.24						
k_f **(nM^{-1} s^{-1})**	1.2E-2						
k_{rep} **(nM^{-1} s^{-1})**	1.4E-3						
	Toehold length						
	0	***1***	***2***	***3***	***4***	***5***	***6***
k_{bg} **(nM^{-1} s^{-1})**	7.4E-07 ± 4.4E-09	8.9E-07 ± 4.1E-09	9.9E-07 ± 5.3E-09	1.7E-06 ± 6.1E-09	9.5E-06 ± 2.4E-08	3.5E-05 ± 2.5E-07	2.8E-04 ± 3.6E-06
k_{intra} **(s^{-1})**	8.8E-06 ± 2.4E-07	6.3E-05 ± 5.0E-07	2.9E-04 ± 2.0E-06	2.5E-03 ± 3.6E-05	5.1E-02 ± 1.3E-02	N.D.[a]	N.D.[a]

[a] Not determined. At a toehold length of 5 and 6 nucleotides the ATSE reaction is dominated by the background reaction. Therefore, one cannot reliably obtain k_{intra}.

4.3 Simulations

Kinetic simulations

Using the experimentally obtained kinetic parameters k_b, k_f, k_{rep}, k_{bg} and k_{intra}, we simulated the concentration of the individual reaction components as a function of time for the system with the optimal toehold length of 3 nucleotides. In the simulation shown in Figure 4.7, all the components of the ATSE reaction except **I** were premixed and allowed to reach thermodynamic equilibrium before the start of the reaction. At t=0 the ATSE reaction was initiated by the addition of 5 nM **I**. Figure 4.7A shows a decrease in species **I** and an increase in **BO** resulting from the addition of 5 nM **I** to the pre-equilibrated mixture of species **BO**, **Ab** and **F·Q**. This behavior is caused by competition of species **BO** and **I** for the same binding sites of specie **Ab**. Likewise, species **Ab·BO** and **Ab·(BO)$_2$** show a relatively fast initial decrease resulting from equilibration of binding of species **BO**, **I** and **Ab** after addition of species **I**. Next, a more gradual decrease results from cyclization. Furthermore, species **Ab·I**, **Ab·I$_2$** and **Ab·BO·I** show a relatively fast initial increase resulting from equilibrating of binding of species **BO**, **I** and **Ab** after addition of species **I**, followed by a more gradual decrease resulting from intramolecular cyclization. In Figure 4.7C and Figure 4.7F the time traces of the products of cyclization (**Ab·B·I** and **O**) are shown. Figure 4.7F shows that the amount of free output **O** increases in the first few minutes of the reaction, indicating that the anti-HA antibody (**Ab**) rapidly induces the toehold-mediated strand exchange reaction to form the intramolecular cyclic complex (**Ab·B·I**). Subsequently, **O** reacts rapidly with **Rep** in the downstream displacement reaction, establishing a low pseudo steady-state concentration of **O**. At this stage the increase in fluorescence closely mirrors the kinetics of the ATSE reaction as defined by the formation of the **Ab·B·I** complex. The analysis also shows that the background reaction only starts to contribute significantly to the fluorescence after 60 min, when the ATSE reaction has reached completion.

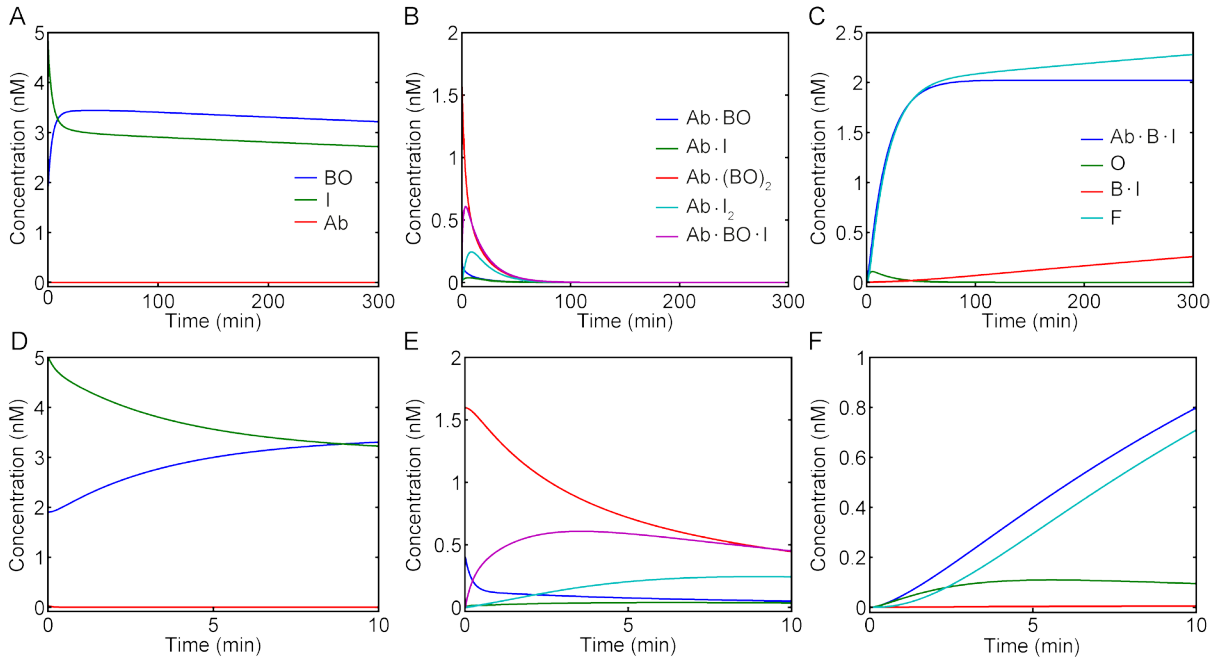

Figure 4.7: Simulation of the various species formed during the ATSE reaction. A-C) The time traces of the various species were simulated by solving Equations 4.10 numerically in time using Matlab with the kinetic parameters as shown in Table 4.1 for a toehold length of 3 nt. The simulations were performed with concentrations of 2 nM, 5.5 nM, 5 nM and 10 nM for the species **Ab, BO**, **I** and probe **F·Q** respectively, with species **BO**, **Ab** and **F·Q** being pre-equilibrated. D-F) The time traces of the species for the first ten minutes of the simulation.

Finding optimal conditions for the ATSE reaction

Importantly, the ODE model can also be used to determine the optimal conditions for the ATSE reaction by assessing the influence of both the oligonucleotides (**BO**, **I**) and antibody (**Ab**) concentrations. Figure 4.8A and Figure 4.8B show the amount of **F** formed at t=180 min for the background and antibody-templated reaction, respectively. As expected, the background increases proportional to increasing concentrations of **BO** and **I**, whereas the antibody-templated signal strongly depends on the concentrations of **BO**, **I** and **Ab**. The signal-to-background ratios (S/B, Figure 4.8C), obtained by dividing the fluorescence formed in the presence of antibody (S) by the fluorescence of the background reaction (B), shows a maximum at a concentration of **Ab**~K_d and low concentrations of **BO** and **I**. The latter is caused by the strong, linear dependence of the background reaction on the concentration of **BO** and **I**. However, since the absolute increase in fluorescence becomes increasingly difficult to distinguish above the background fluorescence for low concentrations of **BO** and **I**, we defined an empirical formula for the optimal ATSE conditions as the product of the signal-to-background ratio (S/B) and the absolute dynamic range (S–B; Figure 4.8D). The latter formula shows optimal performance at stoichiometric concentrations of antibody and

oligonucleotides, but the ATSE reaction is relatively robust and antibody can also be clearly detected above background at suboptimal stoichometries of antibody and oligonucleotides.

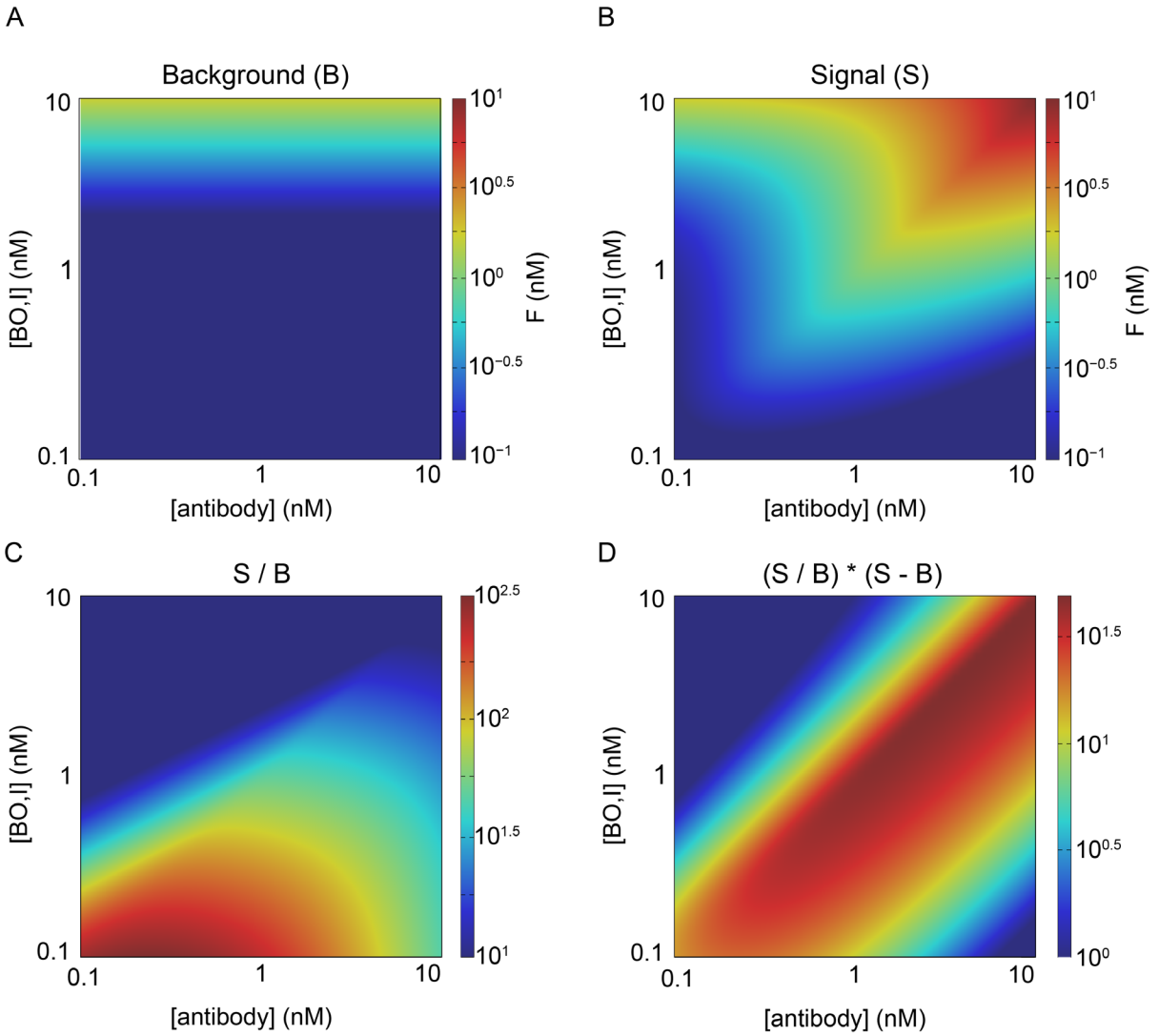

Figure 4.8: A) Simulated background fluorescence as a function of initial [**BO**, **I**] and [**Ab**] after 3 h. B) Simulated fluorescence of the anti-HA antibody-templated toehold-mediated strand exchange reaction as a function of initial [**BO**, **I**] and [**Ab**] after 3 h. C) Simulated signal-to-background (S/B) ratio as a function of initial [**BO**, **I**] and [**Ab**] after 3 h. D) Simulated product of signal-to-background (S/B) ratio and dynamic range (S–B) as a function of initial [**BO**, **I**] and [**Ab**] after 3 h, yielding an empirical estimation of optimal initial conditions. Results were obtained by solving Equations 4.10 numerically in time with parameters values as shown in Table 4.1.

The effect of the association and dissociation rate constant of epitope-antibody binding

The ATSE reaction is generalizable to any antibody for which an epitope can be attached to a DNA-strand. However, the kinetics and thermodynamics of antibody-epitope binding vary among antibody-epitope pairs. In order to study the effect of the kinetics (k_f, k_b) and thermodynamics (K_d) of the antibody-peptide interaction on the performance of the ATSE

reaction we simulate the empirical estimation as a function of reactant concentrations and association (k_f) and dissociation (k_b) rate constants, shown in Figure 4.9. The heat map in the center is obtained from simulations with parameters as in Table 4.1, i.e. the heat map is identical to the heat map in Figure 4.8D. From the results it can be observed that a decrease in k_f causes a shift of the optimal concentration regime to higher stoichiometric concentrations of reactants. This is followed from a shift of the optimal S/B ratio towards concentrations close to the K_d (= k_b/k_f). Likewise, a decrease in k_b results in a shift of optimal concentration regime to lower stoichiometric concentrations of **BO**, **I** and **Ab**. However, when the kinetics are too slow the shift in concentration of reactants for which the system performs optimal does not reach the value of K_d as shown clearly in Figure 4.9 by the heat maps on top. While a decreased k_b, and thereby an enhanced binding affinity of the antibody and the epitope, results in an increased concentration of **BO** and **I** bound to **Ab**, the exchange rate of **BO** and **I** at **Ab** is decreased. This leads to an increased time to obtain the right configuration of **BO**, **I** and **Ab** required to form the cyclic product and, hence, a decreased S/B ratio. This effect is not observed for relatively high values of k_f as the reaction is complete within 3 hours, even if the value of k_b is low. Furthermore, with increasing k_f and k_b the optimal concentration regime increasingly broadens to sub stoichiometric concentrations of reactants. In other words, with relatively fast exchange rates of **BO** and **I** at **Ab** an increasing concentration of **Ab** beyond the concentrations of **BO** and **I** gives a constant value of S as the overall reaction rate is not limited by k_b and k_f. However, with increasing **Ab** beyond the concentrations of **BO** and **I** the chance to obtain the right configuration of **BO**, **I** and **Ab** is decreasing. Hence, at a given concentration of **Ab** this effect starts to dominate and limits the production rate of S. In summary, when the kinetics are relatively fast, the minimal stoichiometric concentrations of reactants required for optimal performance are mainly determined by the thermodynamic dissociation constant of antibody-epitope binding while the range of sub stoichiometric concentrations of **BO, I** and **Ab** for which the system keeps its optimal performance is determined by the kinetics of antibody-epitope binding.

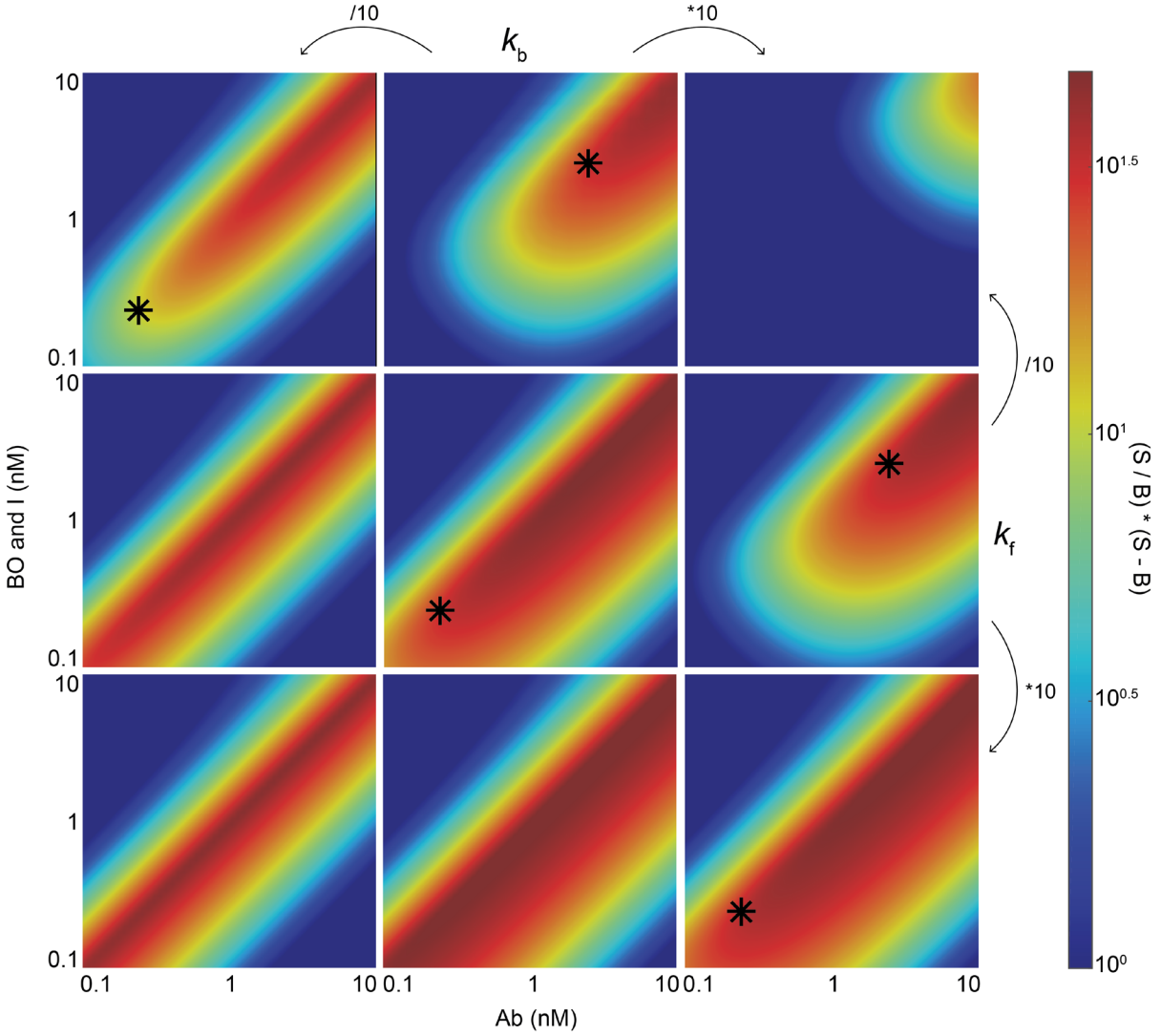

Figure 4.9: Simulated product of signal-to-background (S/B) ratio and dynamic range (S–B) as a function of initial concentrations of **Ab**, **BO** and **I** and association and dissociation rate constant of epitope-antibody binding. The black stars show the value of the thermodynamic dissociation constant (K_d) of antibody-epitope binding. Results were obtained by solving Equations 4.10 numerically in time with parameter values of k_{rep}, k_{bg} and k_{intra} as shown in Table 4.1 for a toehold length of 3. The heat map in the center is simulated with a value of k_f as shown in Table 4.1 and k_b calculated from k_f and K_d.

4.4 Discussion

Our work shows that antibody-templated strand exchange (ATSE) enables the translation of an antibody to a unique output strand. In presence of an antibody strand exchange is promoted thermodynamically by the formation of a 1:1 cyclic complex of the peptide-dsDNA with the bivalent antibody. Furthermore, colocalization enhances the effective concentration of reactions and, thereby, increases the reaction rate. The ATSE reaction allows the use of antibodies as input for DNA-based molecular computing and the actuation of DNA-based architectures, as was validated experimentally.[28] Here, by

developing a theoretical model, we obtained a fundamental understanding of the involved reaction steps and kinetics of the ATSE reaction. We found that the system performs optimal at stoichiometric concentrations of antibody and oligonucleotides, but the ATSE reaction is relatively robust and antibody can also be clearly detected above background at suboptimal stoichiometry of antibody and oligonucleotides. Moreover, results of simulations show the ATSE reaction performs well for varying association and dissociation rates of antibody-peptide binding showing the genericity of the ATSE reaction which in principle can be applied to any antibody for which the epitope is known. This was also validated by the experimental implementation of the ATSE reaction with the anti-HIV1-p17 antibody as input, using peptide epitopes derived from the p17 coat protein of the HIV1 virus that bind with a monovalent K_d of 16 nM.[28] The kinetic model describing the ATSE can also be applied to other molecular systems in which bivalent interactions dominate the performance of the molecular system. For example, Ricci and coworkers developed a DNA-based nanomachine generating an output strand in presence of an antibody using a different strategy than ours.[29] The DNA nanomachine consists of a DNA strand forming a clamp-like structure carrying a cargo strand by Watson-Crick base pairs and Hoogsteen interactions. The DNA-based clamp is conjugated at each end with an antigen. Binding of these antigens to the bivalent antibody is energetically more favourable and disrupts the Hoogsteen interactions resulting in the release of the cargo strand. Likewise to the work presented here, the theoretical model could be applied to obtain insights in the thermodynamics and kinetics of the DNA-nanomachine. Furthermore, the theoretical model could predict the optimal concentration regime of reactants for any antibody-epitope pair which is highly valuable for the experimental implementation of new antibody-epitope pairs. Additionally, such mathematical models can be used to find limiting conditions in the molecular system such as the minimal binding affinity required to obtain both a sufficient signal/background ratio and a high dynamic range for concentrations of reactants experimentally realizable. Hence, this work provides an entry point for the quantitative insights into DNA-based circuits generating an output by making use of the bivalent character of the input and paves the way for the optimal use of such systems.

4.5 References

1. Douglas, S.M., Bachelet, I. & Church, G.M. A logic-gated nanorobot for targeted transport of molecular payloads. *Science* **335**, 831-834 (2012).
2. Gu, H., Chao, J., Xiao, S.-J. & Seeman, N.C. A proximity-based programmable DNA nanoscale assembly line. *Nature* **465**, 202-205 (2010).
3. Lund, K. et al. Molecular robots guided by prescriptive landscapes. *Nature* **465**, 206-210 (2010).
4. Wickham, S.F.J. et al. A DNA-based molecular motor that can navigate a network of tracks. *Nat. Nanotechnol.* **7**, 169-173 (2012).
5. Yurke, B., Turberfield, A.J., Mills, A.P., Simmel, F.C. & Neumann, J.L. A DNA-fuelled molecular machine made of DNA. *Nature* **406**, 605-608 (2000).
6. Stojanovic, M.N., Mitchell, T.E. & Stefanovic, D. Deoxyribozyme-based logic gates. *J. Am. Chem. Soc.* **124**, 3555-3561 (2002).
7. Han, D. et al. A cascade reaction network mimicking the basic functional steps of adaptive immune response. *Nat. Chem.* **7**, 835-841 (2015).
8. Qian, L., Winfree, E. & Bruck, J. Neural network computation with DNA strand displacement cascades. *Nature* **475**, 368-372 (2011).
9. Zhang, D.Y., Turberfield, A.J., Yurke, B. & Winfree, E. Engineering entropy-driven reactions and networks catalyzed by DNA. *Science* **318**, 1121-1125 (2007).
10. Seelig, G., Soloveichik, D., Zhang, D.Y. & Winfree, E. Enzyme-free nucleic acid logic circuits. *Science* **314**, 1585-1588 (2006).
11. Kim, J., White, K.S. & Winfree, E. Construction of an in vitro bistable circuit from synthetic transcriptional switches. *Mol. Syst. Biol.* **2**, 68-68 (2006).
12. Montagne, K., Plasson, R., Sakai, Y., Fujii, T. & Rondelez, Y. Programming an in vitro DNA oscillator using a molecular networking strategy. *Mol. Syst. Biol.* **7**, 466 (2011).
13. Qian, L. & Winfree, E. Scaling up digital circuit computation with DNA strand displacement cascades. *Science* **332**, 1196-1201 (2011).
14. Modi, S., Nizak, C., Surana, S., Halder, S. & Krishnan, Y. Two DNA nanomachines map pH changes along intersecting endocytic pathways inside the same cell. *Nat. Nanotechnol.* **8**, 459-467 (2013).
15. Zhu, G. et al. Self-assembled, aptamer-tethered DNA nanotrains for targeted transport of molecular drugs in cancer theranostics. *Proc. Natl. Acad. Sci. U.S.A.* **110**, 7998-8003 (2013).
16. Rudchenko, M. et al. Autonomous molecular cascades for evaluation of cell surfaces. *Nat. Nanotechnol.* **8**, 580-586 (2013).
17. Groves, B. et al. Computing in mammalian cells with nucleic acid strand exchange. *Nat. Nanotechnol.* **11**, 287-294 (2016).
18. Chen, Y.-J., Groves, B., Muscat, R.A. & Seelig, G. DNA nanotechnology from the test tube to the cell. *Nat. Nanotechnol.* **10**, 748-760 (2015).
19. Han, D. et al. A logical molecular circuit for programmable and autonomous regulation of protein activity using DNA aptamer–protein interactions. *J. Am. Chem. Soc.* **134**, 20797-20804 (2012).
20. Prokup, A. & Deiters, A. Interfacing synthetic DNA logic operations with protein outputs. *Angew. Chem. Int. Ed. Engl.* **53**, 13192-13195 (2014).
21. Janssen, B.M.G., van Rosmalen, M., van Beek, L. & Merkx, M. Antibody activation using DNA-based logic gates. *Angew. Chem. Int. Ed. Engl.* **54**, 2530-2533 (2015).
22. Meijer, L.H.H. et al. Hierarchical control of enzymatic actuators using DNA-based switchable memories. *Nature Commun.* **8**, 1117 (2017).
23. Li, F. et al. Dynamic DNA assemblies mediated by binding-induced DNA strand displacement. *J. Am. Chem. Soc.* **135**, 2443-2446 (2013).
24. Leavy, O. Therapeutic antibodies: past, present and future. *Nat. Rev. Immunol.* **10**, 297-297 (2010).
25. Weiner, L.M., Dhodapkar, M.V. & Ferrone, S. Monoclonal antibodies for cancer immunotherapy. *Lancet* **373**, 1033-1040 (2009).
26. Zhang, D.Y. & Winfree, E. Control of DNA strand displacement kinetics using toehold exchange. *J. Am. Chem. Soc.* **131**, 17303-17314 (2009).

27. Janssen, B. et al. Reversible blocking of antibodies using bivalent peptide-DNA conjugates allows protease-activatable targeting. *Chem. Sci.* **4**, 1442–1450 (2013).
28. Engelen, W., Meijer, L.H.H., Somers, B., de Greef, T.F.A. & Merkx, M. Antibody-controlled actuation of DNA-based molecular circuits. *Nat. Commun.* **8**, 14473 (2017).
29. Ranallo, S., Prévost-Tremblay, C., Idili, A., Vallée-Bélisle, A. & Ricci, F. Antibody-powered nucleic acid release using a DNA-based nanomachine. *Nat. Commun.* **8**, 15150 (2017).

5

Noise in cell-free gene expression

Abstract Gene expression varies among identical cells resulting from the stochastic nature of collisions between reactants, which are present at low numbers. However, it is unknown how the physical environment contributes to the variation in gene expression level. Our experimental partners developed a robust method to quantify the variation in gene expression *in vitro* in picoliter droplets. To support the experimental findings and to obtain a detailed characterization of the *in vitro* system, we here develop two independent theoretical models including a Gillespie based model and a particle-based reaction-diffusion model. We study the variation in cell-free gene expression as a function of copy number and macromolecular crowding. We find that decreasing diffusion coefficients and the formation of heterogeneous micro-environments caused by macromolecular crowding enhance uncorrelated noise in gene expression

The work in this chapter has been partly published in:
Maike M.K. Hansen, Lenny H.H. Meijer, Evan Spruijt, Roel J.M. Maas, Marta Ventosa Roquelles, Joost Groen, Hans A. Heus and Wilhelm T.S. Huck – Nature Nanotechnology, **2016**, 11, 191

5.1 Introduction

Variation in gene expression is ubiquitous in all living cells and results from genetic and environmental differences. However, even genetically identical cells which have the same history and environmental exposure exhibit a remarkable variation in gene expression.[1] Variation, or noise, in gene expression has been extensively studied in prokaryotes and eukaryotes[2] as well as in stem cells,[3] cancer cells[4] and cells expressing viruses.[5] While biochemical reaction networks inside cells involve many different biomolecules, the concentration of each biomolecule is rather low. Hence, a degree of randomness in these reaction networks is expected and it is generally accepted that variation in gene expression results from the low number of reactants together with the stochastic nature of molecular collisions by diffusion.[6-9] However, model systems of biochemical reactions often involve high concentrations of reactants in a dilute environment. Besides, while the cell's interior is an inhomogeneous crowded environment macromolecular crowding is often ignored in model systems of biochemical reactions. For example ~30% of the cell volume of bacteria is occupied by macromolecules resulting in highly reduced diffusion.[10,11] It has been shown that macromolecular crowding can lead to a heterogeneous environment due to limited diffusion of mRNA molecules.[12] Besides decreasing the diffusion of molecules,[13] macromolecular crowding has been shown to affect the reaction rates and dynamics of cellular processes.[14-16] Most studies thus far have dealt with either the quantification of noise[17] or how cells exploit or suppress noise.[2,18] It has been shown *in silico* using Green's function reaction dynamics[19] that diffusivity plays a role in gene expression noise. However, the explicit effect of macromolecular crowding on the variation in gene expression has not been studied *in silico*. Furthermore, no experimental work has estimated the magnitude of the effect of cellular composition or crowded environment within a cell-sized compartment on the noise in biochemical reactions.

In collaboration with our experimental partners, Dr. Maike Hansen, Dr. Evan Spruijt and Prof. Dr. Wilhelm Huck (Radboud University), we studied noise in gene expression in dilute environment and in a crowded environment. To this end, our experimental partners measured *in vitro* cell-free transcription and translation (IVTT) of cyan fluorescent protein (CFP) and yellow fluorescent protein (YFP) in monodisperse picoliter droplets.[20,21] They measured noise in gene expression as a function of DNA copy number and macromolecular crowding. They applied the method developed by Elowitz[22] as a reliable method to estimate the magnitude of

variation in gene expression, which has been used to study noise both *in vivo* and *in vitro*.[20,23,24]

Here, we support and quantify the experimental results with two theoretical models including a Gillespie based theoretical model and an off-lattice particle based reaction-diffusion model (PBRD). The Gillespie model is used to analyse the noise of the IVTT system and its origins in a dilute environment. Specifically, we determine the contribution of different factors to noise in the IVTT system, including the stochastic reaction steps, the different folding rates of CFP and YFP and the plasmid distribution over the droplets. The PBRD model is used to study the effect of macromolecular crowding on noise in gene expression and allows us to study how a crowded environment affects noise in gene expression. Hence, these models allow us to obtain a detailed characterization of our IVTT set-up.

5.2 Uncorrelated noise in cell-free gene expression

Noise in gene expression has multiple sources leading to either extrinsic or intrinsic noise. Consider an *in vivo* model system in which two identical independent genes are expressed in a population of cells. Extrinsic noise arises from fluctuations in the cellular state or composition and results in differences in gene expression between cells while fluctuations of gene expression within one cell are correlated. By contrast, uncorrelated fluctuations of protein expression from two identical genes within a cell, resulting from the stochasticity of biochemical processes or other factors, is considered as intrinsic noise.[22] In order to avoid misconceptions with other studies and taking into account the experimental setup, we here make the distinction between uncorrelated and correlated noise (Fig. 4.1a and 4.1b).[25-27] In our experimental set-up, correlated noise arises from the inhomogeneous distribution of reactants over the population of droplets, leading to variation in gene expression between droplets, while CFP and YFP expression within a droplet is correlated. Hence, correlated noise can be quantified by the covariance between normalized CFP and YFP levels over the droplets. By contrast, uncorrelated noise is quantified by the extent to which CFP and YFP levels vary differently among droplets[17,22] and, is calculated as the normalized root mean square distance from the line CFP = YFP. In the experimental set-up we identify four factors which contribute to uncorrelated noise. First, the Poisson distributions of the CFP and YFP plasmids over the droplets results in different quantities of CFP and YFP within one droplet and, therefore, contribute to uncorrelated noise. Additionally, uncorrelated noise arises from the low number of reacting biomolecules leading to stochastic biochemical reactions.

Furthermore, as the maturation time of CFP and YFP differ, we also consider this as a potential factor contributing to uncorrelated noise. Finally, we analyse the effect of macromolecular crowding, which causes limited diffusion and, thereby, potentially leads to an enhancement of uncorrelated noise.

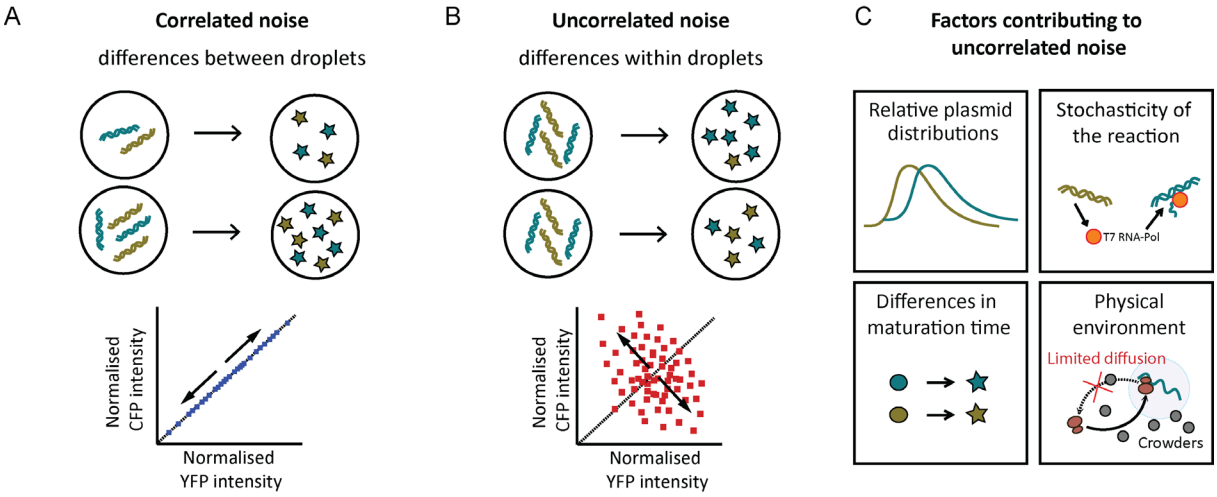

Figure 5.1: Correlated and uncorrelated noise in gene expression. A) Correlated noise in gene expression arises from the inhomogeneous Poisson distribution of reactants among droplets. The graph visually shows the normalized CFP intensity versus the normalized YFP intensity for a population of droplets with correlated noise in gene expression. Each dot represents the normalized CFP and YFP intensities for one droplet. Correlated noise results in differences in gene expression between droplets, while CFP and YFP levels within a droplet are correlated. B) Uncorrelated noise is quantified by the extent to which CFP and YFP levels vary independently among droplets. The graph visually shows the normalized CFP intensity versus the normalized YFP intensity for a population of droplets. Each dot represents the normalized CFP and YFP intensities for one droplet. Uncorrelated noise is the noise orthogonal to the line CFP=YFP. C) In our experimental set-up we analyse the contribution of the Poisson distributions of the plasmids, stochasticity of the biochemical reactions, differences in the maturation time of CFP and YFP and a crowded environment to uncorrelated noise.

5.3 A stochastic model to analyse uncorrelated noise in gene expression under dilute conditions

Gene expression of CFP and YFP was experimentally followed in time for a population of at least 200 picoliter droplets generated using a microfluidic chip (Figure 5.2A). The average expression of both fluorescent proteins over all droplets (Figure 5.2B) shows a constant increase in protein concentrations, as there was no protein degradation in the experiments. To obtain a quantitative understanding of the experimental set-up we developed a theoretical model based on Gillespie's algorithm. The theoretical model describes transcription, translation and protein folding (Figure 5.2D) as single step reactions each with a different probability based on the corresponding reaction rates which are calculated using Michaelis-Menten kinetics including substrate competition:

$$P_{Tx,CFP} = \frac{V_{\max,Tx} p_{CFP}}{K_{M,Tx}\left(1 + \frac{p_{CFP}}{K_{M,Tx}} + \frac{p_{YFP}}{K_{M,Tx}}\right)} \quad (5.1a)$$

$$P_{Tl,CFP} = \frac{V_{\max,Tl} mRNA_{CFP}}{K_{M,Tl}\left(1 + \frac{mRNA_{CFP}}{K_{M,Tl}} + \frac{mRNA_{YFP}}{K_{M,Tl}}\right)} \quad (5.1b)$$

$$P_{f,CFP} = k_{f,CFP} CFP_{uf} \quad (5.1c)$$

$$P_{Tx,YFP} = \frac{V_{\max,Tx} p_{YFP}}{K_{M,Tx}\left(1 + \frac{p_{CFP}}{K_{M,Tx}} + \frac{p_{YFP}}{K_{M,Tx}}\right)} \quad (5.1d)$$

$$P_{Tl,YFP} = \frac{V_{\max,Tl} mRNA_{YFP}}{K_{M,Tl}\left(1 + \frac{mRNA_{CFP}}{K_{M,Tl}} + \frac{mRNA_{YFP}}{K_{M,Tl}}\right)} \quad (5.1e)$$

$$P_{f,YFP} = k_{f,YFP} YFP_{uf} \quad (5.1f)$$

Here $P_{\mathrm{Tx,CFP/YFP}}$, $P_{\mathrm{Tl,CFP/YFP}}$ and $P_{\mathrm{f,CFP/YFP}}$ are the probabilities of transcription, translation and folding of CFP/YFP respectively. Furthermore, $\mathbf{p_{CFP/YFP}}$, $\mathbf{mRNA_{CFP/YFP}}$ and $\mathbf{CFP/YFP_{uf}}$ indicate the amount of plasmid, mRNA and unfolded CFP/YFP respectively. The distribution of CFP and YFP plasmids over the droplets was simulated by a Poisson distribution of both CFP and YFP over 200 iterations. Importantly, as we here focus on uncorrelated noise the Poisson distribution of other reactants was not included in the theoretical model. The $V_{\mathrm{max,Tx}}$, Michaelis-Menten parameter of transcription ($K_{\mathrm{M,Tx}}$) and first-order rate constants of posttranslational folding ($k_{\mathrm{f,CFP}}$ and $k_{\mathrm{f,YFP}}$) were determined by our experimental partners (Table 5.1). The Michaelis-Menten parameter of translation ($K_{\mathrm{M,Tl}}$) was calculated using values previously determined by Stögbauer and co-workers.[28] The only unknown parameter in the stochastic model is the maximum rate of translation ($V_{\mathrm{max,Tl}}$). An estimate of $V_{\mathrm{max,Tl}}$ was obtained by performing non-linear least square analysis of the stochastic model (Equation 5.1), from which the mean expression of CFP and YFP was obtained from 200 iterations, and the mean *in vitro* expression of CFP and YFP in 200 droplets with a plasmid copy number of 7600 (Figure 5.2B and Figure 5.2E).

Table 5.1: Overview of parameters used in the mathematical models

Parameters used in Gillespie based simulations			
$K_{\mathrm{M,Tx}}$[1]	3613.2 plasmids	$V_{\mathrm{max,Tx}}$[1]	722.64 mRNA $\mathrm{min^{-1}}$
$K_{\mathrm{M,Tl}}$[2]	4.3573E05 mRNA	$V_{\mathrm{max,TL}}$[1]	7200 prot $\mathrm{min^{-1}}$
$k_{\mathrm{f,YFP}}$[1]	0.0185 $\mathrm{min^{-1}}$	$k_{\mathrm{f,CFP}}$[1]	0.0121 $\mathrm{min^{-1}}$

[1] determined by our experimental partners

[2] determined by Stögbauer and co-workers.[28]

By following the expression of both proteins per droplet or iteration, we can calculate the time evolution of uncorrelated, correlated and total noise. For every time point the same procedure from Elowitz and co-workers was followed.[22] For each droplet the mean intensity of all pixels was calculated. Then, the mean intensity of each droplet was normalized by the mean intensity of all droplets. This was done for both CFP and YFP. Likewise, the *in silico* simulations were analysed by normalizing the number of CFP and YFP per iteration to the average amount of CFP and YFP respectively over the 200 iterations. The uncorrelated (η_u), correlated (η_c) and total noise can be calculated according:

$$\eta_c^2 = \frac{\langle I_{CFP} I_{YFP} \rangle - \langle I_{CFP} \rangle \langle I_{YFP} \rangle}{\langle I_{CFP} \rangle \langle I_{YFP} \rangle} \tag{5.2}$$

$$\eta_u^2 = \frac{\langle (I_{CFP} - I_{YFP})^2 \rangle}{2\langle I_{CFP} \rangle \langle I_{YFP} \rangle} \tag{5.3}$$

$$\eta_{tot}^2 = \frac{\langle I_{CFP}^2 + I_{YFP}^2 \rangle - 2\langle I_{CFP} \rangle \langle I_{YFP} \rangle}{2\langle I_{CFP} \rangle \langle I_{YFP} \rangle} \tag{5.4}$$

Here I_{CFP} and I_{YFP} are the mean normalized intensities of CFP and YFP (or number of CFP and YFP) respectively of one droplet/iteration). Angled brackets indicate means over the droplet population/iterations. The results in Figure 5.2C show that uncorrelated noise decrease over time, which is in agreement with the observed increase in protein concentration over time and is also shown by results of our theoretical model (Figure 5.2F). The significant difference in noise values in the experimental set-up and theoretical prediction arises from the background noise due to image analysis. Furthermore, as the Poisson distribution of reactants other than the plasmids was not included in the theoretical model the correlated noise values obtained from the simulations is equal to zero.

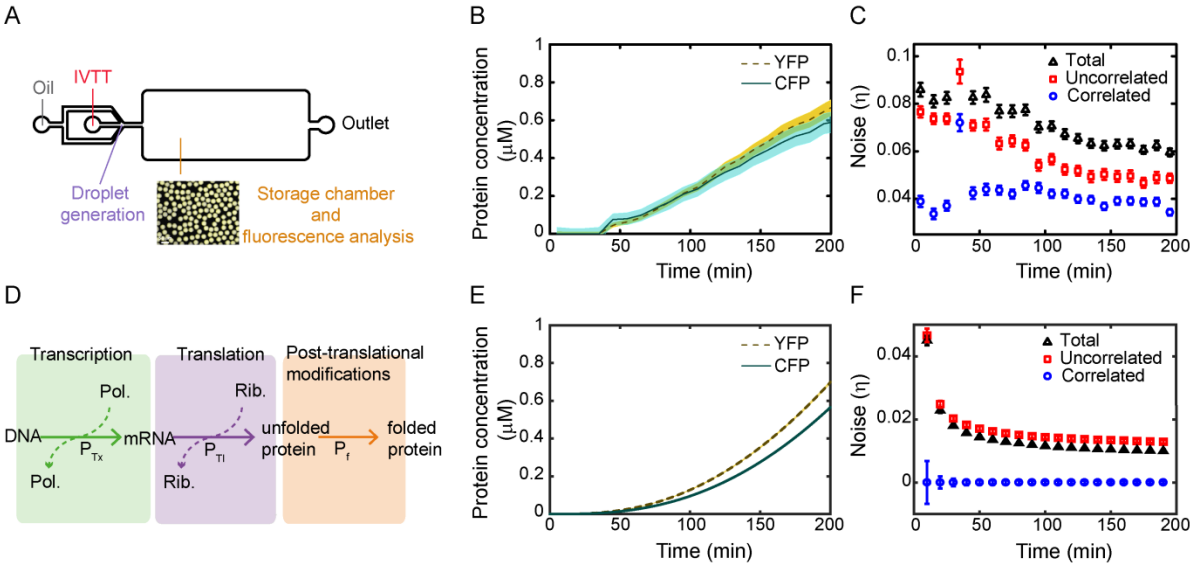

Figure 5.2: Quantifying noise in cell-free gene expression in picoliter droplets. A) Schematic illustration of the microfluidic chip including an inlet for the oil and an inlet for the IVTT reagents, an outlet and a storage chamber for the droplets. The IVTT mixture is pinched off by oil at regular intervals generating water in oil emulsions. The droplets are stored in the storage chamber and protein expression of CFP and YFP is monitored over time with fluorescence microscopy. B) The average CFP and YFP expression over all droplets. C) Uncorrelated (red squares), correlated (blue circles) and total noise (black empty triangles) values over time for on average 7600 copies of each plasmid per droplet. D) Schematic illustration of the Gillespie-based model of cell-free gene expression which includes transcription, translation and protein folding. Transcription and translation are described by the Michaelis-Menten approximation including substrate competition, while protein folding is simulated as a first-order reaction. Furthermore, simulations were performed with CFP and YFP numbers according to a Poisson distribution over the iterations. The parameters of the simulation are shown in Table 5.1. E) Results of the simulations displaying the average CFP and YFP expression over 200 iterations. F) Uncorrelated (red squares), correlated (blue circles) and total noise (black empty triangles) values over time for on average 7600 copies of each plasmid per iteration. B and E) Envelops represent the standard deviation of protein expression over the 200 droplets or iterations. C and F) Error bars show 95% confidence intervals, which were calculated by bootstrapping from the original distribution.

5.3.1 Uncorrelated noise increases with decreasing plasmid copy number

In order to analyse the effect of stochasticity on uncorrelated noise in the experimental set-up and our theoretical model we repeated the *in vitro* and *in silico* experiments for a wide range of initial plasmid concentrations and plotted noise versus the plasmid copy number (Figure 5.3A). The concentrations of all other components were kept constant throughout the experiments and simulations. From the results in Figure 5.3A and Figure 5.3D it can be observed that the correlated noise, i.e. distribution of biomolecules over the droplets/iterations, shows no statistically significant correlation with plasmid copy number (-0.393 Spearman's rho correlation for experimental results). However, uncorrelated noise shows a clear negative correlation with plasmid copy number for both the experimental (-0.929 Spearman's rho correlation) and theoretical results. This is caused by gene expression

becoming increasingly stochastic with decreasing numbers of reacting molecules, which is in line with the theory of stochasticity.[29] Moreover, this trend is also visible 30 and 50 minutes after the start of expression (Figure 5.3B and Figure 5.3E), indicating that it is independent of the number of proteins produced. We chose to calculate noise 100 minutes after the start of fluorescence increase as this yielded experimentally higher signal-to-background ratios and thus more reliable data. Furthermore, we plotted uncorrelated noise at equal average protein concentration over the population of droplets/iterations for all DNA copy numbers (Figure 5.3C and Figure 5.3F) to confirm that uncorrelated noise increases as we decrease copy number and is not due to lower protein levels.

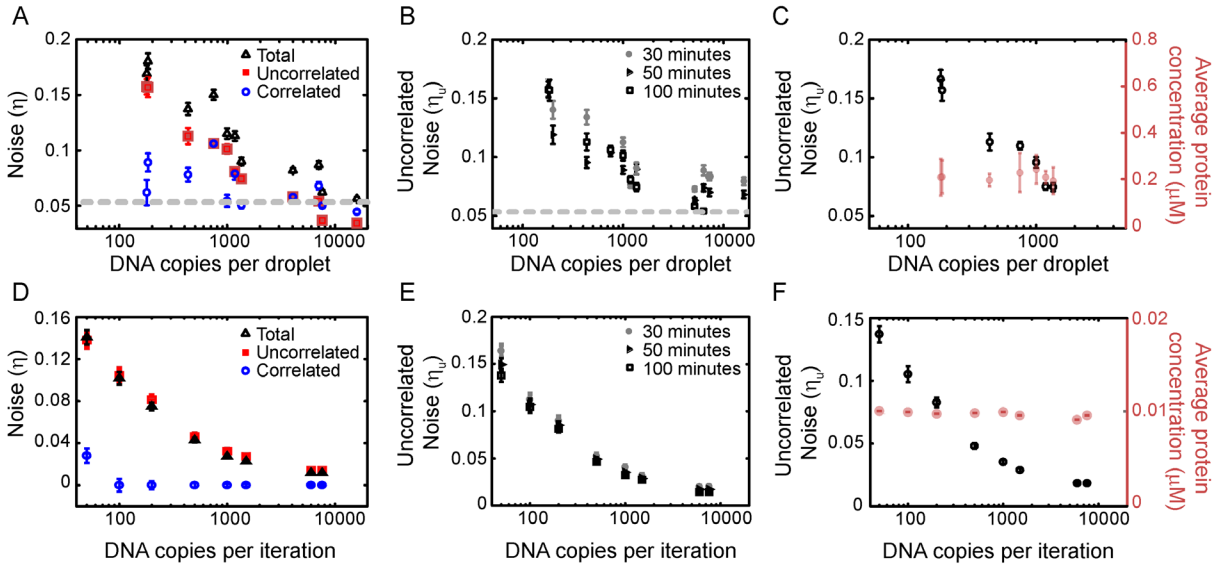

Figure 5.3: Effect of a decreasing copy number on the inherent stochasticity of gene expression. A-C) Results of the IVTT reaction in picoliter droplets. The dotted line represents the background noise due to imaging and analysis. D-F) Results of simulations using the Gillespie algorithm. The probabilities of transcription, translation and protein folding were calculated according to Equation 5.1 using the parameter values in Table 5.1. A/D) Uncorrelated (red squares), correlated (blue empty circles) and total noise (black empty triangles) at 100 minutes after start of protein expression for a range of DNA concentrations. B/E) Uncorrelated noise values versus DNA copy number at 10 (empty triangles), 30 (full circles), 50 (full triangles) and 100 (empty squares) minutes after start of protein expression. C/F) DNA copy number versus uncorrelated noise values (empty circles) determined at time points where the average protein concentration over the droplets/iterations had reached 0.2 μM for the IVTT experiments and 0.01 μM for the Gillespie simulations (full circles). A-F) Error bars show 95% confidence intervals, which were calculated by bootstrapping from the original distribution.

5.3.2 The contribution of DNA copy number, Poisson distribution and protein folding to uncorrelated noise in gene expression

To obtain a deeper understanding of the contribution of the Poisson distribution of plasmids, protein folding and stochasticity to uncorrelated noise we first simulated transcription and translation with stochasticity as the only contributing factor (Figure 5.4). Thereby, we

excluded the Poisson distribution of the plasmids and protein maturation. Addition of the Poisson distribution of CFP and YFP shows a significant increase in uncorrelated noise values. However, as can be observed in Figure 5.4 the addition of folding of proteins only slightly enhances uncorrelated noise values. In conclusion, we find that protein folding barely increases uncorrelated noise (mean of 1% over the plasmid copy numbers) while the average contributions of stochasticity of the reactions and Poisson distributions of the plasmids are 18% and 40% respectively.

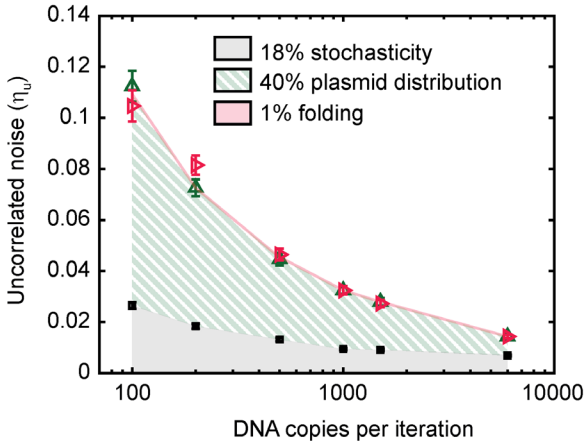

Figure 5.4: The contribution of stochasticity, plasmid distribution and protein maturation to uncorrelated noise in Gillespie-based simulations of gene expression. First, the contribution of stochasticity to uncorrelated noise was determined by performing Gillespie-based simulations including only transcription and translation and using a constant plasmid number of CFP and YFP over the 200 iterations. The contribution of the plasmid distribution and protein folding were determined by adding the Poisson distribution of the plasmids over the 200 iterations followed by the addition of protein maturation. The probabilities of transcription, translation and protein folding required for the Gillespie-based simulations were calculated according to Equation 5.1 using the parameter values in Table 5.1. Error bars show 95% confidence intervals, which were calculated by bootstrapping from the original distribution.

5.4 A particle based reaction-diffusion model to analyse uncorrelated noise in gene expression in crowded environments

The particle based reaction-diffusion (PBRD) model is based on several experimental observations. Hence, prior to discussing the PBRD model we shortly summarize the key experimental results which form the foundation of the model. Our experimental partners performed a study in which Ficoll 70 was added to the IVTT system (Figure 5.4A), a common macromolecular crowding agent, to mimic the crowded conditions inside cells.[30,31] Uncorrelated noise values were obtained from cell-free gene expression for a range of DNA concentrations in the presence of 0, 40, 70 and 90 mg mL^{-1} Ficoll. In the presence of 40 mg mL^{-1} Ficoll 70 the levels of uncorrelated noise were similar to those in the absence of Ficoll

70. However, the results of protein expression in presence of both 70 and 90 mg mL^{-1} Ficoll showed an enhancement of uncorrelated noise. Hence, macromolecular crowding enhances uncorrelated noise of gene expression.

As limited diffusion induced by macromolecular crowding could potentially limit the homogeneous distribution of synthesized mRNA molecules,[12,32] thereby increasing the spatial heterogeneity, our experimental partners decided to study the spatial distribution of mRNA molecules. They found that transcription in crowded droplets leads to a heterogeneous spatial distribution of mRNA molecules (Figure 5.4B) and, hence, that this is a potential factor contributing to uncorrelated noise.

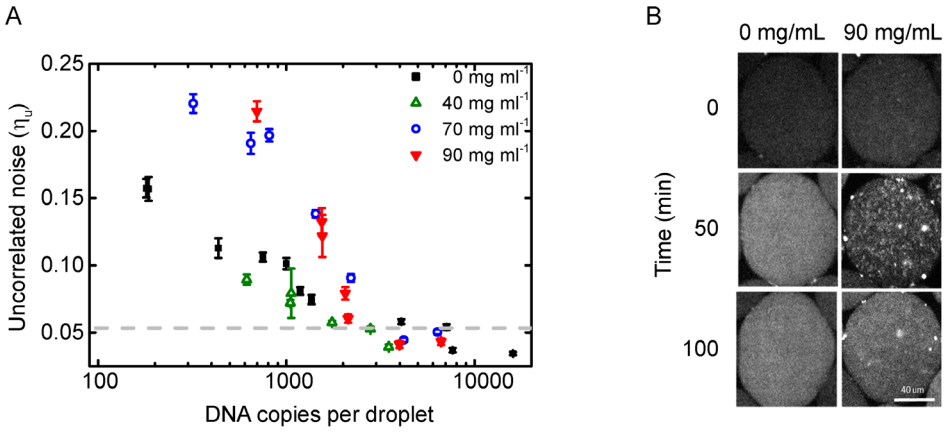

Figure 5.5: A) Uncorrelated noise at 100 minutes after the start of protein expression as a function of DNA copy number at different Ficoll concentrations including 0 mg mL^{-1} (black full squares), 40 mg mL^{-1} (green empty triangles), 70 mg mL^{-1} (blue empty circles) and 90 mg mL^{-1} (red full triangles). The dotted line represents the background noise due to imaging and analysis and error bars show 95% confidence intervals, which were calculated by bootstrapping from the original distribution. B) *In vitro* transcription only experiments in droplets with 0.6 nM pET-32xBT showing the distribution of mRNA using a molecular beacon in dilute environment (left) and in presence of 90 mg mL^{-1} of Ficoll (right).

Here, we examine whether decreased diffusion caused by molecular crowding could play a role in localised gene expression resulting from the heterogeneous distribution of mRNA molecules and, hence, could enhance uncorrelated noise in gene expression. To this end, we simulate gene expression using a particle based reaction-diffusion (PBRD) model. Different techniques have been developed to simulate PBRD including lattice-based models and continuous space models. While lattice-based approaches in which the position of particles are restricted to an artificial grid are computationally efficient, these models are less accurate to simulate the effect of limited diffusion.[33] Hence, we here use a model which simulates Brownian motion of particles in continuous space and implement this model using the freely available software package Smoldyn. Using this model we can track every single molecule

and, hence, follow the distribution of molecules in space and time. Molecules are represented by point-like particles in 2-dimensional continuous space (100 µm x 100 µm), diffuse and react when they collide. We simulate protein expression as a very simple two-step process involving transcription and translation. Importantly, macromolecular crowding can increase or decrease reaction rates. However, here we are not interested in the effect of macromolecular crowding on the production rate of mRNA, but we focus on the effect of limited diffusion of mRNA molecules on uncorrelated noise. Hence, in order to keep the model simple, we simulate transcription as a first-order reaction. Translation is simulated as a second-order reaction where ribosomes react with the mRNA molecules. Furthermore, mRNA molecules are degraded over time allowing the number of mRNA molecules to equilibrate. In total we track 7 species by simulating the expression of CFP and YFP according to the following reaction scheme:

$$\text{plasmid} \xrightarrow{k_{Tx}} \text{plasmid} + \text{mRNA}$$

$$\text{mRNA} + \text{ribosome} \xrightarrow{k_{Tl}} \text{mRNA} + \text{ribosome} + \text{protein}$$

$$\text{mRNA} \xrightarrow{k_{deg}} \varnothing$$

The first-order rate constant k_{Tx} represents the rate constant of transcription (Table 5.2) which was calculated by assuming a transcription rate of 80 nucleotides per second.[34] Furthermore, mRNA degradation is described by the first-order rate constant k_{deg} which is assumed to be 0.0042 s^{-1} calculated by assuming a mRNA lifetime of 4 minutes.[35] The rate constant k_{Tl} is the translation rate of a single ribosome and is calculated by assuming a translation rate of 20 amino acids per second.[36]

Table 5.2: Overview of parameters of reaction rates used in the particle based reaction-diffusion model

Reaction rates			
k_{Tx}[1]	0.11 s^{-1}	k_{TL}[2]	0.08 $protein^{-1}$ s^{-1}
k_{deg}[3]	0.0042 s^{-1}		

[1] calculated by assuming a transcription rate of 80 nucleotides per second.[34]

[2] calculated by assuming a translation rate of 20 amino acids per second[36]

[3] calculated by assuming a mRNA lifetime of 4 minutes[35]

To simulate a trajectory based on Brownian motion,time is discretized in small fixed time steps Δt. The new particle position is calculated by:

$$x(t+\Delta t) = x(t) + \sqrt{2D\Delta t}\xi \tag{5.5}$$

with $x(t+\Delta t)$ the new particle position in the x- or y-direction, $x(t)$ the current particle position, ξ a normally distributed random number, D the diffusion coefficient ($\mu m^2\ s^{-1}$) and Δt the time step (s). Equivalently the new position is calculated for the other space coordinate. To solely analyse the effect of a decreased diffusion coefficient of mRNA molecules and ribosomes we chose the plasmids to not diffuse in the simulation area. After each time step, molecules diffuse and react. In order to establish whether a reaction takes place, Smoldyn converts the reaction rate to a reaction probability for unimolecular reactions, while a binding radius is calculated for bimolecular reactions. When an mRNA molecule and a ribosome have reacted and produced a protein the molecules are placed 1.5 times the binding radius from each other preventing the occurrence of the same reaction. Smoldyn becomes more accurate, but runs more slowly, with decreasing Δt. We chose a time step of 0.0001 seconds to be a fair trade-off between accuracy and simulation time, which results in a spatial resolution of at least 0.06 μm. Furthermore, we use periodic boundaries to avoid edge effects.

5.4.1 Macromolecular crowding decreases the effective diffusion coefficients

Generally, macromolecular crowding affects the diffusion rates of biomolecules. Hence, we first investigate the effect of the presence of crowder molecules on the diffusion constants in the simulations. To this end, we use Smoldyn to generate static crowder molecules with a diameter of 2 μm. These crowder molecules are randomly distributed over the simulation area and the number of crowder molecules is dependent on the chosen fraction of depleted volume. We simulate the trajectories of 100.000 mRNA molecules and ribosomes for increasing fraction of crowder molecules and obtain the mean squared displacement (MSD):

$$MSD \equiv \left\langle (x - x_0)^2 \right\rangle = \frac{1}{N}\sum_{n=1}^{N} (x_n(t) - x_n(0))^2 \tag{5.6}$$

As expected, Figure 5.6A-B shows a decreasing MSD with increasing fraction of crowder molecules. Moreover, molecules are subjected to anomalous diffusion as the MSD curves are not linear. In order to quantify the diffusion of the molecules in more detail we determine the

long-time or effective diffusion constants of the mRNA molecules and ribosomes from the MSD at 1.5 seconds and Equation 5.7:

$$D = \frac{MSD}{2 \cdot d \cdot t} \tag{5.7}$$

with D the diffusion constant ($\mu m^2\ s^{-1}$), d the dimensions of the simulation are and t the time at which the MSD was determined. Figure 5.6A-B shows a negative linear correlation between the effective diffusion constant of mRNA and the fraction area occupied by the crowder molecules. However, results of experiments, performed by our experimental partners, show an exponential decay of the effective diffusion constant of ribosomes with increasing crowder density (Figure 5.6C), as also shown in other experimental studies.[11,37] They found a diffusion coefficient of 70S ribosomes of 4.7 ± 0.215 $\mu m^2\ s^{-1}$ in the absence of Ficoll and 0.4 ± 0.001 $\mu m^2\ s^{-1}$ in the presence of 90 mg mL^{-1} of Ficoll. Clearly, the decrease in diffusion constant with increasing crowder in the simulations is biased and is not representative. This dissimilarity results from the relative simplicity of the mathematical model. For example, whereas the viscosity of the solution is not incorporated in the simulations it determines the effective diffusion constant in the experiments (Stokes-Einstein relation) and has a positive exponential relation to the crowder density.[38] In addition, Smoldyn simulates molecules as point-like particles with no volume and, hence, the excluded volume effect resulting from crowder molecules is considerably low explaining the relatively small decrease in effective diffusion constants with increasing fraction of crowder molecules. Hence, in order to simulate the effect of macromolecular crowding we refrain from adding crowder molecules to the simulation area but will simulate the effect of crowding by adjusting the diffusion coefficients.

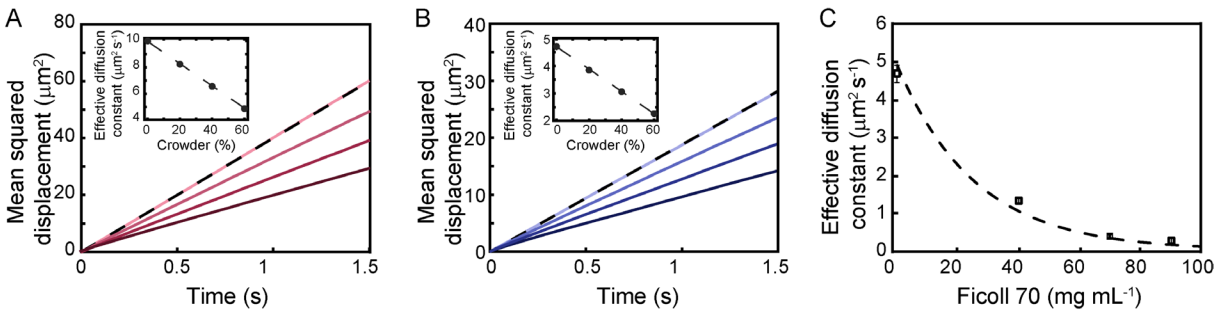

Figure 5.6: Macromolecular crowding enhances uncorrelated noise. A) Mean squared displacement (MSD) of 100.000 mRNA molecules in presence of crowder occupying 0%, 20%, 40% and 60% (from light to dark color) of the simulation area. The dotted black line represents the MSD in dilute environment predicted by theory (Equation 5.6). The inset shows the effective diffusion constant of mRNA over the percentage of occupied area by crowder molecules calculated from the MSD after 100 minutes and Equation 5.6. The dashed line is a linear fit to the effective diffusion constants for a clear visualization. B) Mean squared displacement (MSD) of 100.000 ribosomes in presence of crowder occupying 0%, 20%, 40% and 60% (from light to dark color) of the simulation area. The dotted black line represents the MSD in dilute environment predicted by theory (Equation 5.6). The inset shows the effective diffusion constant of ribosomes calculated from the MSD after 100 minutes and Equation 5.6. The dashed line is a linear fit to the effective diffusion constants for a clear visualization. C) Experimentally determined effective diffusion coefficients of ribosomes over a range of Ficoll 70 concentrations using fluorescence recovery after photo bleaching. The dashed line is a Stokes-Einstein fit of the effective diffusion coefficients where $D \sim 1/\mu$, with μ being the concentration-dependent dynamic viscosity of Ficoll 70.

5.4.2 Uncorrelated noise increases with decreasing effective diffusion coefficients

Simulations with Smoldyn show that the effect of the crowder molecules on the effective diffusion constants is not representative. To capture a more realistic effect of the decreasing diffusion constants in presence of macromolecular crowding, we simulate gene expression for decreasing diffusion coefficients of the reactants in a dilute environment. To this end, we use diffusion coefficients for the ribosomes as experimentally determined (Figure 5.6C). Furthermore, the diffusion coefficients of the mRNA molecules and proteins are assumed to follow the same trend over the range of Ficoll 70 concentrations as for the ribosomes. The diffusion coefficient of mRNA at 0 mg mL^{-1} Ficoll 70 is calculated by the Stokes-Einstein relation using room temperature and the viscosity of water and assuming a radius of gyration of 20 nm (Table 5.3).[39]

Table 5.3: Overview of diffusion coefficients used in the particle based reaction-diffusion model

Plasmid	0 $\mu m^2 s^{-1}$	Protein[3]	77 $\mu m^2 s^{-1}$
Diffusion constants over the concentration range of Ficoll 70			
Ficoll 70 (mg mL^{-1})	Ribosome[2] ($\mu m^2 s^{-1}$)	mRNA[1] ($\mu m^2 s^{-1}$)	
0	4.7	10	
10	3.2	6.81	
20	2.18	4.64	
40	1.01	2.15	
70	0.32	0.68	

[1] Calculated by the Stokes-Einstein relation using room temperature and the viscosity of water and assuming a radius of gyration of 20 nm.[39]

[2] Determined experimentally in isolation using FRAP

[3] From Bu et al.[40]

Figure 5.7B shows the results of simulations with diffusion coefficients representing a dilute environment. In agreement with experimental results (*vide supra*) and results from the Gillespie model (*vide supra*) uncorrelated noise decreases in time, while correlated noise is constant. As we are interested in the contribution of translation to uncorrelated noise we also follow the synthesis of mRNA molecules in time and calculate the noise values (Figure 5.7C). We repeat the simulations for decreasing diffusion coefficients of the mRNA molecules and ribosomes representing increasing concentration of Ficoll 70. The results in Figure 5.7D show that uncorrelated noise at the mRNA level is independent of the diffusion coefficient which is expected as the production rate and degradation rate of the mRNA molecules are described as zeroth order reactions and, hence, independent of the diffusion coefficients. After approximately 12 minutes the average production and degradation rates of mRNA are balanced meaning that on average every 10 seconds 1 mRNA is produced and degraded (Table 5.2). Uncorrelated noise at the protein level increases with decreasing diffusion coefficients representing concentrations of Ficoll 70 beyond 20 mg mL^{-1}. The sudden increase in uncorrelated noise with increasing concentrations of Ficoll 70 was also observed in experimental results. In conclusion, translation provides an additional source to uncorrelated noise in presence of sufficient macromolecular crowding agent.

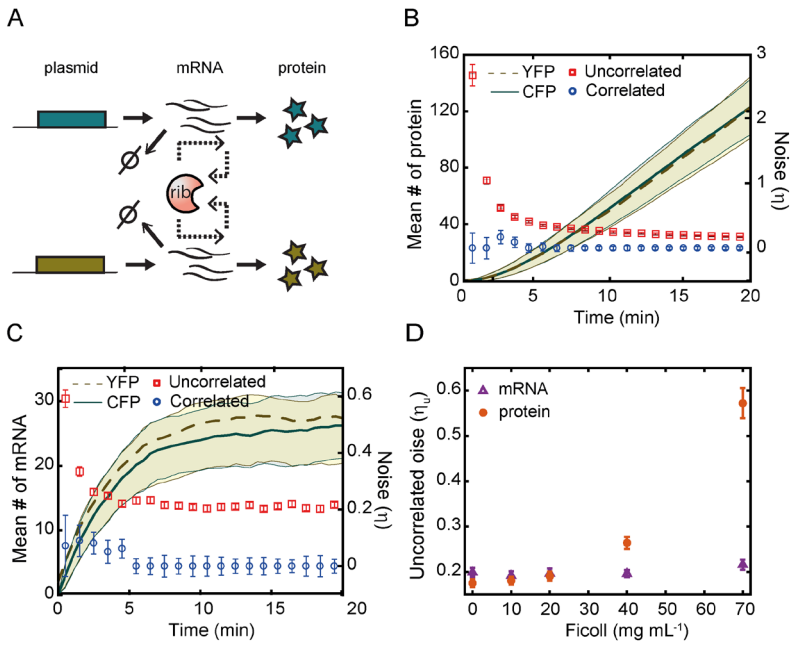

Figure 5.7: Illustration of the theoretical model based on Brownian dynamics in continuous space using Smoldyn. The particle-based model includes transcription and translation. B-C) Results of the off-lattice particle-based tracking simulations over 200 iterations in dilute environment. The simulations were performed with 1 plasmid for both CFP and YFP production with rate constants and diffusion coefficients as shown in Table 5.2 and Table 5.3. B) Results of the off-lattice particle-based tracking simulations displaying the average CFP and YFP expression and noise values over time. C) Results of the off-lattice particle-based tracking simulations displaying the average mRNA for the production of CFP and YFP and noise values at the mRNA level over time. D) Uncorrelated noise of mRNA and protein expression at 20 minutes after start of expression as a function of Ficoll concentration. All simulations where performed in dilute environment with decreasing diffusion coefficients for mRNA and the ribosome (Table 5.3) representing the effect of increasing concentrations of Ficoll 70. Error bars show 95% confidence intervals, which were calculated by bootstrapping from the original distribution. Envelops represent the standard deviation of protein expression over the 200 iterations.

5.4.3 Decreasing diffusion coefficients and the formation of heterogeneous micro-environments enhance uncorrelated noise

Interestingly, decreasing diffusion coefficients of mRNA and ribosomes result in translational bursting (Figure 5.8A-B). It has been reported that translational bursting is a major source of gene expression noise in prokaryotes.[41-43] In order to obtain a deeper understanding how uncorrelated noise increases with decreasing diffusion coefficients we examine the spatial distribution of the mRNA molecules. Figure 5.8D-E displays the distribution of mRNA molecules with diffusion coefficients in dilute environment and in presence of 70 mg mL^{-1} Ficoll 70. Clearly, the diffusion coefficient of mRNA greatly affects the spatial distribution of respective molecule. From the spatial distribution of the mRNA molecules we can calculate the mean distance to the plasmid from which it is produced. Figure 5.8C displays the mean distance of the mRNA molecules to the plasmid as a function of Ficoll 70 (decreasing diffusion coefficients). As can be observed the spatial distribution of the mRNA molecules

becomes increasingly heterogeneous beyond 20 mg mL^{-1} Ficoll 70. Obviously, the decreasing diffusion coefficients of mRNA result in an increased heterogeneous distribution of synthesized mRNA molecules in our simulations. However, the increase in uncorrelated noise with increasing Ficoll 70 can result from an increasing heterogeneous distribution of mRNA molecules and/or decreasing diffusion coefficient of the ribosomes. In order to analyse the effect of the spatial distribution of the mRNA molecules and the decreasing diffusion constants of ribosomes to uncorrelated noise separately we developed a theoretical model using Smoldyn in which we simulate only translation in the same manner as in the transcription-translation simulations. In these simulations mRNA molecules are fixed to specific positions and are not degraded, while ribosomes diffuse in the simulation area. First, we quantified uncorrelated noise as a function of Ficoll 70 representing both an increasing spatial heterogeneous distribution of the mRNA molecules and decreasing diffusion constant of the ribosomes (D_R), shown in Figure 5.8F. To this end, the positions of the mRNA molecules over the range of Ficoll 70 were obtained from the transcription-translation simulations after 20 minutes of protein expression while the decreasing diffusion constants were obtained from experimental results (Table 5.3). Similar to the results of the transcription-translation simulations, uncorrelated noise increases at concentration of Ficoll 70 at 40 and 70 mg mL^{-1}. Subsequently, we plotted uncorrelated noise as a function of Ficoll 70 representing solely a decreasing diffusion constant of the ribosome. While uncorrelated noise shows a similar increase at 40 mg mL^{-1} the enhancement at 70 mg mL^{-1} is significantly lower compared to the results including both factors. Finally, we determine uncorrelated noise as a function of Ficoll 70 representing solely an increasing spatial heterogeneous distribution of the mRNA molecules. As can be observed, uncorrelated noise increases at 40 mg mL^{-1} and 70 mg mL^{-1} Ficoll 70 when these simulations were performed with a diffusion constant of ribosomes of 0.32 μm^2 s^{-1}. However, uncorrelated noise is not increasing with an increasing spatial heterogeneous distribution of mRNA molecules when these simulations were performed with a diffusion constant of ribosomes of 4.7 μm^2 s^{-1}. Hence, a heterogeneous distribution of mRNA molecules only contributes to uncorrelated noise at sufficient low diffusion coefficients of ribosomes. This also explains why the heterogeneous spatial distribution of mRNA molecules at 40 mg mL^{-1} does not provide an additional contribution to uncorrelated noise as here the ribosomes are moving relatively fast and do not sense the heterogeneous environment. However, at 70 mg mL^{-1} the heterogeneous distribution of mRNA molecules significantly enhances uncorrelated noise. Not much is known about the

exact mechanism of localised transcription and translation in bacterial cells, though there has been much speculation that slower diffusion plays a role.[44,12] Our results show that decreasing diffusion coefficients and the formation of spatial heterogeneous microenvironments could play a prominent role in localised gene expression and translational bursting and enhance uncorrelated noise of gene expression.

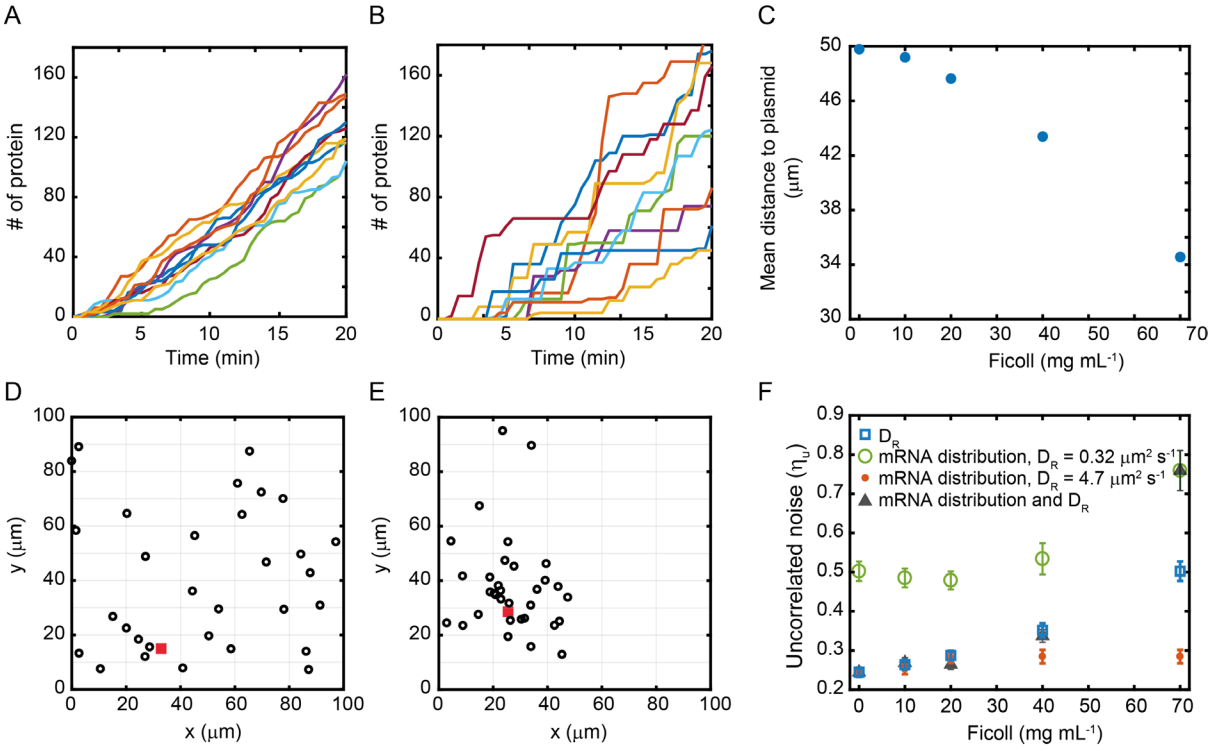

Figure 5.8: A) Protein expression of 10 iterations using the off-lattice PBRD model including transcription and translation with diffusion constants representing dilute environment. B) Protein expression of 10 iterations using the off-lattice PBRD model including transcription and translation with diffusion constants representing 70 mg mL^{-1} Ficoll 70. C) Mean distance to plasmid of the mRNA molecules as a function of Ficoll 70 (representing the decreasing diffusion constants of mRNA and ribosome) at 20 minutes of expression using the off-lattice PBRD model including transcription and translation. The mean distance was calculated from the mRNA distribution of 200 iterations at 20 minutes after expression. D-E) Results of the off-lattice particle-based tracking simulations displaying the distribution of mRNA molecules at 20 minutes of transcription and translation, produced from a single plasmid (square) with diffusion coefficients representing (D) dilute environment and (E) 70 mg mL^{-1} Ficoll 70. F) Results of simulations including only translation were mRNA molecules are fixed to specific positions and are not degraded, while ribosomes diffuse in the simulation area. Uncorrelated noise was determined as a function of Ficoll 70 representing solely the decreasing diffusion coefficients of ribosomes, D_R (squares), an increasing spatial heterogeneous distribution of the mRNA molecules (circles) and the combination of both (triangles). Simulations were performed using the position of mRNA molecules obtained from the transcription-translation simulations after 20 minutes for the range of Ficoll 70. Moreover, diffusion constants of ribosomes for the range of Ficoll 70 were obtained by experiments (Table 5.3).

5.5 Conclusions

In collaboration with our experimental partners, we here studied noise in gene expression *in vitro* and *in silico* in dilute environment and in a crowded environment. Using *in silico* Gillespie simulations we find that, additional to the stochastic nature of the reactions, uncorrelated noise in dilute environment in our *in vitro* set-up mostly results from the plasmid distribution over the droplets, while protein folding barely enhances uncorrelated noise. Importantly, our results show that decreasing diffusion coefficients and the formation of spatial heterogeneous microenvironments result in increased translational bursting and an enhancement of uncorrelated noise of gene expression. Due to the low diffusion constants of mRNA, a heterogeneous environment is maintained which enhances any already existing stochasticity caused by transcription and translation of low copies of DNA. It is expected that the formation of heterogeneous environments of mRNA is even more pronounced in the *in-vitro* set-up resulting from two factors. First, the diffusion coefficient of mRNA as a function of concentration of crowder molecules was assumed to follow the same trend as for the ribosomes. However, mRNA molecules are reported to have a larger diameter[39] compared to ribosomes,[45] indicating that the diffusion of mRNA molecules is decreased to a greater extent than their smaller partners in presence of macromolecular crowding.[46] Additionally, multiple ribosomes can interact with one mRNA and associate into a polysome[47] which is expected to be promoted in a crowded environment and results in even lower diffusion coefficients. Different studies have shown the effect of macromolecular crowding on diffusion of reactants and reaction rates.[48,49] Additionally, it has been shown *in silico* that diffusivity plays a role in gene expression noise.[19] We here showed a detailed characterization of the origin of an enhanced uncorrelated noise in a crowded environment by extensive studies using particle-based diffusion reaction model based on Brownian dynamics.

Our finding of the heterogeneous mRNA distributions in crowded transcription-translation systems and the concomitant increase in uncorrelated noise has important implications for our understanding of living cells. It is conceivable that the synthesis of macromolecules (mRNA and proteins) *in vivo* leads to locally heterogeneous systems.[12] This might explain the findings in literature on localisation of mRNA in *E. coli,*[12,44] but also helps to explain the origin of experimentally determined uncorrelated noise in gene expression.[41] Finally, our experiments and simulations enable us not only to take into account, but also predict the magnitude of noise when engineering synthetic biochemical pathways in artificial cellular mimics.

5.6 References

1. Raser, J.M. & O'Shea, E.K. Noise in gene expression: Origins, consequences, and control. *Science* **309**, 2010-2013 (2005).
2. Maamar, H., Raj, A. & Dubnau, D. Noise in gene expression determines cell fate in Bacillus subtilis. *Science* **317**, 526-529 (2007).
3. Chang, H.H., Hemberg, M., Barahona, M., Ingber, D.E. & Huang, S. Transcriptome-wide noise controls lineage choice in mammalian progenitor cells. *Nature* **453**, 544-547 (2008).
4. Gupta, Piyush B. et al. Stochastic state transitions give rise to phenotypic equilibrium in populations of cancer cells. *Cell* **146**, 633-644 (2011).
5. Weinberger, L.S., Burnett, J.C., Toettcher, J.E., Arkin, A.P. & Schaffer, D.V. Stochastic gene expression in a lentiviral positive-feedback loop: HIV-1 Tat fluctuations drive phenotypic diversity. *Cell* **122**, 169-182 (2005).
6. Shahrezaei, V. & Swain, P.S. The stochastic nature of biochemical networks. *Curr. Opin. Biotech.* **19**, 369-374 (2008).
7. Weitz, M. et al. Diversity in the dynamical behaviour of a compartmentalized programmable biochemical oscillator. *Nat. Chem.* **6**, 295-302 (2014).
8. Bratsun, D., Volfson, D., Tsimring, L.S. & Hasty, J. Delay-induced stochastic oscillations in gene regulation. *Proc. Natl. Acad. Sci. U.S.A.* **102**, 14593-14598 (2005).
9. Elowitz, M.B. & Leibler, S. A synthetic oscillatory network of transcriptional regulators. *Nature* **403**, 335-338 (2000).
10. Minton, A.P. How can biochemical reactions within cells differ from those in test tubes? *J. Cell Sci.* **119**, 2863-2869 (2006).
11. Dix, J.A. & Verkman, A.S. Crowding effects on diffusion in solutions and cells. *Ann. Rev. Biophys.* **37**, 247-263 (2008).
12. Montero Llopis, P. et al. Spatial organization of the flow of genetic information in bacteria. *Nature* **466**, 77-81 (2010).
13. Soula, H., Caré, B., Beslon, G. & Berry, H. Anomalous versus slowed-down brownian diffusion in the ligand-binding equilibrium. *Biophys. J.* **105**, 2064-2073 (2013).
14. Zimmerman, S.B. & Harrison, B. Macromolecular crowding increases binding of DNA polymerase to DNA: an adaptive effect. *Proc. Natl. Acad. Sci.* **84**, 1871-1875 (1987).
15. Klumpp, S., Scott, M., Pedersen, S. & Hwa, T. Molecular crowding limits translation and cell growth. *Proc. Natl. Acad. Sci. U.S.A.* **110**, 16754-16759 (2013).
16. Ridgway, D. et al. Coarse-grained molecular simulation of diffusion and reaction kinetics in a crowded virtual cytoplasm. *Biophys. J.* **94**, 3748-3759.
17. Swain, P.S., Elowitz, M.B. & Siggia, E.D. Intrinsic and extrinsic contributions to stochasticity in gene expression. *Proc. Natl. Acad. Sci.* **99**, 12795-12800 (2002).
18. Acar, M., Mettetal, J.T. & van Oudenaarden, A. Stochastic switching as a survival strategy in fluctuating environments. *Nat. Genet.* **40**, 471-475 (2008).
19. van Zon, J.S., Morelli, M.J., Tănase-Nicola, S. & ten Wolde, P.R. Diffusion of Transcription Factors Can Drastically Enhance the Noise in Gene Expression. *Biophys. J.* **91**, 4350-4367 (2006).
20. Nishimura, K., Tsuru, S., Suzuki, H. & Yomo, T. Stochasticity in gene expression in a cell-sized compartment. *ACS Synth. Biol.* **4**, 566–576 (2014).
21. Karig, D.K., Jung, S.-Y., Srijanto, B., Collier, C.P. & Simpson, M.L. Probing cell-free gene expression noise in femtoliter volumes. *ACS. Synth. Biol.* **2**, 497-505 (2013).
22. Elowitz, M.B., Levine, A.J., Siggia, E.D. & Swain, P.S. Stochastic Gene Expression in a Single Cell. *Science* **297**, 1183-1186 (2002).
23. Raser, J.M. & O'Shea, E.K. Control of stochasticity in eukaryotic gene expression. *Science* **304**, 1811-1814 (2004).
24. Hilfinger, A. & Paulsson, J. Separating intrinsic from extrinsic fluctuations in dynamic biological systems. *Proc. Natl. Acad. Sci.* **108**, 12167-12172 (2011).

25. Munsky, B., Neuert, G. & van Oudenaarden, A. Using gene expression noise to understand gene regulation. *Science* **336**, 183-187 (2012).
26. Thattai, M. & van Oudenaarden, A. Intrinsic noise in gene regulatory networks. *Proc. Natl. Acad. Sci. U.S.A.* **98**, 8614-8619 (2001).
27. Paulsson, J. Summing up the noise in gene networks. *Nature* **427**, 415-418 (2004).
28. Stogbauer, T., Windhager, L., Zimmer, R. & Radler, J.O. Experiment and mathematical modeling of gene expression dynamics in a cell-free system. *Integr. Biol.* **4**, 494-501 (2012).
29. Shahrezaei, V. & Swain, P.S. The stochastic nature of biochemical networks. *Curr. Opin. Biotechnol.* **19**, 369-374 (2008).
30. Ellis, R.J. Macromolecular crowding: obvious but underappreciated. *Trends Biochem. Sci.* **26**, 597-604 (2001).
31. Ge, X., Luo, D. & Xu, J. Cell-free protein expression under macromolecular crowding conditions. *PLoS ONE* **6**, e28707 (2011).
32. Gillespie, D.T., Petzold, L.R. & Seitaridou, E. Validity conditions for stochastic chemical kinetics in diffusion-limited systems. *J. Chem. Phys.* **140**, 054111 (2014).
33. Meinecke, L. & Eriksson, M. Excluded volume effects in on- and off-lattice reaction-diffusion models. *IET Syst. Biol.* **11**, 55-64 (2017).
34. Vogel, U. & Jensen, K.F. The RNA chain elongation rate in Escherichia coli depends on the growth rate. *J. Bacteriol.* **176**, 2807-2813 (1994).
35. Bernstein, J.A., Khodursky, A.B., Lin, P.-H., Lin-Chao, S. & Cohen, S.N. Global analysis of mRNA decay and abundance in Escherichia coli at single-gene resolution using two-color fluorescent DNA microarrays. *Proc. Natl. Acad. Sci. U.S.A.* **99**, 9697-9702 (2002).
36. Bremer, H. & Dennis, P. Modulation of chemical composition and other parameters of the cell at different exponential growth rates. *EcoSal Plus* (2008).
37. Banks, D.S. & Fradin, C. Anomalous diffusion of proteins due to molecular crowding. *Biophys. J.* **89**, 2960-2971 (2005).
38. Pradipasena, P. & Rha, C. Effect of concentration on apparent viscosity of a globular protein solution. *Polym. Eng. Sci.* **17**, 861-864 (1977).
39. Gopal, A., Zhou, Z.H., Knobler, C.M. & Gelbart, W.M. Visualizing large RNA molecules in solution. *RNA* **18**, 284-299 (2012).
40. Bu, Z., Biehl, R., Monkenbusch, M., Richter, D. & Callaway, D.J.E. Coupled protein domain motion in Taq polymerase revealed by neutron spin-echo spectroscopy. *Proc. Natl. Acad. Sci. U.S.A.* **102**, 17646-17651 (2005).
41. Ozbudak, E.M., Thattai, M., Kurtser, I., Grossman, A.D. & van Oudenaarden, A. Regulation of noise in the expression of a single gene. *Nat. Genet.* **31**, 69-73 (2002).
42. Friedman, N., Cai, L. & Xie, X.S. Linking Stochastic Dynamics to Population Distribution: An Analytical Framework of Gene Expression. *Phys. Rev. Lett.* **97**, 168302 (2006).
43. Kuwahara, H., Arold, S.T. & Gao, X. Beyond initiation-limited translational bursting: the effects of burst size distributions on the stability of gene expression. *Integr. Biol.* **7**, 1622-1632 (2015).
44. Kim, S., Mlodzianoski, M., Bewersdorf, J. & Jacobs-Wagner, C. Probing spatial organization of mRNA in bacterial cells using 3D super-resolution microscopy. *Biophys. J.* **102**, 278a (2012).
45. Kaczanowska, M. & Rydén-Aulin, M. Ribosome biogenesis and the translation process in Escherichia coli. *Microbiol. Mol. Biol. Rev.* **71**, 477-494 (2007).
46. Minton, A.P. The Influence of macromolecular crowding and macromolecular confinement on biochemical reactions in physiological media. *J. Biol. Chem.* **276**, 10577-10580 (2001).
47. Brandt, F. et al. The native 3D organization of bacterial polysomes. *Cell* **136**, 261-271.
48. Ellis, R.J. Macromolecular crowding: an important but neglected aspect of the intracellular environment. *Curr. Opin. Struct. Biol.* **11**, 114-119 (2001).
49. Zhou, H.-X., Rivas, G. & Minton, A.P. Macromolecular crowding and confinement: Biochemical, biophysical, and potential physiological consequences. *Ann. Rev. Biophys.* **37**, 375-397 (2008).

6

Epilogue

A minor part of the work in this chapter has been published in:
Hendrik W.H. van Roekel[‡], Bas J.H.M. Rosier[‡], Lenny H.H. Meijer[‡], Peter A.J. Hilbers, Albert J. Markvoort, Wilhelm T.S. Huck and Tom F.A. de Greef – Chemical Society Reviews, **2015**, 44, 7465

‡ contributed equally to this work

6.1 Introduction

Cell-free synthetic biology entails the construction of complex molecular networks from simple molecules in a cell-free environment in a controllable fashion. Theoretical and experimental studies of such biochemical networks allow the extraction of fundamental principles of cellular network organization and function. The studies described in chapter 2-4 involve the *de novo* construction of molecular networks. In chapter 2 we introduced the PEN toolbox and a heuristic model for the detailed characterization of PEN-based networks. In chapter 3, inspired by the hierarchical layers of signal generation and processing in cells, we expanded the chemical complexity by engineering hierarchical control of enzymatic actuators using the PEN-based bistable switch. To this end, we developed a translator module which converts signaling molecules from the upstream network to unique DNA strands driving downstream actuators. Furthermore, we quantified the effect of retroactivity by a detailed computational analysis of the experimental results. We showed our modular approach by coupling of a previously engineered switchable memories circuit to downstream actuators based on β-lactamase and luciferase. To further expand the scope of DNA-based molecular programming, we introduced the concept of antibody-templated strand exchange (ATSE), allowing the use of antibodies as input for DNA-based computing. In chapter 4 we developed a comprehensive model that described the kinetics of the ATSE system. The model provided a fundamental understanding of the ATSE reaction and was used to find optimal concentration regimes and to study the effect of thermodynamics and kinetics of antibody–epitope binding on the ATSE reaction.

The study described in chapter 5 involved the reconstitution of protein expression in a crowded environment under cell-free conditions. To support the experimental findings and to obtain a detailed characterization of the experimental setup we developed two independent theoretical models. We studied the variation in cell-free gene expression as a function of copy number and macromolecular crowding. We found that decreasing diffusion coefficients and the formation of heterogeneous micro-environments caused by macromolecular crowding enhance uncorrelated noise in gene expression.

This chapter discusses the aim and significance of cell-free synthetic biology followed by a discussion on the value of systems biology to this field. The subsequent sections elaborate on the prospective applications.

6.2 Cell-free synthetic biology: what have we learned?

The cell is composed of many biomolecules interacting with high specificity in a crowded environment. These biomolecules form complex sets of interactions enabling the cell to respond to input cues, to withstand perturbations and to adapt to environmental changes. Our current knowledge of cellular circuits and feedback systems has raised the awareness of the daunting complexity of the cell. Yet, the tremendous developments in experimental and theoretical techniques have shifted the descriptive stage of biology to a stage where questions are amenable to experimental studies and theoretical approaches taken from biophysical and engineering sciences. Importantly, this allowed the rise and development of new research areas such as cell-free synthetic biology. Cell-free synthetic biology is a research area within the field of synthetic biology involving the engineering of biomolecular networks in a cell-free controllable environment. This thesis is focussed on the cell-free construction of biochemical networks in which the main goal is to obtain a deeper understanding of the complex behaviour of cellular biochemical interactions. The cell-free reconstitution of existing intracellular networks using purified biological components has been shown to be a valuable method. For example, using this methodology the oscillatory phosphorylation of KaiC was shown to result from the synergistic action of KaiA and KaiB and even persists without transcription and translation.[1] Moreover, Lim and coworkers applied this strategy to obtain a deeper understanding of Ras GTPase signaling, which is a protein crucial in cell proliferation and morphology.[2] Clearly, the cell is governed by a vast number of reactions and biochemical networks each having a specific role. However, the existence and continuation of these networks in living cells are subjected to the central process of transcription and translation of genetic information to functional proteins. Transcription and translation are extremely complex processes involving multiple steps and numerous components. Hence, *in vitro* transcription and translation (IVTT) provides a unique platform to study the reaction steps involving the flow of information from genes to protein in a controlled fashion.[3-5] IVTT is based on the finding that transcription and translation machinery is also active isolated from the cell and, hence, the cell integrity is not necessary for protein synthesis. In chapter 5 we described the IVTT set-up, implemented by our experimental partners, used to study the effect of macromolecular crowding on the uncorrelated noise in gene expression. IVTT allowed the manipulation of the concentration of plasmids and the concentration of crowding agent, which is not possible in an *in vivo* set-up. Supported by results from *in silico* simulations, we find that uncorrelated noise in gene expression in our IVTT set-up was enhanced by the heterogeneous distribution of mRNA

molecules by macromolecular crowding. It is very plausible that the synthesis of macromolecules *in vivo* creates locally heterogeneous systems, as production rates are often larger than local diffusion rates.[6] Besides explaining the findings on localisation of mRNA in *E. coli,*[6,7] our results explained the origin of experimentally determined uncorrelated noise in gene expression.[8]

Besides the reconstitution of existing regulatory circuits using purified biochemical components, cell-free synthetic biology entails the rational design of new signaling circuits by applying a bottom-up approach. These *de novo* circuits consist of naturally occurring biomolecules or derivatives with well-established functions, which are now used in an unnatural network configuration and, hence, these biomolecules govern the interplay naturally not occurring in cells. Even when the biomolecules are not in their natural configuration studies on these networks provide valuable knowledge of signaling circuits, topology, dynamics and kinetics. While studies performed *in vivo* have provided valuable insights in cellular networks, cell-free mimics enable the detailed kinetic characterization and exploration of characteristic features such as bifurcations, unstable points, attractors and limit cycles.[9] Maybe obvious, yet interesting, is that the kinetics is as important as the topology for the performance of a molecular circuit. For example, while a network topology consisting of two nodes with mutual inhibition implemented by the genelet toolbox gives rise to bistable behavior,[10] implementation using the PEN toolbox does not show bistability as the kinetics are too linear.[11] In order to make the PEN-based circuit bistable, Rondelez and coworkers extended their topology by two additional autocatalytic loops and, thereby, increased the kinetic nonlinearity in their system.[12] Similarly, a delicate balance between production rates and degradation rates is required regarding the functioning of a network.[13] Additionally, competition for resources causes hidden layers of interactions in cells. While competition is often masked *in vivo* by the large number of for example substrates competing for the same enzyme rendering the kinetics pseudo-first order,[14] cell-free studies clearly show the effect of competition. For example Rondelez and coworkers showed in an experimental study that two independent PEN-based oscillators with distinct frequencies might synchronize when they were run in the same tube, resulting from competing for the same enzymes.[15] Maybe cells exploit the global coupling among molecules by competition allowing the cells to synchronize pathways using fewer molecular connections. Hence, while competition for resources increases the complexity and unpredictability of the network by the non-linear interactions, it is not necessarily a nuisance. In addition, competition of different sigma

factors for the polymerase can be used to regulate gene expression.[5] Moreover, De Greef and colleagues showed with an *in silico* model that competition for an enzyme responsible for degradation enhanced the quality and robustness of a PEN-based circuit with an adaptive response. Additionally, *de novo* engineered model systems have shown that competition can be used to generate winner-take-all behavior[16] or amplify fluctuations in concentration.[17] On a similar line, while in general low retroactivity is desired as this increases the unpredictability of the coupling of modules, we showed in chapter 3 by a *de novo* cell-free model system that retroactivity can sometimes increase the robustness of a circuit.

Understanding the biochemical and mechanical features of cell-free limited subsystems does not suffice to tackle cellular complexity, let alone the function and organization of a complete organism. Yet, cell-free synthetic biology provides a deeper understanding of complex phenomena in cells by either rebuilding a target property or circuit or the *de novo* construction of signaling circuits. Besides, these cell-free molecular systems can be applied in different areas such as diagnostics, therapeutics and for the construction of a minimal cell which will be discussed in the last section of this chapter.

6.3 Synthetic biology and systems biology

It has become apparent in recent years that synthetic biology is more than simply the addition or removal of modules to molecular circuits. Every module added or changed inevitably affects the dynamics and kinetics of the already existing circuit. Therefore, instead of focusing on a single module the design and study of whole systems and circuits has tremendously increased. However, to be successful, synthetic biology has to join forces with systems biology as this provides a qualitative and quantitative understanding of fundamental properties of the target function. For this reason, the number of examples in literature of cell-free systems which are analysed and supported by tools from systems biology has grown immensely. In this thesis we have developed several theoretical models using tools from systems biology. In chapter 2, 3 and 4 we constructed models based on ordinary differential equations and obtained a fundamental understanding of the involved reaction steps and kinetics of the systems. Moreover, we could identify the critical parameters and concentrations as well as analyze the system's robustness. Understanding the system's behaviour, dynamics and performance is highly important in the field of synthetic biology as this allows the manipulation of respective system by the addition, removal or interchanging of modules in a controlled manner. For example, the theoretical model in chapter 4 can predict the performance of the ATSE reaction and the optimal concentration

regimes of reactants for new antibody-epitope pairs. In addition, mathematical models are often essential for the validation of a hypothesis. For example, the reaction-diffusion model described in chapter 5 supports the experimental observations and validates that macromolecular crowding enhances uncorrelated noise by the increased heterogeneous distribution of mRNA molecules. These examples show that systems biology is crucial in the field of (cell-free) synthetic biology in order to understand, manage and control these synthetic systems.

6.4 Applications of engineered biomolecular circuits

The principles and knowledge from the engineering of cell-free biomolecular systems drives the construction of artificial cells with custom designed properties and function.[18] While significant steps have been made in the field of (cell-free) synthetic biology, the engineering of a synthetic cell capable of self-maintaining, replicating and evolving is still far away as it involves the integration of many complex aspects such as metabolism, membrane regeneration, communication and genetic expression.[19,20] However, on the road towards the construction of artificial cells valuable insights are obtained and engineered platforms can be readily applied for various purposes. Moreover, due to the modularity and inherent biocompatibility of engineered biomolecular circuits, applications of this technology in the biomedical sciences are within reach. In this section, we will briefly highlight several applications of this technology. First we focus on cell-free genetic biosensors and biological nanofactories capable of sensing and responding to the environment. We continue with a discussion on employing these systems in the intracellular environment. Then, we discuss the applications of non-living cellular mimics based on molecular circuits encapsulated in liposomes. Finally, we highlight applications in the area of autonomous materials.

A first emerging application comprises cell-free genetic biosensors. In contrast to genetically engineered biosensing cells, which might have limited detection ranges due to membrane impermeability of the analytes and which may be difficult to commercialize due to official regulations of genetically modified organisms, cell-free biosensors can be readily made using coupled *in vitro* transcription translation systems. Pellinen *et al.* for instance used an *E. coli* extract to produce firefly luciferase as reporter in response to specific analytes.[21] The authors show that their cell-free approach allowed for improved sensitivity, wider detection range and faster assays combined with minimal preparation times. Collins *et al.*[22] have taken this approach to the next level by freeze drying cell-free synthetic gene networks onto paper and other porous materials (Figure 6.1A). The resulting abiotic materials are sterile and stable at

room temperature, allowing for facile storage and distribution. Retaining their *in vitro* transcription and translation capability, these materials can be activated at will by simply adding water. As such, the paper-based platform allows for the safe use of engineered gene networks beyond the lab, *e.g.*, in the clinic and industry, presumably at a low cost. The authors demonstrated their platform as glucose sensors and strain-specific Ebola virus sensors making use of a colorimetric output. Due to the modularity of the paper-based approach, arbitrary reaction networks from the ever growing toolbox of synthetic biology can be added resulting in paper-based biosensors for ultrasensitive multiplexed diagnostics. In addition, simple cameras present on many contemporary mobile phones can be used to quantitatively detect the optical readout. Therefore, this technique paves the way for the creation of low-cost biosensors that can be embedded ubiquitously into daily life.

A second emerging application of cell-free circuits consists of biological nanofactories which sense and respond to a specific input cue. For example, Tan and coworkers designed and implemented a cell-free non-enzymatic DNA-based molecular automaton which released a coagulation inhibitor when the input, thrombin, exceeded a predefined threshold.[23] Expanding the range of inputs available for DNA-based molecular automatons in chapter 4 we introduced antibody-templated strand exchange allowing the translation of an antibody to a unique DNA strand. While non-enzymatic circuits are capable of basic information processing functions such as logic operations, amplification and input thresholding, enzymatically-driven systems can display a much broader range of system-level behaviours such as bistability, oscillations and perfect adaptation.[24,25] In chapter 3 we expand the chemical complexity of enzymatically enriched DNA-based circuits by demonstrating that enzymatically-enriched DNA circuits that are capable of displaying higher-order regulatory behaviour can be connected to biochemical actuators *in vitro*. Also making use of enzymatically-enriched DNA computing, Shapiro and colleagues combined DNA and a restriction enzyme to construct a cell-free circuit that detects the levels of mRNA disease indicators and in response produces an output ssDNA which affects gene expression.[26] Taking this a step further, this technology can be applied to communicate with cells as these sense and respond to their environment, and each other, using extracellular molecules. Bentley *et al.*[27] engineered nanofactories, *i.e.* macromolecules consisting of modules that can target, sense and synthesize molecules, to trigger communication between different bacterial populations. Their design comprises an antibody to selectively target the outer-membrane of bacteria where it triggers a quorum sensing response by means of cell-surface synthesis and

delivery of quorum signalling molecules (Figure 6.1B). In addition, the technology was used to trigger communication between two bacterial populations that otherwise are non-communicative.

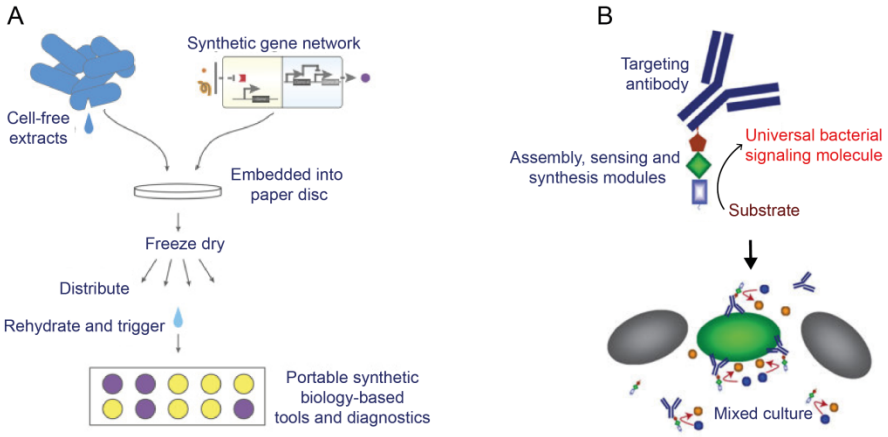

Figure 6.1: Selected emerging applications of engineered biomolecular circuits in the fields of cell-free biosensing and cell-free nanofactories. A) Usage of synthetic-biology-based technologies outside the laboratory is facilitated by paper-based technology where cell-free genetic networks are freeze-dried and, after distribution, reactivated by rehydration. Figure from reference 21. B) Biological nanofactories consisting of a targeting (cell targeting antibody), sensing, synthesis and assembly module. The nanofactories bind specifically to the targeted bacteria (green circle) and trigger the quorum sensing response. Figure from reference 26.

Molecular circuits which are able to receive and respond to specific signals from their environment could be used as diagnostic and/or therapeutic devices. Using these circuits in cells is rather challenging. For example, cellular uptake efficiency and timing, cell viability, lifetime of the nanofactories in cells, the effect of macromolecular crowding on the performance of the nanofactories and the activation of the immune response are just a few examples of limitations to overcome.[28] Yet, several molecular circuits have been developed that operate within cells. For example, Modi and coworkers engineered a DNA-based nanomachine allowing the detection and visualization of the pH of endosomal pathways in living cells[29] and, additionally, the pH-sensor could map multiple pathways simultaneously.[30] In addition, Pei et al. constructed a DNA logic-gate system based on a tetrahedral DNA nanostructure which changed its shape in response to intracellular ATP.[31] This demonstrates the potential of employing a DNA nanostructure to sense and respond to an intracellular signal, which is essential for any 'smart drug' system. In addition, nanoflares, which consist of gold nanoparticles functionalized with DNA oligonucleotides, have been shown to be able to detect and regulate intracellular mRNA levels via strand displacement reactions[32-34] and can be used to detect tumor cells from human blood.[35] DNA strand displacement reactions have also shown to be a valuable method for logic gate operations in living cells to detect

combinations of miRNA[36] or for the *in vivo* assembly of a functional siRNA to control gene expression.[37]

Biochemical nanofactories have great promise in the fields of biomolecular diagnostics and therapeutics. Encapsulation these molecular systems in liposomes, often referred to as synthetic minimal cells, allow biochemical reactions to proceed in an isolated controlled environment. Here we highlight several studies and applications of these synthetic minimal cells. Mansy and coworkers engineered artificial, non-living cellular mimics to activate (or repress) existing sensory pathways of living cells through chemical communication.[38] They expanded the senses of *E. coli* by adding liposomes containing a genetic network that converts a chemical message that *E. coli* cannot sense to a molecule that activates a natural cellular response (Figure 6.2A). This approach paves the way to revolutionize the treatment of bacterial infections as molecules that interrupt or modulate bacterial communication rather than their viability exert less selective pressure to develop resistance. This approach may allow for new opportunities in engineering cellular behaviour without exploiting genetically modified organisms. On a similar line, a recent study showed for the first time that artificial liposome-based cellular mimics containing the machinery for protein expression can be used for the production of anticancer proteins inside tumors in *in vivo* mice models.[39] The authors developed a platform where liposomes were able to interact with their environment via diffusion of low-molecular weight nutrients over the membrane prolonging protein expression inside the tumors. Moreover, the anticancer proteins possessed a translocation domain directing the proteins across the lipid membrane. Synthetic minimal cells might represent a new drug delivery approach in the treatment for cancer or other diseases as these platforms might be powerful for the controlled production of drugs according to a predefined algorithm at the disease site and when desired. Demonstrating the versatility of liposome-based synthetic minimal cells, Boyden and coworkers engineered multiple genetic cascades in liposomes controlled by external signals.[40] Moreover, they showed communication between liposomes and controlled fusion of liposomes so that products of incompatible reactions can be brought together. In addition, the incorporation of mechanosensitive channels in the membrane allows non-permeable liposomes to sense the osmotic pressure and adapt accordingly, as shown by Liu and coworkers.[41] To this end, they co-expressed the *E. coli* channel MscL together with a biosensor which fluoresces upon binding of calcium in the liposomes (Figure 6.1B). MscL senses an increase in membrane tension and opens a pore allowing the diffusion of molecules down the concentration gradient. The mechanosensitive

liposomes were capable of sensing the osmotic pressure and allowed the influx of calcium under hypo-osmotic shock. This approach provides increased mechanical robustness to non-permeable liposomes and, additionally, allows the passage of small nutrients to fuel synthetic cells on demand while keeping the protein expression machinery inside.

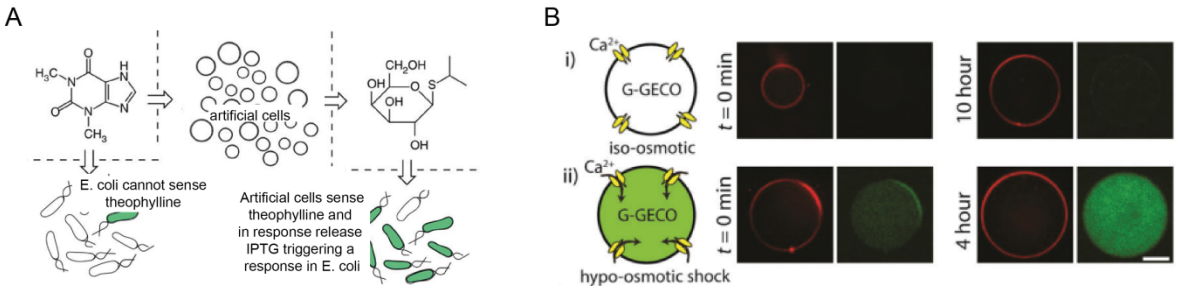

Figure 6.2: Engineered artificial non-living cellular mimics based on liposomes. A) Cellular mimics activate (or repress) natural sensory pathways in living cells through chemical communication, allowing new opportunities in controlling cellular behaviour without the use of genetically modified organisms. Figure from reference 37. B) Expressing MscL in liposomes enables the influx of calcium under hypo-osmotic shock and, thereby, provides increased mechanical robustness to the vesicles and allows the passage of small nutrients. Figure from reference 40.

Other interesting applications of engineered circuits may arise from the coupling of biochemical and mechanical processes. Mechano-chemical conversions are abundant in living systems, which are able to mechanically respond to a changing chemical environment. However, although being a highly desired property for next-generation materials and biosensors, mechano-chemical feedback is generally lacking in synthetic systems. Interesting in this respect is the development of Self-regulated Mechano-chemical Adaptively Reconfigurable Tunable Systems (SMARTS) by Aizenberg and coworkers.[42] This technology utilizes catalyst-bearing microstructures embedded into a hydrogel which mechanically deforms upon a biochemical signal. In this way for instance a pH change can switch on/off an optical output producing biochemical process (Figure 6.3). The vast variety of switchable biochemical reactions in combination with the wide variety of triggers that induce a hydrogel response (ranging from pH, glucose or other metabolic compounds, light to temperature) and the range of possible outputs (*i.e.* fluorescence, gas generation, visible colour change) paves the way for a new generation of bio-responsive materials and biosensors that can autonomously function in and on the human body.

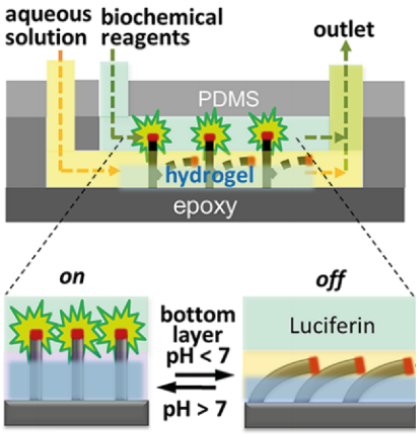

Figure 6.3: A signal converter translating chemical signals at the nanoscale (pH changes) to macroscopic optical outputs using chemo-mechanical feedback loops. Figure from reference 41.

6.5 Conclusion

Cell-free synthetic biology relies on the controllable construction of molecular networks, which are completely defined and can be easily manipulated. The developments made in the field of cell-free synthetic biology drive fundamental understanding of complex signalling circuits. In this thesis DNA-based reaction networks were systematically increased in complexity using a learning-by-building approach. Our work shows the possibility of connecting enzymatically-enriched DNA circuits that are capable of displaying higher-order regulatory behaviour to biochemical actuators *in vitro*, such as a TEM1 β-lactamase and a luciferase based system. Such efforts should be expanded to networks based on other platforms, for example those based on solely DNA, genelets or transcription-translation. In addition, we introduce a generic approach, based on antibody-templated strand exchange, enabling the use of antibodies as input for DNA-based computing and the actuation of 3D DNA-nanoarchitectures. As a generic mechanism that allows protein-based control of DNA circuits, antibody-templated strand exchange complements developed molecular approaches for DNA-based control of protein activity. Such platforms can be integrated expanding the range of combinations of inputs received and processed by DNA-based circuits and the outputs produced by these circuits. Besides expanding network structures, input and output functions we explored the effect of macromolecular crowding on the variability of biochemical processes, a phenomenon which cannot be ignored in cells. We found that decreasing diffusion coefficients and the formation of spatial heterogeneous

microenvironments increased translational bursting and enhanced uncorrelated noise of gene expression. Our experiments and simulations enabled us not only to take into account, but also predict the magnitude of noise when engineering synthetic biochemical pathways in artificial cellular mimics. Finally, the engineered synthetic platforms and concomitant knowledge serve to affect and mimic cellular signaling pathways that can be applied in fields such as diagnostics, therapeutic, autonomous materials, and eventually, in the far future, could result in the construction of an artificial cell with programmed behaviour.

6.6 References

1. Nakajima, M. et al. Reconstitution of circadian oscillation of cyanobacterial KaiC phosphorylation in vitro. *Science* **308**, 414-415 (2005).
2. Coyle, S.M. & Lim, W.A. Mapping the functional versatility and fragility of Ras GTPase signaling circuits through in vitro network reconstitution. *eLife* **5**, e12435 (2016).
3. Sokolova, E. et al. Enhanced transcription rates in membrane-free protocells formed by coacervation of cell lysate. *Proc. Natl. Acad. Sci. U.S.A.* **110**, 11692-11697 (2013).
4. Hansen, M.M.K. et al. Protein synthesis in coupled and uncoupled cell-free prokaryotic gene expression systems. *ACS Synth. Biol.* **5**, 1433-1440 (2016).
5. Shin, J. & Noireaux, V. An E. coli Cell-Free Expression Toolbox: Application to Synthetic Gene Circuits and Artificial Cells. *ACS Synth. Biol.* **1**, 29-41 (2012).
6. Montero Llopis, P. et al. Spatial organization of the flow of genetic information in bacteria. *Nature* **466**, 77-81 (2010).
7. Kim, S., Mlodzianoski, M., Bewersdorf, J. & Jacobs-Wagner, C. Probing spatial organization of mRNA in bacterial cells using 3D super-resolution microscopy. *Biophys. J.* **102**, 278a (2012).
8. Ozbudak, E.M., Thattai, M., Kurtser, I., Grossman, A.D. & van Oudenaarden, A. Regulation of noise in the expression of a single gene. *Nat. Genet.* **31**, 69-73 (2002).
9. Genot, A.J., Fujii, T. & Rondelez, Y. In vitro regulatory models for systems biology. *Biotechnol. Adv.* **31**, 789-796 (2013).
10. Kim, J., White, K.S. & Winfree, E. Construction of an in vitro bistable circuit from synthetic transcriptional switches. *Mol. Syst. Biol.* **2**, 68-68 (2006).
11. Montagne, K., Plasson, R., Sakai, Y., Fujii, T. & Rondelez, Y. Programming an in vitro DNA oscillator using a molecular networking strategy. *Mol. Syst. Biol.* **7**, 466 (2011).
12. Padirac, A., Fujii, T. & Rondelez, Y. Bottom-up construction of in vitro switchable memories. *Proc. Natl. Acad. Sci. U.S.A.* **109**, 3212-3220 (2012).
13. Kim, J. & Winfree, E. Synthetic in vitro transcriptional oscillators. *Mol. Syst. Biol.* **7**(2011).
14. Wong, W.W., Tsai, T.Y. & Liao, J.C. Single-cell zeroth-order protein degradation enhances the robustness of synthetic oscillator. *Mol. Syst. Biol.* **3**, 130 (2007).
15. Fujii, T. & Rondelez, Y. Predator - prey molecular ecosystems. *ACS Nano* **7**, 27-34 (2013).
16. Kim, J., Hopfield, J. & Winfree, E. *Neural Network Computation by In Vitro Transcriptional Circuits*, (MIT Press, 2004).
17. Genot, A.J., Fujii, T. & Rondelez, Y. Computing with Competition in Biochemical Networks. *Phys. Rev. Lett.* **109**, 208102 (2012).
18. Lim, W.A. Designing customized cell signalling circuits. *Nat. Rev. Mol. Cell Biol.* **11**, 393 (2010).
19. Hammer, D.A. & Kamat, N.P. Towards an artificial cell. *FEBS Lett.* **586**, 2882-2890 (2012).
20. Blain, J.C. & Szostak, J.W. Progress toward synthetic cells. *Annual Review of Biochemistry* **83**, 615-640 (2014).
21. Pellinen, T., Huovinen, T. & Karp, M. A cell-free biosensor for the detection of transcriptional inducers using firefly luciferase as a reporter. *Anal. Biochem.* **330**, 52-57 (2004).
22. Pardee, K. et al. Paper-Based Synthetic Gene Networks. *Cell* **159**, 940-954 (2014).
23. Han, D. et al. A logical molecular circuit for programmable and autonomous regulation of protein activity using DNA aptamer–protein interactions. *J. Am. Chem. Soc.* **134**, 20797-20804 (2012).
24. Tyson, J.J., Chen, K.C. & Novak, B. Sniffers, buzzers, toggles and blinkers: dynamics of regulatory and signaling pathways in the cell. *Curr. Opin. Cell Biol.* **15**, 221-231 (2003).
25. Van Roekel, H.W.H. et al. Programmable chemical reaction networks: emulating regulatory functions in living cells using a bottom-up approach. *Chem. Soc. Rev.* **44**, 7465-7483 (2015).
26. Benenson, Y., Gil, B., Ben-Dor, U., Adar, R. & Shapiro, E. An autonomous molecular computer for logical control of gene expression. *Nature* **429**, 423 (2004).
27. Fernandes, R., Roy, V., Wu, H.-C. & Bentley, W.E. Engineered biological nanofactories trigger quorum sensing response in targeted bacteria. *Nat. Nanotech.* **5**, 213 (2010).
28. Chen, Y.-J., Groves, B., Muscat, R.A. & Seelig, G. DNA nanotechnology from the test tube to the cell. *Nat. Nanotechnol.* **10**, 748-760 (2015).

29. Modi, S. et al. A DNA nanomachine that maps spatial and temporal pH changes inside living cells. *Nat. Nanotechnol.* **4**, 325 (2009).
30. Modi, S., Nizak, C., Surana, S., Halder, S. & Krishnan, Y. Two DNA nanomachines map pH changes along intersecting endocytic pathways inside the same cell. *Nat. Nanotechnol.* **8**, 459-467 (2013).
31. Pei, H. et al. Reconfigurable three-dimensional DNA nanostructures for the construction of intracellular logic sensors. *Angew. Chem. Int. Ed.* **51**, 9020-9024 (2012).
32. Rosi, N.L. et al. Oligonucleotide-modified gold nanoparticles for intracellular gene regulation. *Science* **312**, 1027-1030 (2006).
33. Alhasan, A.H., Patel, P.C., Choi, C.H.J. & Mirkin, C.A. Exosome encased spherical nucleic acid gold nanoparticle conjugates as potent microRNA regulation agents. *Small* **10**, 186-192 (2014).
34. Prigodich, A.E. et al. Nano-flares for mRNA Regulation and Detection. *ACS Nano* **3**, 2147-2152 (2009).
35. Halo, T.L. et al. NanoFlares for the detection, isolation, and culture of live tumor cells from human blood. *Proc. Natl. Acad. Sci. U.S.A.* **111**, 17104-17109 (2014).
36. Hemphill, J. & Deiters, A. DNA computation in mammalian cells: MicroRNA logic operations. *J. Am. Chem. Soc.* **135**, 10512-10518 (2013).
37. Afonin, K.A. et al. Activation of different split functionalities upon re-association of RNA-DNA hybrids. *Nat. Nanotechnol.* **8**, 296-304 (2013).
38. Lentini, R. et al. Integrating artificial with natural cells to translate chemical messages that direct E. coli behaviour. *Nat. Commun.* **5**, 4012 (2014).
39. Krinsky, N. et al. Synthetic cells synthesize therapeutic proteins inside tumors. *Adv. Healthc. Mater.*, 1701163-n/a.
40. Adamala, K.P., Martin-Alarcon, D.A., Guthrie-Honea, K.R. & Boyden, E.S. Engineering genetic circuit interactions within and between synthetic minimal cells. *Nat. Chem.* **9**, 431-439 (2017).
41. Majumder, S. et al. Cell-sized mechanosensitive and biosensing compartment programmed with DNA. *Chem. Commun.* **53**, 7349-7352 (2017).
42. He, X., Friedlander, R.S., Zarzar, L.D. & Aizenberg, J. Chemo-Mechanically Regulated Oscillation of an Enzymatic Reaction. *Chem. Mater.* **25**, 521-523 (2013).

Summary

The cell is composed of many biomolecules interacting in a high non-linear fashion in a crowded environment. These biomolecules form complex sets of interactions enabling the cell to respond to input cues, to withstand perturbations and to adapt to environmental changes. The main goal of cell-free synthetic biology is to obtain a deeper understanding of the *modus operandi* of molecular networks inside living cells by emulating a target property or feature of the cell. The goal of this thesis is to expand the scope of DNA-based molecular networks by developing tools enriching these networks and providing additional knowledge of biomolecular reactions in cells. To this end, we extended reaction networks based on the polymerase-exonuclease-nickase (PEN) toolbox. The PEN toolbox, developed by Rondelez and co-workers, allows the construction of biochemical circuits emulation complex dynamic behaviour in time and space similar to those in natural cells. We first implemented an INVERTER circuit and a previously designed bistable switch and introduced a heuristic model which we used for the detailed characterization of PEN-based networks. While regulatory circuits in cells control downstream processes through hierarchical layers of signal processing, coupling of enzymatically-driven DNA-based networks to downstream processes has rarely been reported. We engineered hierarchical control of enzymatic actuators using the PEN-based bistable switch. We developed a translator module which converted signaling molecules from the upstream network to unique DNA strands driving downstream actuators with minimal retroactivity and supported these findings with a detailed computational analysis. We showed our approach by coupling of a previously engineered switchable memories circuit to downstream actuators based on β-lactamase and luciferase. Moreover, while in general low retroactivity is desired, our work showed that retroactivity not necessarily has a negative effect. To further expand the scope of DNA-based molecular programming, we introduced a generic approach, based on antibody-templated strand exchange (ATSE), enabling the use of antibodies as input for DNA-based computing. In this thesis we developed a comprehensive model that described the kinetics of the ATSE system. The model provided a fundamental understanding of the ATSE reaction and was used to find optimal concentration regimes and to study the effect of thermodynamics and kinetics of antibody–epitope binding

While cell-free biochemical reaction networks are often studied at high reactant concentrations in a well-stirred environment, the cell's interior is an inhomogeneous crowded environment where reactions between biomolecules occur at low concentrations. Low

concentrations of biomolecules result in stochastic gene expression in cells. However, it is unknown how the physical environment contributes to the variation in signaling circuits. In this thesis, we studied the variation in cell-free gene expression as a function of plasmid copy number and macromolecular crowding. To support the experimental findings and to obtain a detailed characterization of the experimental setup we developed two independent theoretical models. We found that decreasing diffusion coefficients and the formation of heterogeneous micro-environments caused by macromolecular crowding enhance uncorrelated noise in gene expression.

The cell-free networks developed in this thesis can provide further fundamental insights into biochemical reaction networks and correlated function, and/or can be applied in molecular therapeutics or diagnostics. Finally, in the far future, such molecular networks can aid in the construction of a synthetic cell with preprogrammed behaviour.

Samenvatting

De cel bestaat uit enorm veel verschillende biomoleculen die via niet-lineaire processen met elkaar reageren in een omgeving volgepakt met macromoleculen. Deze biomoleculen vormen door hun interacties complexe signaalnetwerken waardoor de cel specifieke moleculen uit de omgeving kan ontvangen, verwerken, en hierop kan reageren. Hierdoor is de cel bestand tegen verstoringen of kan zich aanpassen aan veranderingen in de omgeving. Het voornaamste doel van het onderzoeksveld van de celvrije synthetische biologie is het begrijpen van de *modus operandi* van biomoleculaire netwerken in cellen door het emuleren van specifieke cellulaire eigenschappen. In dit proefschrift worden nieuwe modules of methodes beschreven die biomoleculaire signaalsystemen verrijken en potentieel aanvullende kennis bieden over reacties in cellen. Allereerst beschrijven we de ontwikkeling van een vertaalmodule die reactienetwerken gebaseerd op de polymerase-exonuclease-nickase-methode (PEN-methode) verrijkt. De PEN-methode is ontwikkeld door Rondelez en collegae. Deze methode kan toegepast worden om netwerken te construeren die complex gedrag in de tijd en de ruimte vertonen dat overeenkomstig is met dat van natuurlijke cellen. We implementeren een INVERTER-netwerk en een eerder ontwikkeld netwerk dat bistabiel gedrag vertoont. Regulerende netwerken in de cel vormen een hiërarchische structuur waarbij geproduceerde signalen als regulator dienen voor andere biochemische processen. De koppeling van op DNA gebaseerde enzymatisch gedreven netwerken aan andere biochemische processen is echter nauwelijks gerapporteerd in de literatuur. In dit proefschrift laten we zien dat het mogelijk is om twee verschillende op enzymen gebaseerde actuators aan te sturen via een PEN-gebaseerd systeem dat bistabiel gedrag vertoont. We hebben een vertaalmodule ontwikkeld die signaalmoleculen van het PEN-gebaseerd netwerk vertalen naar unieke DNA-sequenties die de actuators aansturen. Hierbij hebben we ervoor gezorgd dat de retroactiviteit die ontstond bij het koppelen van de modules zo laag mogelijk bleef. We hebben onze bevindingen ondersteund met behulp van een theoretisch model, en hebben de functionaliteit van de translatormodule laten zien door middel van het koppelen van het bistabiele netwerk aan actuators gebaseerd op β-lactamase en luciferase. Terwijl over het algemeen een lage retroactiviteit gewenst is, laten we in dit proefschrift zien dat retroactiveit niet altijd een negatief effect heeft op het gedrag van het netwerk.

Om de variëteit aan types moleculen die ontvangen kunnen worden door op DNA gebaseerde netwerken uit te breiden, beschrijven we het principe van antilichaam-geïnduceerde

uitwisseling van DNA-strengen (AGUD). De AGUD-methode zorgt ervoor dat de aanwezigheid van een antilichaam wordt vertaald naar een DNA-streng die vervolgens gebruikt wordt in het op DNA gebaseerde netwerk. We hebben een theoretisch model ontwikkeld dat de kinetiek van het AGUD-systeem beschrijft. Het model werd gebruikt om de optimale concentratiegebieden van de reagerende moleculen te vinden, en om het effect van de thermodynamische en kinetische eigenschappen van de binding tussen antilichaam en epitoop op het AGUD-systeem te bestuderen.

Celvrije signaalsystemen worden meestal bestudeerd bij hoge concentraties van de reagerende moleculen in een homogene omgeving. De inhoud van een cel, daarentegen, is een heterogene omgeving die volgepakt is met macromoleculen waarin reacties tussen moleculen bij lage concentraties plaatsvinden. Door de lage concentraties van reagentia is genexpressie in cellen een stochastisch proces. Het is echter onbekend hoe de fysische omgeving bijdraagt aan de variatie in signaalnetwerken. In dit proefschrift hebben we de variatie in genexpressie in een celvrije omgeving als functie van het aantal plasmiden en de concentratie van macromoleculen bestudeerd. We hebben twee afzonderlijke theoretische modellen ontwikkeld om de experimentele bevindingen te ondersteunen en om een gedetailleerd begrip van de experimentele opzet te krijgen. Onze bevindingen laten zien dat een afname in diffusiecoëfficiënt en de vorming van heterogene micro-omgevingen door de aanwezigheid van macromoleculen de variatie in genexpressie verhogen.

De celvrije netwerken die ontwikkeld en beschreven zijn in dit proefschrift verlenen verdere inzichten in de organisatie en functie van signaalnetwerken en/of kunnen in de toekomst mogelijk toegepast worden in moleculaire therapie of diagnostiek. Uiteindelijk kunnen dergelijke moleculaire netwerken hun toepassing vinden in de constructie van een synthetische cel met voorgeprogrammeerd gedrag.

Curriculum Vitae

Lenny Meijer was born on December 18th, 1988 in Sint Hubert, the Netherlands. After she obtained her athenaeum at the Elzendaal College in Boxmeer, she studied biomedical technology at the Eindhoven University of Technology. During this program, she performed an internship in the research group of prof. dr. W.T.S. Huck where she studied the effect of plasmid copy number on the variation in gene expression in a cell-free set-up. During her graduation project in the research group of prof. E.W. Meijer she engineered adaptation in DNA-based enzymatic networks *in vitro* using *in silico* models. Additionally to the ordinary master's program she followed the graduate program of the Institute for Complex Molecular Systems which included additional courses and an additional internship in the group of prof. dr. S. Han. After receiving her master's degree (with great appreciation) in 2014, Lenny started her PhD research under supervision of prof. dr. P.A.J. Hilbers, prof. dr. M. Merkx and dr. T.F.A. de Greef. Lenny's research focused on the engineering of signaling circuits using a cell-free synthetic biology approach. The highlights of this research are presented in this thesis.

Lenny Meijer werd geboren op 18 december 1988 te Sint Hubert. Nadat zij in 2007 haar VWO heeft gehaald aan het Elzendaal College te Boxmeer, begon zij aan de opleiding Biomedische Technologie aan de Technische Universiteit Eindhoven. Tijdens deze opleiding heeft zij stage gelopen in de onderzoeksgroep van prof. dr. W.T.S. Huck waar zij het effect van aantal plasmiden op de variatie in genexpressie onderzocht in een cel-vrije setting. Tijdens haar afstudeerproject werkte zij in de groep van prof. dr. E.W. Meijer aan het ontwerpen van een *in vitro* DNA-gebaseerd enzymatisch netwerk dat adaptatie vertoont met behulp van *in silico* modellen. Naast het curriculaire traject nam zij deel aan het programma van het Institute for Complex Molecular Systems waar zij extra vakken heeft gehaald en een een stage heeft gelopen in de groep van prof. dr. S. Han. Na het behalen van haar masterdiploma (met grote waardering) in 2014 begon Lenny haar promotieonderzoek onder leiding van prof. dr. P.A.J. Hilbers, prof. dr. M. Merkx en dr. T.F.A. de Greef. In dit onderzoek richtte zij zich op het ontwerpen van signaalnetwerken gebruikmakend van celvrije synthetische biologie. De belangrijkste resultaten van dit onderzoek staan beschreven in dit proefschrift.

List of publications

Lenny H.H. Meijer, Alex Joesaar, Erik Steur, Wouter Engelen, Rutger A. van Santen, Maarten Merkx and Tom F.A. de Greef. Hierarchical control of enzymatic actuators using DNA-based switchable memories. *Nat. Commun.,* **2017**, 8, 1117

Wouter Engelen, Kayleigh M. van de Wiel, Lenny H.H. Meijer, Bedabrata Saha and Maarten Merkx. Nucleic acid detection using BRET-beacons based on bioluminescent protein-DNA hybrids. *Chem. Commun.,* **2017**, 53, 2862

Wouter Engelen, Lenny H.H. Meijer, Bram Somers, Tom F.A. de Greef and Maarten Merkx. Antibody-controlled actuation of DNA-based molecular circuits. *Nat. Commun.,* **2017**, 8, 14473

Maike M.K. Hansen, Lenny H.H. Meijer, Evan Spruijt, Roel J.M. Maas, Marta Ventosa Roquelles, Joost Groen, Hans A. Heus and Wilhelm T.S. Huck. Macromolecular crowding creates heterogeneous environments of gene expression in picolitre droplets. *Nat. Nanotech.*, **2016**, 11, 191

Chi-Yuan Cheng, Jinsuk Song, Jolien Pas, Lenny H.H. Meijer and Songi Han. DMSO Induces Dehydration near Lipid Membrane Surfaces. *Biophys. J.*, **2015**, 109, 330

Hendrik W.H. van Roekel[ǂ], Bas J.H.M. Rosier[ǂ], Lenny H.H. Meijer[ǂ], Peter A.J. Hilbers, Albert J. Markvoort, Wilhelm T.S. Huck and Tom F.A. de Greef. Programmable chemical reaction networks: emulating regulatory functions in living cells using a bottom-up approach. *Chem. Soc. Rev.*, **2015**, 44, 7465

Hendrik W.H. van Roekel, Lenny H.H. Meijer, Saeed Masroor, Zandra C. Félix Garza, André Estévez-Torres, Yannick Rondelez, Antonios Zagaris, Mark A. Peletier, Peter A.J. Hilbers and Tom F.A. de Greef. Automated design of programmable enzyme-driven DNA circuits. *ACS Synth. Biol.,* **2014**, 4, 735

ǂ contributed equally to this work

Dankwoord

De afgelopen vier jaar is een bijzondere tijd geweest waar ik met een goede blik op zal terugkijken. Dit proefschrift is echter niet alleen door mij tot stand gekomen, maar ook dankzij vele anderen die ik hier graag wil bedanken.

Professor Hilbers, beste Peter, ik wil u hartelijk danken voor het vertrouwen in mij om dit onderzoek te kunnen doen. Verder wil ik u graag bedanken voor uw hulp en advies en voor de prettige and stimulerende sfeer die u creëert in de groep waardoor ik altijd met plezier aanwezig was tijdens meetings en groepsuitjes.

Professor Merkx, beste Maarten, als tweede promotor wil ik jou bedanken voor de fijne begeleiding en samenwerking. Naast je kritische blik en waardevolle suggesties waardeer ik je manier van begeleiden en communiceren enorm. Ik denk dat de samenwerking een mooi resultaat heeft opgeleverd.

Dr. de Greef, beste Tom, onder jou directe begeleider als copromotor heb ik dit proefschrift geschreven. Heel erg bedankt voor je stimulerende begeleiding en hulp. Naast de vele inzichten in complex gedrag, heb ik dankzij jou flinke stappen gemaakt in het schrijven van een goed wetenschappelijk artikel. Het was een eer om een van de eerste PhD-studenten in jouw groep te zijn en om te zien hoe je groep de afgelopen tijd is gegroeid. Daar hebben jouw passie en ongekende kennis van de literatuur een belangrijke rol bij gespeeld. Hartelijk dank voor de afgelopen vier jaar.

Graag wil ik ook de leden van mijn promotiecommissie bedanken. Allereerst prof. Luc Brunsveld, dank u voor het voorzitten van de commissie. Ook wil ik prof. Ilja Voets, prof. Kees Storm, prof. Pascal Jonkheijm en dr. Evan Spruijt hartelijk danken voor het kritisch lezen en beoordelen van mijn proefschrift en de deelname aan de promotiezitting.

I would like to thank all the members and old-members of the CBio group, Biolab and the Chemical Biology group for the fruitful discussions and suggestions during meetings, and for the pleasant lunches, parties, retreats, and great working environment. I wish you all the best with your PhDs, postdocs, and future careers. I would also like to thank the members and old-members of the Macro-Organic Chemistry group of Bert Meijer, the Molecular Materials and Nanosystems group of René Janssen, and the Supramolecular Polymer Chemistry group of Rint Sijbesma, for the discussions and suggestions during meetings and colloquia.

Hierbij wil ik meteen Rina, Marjo, Margot, Martina, Carla, Cindy en Thea bedanken voor het regelen van verschillende zaken en de bereidheid om altijd te helpen. Ook Hans wil ik bedanken voor alle bestellingen die hij heeft geregeld. Henk, zonder jou koffie zou de start in de ochtend toch wat langer duren. Bedankt, en natuurlijk ook voor het regelen van andere

zaken van pakketjes versturen tot kantoor reparaties. Een bijzonder woord van dank gaat uit naar Peggy voor het managen van het biolab. Ik waardeer het heel erg dat je zorgt dat alles op orde is en een veilige werkomgeving creëert.

Natuurlijk wil ik ook graag de mensen bedanken met wie ik intensief heb samengewerkt en die een grote bijgedrage hebben geleverd aan de projecten beschreven in dit proefschrift. Wat begon als een stage tijdens mijn master, is één van mijn projecten tijdens mijn promotie geworden. Beste prof. Wilhelm Huck, ik bewonder de experimentele vaardigheden en kennis in uw groep enorm en heb erg veel geleerd in uw groep waar ik u graag voor wil bedanken. Dr. Hansen, beste Maike, heel erg bedankt voor jou goede begeleiding en de samenwerking die ik zal blijven herinneren als heel productief en ook als zeer plezierig. Ik wens je veel succes en geluk voor de toekomst! Wouter, ik denk dat jou experimentele vaardigheden in combinatie met mijn kennis van modelleren tot mooie resultaten heeft geleid waar we trots op kunnen zijn. Je bent een enthousiast persoon en altijd in voor een praatje, zowel werk gerelateerd als op persoonlijk vlak. Ik wens je heel veel succes met het afronden van jou proefschrift en heel veel succes en geluk samen met Nirja in München. Beste dr. Erik Steur en prof. Rutger van Santen, ik wil jullie hartelijk danken voor jullie bijdrage aan het werk van de bistabiele switch. Erik, jou wiskundige kennis heeft ons veel inzicht gegeven in het complexe systeem wat de kwaliteit van het werk zeker heeft verhoogd. Ik wens je veel succes met je verdere carrière. Beste Rik, het is al een tijdje geleden dat jij je promotie hebt afgerond. Ik wil je graag bedanken voor de plezierige en productieve samenwerking die tot mooie resultaten hebben geleid. Ik wens ook jou heel veel geluk en succes in de toekomst.

Hiernaast wil ik nog jullie, Alex, Minke en Paula, bedanken voor al jullie werk tijdens jullie stage. Alex, you were really enthusiastic and motivated as a student and, therefore, a pleasure to guide. I wish you all the best during the rest of your promotion. I am sure you will successfully obtain you doctoral degree. Minke, ik heb je tijdens je afstuderen erg zien groeien en ik vind je een inspirerend persoon. Je bent supergoed in het overbrengen van wetenschappelijke kennis onder andere door je creatieve persoonlijkheid. Wat natuurlijk ook tot uiting komt in de mooie kaft van dit proefschrift, heel erg bedankt hiervoor. Heel veel geluk en succes in Denemarken! Paula, ook over jou heb ik geen twijfel dat je je afstudeerproject goed gaat afronden. Veel succes en natuurlijk ook met jou vervolgcarrière.

Erg belangrijk op het werk is een goede basis. STO 3.26, bedankt voor de super leuke tijd die ik met jullie heb gehad! Rachel and Beda, it was a great time having you in the office with lots of laughter and also serious talks. Sam, Bas en Roy, het grootste deel van mijn PhD

heb ik het kantoor met jullie gedeeld. Ik heb een hele leuke tijd gehad met jullie. Bedankt voor jullie gezelligheid en steun, en natuurlijk de leuke (onbedoelde) woordgrappen! Helaas heb ik deze woordgrappen in dit proefschrift rechts laten liggen. Sam, Roy en Bas, veel succes met het afronden van jullie promotieonderzoek en veel geluk voor de toekomst!

Paranimfen, Lenne en Anniek, ook jullie wil ik natuurlijk bedanken. Anniek, wat een leuke tijden hebben wij gehad. Bedankt voor jou ongekende optimisme, je peptalks en voor het organiseren van verschillende uitjes. Ik denk dat ik niet alleen voor mezelf spreek als ik zeg dat je een motiverend en stimulerend persoon bent. En natuurlijk ook bedankt voor de boost van mijn danscarrière. Ik wens jou samen met Ronald heel veel geluk en alle goeds voor de toekomst! Lenne, ook jij bedankt voor jou gezelligheid en steun. Jou humor maakte voor mij iedere dag nog leuker en altijd stipt om twaalf uur ben je klaar voor de lunch wat ik erg waardeer en waar velen van kunnen leren. Ik wens jou heel veel geluk samen met Maaike en veel succes met het afronden van jou PhD!

Om goed werk af te leveren is ontspanning heel erg belangrijk. Sam, Maarten, Loes, Wouter, Eva, Jurgen, Anniek, Bas, Sjors, Wouter, Eline en Dan Jing bedankt voor de leuke feestjes en festivals! Dan Jing, het was een eer een tent met je te delen bij Lowlands! Anniek, Lenne en Dan Jing, bedankt voor de leuke etentjes, dat we nog vele verschillende frieten mogen gaan proeven! BMT meiden Berly, Laura, Annette, Nicole en Ashley, bedankt voor alle gezellige high teas en borreltjes. Ik hoop dat we dit nog lange tijd doen! Ook wil ik graag mijn oude schoolvrienden, Eline, Emy, Pien, Loes, Ilse, Mark, Luc en Gijs bedanken voor de leuke uitjes, weekendjes en etentjes. Ik ben blij dat we elkaar na al die jaren nog steeds zien!

Een woord van dank aan mijn schoonfamilie. Boujema, Fadma, Amine, Laila, Nora en Seloua, bedankt voor jullie warme welkom en al jullie steun en hulp de afgelopen jaren!

Pap en mam, jullie hebben me de basis gegeven in het leven en altijd gemotiveerd om te doen wat ik leuk vind. Bedankt voor alles wat jullie hebben gedaan en doen voor ons en voor jullie onvoorwaardelijke steun en hulp! Mijn zussen, Hanneke, Ilse en Tineke, bedankt voor jullie steun en gezelligheid. Ik ben dankbaar dat we elkaar regelmatig zien en leuke dingen ondernemen! En ook wil ik mijn schoonbroers Frank en Ralf en mijn neefjes Ben, Otto en Ties en nichtje Fien bedanken voor de gezelligheid die jullie brengen in onze familie.

De laatste woorden zijn voor de persoon die mijn promotieonderzoek van het meest dichtbij heeft ervaren. Lieve Youssef, bedankt voor alle mooie jaren samen en je geduld als ik weer eens niet op tijd thuis was voor het eten. Letterlijk en figuurlijk hebben we al heel wat bergen beklommen. Je hebt me altijd gesteund in wat ik ook doe en geeft me het vertrouwen dat ik het kan. Ik ben een gelukkig mens samen met jou! Ik kijk uit naar de toekomst!